SYNTHESIS AND CHARACTERIZATION OF ADVANCED MULTIFUNCTIONAL MAGNETIC NANOPARTICLES FOR BIOMEDICAL APPLICATIONS

A thesis submitted in partial fulfilment of the requirements for the degree of

Doctor of Philosophy
in

NANOSCIENCE AND TECHNOLOGY

By
MOHD QASIM
(12ENPH03)

Under the guidance of
PROF. DIBAKAR DAS

SCHOOL OF ENGINEERING SCIENCES AND TECHNOLOGY
UNIVERSITY OF HYDERABAD
HYDERABAD-500046
INDIA

2017

DEDICATED TO MY PARENTS

Mr. Mohd Zameer

and

Mrs. Tahera Khatoon

DECLARATION

I, **Mohd Qasim**, hereby declare that the work embodied in this thesis entitled, "**Synthesis and Characterization of Advanced Multifunctional Magnetic Nanoparticles for Biomedical Applications**" submitted to **School of Engineering Sciences and Technology, University of Hyderabad** for partial fulfilment of the requirements for award of **Doctor of Philosophy** in **Nanoscience and Technology** is a bonafide work carried out by me under the supervision of **Dr. Dibakar Das,** Professor, School of Engineering Sciences and Technology, University of Hyderabad. I also declare that this work has not been submitted previously in part or in full to this University or any other University or Institution for the award of any degree or diploma.

Mohd Qasim
(12ENPH03)

Place: Hyderabad
Date:

Certificate

This is to certify that the thesis entitled "**Synthesis and Characterization of Advanced Multifunctional Magnetic Nanoparticles for Biomedical Applications**" Submitted by **Mohd Qasim** bearing registration number **12ENPH03 (Ph.D. Nano Science and Technology)** in partial fulfilment of the requirements for award of **Doctor of Philosophy** in the **School of Engineering Sciences and Technology** is a bonafide work carried out by him under my supervision and guidance.

This thesis is free from plagiarism and has not been submitted previously in part or in full to this or any other University or Institution for award of any degree or diploma.
Parts of this thesis have been:

A. published in the following publications:

1. **Mohd Qasim**, K. Asghar, G. Dharmapuri, and D. Das, Investigation of novel superparamagnetic $Ni_{0.5}Zn_{0.5}Fe_2O_4$@albumen nanoparticles for controlled delivery of anti-cancer drug, *Nanotechnology* 28 (2017) 365101
2. **Mohd Qasim**, K. Asghar, Dibakar Das, Facile Synthesis of Fe_3O_4 and multifunctional Fe_3O_4@Albumen Nanoparticles for Biomedical Application, *AIP Proceedings* (2017) 1832, 050116,
3. **Mohd Qasim**, K. Asghar, D. Das, Synthesis and characterization of $Ni_{0.5}Zn_{0.5}Fe_2O_4$@mSiO_2 core shell nanocarrier for drug delivery applications, Chapter 5, *Proceedings of the 3rd Pan-American Materials Congress*, The Minerals, Metals & Materials Series. Springer, Cham (2017) ISBN 978-3-319-52132-9, 47-54
4. **Mohd Qasim**, Braj R Singh, A H Naqvi, P Paik and D Das, Silver nanoparticles embedded mesoporous SiO_2 nanosphere: an effective anticandidal agent against Candida albicans 077, *Nanotechnology* 26 (2015) 285102.
5. **Mohd Qasim**, K Asghar, BR Singh, S Prathapani, W Khan, AH Naqvi, D Das, Magnetically recyclable $Ni_{0.5}Zn_{0.5}Fe_2O_4/Zn_{0.95}Ni_{0.05}O$ nano-photocatalyst: Structural, optical, magnetic and photocatalytic properties, *Spectrochimica Acta Part A: Molecular and Biomolecular Spectroscopy* 137 (2015) 1348–1356.

and

B. presented in the following conferences:

1. **Mohd Qasim**, B. R. Singh, K. Asghar, P. Paik, A. H. Naqvi, and D. Das, "Synthesis and characterization of Ag nanoparticles decorated mesoporous SiO_2 nanosphere and its anticandidal activity against Candida albicans 077", Dec16-20, 2013, IUMRS-ICA 2013, IISc Bangalore.
2. **Mohd Qasim**, K. Asghar, B R. Singh, S. Prathapani, G. Afreen, W. Khan, A.H. Naqvi, D. Das "Structural, optical, thermal, Magnetic and photocatalytic properties of $Ni_{0.5}Zn_{0.5}Fe_2O_4/Zn_{0.95}Ni_{0.5}O$ nanocomposites synthesized by sol-gel using egg albumin" Dec 05-07; 2013, MagMa- 2013, IIT Guwahati
3. **Mohd Qasim**, K. Asghar, P. Paik, D. Das, "Synthesis and Characterization of Multifunctional $Ni_{0.5}Zn_{0.5}Fe_2O_4$/ $Zn_{0.95}Ni_{0.5}O$ Nanocomposites" Feb 19-21, 2014, ICAFM 2014, Thiruvananthapuram.

4. **Mohd Qasim**, B R. Singh, K. Asghar, A. H. Naqvi, D. Das, "Anticandidal activity against Candida albicans077 of Ag nanocrystal decked mesoporous SiO_2 nanoparticle" March 8th – 10th 2014, Aligarh Nano IV International, Aligarh,
5. **Mohd Qasim**, K. Asghar, D. Das, "Multi-functional $Ni_{0.5}Zn_{0.5}Fe_2O_4$/ZnO@mSiO2 and $Ni_{0.5}Zn_{0.5}Fe_2O_4$@$mSiO_2$ core shell nanocomposites" Feb 19-2, 2015, ISNACT-2015, IIT Mumbai
6. **Mohd Qasim**, K. Asghar and D. Das, "Development of Magnetic Protein Nanoparticles for Controlled Release of Anti-Cancer Drug" Oral talk in NICAMPC-2016, 4-6 January 2016, NIT Warangal
7. **Mohd Qasim**, K. Asghar, and D. Das, "Novel Superparamagnetic Protein Nanocarrier for Drug Delivery Application" Oral talk in Aligarh Nano V & STEMCON 16, 12-15 March 2016
8. **Mohd Qasim**, K. Asghar, D. Das, "Facile Synthesis of Fe_3O_4 and multifunctional Fe_3O_4@Albumen Nanoparticles for Biomedical Applications" 61st DAE, SSPS, Dec 26-30, 2016, KIIT, Bhubaneswar
9. **Mohd Qasim,** Dibakar Das, "Mesoporous $CaCO_3$ Based Multifunctional Magnetic Nanoparticles for Anticancer Drug Delivery Application" ICCGREI, IICT 2016, Hyderabad
10. **Mohd Qasim**, K. Asghar, D. Das, "$CoFe_2O_4$ and albumen based multifunctional magnetic protein nanocomposite for biomedical application" oral presentation in ICNANO, 1-3 March 2017, VBRI Allahabad.
11. **Mohd Qasim**, K. Asghar and D. Das, "Green Synthesis of Magnetic Nanoparticle Impregnated Mesoporous $CaCO_3$ Based Multifunctional Nanocarrier for Controlled Delivery of Anticancer drug" Oral talk in Nanotech 2017 held during 3-5 April 2017 in Dubai.

Further, the student has passed the following courses towards fulfilment of coursework requirement for Ph.D.

Course Code	Name	Credits	Pass/Fail
MT801	Research Methodology	4	Pass
NT801	Thermodynamics and Phase Equilibria	4	Pass
NT802	Characterization of Materials	4	Pass
NT803	Advanced Engineering Mathematics	4	Pass
NT804	Seminar	2	Pass
NT805	Concepts of Nano Science and Technology	4	Pass
NT806	Synthesis and Applications of Nanomaterials	4	Pass
NT807	Materials Processing & Characterization Laboratory	4	Pass
NT808	Polymer Science and Technology	2	Pass

Supervisor **Dean of School**

ACKNOWLEDGEMENTS

The whole tenure of my Ph.D journey has been a wonderful learning and overwhelming experience. It has provided me with real learning experience on the importance of multitask while being focused. It has instilled me with essence of research and life through various concepts and interesting people. So, it is my duty to thank each and every one, who was influential in this pivotal period of my life.

First and foremost I wish to offer my sincerest gratitude to my guide ***Prof. Dibakar Das****, for accepting me as his Ph.D student and introducing me with such a fascinating, dynamic and wonderful area of multifunctional magnetic nanoparticles research. He is an excellent human being to work with and has honestly fulfilled his duties of a real supervisor. Under his supervision I really felt freedom and curiosity of learning new things and generating ideas. It has been wonderful and satisfied journey with him during my Ph.D tenure and a lot of thanks for all his inspiring guidance, encouragement, motivation, regular pushes, patience and valuable suggestions throughout my research work.*

I am also very thankful to Dean of SEST ***Prof. Ghanashyam Krishna****, Former Dean* ***Prof. R. Singh and Prof. M. Sundararaman*** *and all other faculties in department for providing me the facilities and the guidance to carry out my research work. In particular I would like to record my gratitude to* ***Dr. Nooruddin Khan (SLS) and Dr. R Chandrasekar (SOC)*** *for their constant encouragement and support during the doctoral committee meetings.*

I would like to acknowledge the financial support ***(2012-13/MANF-2012-13-MUS-UTT-15733)*** *obtained from the Ministry of Minority Affairs, through the University Grants Commission (UGC), in the form of* ***MANF fellowship*** *in carrying out this research work.*

I would like to thank Prof. A.H Naqvi, Prof. Ameer Azam, Dr. Wasi Khan (AMU) as their ideas and concepts have a remarkable influence on my understanding in the field of nanotechnology.

I wish to express my sincere thanks to Dr. B.R Singh, and Dr Jyotsnendu Giri (IITH), for their help, suggestions and encouragements. More particularly my thanks

to Dr. Gangappa Dharmapuri (SLS) for biological test and Dr. B.R Singh for antifungal activity measurements.

I would sincerely like to thank all my lab mates as well as friends Paul Praveen, Khushnuma Asghar, P Parthibhan, Urbashi, Srinivas Indla, Swathi, Vinitha, Chandrakala, Jaishree, Sateesh Prathapani, Nalla Somaiya, Mallesh, Ummen and Mahesh for their constant support, cooperation, providing a joyful environment in the lab and helping me in all ways.

I would like to mention that without continuous support of my friends, completion of this work was not possible, and would like to say a special word of thanks to all my friends, Khushnuma, Parthibhan, Urbashi, Indla, Naga Raju, Akanksha, Sateesh, Shoeb, Faraz, Sharique, and many more.

I would like to thank other research scholars in SEST, Pardhu Sir, Bikas Borah, Pandu Sunil, Mokhtar, Shaikshawali, Hussen, Chander, Sandeep, RV and Varalaxmi and other my friends Sajid, Ehtesham, Fahad, and Akbar bhai, for their direct and indirect help during my Ph.D. I would also like to thank all my department friends for their moral support and good wishes.

I would also like to thank the technicians and non-teaching staff of SEST Venu anna, Balakrishna, Gridhar Sir, Mallesh anna, Malathy madam and Kranthi madam. I would also like to thank Pankaj, Durga Prashad for TEM, Dr Manjunath for VSM, Rajesh Sir for TGA, Sunitha for FESEM and Sandhya madam for UV-Vis spectroscopic measurements.

I would like to acknowledge the technical support received from the School of Engineering Sciences & Technology (SEST), Center for Nanotechnology, Central Instruments Laboratory (CIL), and School of Physics (SOP) at the University of Hyderabad and Center of Excellence in Materials Science (Nanomaterials) Aligarh Muslim University.

Specially, I would like to thank my parents ***Mohd Zameer and Tahera Khatoon*** *for their constant trust, support and encouragement. I would also like to thank my siblings Yasmin Khatoon, Razia, Wasfa and Mohd Asim, and my all family members for their encouragement.*

Contents

List of figures

Chapter 1:

Chapter 3:

Chapter 4:

Section 4.1:

Section 4.2:

Section 4.3:

Section 4.4:

Section 4.5:

Section 4.6:

Section 4.7:

Section 4.8:

List of Publications

(A) List of peer-reviewed publications from the thesis work

1. **Mohd Qasim**, Khushnuma Asghar, G. Dharmapuri, and Dibakar Das, Investigation of novel superparamagnetic $Ni_{0.5}Zn_{0.5}Fe_2O_4$@albumen nanoparticles for controlled delivery of anti-cancer drug, *Nanotechnology* 28 (2017) 365101

2. **Mohd Qasim**, Khushnuma Asghar, Dibakar Das, Facile Synthesis of Fe_3O_4 and multifunctional Fe_3O_4@Albumen Nanoparticles for Biomedical Application, *AIP Proceedings* (2017) 1832, 050116,

3. **Mohd Qasim**, Khushnuma Asghar, Dibakar Das, Synthesis and characterization of $Ni_{0.5}Zn_{0.5}Fe_2O_4$@mSiO_2 core shell nanocarrier for drug delivery applications, Chapter 5, *Proceedings of the 3rd Pan-American Materials Congress*, The Minerals, Metals & Materials Series. Springer, Cham (2017) ISBN 978-3-319-52132-9, pp 47-54

4. **Mohd Qasim**, Braj R Singh, A H Naqvi, P Paik and Dibakar Das, Silver nanoparticles embedded mesoporous SiO_2 nanosphere: an effective anticandidal agent against Candida albicans 077, *Nanotechnology* 26 (2015) 285102.

5. **Mohd Qasim**, Khushnuma Asghar, BR Singh, S Prathapani, W Khan, AH Naqvi, Dibakar Das, Magnetically recyclable $Ni_{0.5}Zn_{0.5}Fe_2O_4/Zn_{0.95}Ni_{0.05}O$ nano-photocatalyst: Structural, optical, magnetic and photocatalytic properties, *Spectrochimica Acta Part A: Molecular and Biomolecular Spectroscopy* 137 (2015) 1348–1356.

(B) Manuscripts to be communicated soon

1. **Mohd Qasim**, Dibakar Das, Green Synthesis of $CaFe_2O_4$ Impregnated Mesoporous $CaCO_3$ Based Multifunctional Nanocarrier for Controlled Delivery of Anticancer drug

2. **Mohd Qasim**, Dibakar Das, Magnetic nanoparticle embedded stimuli-responsive mesoporous silica nanoparticles for anticancer drug delivery application

3. **Mohd Qasim**, Khushnuma Asghar, Dibakar Das, Facile Synthesis of $CoFe_2O_4$ and multifunctional $CoFe_2O_4$@Albumen Nanoparticles for Biomedical Application

(C) Other peer reviewed Publications

1. Khushnuma Asghar, **Mohd. Qasim**, G. Dharmapuri and D. Das, Investigation on a smart nanocarrier with a mesoporous magnetic core and thermoresponsive shell for

co-delivery of doxorubicin and curcumin: a new approach towards combination therapy of cancer, RSC Adv., 2017, 7, 28802–28818

2. V S S. Mosali, **Mohd Qasim**, Bhanu Mullamuri, Basavaiah Chandu, and Dibakar Das, Synthesis and Characterization of Ag/$CoFe_2O_4$/Polyaniline Nanocomposite for Photocatalytic Application, J. Nanosci. Nanotechnol. 2017, Vol. 17 (12) (2017), 8918-8924

3. Khushnuma Asghar, **Mohd Qasim**, Dibakar Das One-Pot Green Synthesis of Carbon Quantum Dot for Biological Application, AIP Proceeding 1832, 050117, 2017

4. J. A. Khan* **Mohd Qasim***, Braj Raj Singh, Wasi Khan, Dibakar Das, Alim H. Naqvi, Polyaniline/$CoFe_2O_4$ nanocomposite inhibits the growth of Candida albicans 077 by ROS production, by C. R. Chimie 17 (2014) 91–102, (Impact Factor 1.798) (***Equal contribution**)

5. **Mohd Qasim**, J. Ananthaiah, S. Dhara, P. Paik, and D. Das, Synthesis and Characterization of Ultra-Fine Colloidal Silica Nanoparticles, Advanced Science, Engineering and Medicine, 6 (2014) 965–973

6. J.A. Khan, **Mohd Qasim**, Braj Raj Singh, Sneha Singh, Mohd Shoeb, Wasi Khan, Dibakar Das, A H. Naqvi, Synthesis and characterization of structural, optical, thermal and dielectric properties of polyaniline/$CoFe_2O_4$ nanocomposites with special reference to photocatalytic activity, by Spectrochimica Acta Part A: Molecular and Biomolecular Spectroscopy 109 (2013) 313–321.

7. Khushnuma Asghar, **Mohd Qasim**, DM Nelabhotla, D Das, Effect of surfactant and electrolyte on surface modification of c-plane GaN substrate using chemical mechanical planarization (CMP) process, Colloids and Surfaces A: Physicochemical and Engineering Aspects 497,2016, 133-145

8. Khushnuma Asghar, **Mohd Qasim**, and D. Das, Effect of Polishing Parameters on Chemical Mechanical Planarization of C-Plane (0001) Gallium Nitride Surface Using SiO_2 and Al_2O_3 Abrasives, ECS Journal of Solid State Science and Technology, 3 (7) (2014) 277-284

(D) List of participated Conferences to present thesis work

1. Mohd Qasim, B. R. Singh, Khushnuma Asghar, P. Paik, A. H. Naqvi, and D. Das, "Synthesis and characterization of Ag nanoparticles decorated mesoporous SiO_2 nanosphere and its anticandidal activity against Candida albicans 077", Dec16-20, 2013, IUMRS-ICA 2013, IISc Bangalore.

2. Mohd Qasim, Khushnuma Asghar, B R. Singh, S. Prathapani, G. Afreen, W. Khan, A.H. Naqvi, D. Das "Structural, optical, thermal, Magnetic and photocatalytic

properties of $Ni_{0.5}Zn_{0.5}Fe_2O_4/Zn_{0.95}Ni_{0.5}O$ nanocomposites synthesized by sol-gel using egg albumin" Dec 05-07; 2013, MagMa- 2013, IIT Guwahati

3. **Mohd Qasim**, Khushnuma Asghar, P. Paik, D. Das, "Synthesis and Characterization of Multifunctional $Ni_{0.5}Zn_{0.5}Fe_2O_4$/ $Zn_{0.95}Ni_{0.5}O$ Nanocomposites" Feb 19-21, 2014, ICAFM 2014, Thiruvananthapuram.

4. **Mohd Qasim**, B R. Singh, Khushnuma Asghar, A. H. Naqvi, D. Das, "Anticandidal activity against Candida albicans077 of Ag nanocrystal decked mesoporous SiO_2 nanoparticle" March 8th – 10^{th} 2014, Aligarh Nano IV International, Aligarh,

5. **Mohd Qasim**, Khushnuma Asghar, D. Das, "Multi-functional $Ni_{0.5}Zn_{0.5}Fe_2O_4$/ZnO@mSiO2 and $Ni_{0.5}Zn_{0.5}Fe_2O_4$@$mSiO_2$ core shell nanocomposites" Feb 19-2, 2015, ISNACT-2015, IIT Mumbai

6. **Mohd Qasim**, Khushnuma Asghar and D. Das, "Development of Magnetic Protein Nanoparticles for Controlled Release of Anti-Cancer Drug" Oral talk in NICAMPC-2016, 4-6 January 2016, NIT Warangal

7. **Mohd Qasim**, Khushnuma Asghar, and D. Das, "Novel Superparamagnetic Protein Nanocarrier for Drug Delivery Application" Oral talk in Aligarh Nano V & STEMCON 16, 12-15 March 2016

8. **Mohd Qasim**, Khushnuma Asghar, D. Das, "Facile Synthesis of Fe_3O_4 and multifunctional Fe_3O_4@Albumen Nanoparticles for Biomedical Applications" 61^{st} DAE, SSPS, Dec 26-30, 2016, KIIT, Bhubaneswar

9. **Mohd Qasim,** Dibakar Das, "Mesoporous $CaCO_3$ Based Multifunctional Magnetic Nanoparticles for Anticancer Drug Delivery Application" ICCGREI, IICT 2016, Hyderabad

10. **Mohd Qasim**, Khushnuma Asghar, D. Das, "$CoFe_2O_4$ and albumen based multifunctional magnetic protein nanocomposite for biomedical application" oral presentation in ICNANO, 1-3 March 2017, VBRI Allahabad.

11. **Mohd Qasim**, Khushnuma Asghar and D. Das, "Green Synthesis of Magnetic Nanoparticle Impregnated Mesoporous $CaCO_3$ Based Multifunctional Nanocarrier for Controlled Delivery of Anticancer drug" Oral talk in NANOTECH 2017 held during 3-5 April 2017 in **Dubai**.

Abbreviations

NP_S	Nanoparticles
MNPs	Magnetic Nanoparticles
MFMNPs	Multifuntional Magnetic Nanoparticles
AMFMNPs	Advanced Multifuntional Magnetic Nanoparticles
NC	Nanocomposite/Nanocarriers
MPNs	Magnetic Protein Nanoparticles
ROS	Reactive Oxygen Species
MSN	Mesoporous Silica Nanoparticle
P(NIPAM)	Poly(N-isopropylacrylamide)
P(NIPAM-AA)	Poly (N-isopropylacrylamide-acrylic acid)
NZF	$Ni_{0.5}Zn_{0.5}Fe_2O_4$
IO NPs	Iron Oxide NPs (Fe_3O_4 NPs)
CF NPs	$CoFe_2O_4$ NPs
DOX	Doxorubicin
CUR	Curcumin
ALB	Egg Albumen
HSA	Human Serum Albumin
BSA	Bovine Serum Albumin
LCST	Lower Critical Solution Temperature
MPS	3-mercaptopropyltrimethoxysilane
PBS	Phosphate buffer saline
IFFT	Inverse Fast Fourier transform
MTT	3-(4,5-dimethylthiazol-2-yl)-2,5-diphenyltetrazolium bromide
LE	Loading Efficiency
LC	Loading Capacity
FESEM	Field Emission Scanning Electron Microscopy

Abstract

Magnetic nanoparticles (MNPs) have potential applications in the various biomedical fields including anticancer drug delivery, magnetic resonance imaging (MRI), destruction of the tumor via hyperthermia, bio-separation, catalysis, etc. Development of multifunctional magnetic nanoparticles (MFMNPs) could significantly expand the properties of existing magnetic nanoparticles as it combines many different functionalities in a single platform which make them suitable candidates to achieve simultaneous diagnosis and therapy for cancer treatment. Particularly, the design and synthesis of MFMNPs is an extremely focused and dynamic area of present biomedical research because of their potentials applications in targeted drug delivery, multimodal imaging, hyperthermia, photothermal therapy etc. Different combinations of functional materials with different size and shape have been explored to develop MFMNPs based nanocarriers aiming to enhance the effectiveness and safety of anticancer drugs. In this thesis, preparation, characterization and biomedical applications of various advanced multifunctional magnetic nanoparticles have been discussed. First, different types of MNPs have been synthesized and characterized. Then, different multifunctional nanocomposites nanoparticles such as NZF@Alb, Fe_3O_4@Alb, CF@Alb, $mSiO_2$-$CaFe_2O_4$@P(Nipam-Aa), meso$CaCO_3$@$CaFe_2O_4$, NZF@$mSiO_2$, NZF@$mSiO_2$-CuS-PEG, NZF/$Zn_{0.95}Ni_{0.05}O$, NZF/$Zn_{0.95}Ni_{0.05}O$-$mSiO_2$, meso$CaFe_2O_4$ NPs, $mSiO_2$@AgNPs and $mSiO_2$@Ag-Fe_3O_4@P(Nipam) have been prepared. The structural, morphological, thermal, optical, magnetic properties and drug loading/release behaviour as well as biocompatibility/cytotoxicity of prepared multifunctional magnetic nanoparticles have been investigated. Anticancer activities of prepared anticancer drug-loaded multifunctional nano-formulations have been studied against Hela cells. Obtained results show that the present study could be extremely useful for the advancement of multifunctional magnetic nanocarrier's design and development for biomedical applications.

CHAPTER 1: INTRODUCTION

Chapter 1

Introduction

In this chapter a general introduction about nanoparticles, nanoparticles for biomedical applications, nanocarriers based drug delivery, magnetic nanoparticles, multifactional magnetic nanoparticles for biomedical applications and different multifunctional magnetic nanocarriers for biomedical applications have been presented.

1.1 Nanoparticles (NPs)

The meaning of word Nano is dwarf. Nanoscience and nanotechnology are the studies, manipulation, and application of extremely small things. Due to their superiority over the conventional materials, nano-based innovations are becoming the forefront of biological, engineering, medical fields of research and application. Nanotechnology has enormous capability to revolutionize the biomedical field, specially theragnostic & imaging [1]. Recent nano-based investigations have resulted in the fruitful improvement of conventional means of cancer treatment such as drug delivery system, imaging etc. Nano-based diagnostic tools or imaging methods could detect diseases at very early stage, which helps to cure diseases before they spread. A nanoparticle (NP) is nothing but a particle having the size in the range of 1 to 100 nm. Because of their very small size, nanoparticles (NPs) have very high surface to volume ratio. NPs show distinct physical and chemical properties than their bulk counterpart and they also exhibit size-dependent properties. Surface-related properties and quantum effect give NPs fundamentally different behavior compared to bulk systems. When the material is scaled down to the nano level the major changes occur to its thermal (melting point), optical (band gap), catalytic (surface area of catalyst), magnetic (coercivity, permeability, and saturation magnetization), mechanical (hardness), and antibacterial properties [2]. NPs can be classified into various categories depending on their structure, shape, composition etc. Depending on their size and shape they are divided into three categories such as quantum dot (0 D, nanoparticles), quantum wire (1D, nanowire such as CNT), quantum well (2D, nanosheet such as graphene) [2]. Depending on the composition NPs can be classified into metal NPs, metal oxide NPs, polymers NPs, carbon-based NPs etc. NPs can exist in different structure, shapes and morphologies such as mesoporous (2-50 nm pore), hollow (empty core), cylinders, spheres,

disc, platelets, tubes etc. [3]. Size, shape, and structure of NPs can be varied or controlled by controlling reaction parameters of synthesis method. Bottom-up (assembling atoms to get NPs) and top-down (cutting down a bulk material to get NPs) approach are the two-main methods to produce NPs. Bottom-up approach, which produces uniform and monodispersed NPs, is commonly used for NPs development for biomedical applications.

1.2 Nanoparticles for biomedical applications

NPs are used for a number of biomedical applications such as in diagnosis, tissue engineering, therapeutic targeted drug delivery, regenerative medicine, biosensors, imaging, antimicrobial agent, bio-separation, etc. [4, 5]. The area of cancer treatment has reached significant advancement with the help of NPs based diagnostic and therapeutic agent. Very small size of NPs (comparable to the smaller biological unit) makes it very interesting to be used as probe or vehicles to examine or cure diseases even at the very beginning stage. For example, mesoporous or polymeric NPs has applications in drug delivery as a nanocarrier. Fluorescent and magnetic NPs have been used for targeted drug delivery, diagnostic purposes such as imagining, MRI etc. Fluorescent Quantum dots have superior photostability than conventionally used organic molecules for cell imaging and tracking.

1.2.1 Nanocarriers based controlled and targeted drug delivery:

1.2.1.1 Drug Nanocarrier

Recent progress of nanotechnology in biomedical field has proven that nanoparticles have a great potential as drug carriers. A nanocarrier is nothing but a nanoparticle which acts as nano-sized bag to load and parcel drugs molecules (as cargo) at the desired site of the body. The cargo drug molecules can be attached to the surface of nanocarrier (in case of solid nanocarrier) or can be loaded within the cavity of the nanocarrier (in case of porous nanocarrier). The size of nanocarrier generally ranges from ~10-700 nm (for drug delivery). Generally, nanocarriers of size less than 200 nm is preferred. In spite of enormous research effort towards developing anticancer agents, cancer still remains one of the deadliest diseases and a leading cause of mortality in the world [6]. Biomedical scientific communities have made significant contribution in arresting cancer proliferation and thus several types of molecular anticancer drugs have been developed [7]. Efficacy of conventional molecular anticancer drugs (size < 7 nm), presently being used in cancer treatment, suffer from several limitations including rapid clearance (clearance through hepatic metabolism or renal clearance with a cut-off around 7

nm), lack of selectivity, toxicity toward normal cells, short blood circulation time, rapid metabolization in vivo, and poor water solubility. Due to rapid drug clearance, drug resistance and recurrence rates, use of maximum tolerated drug doses in cancer therapy results in high level of toxicity to normal tissues and thus limits their clinical applicability. Promoting active drug accumulation in tumour tissues would minimize such issues and improve therapeutic outcomes [8]. Renal clearance can mostly be minimized by increasing the size of the drug through conjugation to a large entity which acts as carriers. Emergence of nanotechnology and nanobiotechnology has helped researchers to overcome these problems by enabling them to develop smarter nanocarriers for encapsulating and delivering anticancer drugs at targeted site in the patient body. A primary aim of nanocarrier based drug delivery system is to develop a platform that effectively reduces toxicity of drugs while retaining their pharmacological activity. Nanocarrier based drug delivery systems offer several advantages over the administration of molecular free drugs viz. specific targeting ability, enhanced permeability and retention (EPR), controlled drug release, improved solubility and stability of drugs, low toxicity to normal cell, low clearance, long circulation time etc. and all these contribute to enhanced tumour cell death [9].

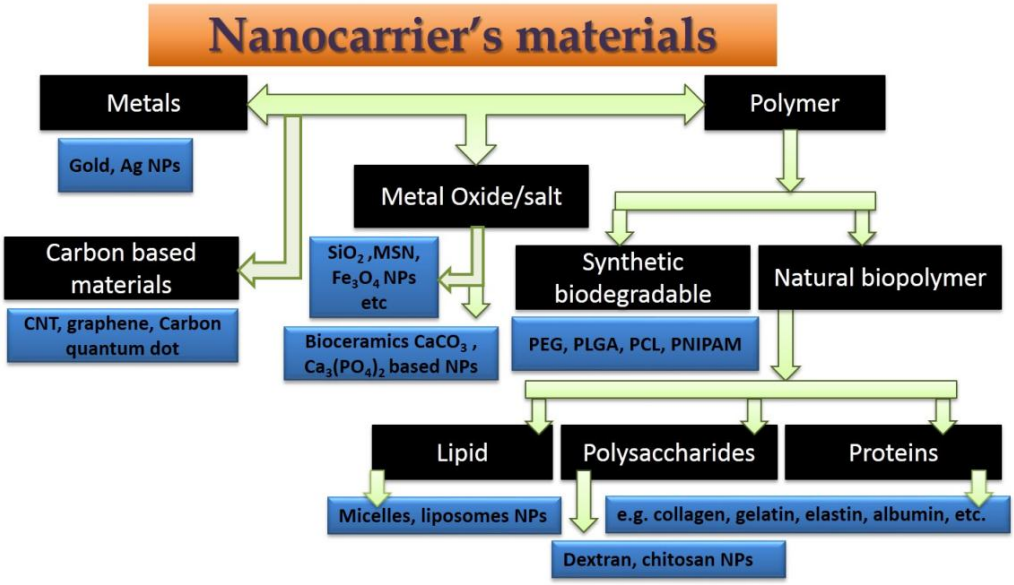

Figure 1.1. Classification of materials being used for nanocarrier development.

Various kinds of nanocarriers having different compositions (metal, metal oxide, polymers, carbon based materials), morphologies (spherical, elongated etc.), structures (solid quantum dot, mesoporous, hollow etc.) and sizes (from a few tenths to a few hundreds of nanometres) have been developed aiming to improve the therapeutic efficacy and safety of anticancer drugs

[10]. Several types of materials used for nanocarriers developments are classified in figure 1.1. Materials to be chosen for nanocarrier development should be biocompatible, biodegradable and hydrophilic in nature. Due to excellent biocompatibility and biodegradability synthetic biodegradable polymers (PLA, PLGA, PCL, PNIPAM and their hybrids etc.), natural biopolymer such as lipid, polysaccharides and proteins (collagen, gelatin, elastin, albumin, etc.) have been explored as drug delivery nanocarriers. Commonly used nanocarriers for the drug delivery application includes liposome, mesoporous metal oxide nanoparticles, mesoporous bio-ceramic nanoparticles, metal nanoparticles, polymeric nanoparticles, magnetic nanoparticles, quantum dots, carbon nanotube, hydrogel nanocapsule, dendrimers etc. The physicochemical properties of nanocarriers are being modified to load and deliver drugs of different nature such as hydrophobic and hydrophilic drugs [11]. Nanocarrier has brought revolutionary changes in the drug delivery field. Mesoporous metal oxide nanoparticles such as SiO_2, Al_2O_3, ZrO_2 etc. are having mesopores (pore size 2-50 nm) on its surfaces. Due to its excellent biocompatibility and high porosity mesoporous silica is most commonly used metal oxide based nanocarrier. Bio-ceramic nanoparticles refer to the nanoparticles of $CaCO_3$, $CaPO_4$ based materials derived from biological source.

1.2.1.2 Controlled and targeted drug delivery using nanocarriers

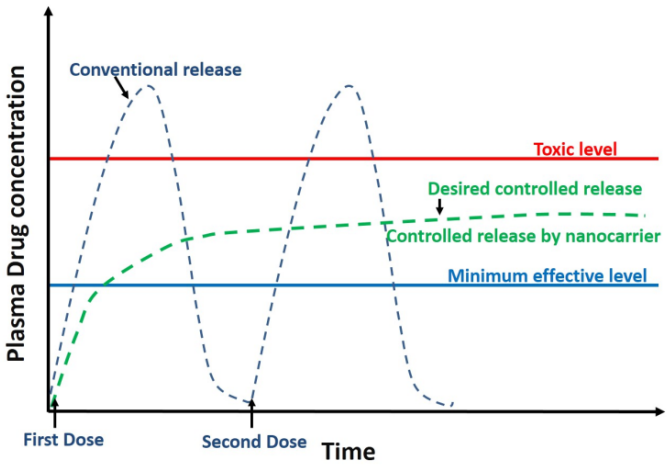

Figure 1.2. A comparison of blood plasma drug profiles obtained by conventional administration and nanocarrier based controlled release.

Targeted and controlled parceling of drug molecules to the affected sites of the body is a major problem in the treatment of many diseases especially in the cancer treatment. The conventional methods for delivery of drug suffer from many limitations including poor biodistribution, less effectiveness, side effect, and lack of selectivity etc. In addition, when drug

molecules are taken orally they must pass through several biological barriers such as the harsh acidic environment of the stomach, filtration by the liver, bloodstream and blood-brain barrier. Drug molecules have to surpass these biological hindrances to provide an effective result. Generally, a major portion of the drug is lost in the ways and very less amount of it reaches to the actual site of action. Further, Figure 1.2 shows a comparison of blood plasma drug profiles obtained by the conventional administration and nanocarrier based controlled release. When a drug is conventionally ingested in the body, amount of drug in the blood plasma suddenly reaches to a very high level and even surpass the toxic level. After some time, the level of the drug decreases and become lower than the even minimum required amount. For the better performance of a drug, the level of the drug should be maintained between the minimum required amount and toxic level. Strategies like the controlled and sustained release of drug molecules from a matrix (nanocarrier) can potentially overcome these limitations. Drug can be loaded into the nanocarriers and such drug-loaded nanoparticles can overcome above mentioned biological barriers and release the payload in a controlled manner at the targeted site [12]. In doing so, the level of drug in the blood plasma remained in the desired concentration ranges for a long time which eventually give better results. Thus, nanocarriers based drug delivery system aims to deliver a drug at the right place, at right time and in the right dose. Due to their very small size nanocarriers can deliver drugs to the sites in the body which are conventionally inaccessible. Nanocarriers are important in drug delivery application because they can deliver drugs at the targeted affected part (tumor) of the body and does not deliver drugs to the other normal parts of the body. This site-specific drug delivery process is generally, known as targeted drug delivery. Targeted delivery of a drug is very important and of major therapeutic benefit since it prevents side effects of the drugs. Since the anticancer drugs are highly toxic to the normal cells thus it must only be delivered to the tumors cells. Loading of a drug into a carrier may take place in many ways such as by physical adsorption, dispersion, covalent bonding, electrostatic interaction, hydrophobic interaction etc.

There are many ways in which nanocarrier can deliver drug at a targeted site such as active targeting, passive targeting, pH specificity, temperature specificity and magnetic targeting etc. *Active targeting* involves decoration of targeting agents on the surface of nanocarriers [5]. These targeting agent binds only to the specific receptor present on the cancerous cells. The *passive targeting* involves accumulation of nanocarriers at the tumor site due to the enhanced permeability and retention (EPR) effect. Due to the biocompatible nature of poly(ethylene oxide) (PEO) coating on the surface of nanocarriers, they easily travel down

to the tumor through the pores of leaky vasculature. These pores allow nanocarriers inside them but due to the tortuosity of the pore channels they get trapped inside resulting in accumulation of the drug loaded nanocarriers inside the tumor. Now a days different nanocarriers which can deliver drugs in response to some stimuli are being used. These stimuli responsive nanocarriers are called smart nanocarriers. The stimuli could be either exogenous (such as temperature, magnetic fields, light etc.) or endogenous (such as change in pH, enzyme concentration etc.). Nanocarrier which has the ability to deliver drugs at only certain pH ranges (such as pH of tumor cells), allows us to deliver drug directly to the tumor site [13]. Targeting and delivering drug at tumor site utilizing its pH responsive ability is known as *pH specificity*. The pH of the tumor is generally slightly acidic (pH 5-6) than normal body pH (pH 7.4). Acidic environment causes structural or chemical changes (conformational changes, degradations etc.) in nanocarriers material which trigger release of loaded drugs. Moreover, the nanocarriers remains stable throughout the body. *Temperature specificity* involves delivery of drug at targeted tumor site utilizing thermos-responsive ability of nanocarriers. Nanocarriers made up of thermos-responsive polymer deliver drugs at only higher temperature (38-45 ^{o}C) or tumor temperature (40 ^{o}C) [14]. Thermos-responsive polymers of nanocarrier get shrinked at tumor temperature allowing release of drugs. Nanocarriers having magnetic component can be accumulated at the targeted site by applying external magnetic field and thus can be made to deliver drugs at desired site. Thus, presence of magnetic nanoparticles in nanocarrier open possibility of *magnetically targeted delivery* of drugs. Magnetic tumor targeting is simple and does not require complicated chemical modification of targeting ligands on the surface of nanocarriers [12]. Magnetic tumor targeting is not dependent on type of specific receptors expressed on different tumor cells, which expands the scope of application of a single magnetic nanocarrier to a wide variety of tumors unlike ligands based targeting. Magnetic nanoparticles (MNPs) have got potential applications in biomedical field.

1.3 Multifunctional Magnetic Nanoparticles for biomedical applications

1.3.1 Magnetic Nanoparticles

Magnetic nanoparticles are the nanoparticles of magnetic metal, alloys or metal oxide. At the nano-size scale these magnetic nanoparticles behave differently than their bulk counterpart. Among the various nanoparticles prepared and tested for biomedical applications, magnetic nanoparticles are considered as superior potential candidate due to their magnetic nature. They have potential applications in different biomedical fields such as in anticancer drug/gene delivery, magnetic resonance imaging (MRI), destruction of tumor via hyperthermia, bio-

separation, catalysis, etc. [15, 16]. Magnetic nature of these nanoparticles helps in developing magnetic based nanocarriers, which can be magnetically targeted and accumulated at desired site of the body subsequently reducing side effect of loaded toxic drugs. Magnetic nanoparticles are suitable for biomedical applications because of various reasons such as their comparable size with biological entities, ease of surface modification with suitable molecules, its location can be controlled by outer magnetic fields, it can generate heat to kill cancerous cells (hyperthermia), it can improve contrast in MRI, etc. As mentioned above magnetic properties of an ultra-small magnetic nanoparticles are different and unique from its bulk. Below certain diameter (generally below 20 nm) these magnetic nanoparticles consist of single magnetic domain (unlike in bulk ferromagnet which is consist of several domains) and spontaneously flip in the direction of applied magnetic field at room temperature. These particles remain in magnetized state in the presence of external magnetic field. On the removal of applied magnetic field these magnetic nanoparticle domains suddenly get randomized due to small thermal fluctuations. Thus, in the presence of magnetic field these nanoparticles remain magnetized and in the absence of magnetic field their behavior become like nonmagnetic nanoparticles. This, phenomenon is known as *superparamagnetism* and the magnetic nanoparticles showing this type of behavior are called *superparamagnetic nanoparticles*. In other words, when the size of magnetic particles become single domain, on further reduction in size of single domain, until a critical size is reached, the coercivity decreases due to thermal effect. Below this critical size the coercivity of single domain magnetic nanoparticles become zero due to thermal effect and at this size the thermal effect is more predominant and can spontaneously randomized/demagnetized a previously magnetized particle [17]. Actually, for very small particles, the energy barriers for reversal of magnetization become very small that thermal fluctuation could easily overcome this barrier and randomize the spins. Bean coined the word superparamagnetic to describe this kind of particles. When the size of a ferromagnetic materials is reduced below a particles dimension smaller than single domain, it does not show ferromagnetic behavior but shows superparamagnetic behavior. Superparamagnetic nanoparticles do not show coercivity and remnant magnetization. This behavior makes them very important for biomedical applications especially for nanocarrier developments as it enables the preparation of a stable dispersion of nanoparticles by avoiding aggregation due to magnetic interactions. Upon removal of magnetic fields superparamagnetic NPs no longer show magnetic interaction (due to negligible coercivity and remanence) and thus aggregation is avoided. It is worthy to mention that magnetic nanoparticles with a permanent magnetic

moment will get agglomerated and settled rapidly during storage in liquid medium due to magnetic interaction. Use of this kind of particles may cause blockade due to large aggregation during the flow in the blood stream.

Majority of investigated magnetic nanoparticle are composed of metal oxide but metals and alloys base MNP (such as Fe, FeCo) also have been tested. Iron based MNP are most investigated because of its biocompatibility [18, 19]. Magnetic properties, chemical stability, and toxicity are primary criteria in choosing and preparing MNP. Magnetic nanoparticles should be made up of non-toxic materials having high magnetization so that their movement can easily be monitored with magnetic field. In the past decade, superparamagnetic magnetite (Fe_3O_4) and maghemite (γ-Fe_2O_3) nanoparticles had been the primary focus and received significant attention in biomedical field because of their biocompatibility and degradability[18]. These iron oxides based nanocrystalline nanoparticles come under ferrite family and have spinel structure where oxygen atoms form fcc lattice and iron atoms are located in tetrahedral and octahedral interstitials sites. Different transition metals based ferrite nanoparticles (MFe_2O_4 where M can be Mn, Fe, Zn, Ni, Co, Ca etc.) with an enhanced magnetic property are being investigated for different biomedical applications [19, 20]. Employed preparation methods have significant effect on the size, shape and surface chemistry of the magnetic nanoparticles and thus on the magnetic properties of MNP. Generally, well crystalline, monodispersed and hydrophilic MNPs are desired for biomedical applications. Different wet chemical methods are being used to prepare magnetic nanoparticles for biomedical applications including sol-gel, coprecipitation, micro emulsion, hydrothermal, high temperature decomposition etc. [19, 21, 22]. Biomedical applications of MNPs can be classified according to their application inside and outside of the body, so called *in vivo* or *in vitro* applications. *In vivo* include therapeutic (such as targeted drug or gene delivery, hyperthermia) and diagnostic applications (such as MRI). The *in vitro* application includes bioseparation, selections, cells marking, etc.

1.3.2 Multifunctional Magnetic Nanoparticles (MFMNPs)

1.3.2.1 Coating/encapsulation of MNP to obtain multifunctional magnetic NP

Generally, for biomedical application MNPs should be colloidally and chemically stable in water and biological media. Very small MNPs get easily oxidized in water and also tend to aggregate in larger cluster due to their hydrophobic nature as well as high surface energy. MNPs show aggregation by both due to surface energy (due to high surface area) and

interparticle dipolar attractions. Thus, protection of MNPs by some types of surface modification or coating or encapsulation is of prime importance to get chemically and physically stable MNPs. These biocompatible coating or encapsulating materials not only provide colloidal and physical stability but simultaneously provides several functions such as oxidation resistance of MNP core, prevention of agglomeration, provide biocompatibility, provide hydrophilicity, and provide functionality to hold drug molecules, targeting ligands etc. In addition, the coated or matrix material provide functionalization ability which facilitate for preparing multifunctional magnetic nanoparticles. Most commonly these coating materials serve as drug reservoir site thus act as drug carrier site. Various kinds of coating/encapsulating materials (or nanocarriers materials) having different compositions such as metal, metal oxide, and polymers have been used to coat or encapsulate MNPs aiming to improve the therapeutic efficacy and safety of drugs [15]. These coating materials are generally same materials which are independently being used for nanocarrier development. Thus, materials represented in Figure 1 also show the types of materials being used for coating of MNPs. Nanocarriers developed using single materials lack in tumor targeting ability. Presence of MNP in these nanocarriers provide magnetic targeting ability, hyperthermia based heating and imaging ability to nanocarriers. As mentioned above materials to be chosen for coating should be biocompatible, biodegradable and hydrophilic in nature. The stabilization or modification or protection of MNPs can be done by the following ways. 1) by surface coating with appropriate polymer, metal or metal oxide, 2) by encapsulating or embedding in polymeric or metal oxide nanosphere [22]. Among the most commonly used coating materials mesoporous silica, albumin proteins, calcium carbonate, PNIPAM etc. are getting more attention because of their biocompatibility and high drug loading ability. Even though nanoparticle based nanocarriers or nanosystem have potential applications in nanomedicine, still it faces several challenges such as real time monitoring of cellular event and nanoprobe, specific or accurate targeting to the action site, controlled drug delivery in the tumor cells etc. Thus, development of a multifunctional platform is desired to overcome these challenges. After coating with the drug reservoir materials on MNPs the outer surface of magnetic nanocarrier is further functionalized with different functional groups, targeting ligands etc. and different functional entities (imaging agents such as fluorescent dye, or luminescent quantum dot etc.) are incorporated in nanocarriers to get the multifunctional magnetic nanoparticle [5, 16].

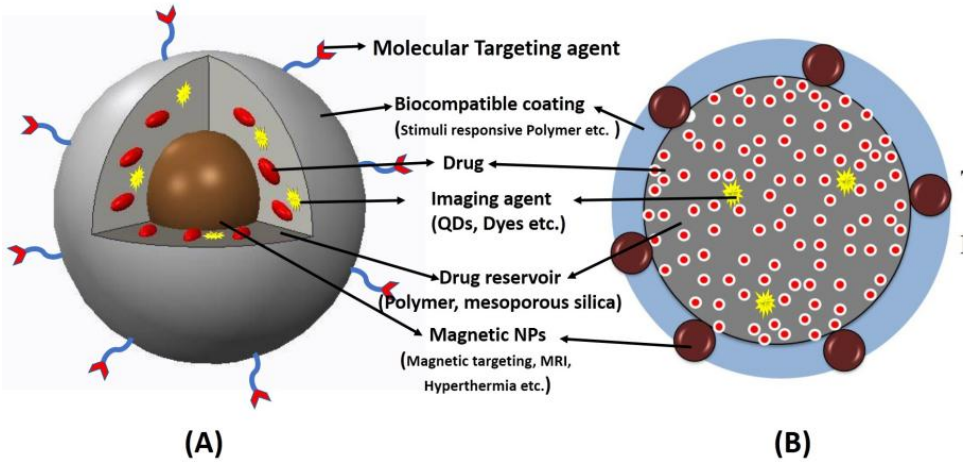

Figure 1.3. Illustration of a multifunctional magnetic nanoparticle for imaging and therapeutic application. Magnetic NPs can be used as core (A) or embedded particles in multifunctional nanocarrier (B).

1.3.2.2 Multifunctional Magnetic Nanoparticles: Introduction, applications and challenges

Development of nanosystem having a combination of various nanomaterials with different properties have been explored. And these multicomponent systems are capable to offer multifunctional nano platform, which make it possible to achieve simultaneous synergetic diagnosis and therapy. A multifunctional nanoparticle could significantly improve already existing nanoparticles properties as it combines many different functionalities in a single platform [23]. Particularly, the design and synthesis of multifunctional magnetic nanoparticles is an extremely focused and active area of current biomedical research. As mentioned above, cancer is one of the deadliest diseases and thus there is urgent need to develop novel approaches for accurate detection of early stage of cancer and for targeted therapies. Conventional anticancer chemotherapies suffer from several limitations such as rapid clearance, lack of selectivity, toxicity toward normal cells, short blood circulation time, rapid metabolization in vivo, and poor water solubility etc. Multifunctional magnetic nanoparticles having various functions including targeting, imaging, therapy etc. have been intensively studied aiming to overcome limitations of conventional cancer treatment. A '*multifunctional nanoparticles*' can be defined as "any nanoparticle that integrally combines two or more properties, i.e., a structural property with an additional functionality such as optical, magnetic, thermal, or electrical etc." [22]. As the name implies a *multifunctional magnetic nanoparticle ((MFMNP)* is multifunctional nanoparticles having magnetic component within it. Figure 3 shows typical illustration of two types of multifunctional magnetic nanoparticle for imaging and therapeutic application where it shows magnetic NPs can be used as core (Fig. 1.3A) or embedded particles

in a multifunctional nanocarrier (Fig. 1.3B). A single multifunctional magnetic nanoparticle simultaneously possesses multiple ability such as it can load and release drug/gene in a controlled way (due to presence of drug reservoir and stimuli sensitive polymer), it can be imaged through MRI (magnetic nanoparticle), it can be optically imaged through fluorescence (fluorescent quantum dot, dye), it can be tracked or located (magnetic nature), it can generate heat to kill cancer cells (MNPs via hyperthermia), and it can be targeted to the tumor (due to MNP and targeting agent) etc. Whereas a monofunctional nanoparticles can perform only such function such as pure mesoporous silica or liposome can only carry drugs but they cannot release in a smart way and at targeted site. Thus, multifunctional magnetic nanoparticles provide anticancer therapy with simultaneous detection or monitoring. It also enables to use same nanosystem for therapeutic as well as diagnostic applications, thus opening window for multi modal imaging and therapy platform.

Multifunctional magnetic nanoparticles have potential applications in targeted drug delivery, multimodal imaging (MRI, PET, optical, MRI-Optical, MRI-PET etc.) hyperthermia, photothermal therapy etc. [16, 22-24]. Due to presence of targeting agent (molecules which specifically bind with receptor present on cancer cells), and magnetic nanoparticles (magnetic targeting) in a multifunctional magnetic nanoparticle, they can deliver a loaded drug at a targeted site in a controlled manner [5]. Multimodal imaging deals with combining two or more imaging techniques together for better results. Multifunctional magnetic nanoparticles, having magnetic and optical component, could be used as multimodal imaging agent for both MRI-Optical imaging [22]. Thus, a single multifunctional magnetic nanoparticle could be used for multiple imaging techniques. Presence of magnetic nanoparticles and optically active component makes multifunctional magnetic nanoparticles suitable for hyperthermia (burning of cancer cells using heat generated by MNP in presence applied external magnetic field) and photothermal therapy (burning of cancer cells using heat generated by NP in presence of applied light). These generated heats could also act as trigger/switch to release drug from a thermos-sensitive multifunctional nanocarriers. Combinations of magnetic hyperthermia with nanoparticles based chemotherapy or photo therapy with chemotherapy or all three together could synergistically improve the effectiveness of these cancer treatment process [25]. Thus, multifunctional magnetic nanoparticles based thermos-chemotherapy, photo-thermo-chemotherapy are promising candidate in cancer treatments [26].

The exceptional features of such multifunctional magnetic nanoparticles based systems or nanocarrier provide advantages over conventional molecular diagnostics as well as

therapeutics. However, there are still many *challenges* in the field of multifunctional magnetic nanoparticles such as very high cost of used materials and targeting ligands, very complex preparation route, low chance of scalability, stability in physiological environment, and nonspecific interaction etc. Thus, facile method to integrate the multiple functional entities together, a versatile combination of materials must be explored to make the multifunctional nanoparticles based applications a practicable option to clinics. The successful development of multifunctional magnetic nanoparticles with appropriate drug reservoir materials, appropriate drug, magnetic materials, imaging materials and surface functionalization (with excellent biocompatibility) for effective and maximum therapeutic outcome is current *challenges* in this field. Loaded drug must be compatible with the drug reservoir and should not degrade upon loading into the nanosystem or during the loading process or storage. Different combinations of functional materials with different size and shape have been explored to develop multifunctional magnetic nanoparticles aiming to improve the therapeutic efficacy and safety of drugs. Among the various types of materials being applied to develop multifunctional nanocarrier mesoporous silica, albumin proteins, calcium carbonate, PNIPAM etc. are getting more attention because of their biocompatibility and high drug loading ability [13] [9] [11, 27, 28]. And, nanocomposites of MNPs with mesoporous silica (MNP/mSiO_2), biopolymers (MNP/albumin) and bio-ceramic ($CaCO_3$-MNPs) could be an ideal multifunctional nanocarriers due their biocompatibility. Thus, present study is focused on the design and development of albumin proteins, mesoporous silica, calcium carbonate, PNIPAM based advanced multifunctional magnetic nanoparticles by incorporating different magnetic and optical component in nanocarrier for simultaneous drug delivery, fluorescence imaging and magnetic resonance imaging. An *advanced multifunctional magnetic nanoparticle* refers to all new multifunctional magnetic nanoparticle and modifications to existing multifunctional magnetic nanoparticle in order to improve its performance for the application under consideration [24]. A brief introduction of the studied (in this thesis) advanced multifunctional magnetic nanoparticles has been discussed below. In a broad term, they can be represented as protein based multifunctional magnetic nanoparticles, mesoporous silica based multifunctional magnetic nanoparticles, calcium carbonate based multifunctional magnetic nanoparticles and mesoporous calcium ferrite based multifunctional magnetic nanoparticles.

1.3.2.3 Protein based multifunctional magnetic nanoparticles:

Protein based multifunctional magnetic nanoparticles involve coating of MNPs (such as Fe_3O_4 NPs, $CoFe_2O_4$ NPs), $Ni_{0.5}Zn_{0.5}Fe_2O_4$ NPs with multifunctional proteins such as human serum albumin, bovine serum albumin, egg albumin etc. Biological recognition mechanisms of our body treat the conventional synthetic nanoparticles as foreign objects to the body and clear them, thereby hindering access to the target. Combining biomolecules with synthetic nanoparticle have emerged as a way to counteract the extraordinary ability of our body to recognize, label, and clear foreign objects [29]. Biomolecules coatings gift nanoparticles with many bioactive functions, such as bypassing of the MPS and negotiation across different biological barriers [29]. In the recent years, natural biopolymers such as proteins are gaining considerably more attention over synthetic polymers (which are commonly used in nanocarrier development) because of their many desirable properties such as low toxicity and biodegradability and thus they are actively being investigated for both pharmaceutical and nutraceutical delivery [30]. In addition, among the range of materials under investigation in nanocarriers research, proteins offer unparalleled structural and functional versatility for designing nanocarriers. Nanoparticles derived from natural proteins are biocompatible, biodegradable, metabolizable, nontoxic, easy to prepare without use of toxic chemicals and easily amenable to surface modifications for attachment of drugs and targeting ligands [30]. Albumin based nanoparticles show high binding capacity with various drugs and targeting ligands and are acceptable in the body without any serious side effects. Egg albumen, a water soluble and highly functional protein, is known to possess excellent gelling, foaming, and emulsifying properties with good binding capacity with metal ions [31]. Thus, egg albumen with different functional groups (–SH, –OH, –COOH and $–NH_2$) can be of potential use to immobilize drug molecules because of its biocompatible and hydrophilic nature [32]. In addition, the cheaper egg albumen being easily metabolized in the human body is a better alternative than commercially available expensive BSA or HSA, which have already been proposed as potential nanocarrier or shell materials. $Ni_{0.5}Zn_{0.5}Fe_2O_4$ nanoparticle (NZF NP) is a versatile MNP as it shows soft magnetic behavior, superparamagnetic nature, high saturation magnetization, high Curie temperature, good chemical stability, low coercivity and biodegradability. It also possesses excellent anticancer activity against variety of cells. Similarly, Fe_3O_4 NPs, and $CoFe_2O_4$ NPs also are well studied and shows excellent biocompatibility and magnetic properties. Thus, these three MNPs have been chosen to obtain protein based multifunctional magnetic nanoparticles. These, protein based multifunctional

magnetic nanoparticles are biocompatible and shows excellent drug loading and pH dependent drug release profile.

1.3.2.4 Mesoporous silica based multifunctional magnetic nanoparticles

In *Mesoporous silica based multifunctional magnetic nanoparticles,* generally mesoporous silica which act as drug reservoir is incorporated with MNP and other functional component such as thermosensitive polymer, ZnO NPs, Ag, CuS NPs etc. Mesoporous silica nanoparticles (MSNs) have been used as carriers for drug/gene/antimicrobial agents due to its biocompatibility, hydrophilicity, stability and drug loading ability (porosity) from many years[33]. CTAB based templating technique has been generally used to synthesize MSNs with high surface areas, and tunable pore sizes. Mesoporous silica nanoparticle has different functional groups on its surface which allow attachment of different molecules and drugs. Pure mesoporous silica nanoparticle (MSN) based nanocarriers (without any surface functionalization) lacks in tumour targeting ability and does not have control over drug release which minimizes efficacy of drugs [34]. Magnetic targeting ability can be achieved in nanocarriers by incorporating MNPs within MSN matrix. Coating of a stimuli-responsive polymer such as P(NIPAM-AA) on the surface of mesoporous nanocarrier provide temperature dependent controlled drug release ability. Multifunctional drug delivery systems with MNPs and stimuli-responsive polymers are being developed to use the hyperthermic effects of MNPs to trigger drug release. Coating of stimuli responsive polymer on MSN and embedding of MNPs in polymer layer can result a multifunctional thermoresponsive magnetic nanocarrier which may overcome limitations of pure mesoporous silica. Incorporation of magnetic nanoparticles (MNPs) within these smart nanocarriers not only provide magnetic targetability but also facilitate imaging and hyperthermia based heating ability [11]. In addition, the ferrites based MNPs of Ni, Mn, Co, Zn although possess good magnetic properties, their inherent toxicity after certain amount reduces their reliability. This, raises worries on their biocompatibility and their effectiveness for biomedical applications. Ferrites of calcium are expected to be more biocompatible since calcium is inherently non-toxic. Thus, use of $CaFe_2O_4$ NP as MNP in multifunctional thermoresponsive magnetic nanocarrier is ideal way to develop a biocompatible nanocarrier. In other system, superparamagnetic $Ni_{0.5}Zn_{0.5}Fe_2O_4$ and MSN together in one entity have been combined to fabricate multifunctional nanocarrier for anticancer drug delivery application. Further, incorporating NIR active CuS NPs and coating of PEG in magnetic mesoporous silica (NZF@$mSiO_2$ NC) will provide a multifunctional system (NZF@$mSiO_2$-CuS-PEG-5Flu) for simultaneous multi-modal imaging and combined

chemo- and photothermal therapies. Low cost, d-d transition based NIR absorption ability, higher NIR absorbance, long term biocompatibility and a better tumor penetrating ability are advantages to the CuS NPs [35]. The incorporated CuS NP can be used to generate thermal energy upon NIR laser irradiation, resulting ablation of cancerous cells. Higher NIR absorbance of CuS NP can enhance the efficiency to reduce the laser power for treatment. Heterostructure based nano-system having magnetic as well as optical properties are increasingly being studied and developed due to their potential use in biomedical applications including imaging, drug delivery etc. Magnetic-optical nanosystem are excellent agent for imaging (confocal and MRI) and targetable nanocarrier through harnessing of their optical and magnetic properties respectively [36]. The combination of ZnO which is having good optical properties with magnetic NZF NP provide an excellent magneto-optical nanocomposite (NZF@ZnO NC) which may find several biomedical applications ranging from multimodal imaging to drug delivery [37]. Further, these type of heterostructures have been proven to have a superior photocatalytic activity which can be used to degrade medical organic waste. Incorporation of magneto-optical NZF@Zn NC in mesoporous silica or preparation multifunctional NZF@Zn-mSiO_2 nano-system will combine superparamagnetic and optical properties along with drug loading properties in single system which could be used for multimodal imaging and drug delivery applications. Further, excellent antifungal agent could be prepared by embedding Ag NPs in mesoporous silica (mSiO_2@AgNPs). The mesoporous silica not only helps the silver nanocrystals to disperse in aqueous solution by protecting the active material from aggregation, but also provides a good stability, long term antimicrobial activity and good binding to microbial cells. Incorporation of Ag NPs and MNP in the mSiO_2 nanocarriers give it multifunctional properties which enabled us to use it for multimodal imaging, magnetic tracking, magnetic separation, and chemo-photothermal therapy applications. Surface coating with thermos-responsive PNIPAM, facilitates multimodal multifunctional nanocarriers with a temperature dependent release ability of payloads.

1.3.2.5 Calcium carbonate based multifunctional magnetic nanoparticles

Calcium carbonate based multifunctional magnetic nanoparticles involve use of mesoporous calcium carbonate as matrix for drug (doxorubicin) reservoir and embedded MNP as magnetic as well as imaging component. $CaCO_3$ has shown promising potential for the development of smart carriers for anticancer drugs because of 1) inexpensiveness, 2) naturally existence in living beings and even in human body, 3) ideal biocompatibility, 4) biodegradability, 5) pH-sensitive properties, and 6) chemical stability. $CaCO_3$ is one of the

most common inorganic material of the nature. $CaCO_3$ is the main component of shells of marine organisms, snails, pearls, and eggshells. Biomaterials such as bones, teeth or shells are composed of hierarchical structure of $CaCO_3$ and calcium phosphate. More ever $CaCO_3$ is already present in blood at relatively high concentration without causing any adverse effect. So, it was believed that development of mesoporous nanocarrier, from biologically derived $CaCO_3$, will be ideal platform due to its inherent biocompatibility (due similarity with biominerals) and high drug loading (mesoporous nature) ability. Mesoporous $CaCO_3$ NPs compare to the $mSiO_2$ will have superior biocompatibility, bio-degradability and also offer pH dependent drug release. $CaCO_3$ NPs have pH responsive drug release properties as it is less soluble at normal blood pH (pH~7.4) but its dissolution accelerates at lower pH (tumor pH 4-6). Hence development of meso$CaCO_3$ based nanocarrier in biomedical research stand to benefit most. $CaCO_3$ and MNPs based nano-carriers are receiving increasing consideration because of their inherent biocompatibility and magnetic controllability, respectively. Waste egg shell could be good and inexpensive source of $CaCO_3$. Mesoporous $CaCO_3$ NPs can be prepared using egg shell, CTAB and lemon juice. The whole synthesis process of mesoporous $CaCO_3$ NPs involves conversion of egg shell to calcium citrate with help of citric acid of lemon juice on the surface CTAB template and further decomposition of calcium citrate and template to mesoporous $CaCO_3$. Multifunctionality and targeting ability to the meso$CaCO_3$ based nanocarrier can be introduced by incorporating biocompatible $CaFe_2O_4$ NP and loading doxorubicin which will result a multifunctional meso$CaCO_3$@$CaFe_2O_4$-Dox NC.

1.3.2.6 Mesoporous calcium ferrite based multifunctional magnetic nanoparticles

Mesoporous calcium ferrite based multifunctional magnetic nanoparticles involve development of mesoporous $CaFe_2O_4$ nanoparticles (meso$CaFe_2O_4$ NPs) which itself can perform multifunction such as drug reservoir, magnetic targeting and imaging etc. Loading of doxorubicin which is a fluorescent anticancer drug in meso$CaFe_2O_4$ NPs will further provide florescence based imaging ability to multifunctional meso$CaFe_2O_4$-Dox NPs.

1.4 References

[1] L.-P.D.L. Labhasetwar Vinod, Biomedical Applications of Nanotechnology, John Wiley & Sons, Inc. (2007) 249.
[2] C.P. Poole, F.J. Jones, F.J. Owens, Introduction to Nanotechnology, John Wiley \\& Sons, Inc.2003.
[3] S. Bhatia, Nanoparticles Types, Classification, Characterization, Fabrication Methods and Drug Delivery Applications, in: S. Bhatia (Ed.), Natural Polymer Drug Delivery Systems: Nanoparticles, Plants, and Algae, Springer International Publishing, Cham, 2016, pp. 33-93.
[4] A. Akbarzadeh, M. Samiei, S. Davaran, Magnetic nanoparticles: preparation, physical properties, and applications in biomedicine, Nanoscale Research Letters 7(1) (2012) 144.
[5] J.P. Mi Kyung Yu, Sangyong Jon, Targeting Strategies for Multifunctional Nanoparticles in Cancer Imaging and Therapy., Theranostics 2(1) (2012) 3-44.

[6] D. Yoo, J.-H. Lee, T.-H. Shin, J. Cheon, Theranostic Magnetic Nanoparticles, Accounts of Chemical Research 44(10) (2011) 863-874.
[7] D.S. J. Wang , N. J. Sebire , I. Lindsay , E. S. Newlands , P. Schmid , P. M. Savage , M. J. Seckl, , Salvage chemotherapy of relapsed or high-risk gestational trophoblastic neoplasia (GTN) with paclitaxel/cisplatin alternating with paclitaxel/etoposide (TP/TE), Ann. Oncol., 19 (2008) 1578-1583.
[8] U. Unzueta, M.V. Céspedes, E. Vázquez, N. Ferrer-Miralles, R. Mangues, A. Villaverde, Towards protein-based viral mimetics for cancer therapies, Trends in Biotechnology 33(5) (2015) 253-258.
[9] Y. Tian, X. Jiang, X. Chen, Z. Shao, W. Yang, Doxorubicin-loaded magnetic silk fibroin nanoparticles for targeted therapy of multidrug-resistant cancer, Advanced materials 26(43) (2014) 7393-8.
[10] S. Mura, J. Nicolas, P. Couvreur, Stimuli-responsive nanocarriers for drug delivery, 12 (2013) 991.
[11] K. Asghar, M. Qasim, G. Dharmapuri, D. Das, Investigation on a smart nanocarrier with a mesoporous magnetic core and thermo-responsive shell for co-delivery of doxorubicin and curcumin: a new approach towards combination therapy of cancer, RSC Adv. 7(46) (2017) 28802-28818.
[12] A. Kumar, P.K. Jena, S. Behera, R.F. Lockey, S. Mohapatra, S. Mohapatra, Multifunctional magnetic nanoparticles for targeted delivery, Nanomedicine: Nanotechnology, Biology and Medicine 6(1) 64-69.
[13] B. Chang, X. Sha, J. Guo, Y. Jiao, C. Wang, W. Yang, Thermo and pH dual responsive, polymer shell coated, magnetic mesoporous silica nanoparticles for controlled drug release, Journal of materials chemistry 21(25) (2011) 9239-9247.
[14] C. Liu, J. Guo, W. Yang, J. Hu, C. Wang, S. Fu, Magnetic mesoporous silica microspheres with thermo-sensitive polymer shell for controlled drug release, Journal of materials chemistry 19(27) (2009) 4764-4770.
[15] J. Chomoucka, J. Drbohlavova, D. Huska, V. Adam, R. Kizek, J. Hubalek, Magnetic nanoparticles and targeted drug delivering, Pharmacological Research 62(2) (2010) 144-149.
[16] C. Fang, M. Zhang, Multifunctional Magnetic Nanoparticles for Medical Imaging Applications, Journal of materials chemistry 19 (2009) 6258-6266.
[17] B.D. Cullity, C.D. Graham, Introduction to Magnetic Materials, Wiley-IEEE Press2008.
[18] S. Laurent, D. Forge, M. Port, A. Roch, C. Robic, L. Vander Elst, R.N. Muller, Magnetic Iron Oxide Nanoparticles: Synthesis, Stabilization, Vectorization, Physicochemical Characterizations, and Biological Applications, Chemical Reviews 108(6) (2008) 2064-2110.
[19] L.H. Reddy, J.L. Arias, J. Nicolas, P. Couvreur, Magnetic Nanoparticles: Design and Characterization, Toxicity and Biocompatibility, Pharmaceutical and Biomedical Applications, Chemical Reviews 112(11) (2012) 5818-5878.
[20] H.Z. Shouheng Sun, David B. Robinson, Simone Raoux, Philip M. Rice, Shan X. Wang, and Guanxiong Li, Monodisperse MFe2O4 (M) Fe, Co, Mn) Nanoparticles, J. AM. CHEM. SOC 126 (2004,) 273-279.
[21] A.K. Gupta, M. Gupta, Synthesis and surface engineering of iron oxide nanoparticles for biomedical applications, Biomaterials 26(18) (2005) 3995-4021.
[22] R. Hao, R. Xing, Z. Xu, Y. Hou, S. Gao, S. Sun, Synthesis, Functionalization, and Biomedical Applications of Multifunctional Magnetic Nanoparticles, Advanced materials 22(25) (2010) 2729-2742.
[23] S.K. Yen, P. Padmanabhan, S.T. Selvan, Multifunctional iron oxide nanoparticles for diagnostics, therapy and macromolecule delivery, Theranostics 3(12) (2013) 975-992.
[24] Y.Y. Nguyen Viet Long, Toshiharu Teranishi, Cao Minh Thi, Yanqin Cao, and Masayuki Nogami, Biomedical Applications of Advanced Multifunctional Magnetic Nanoparticles, Journal of Nanoscience and Nanotechnology 15 (2015) 0091–10107.
[25] G. Song, Q. Wang, Y. Wang, G. Lv, C. Li, R. Zou, Z. Chen, Z. Qin, K. Huo, R. Hu, J. Hu, A Low-Toxic Multifunctional Nanoplatform Based on Cu9S5@mSiO2 Core-Shell Nanocomposites: Combining Photothermal- and Chemotherapies with Infrared Thermal Imaging for Cancer Treatment, Advanced Functional Materials 23(35) (2013) 4281-4292.
[26] V.P. Torchilin, Multifunctional, stimuli-sensitive nanoparticulate systems for drug delivery, Nature Reviews Drug Discovery 13 (2014) 813–827
[27] S. Sharma, A. Verma, B.V. Teja, G. Pandey, N. Mittapelly, R. Trivedi, P.R. Mishra, An insight into functionalized calcium based inorganic nanomaterials in biomedicine: Trends and transitions, Colloids and Surfaces B: Biointerfaces 133(Supplement C) (2015) 120-139.
[28] M. Qasim, K. Asghar, G. Dharmapuri, D. Das, Investigation of novel superparamagnetic Ni0.5Zn0.5Fe2O4@albumen nanoparticles for controlled delivery of anticancer drug, Nanotechnology 28(36) (2017) 365101.
[29] C.C. R. Molinaro, J. O. Martinez, F. Taraballi, M. Evangelopoulos, S. Minardi, I.K. Yazdi, P. Zhao,E. De Rosa, M. B. Sherman, A. De Vita, N. E. Toledano Furman, X. Wang, A. Parodi & E. Tasciotti, Biomimetic proteolipid vesicles for targeting inflamed tissues, Nature Materials 15 (2016) 1037–1046
[30] W. Lohcharoenkal, L. Wang, Y.C. Chen, Y. Rojanasakul, Protein Nanoparticles as Drug Delivery Carriers for Cancer Therapy, BioMed Research International 2014 (2014) 12.

[31] k.A. Mohd Qasim, Braj Raj Singh, Sateesh Prathapani, Wasi Khan, A.H. Naqvi Dibakar Das, Magnetically recyclable Ni0.5Zn0.5Fe2O4/Zn0.95Ni0.05O nano-photocatalyst: Structural, optical, magnetic and photocatalytic properties, Spectrochimica Acta Part A: Molecular and Biomolecular Spectroscopy 137 (2015) 1348–1356
[32] E.S. Taheri, M. Jahanshahi, M.T.H. Mosavian, Preparation, Characterization and Optimization of Egg Albumin Nanoparticles as Low Molecular-Weight Drug Delivery Vehicle, Particle & Particle Systems Characterization 29(3) (2012) 211-222.
[33] M. Qasim, R.S. Braj, A.H. Naqvi, P. Paik, D. Das, Silver nanoparticles embedded mesoporous SiO 2 nanosphere: an effective anticandidal agent against Candida albicans 077, Nanotechnology 26(28) (2015) 285102.
[34] R.E. Yanes, F. Tamanoi, Development of mesoporous silica nanomaterials as a vehicle for anticancer drug delivery, Therapeutic delivery 3(3) (2012) 389-404.
[35] W. Lingjie, W. Ming, Z. Yongyi, Z. Da, Z. Aixian, L. Xiaolong, L. Jingfeng, Multifunctional PEG modified DOX loaded mesoporous silica nanoparticle@CuS nanohybrids as photo-thermal agent and thermal-triggered drug release vehicle for hepatocellular carcinoma treatment, Nanotechnology 26(2) (2015) 025102.
[36] T.-C.C. Nam-Hyuk Cho, Ji Hyun Min, Jun Hua Wu, Sang Jin Lee, Daehong Kim, Jae-Seong Yang, Sanguk Kim, Young Keun Kim & Seung-Yong Seong, A multifunctional core–shell nanoparticle for dendritic cell-based cancer immunotherapy, Nature Nanotechnology 6 (2011) 675–682.
[37] Z.-Y. Zhang, H.-M. Xiong, Photoluminescent ZnO Nanoparticles and Their Biological Applications, Materials 8(6) (2015) 3101-3127.

CHAPTER 2: LITERATURE REVIEW

Chapter 2

Literature review

In this chapter, a thorough critical review on the preparation of MNPs, various multifunctional magnetic nanoparticle and their associated problems and objectives of the present research have been discussed.

2.1 Synthesis of magnetic nanoparticles (MNPs) and magnetic nanocarrier for biomedical applications

Conventional anticancer chemotherapy suffers from several limitations including rapid clearance, lack of selectivity, toxicity toward normal cells, short blood circulation time, rapid metabolization in vivo, drug resistance, and poor water solubility. Emergence of nanotechnology has helped researchers to overcome these problems by enabling them to develop smarter nanocarriers for encapsulating and delivering anticancer drugs at targeted site in the patient body [1]. Superparamagnetic nature and its ability to be guided by external magnetic field make MNPs very useful for targeted drug delivery applications. The most common methods for the preparation of MNPs includes sol-gel, co-precipitation, thermal decomposition, hydrothermal synthesis, microemulsion, and sonochemical etc. [2]. Co-precipitation which is a classic method [3] involves aging of stoichiometric mixture of inorganic salts (metal chloride or nitrate) in aqueous media whereas thermal decomposition method involves high temperature decomposition of metal complex (metal acetylacetonates or metal oleates) in presence of surfactant in an organic solvent. Shouheng Sun et al have prepared well crystalline monodispersed MFe_2O_4 (M = Fe, Co, Mn) NPs of 3-20 nm by thermal decomposition method using metal acetylacetonates precursor [4, 5]. J Park et al have reported synthesis of IONPs of different size 5-22 nm by thermal decomposition method using metal oleates precursor [6]. Even though thermal decomposition method can produce highly monodispersed and crystalline MNPs but they are hydrophobic in nature and require further surfactant based processing [4]. Monodisperse MNPs can be prepared by microemulsion method but very less yield and less crystallinity are its major drawbacks [7]. Co-precipitation method is most suitable for production of biomedically useful MNPs, as it can produce very small and hydrophilic MNPs. Broad distribution and less crystallinity are limitations of co-precipitation method that further require classification of sizes and calcinations to get

monodispersed and well crystalline MNPs. Thus, despite lots of research in the fields of preparation of nanocrystalline magnetic NPs, it is still difficult and hectic to prepare a well crystalline, monodispersed, biocompatible and hydrophilic magnetic nanoparticle. These problems can be addressed by using suitable chemicals and adequate reaction parameters. Synthesis parameters, such as pH, temperature, reducing agent, stabilizing agent and precursor, have huge effect on the size, shape, crystallinity, magnetic property of MNPs. M.Y. Rafique et.al have showed that $NaBH_4$ have significant effect on the particle size, composition, and magnetic properties of $CoFe_2O_4$ NPs [8]. Well crystalline and monodispersed CF NPs and IO NPs have been prepared using $NaBH_4$, hydrazine hydrate, NaOH and oleic acid during co-precipitation. Well crystalline superparamagnetic NZF and $CaFe_2O_4$ NPs were prepared by auto combustion method. MNP of calcium are expected to be more suitable and biocompatible as calcium is biocompatible and nontoxic [9].

To date, different types of nanocarriers such as liposomes, polymer, silica, proteins have been developed [10]. Liposome based nanocarrier have been in the market for more than a decade, but it poses several challenges including non-targeting ability, high production cost, rapid leakage and poor storage stability [11]. Non-targeting ability, low encapsulation capacity and leaking of encapsulated drugs are drawbacks of pure polymer based nanocarriers. Nanocomposites nanocarriers composed of organic and novel inorganic materials could overcome these issues. Nanocarriers developed using single materials lack in tumor targeting ability. Excellent targeting ability in nanocarriers can be achieved by incorporation of MNPs within nanocarrier's matrix or antibody functionalization. R.M. Lu et al has prepared anti-c-Met antibody functionalized Pegylated liposomal Dox by multistep chemical process however magnetic targeting is simple and inexpensive than antibody/ligands based targeting [12]. Y. Ling et al. has reported scAbPSCA antibody functionalized PEG-PLGA-Dtxl/SPIO NPs multistep chemical process. Both the above systems are complex, and highly costly and may suffer leakage problem [13]. The motivation for MNPs based targeting and drug delivery lies in the potential to reduce the side effects of chemotherapy drugs. The concept of using MNP as a targeting agent for drug carrier is dates back to late 1970s [14]. Although early research in the field can be dated back several decades, the recent surge of interest in nanotechnology has significantly expanded the breadth and depth of magnetic NPs research.

2.2 Protein based magnetic NPs

In recent years, due to excellent biocompatibility, low toxicity, and biodegradability, natural biopolymers such as proteins (collagen, gelatin, elastin, albumin, etc) have gained considerable favor over synthetic polymers in the development of nanocarriers. Moreover, protein-based carriers have demonstrated biocompatibility, biodegradability, nontoxicity, prolonged circulatory half-life, low levels of reticuloendothelial system clearance, and improved pharmacokinetic properties [15, 16]. Among different types of proteins, nontoxic, non-immunogenic, biocompatible, biodegradable and water-soluble albumin proteins are considered ideal materials for fabrication of nanocarriers since the success of *abraxane*, paclitaxel loaded HSA NPs [17, 18]. Albumin based NPs show high binding capacity with various drugs and targeting ligands and are acceptable in the body without any serious side effects [19]. Recently, Zhenglin Li et al has prepared Dox loaded HSA-coated Prussian blue NPs and demonstrated a remarkably superior synergistic anticancer activity [16]. NPs prepared only from proteins (albumin) even though shows good anticancer activity [16], lack in tumor-targeting ability that minimizes drug accumulation at tumor site. Few researchers have reported that accumulation of albumin in solid tumors makes it a potential carrier for the site targeted drug delivery [20, 21]. Recently, S. Pulakkat et al reported hyaluronic acid modified Dox-loaded BSA NPs for targeted delivery to over expressed CD44 receptors in metastatic breast cancer cells[20]. These nanocarriers may have shown promising results in preclinical models but the translation of ligand recognition based targeting into the clinic remains challenging [22]. Magnetic targeting obtained by achieved by incorporation of MNPs within nanocarrier's matrix is simpler than complicated ligand based targeting. Albumin proteins coating on MNPs could make them more biocompatible, invisible to the immune system, hydrophilic, stable in biological fluids, and provide long circulation time, which are basic requirements for biomedical applications and hence, they are used to fabricate magnetic albumin NPs, thus they become attractive in biomedical research [23]. Proteins coated magnetic NPs can be prepared by many methods, including simple adsorption, photonic immobilization, free-radical crosslinking, sonochemical method, and covalent immobilization[24-28]. Till date several types of magnetic protein NPs including Fe_3O_4/BSA–Dextron–FA-Dox [26], Fe_3O_4-BSA [27-29], Fe_3O_4-SiO_2-BSA [30], Fe_3O_4-chitosan-BSA[31], GEM-Fe_3O_4-BSA[23], Fe_3O_4-HSA[32, 33], $MnFe_2O_4$-BSA [34] , $Ni_{0.5}Co_{0.5}Fe_2O_4$-BSA[35] , $Ni_{0.5}Zn_{0.5}Fe_2O_4$-BSA[36] etc. have been reported, however most of them contain commercially available expensive BSA or HSA due to their sequence and structural homology. Kaplan group [37] and Ye Tian et al [1] have

successfully prepared doxorubicin (Dox) loaded Silk Fibroin NPs (SFNs-Dox) and Fe_3O_4-SFNs-Dox, respectively, by salting out method. The main disadvantage of these SF based nanocarriers is its complex and long preparation time. $Ni_{0.5}Zn_{0.5}Fe_2O_4$ nanoparticle (NZF NP) is a versatile MNP as it shows soft magnetic behavior, superparamagnetic nature, high saturation magnetization, high Curie temperature, good chemical stability, low coercivity and biodegradability. Al-Qubaisi et al have studied anticancer activity of NZF NPs and concluded that NZF NPs have potential cytotoxicity or anticancer activity against investigated cancer cells [38, 39]. Very recently, L. H. Nie et al have found that NZF NPs have great adsorbing ability for BSA suggesting that NZF NPs are potential BSA-carrier candidate [36]. These studies motivated us to use NZF NPs as magnetic component to provide magnetic guidability and targetability to the nanocarrier. Egg albumen can be of potential use to immobilize drug molecules because of its biocompatible and hydrophilic nature and presence of different functional groups [40, 41]. In addition, the cheaper egg albumen being easily metabolized in the human body is a better alternative than commercially available expensive BSA or HSA, which have already been proposed as potential nanocarrier or shell materials. Egg albumen with desirable properties is the least-explored material for biomedical applications, although it is available in abundance and economically viable [42]. Recently, some researchers have reported the potentials of egg albumen for drug delivery application but they did not address the targeting ability, which ultimately reduces the efficiency of the drug [43-45]. Pharmaceutical industries are turning toward green chemistry due to its profitable and environmentally superior nature [46]. In the present work, we combine the merit of magnetic MNPs and albumen nanoparticle together to fabricate multifunctional NPs for targeted and controlled drug delivery application for cancer treatment. In this study, $Ni_{0.5}Zn_{0.5}Fe_2O_4$@Albumen (NZF@Alb), Fe_3O_4@Albumen (Fe_3O_4@Alb) & $CoFe_2O_4$@Albumen (CF@Alb) NPs core-shell NPs have been prepared by green and simple method using inexpensive chicken egg albumen and have been characterized for different physiochemical properties using different techniques.

2.3 Synthesis of multifunctional $mSiO_2$-$CaFe_2O_4$@P (Nipam-Aa)

Mesoporous silica nanoparticles (MSNs) have been used as carriers for drug/gene/antimicrobial agents due to its biocompatibility, hydrophilicity, stability and high drug loading ability (porosity). Rolando E Yanes at al. have prepared pure MSNs based nanocarrier for drug delivery applications [47]. Pure mesoporous silica nanoparticle (MSN) based nanocarriers (without any surface functionalization) lacks in tumor targeting ability and

does not have control over drug release which minimizes efficacy of drugs [47, 48]. Yang X et al. have reported a complex multifunctional nanoparticle for targeted anticancer drug delivery and PET/MR imaging in which Dox was conjugated with PEGylated SPION. The present system lack in mesoporous component which can provide better drug storage capacity and stability to drug [49]. Multifunctional drug delivery systems with MNPs and stimuli-responsive polymers are being developed to use the hyperthermic effects of MNPs to trigger drug release. Hilt and Satarkar incorporated Fe_3O_4 NPs into temperature-sensitive poly (N-isopropylacrylamide) (PNIPAAm) hydrogels for magnetically-triggered drug release [50]. PNiPAM having LCST of less than body temperature (~32^oC) cannot be used for drug delivery applications in its pure form however LCST of this polymer can be increased by incorporating hydrophilic copolymers [51]. Further, low drug loading, poor storage and premature drug release may be the drawback of the above system. Magnetic targeting ability can be achieved in MSN by incorporating MNP within MSN. Feng-Hua Chen et al. have coated a layer of PEG functionalized porous silica shell onto doxorubicin conjugated Fe_3O_4 NPs core but system does have stimuli sensitivity[52]. Coating of stimuli responsive particularly thermoresponsive polymer on MSN and embedding of MNPs in polymer layer can result a multifunctional thermoresponsive magnetic nanocarrier which may overcome above limitations. The use of smart and stimuli responsive drug nanocarrier in drug delivery is getting increasing attention due to its remotely controlled drug release [53]. Among them temperature responsive multifunctional mesoporous nanocarriers are most promising [54, 55]. Congying Liu et al. have reported thermo-sensitive P(NIPAM-co-NHMA) copolymer coated magnetic mesoporous silica for controlled drug release [55]. Baisong Chang et al have prepared thermo and pH dual responsive (P(NIPAM-co-MAA)) coated magnetic mesoporous silica NPs (M-MSN) via precipitation polymerization for controlled delivery of Dox [54]. It is very hectic to incorporate MNP exactly in core and required lots of optimization process than embedding MNP on the surface of nanocarrier. Ferrites of calcium are expected to be more biocompatible since calcium is inherently non-toxic, thus it was chosen as MNP [9]. In this work, $mSiO_2$-$CaFe_2O_4$@P(NIPAM-Aa) nanocarriers were prepared and characterized.

2.4 $CaCO_3$ based multifunctional nanocarrier (meso$CaCO_3$@$CaFe_2O_4$ NC)

$CaCO_3$ has shown promising potential for the development of smart carriers for anticancer drugs because of its ideal biocompatibility, biodegradability and chemical similarity to human hard tissue (bone and teeth). More ever $CaCO_3$ is already present in blood at relatively

high concentration without causing any adverse effect. $CaCO_3$ based NPs can be prepared using various method such as coprecipitation, sol gel, hydrothermal, microemulsion etc. but these conventional methods involve use of synthetic chemical which could leave toxic residue on the surface of prepared NPs which limit its biological uses [56]. $CaCO_3$ based NPs have been used in different biomedical applications such as delivery of anticancer drug, insulin, antibody, gene, RNA, and bone repair etc. [56]. Betamethasone or bioactive protein loaded $CaCO_3$ NPs showed improved chemical stability and sustained release [57]. $CaCO_3$ NPs loaded with siRNA have shown drastic suppression of tumor growth without any cytotoxicity in cell culture or mortality in animal model [58]. Ying et al. synthesized $CaCO_3$ NPs with a size of 420 nm using a starch–octanoic acid micelle as the template, which displayed a doxorubicin (DOX) encapsulation efficiency of about 20% [59]. Jun Wang et al have prepared $CaCO_3$/Carboxy Methyl Chitosan hybrid microspheres and nanospheres by the precipitation of calcium carbonate in an aqueous solution containing CMC which showed 60% encapsulation efficiency of doxorubicin (DOX) [60]. Targeting ligands functionalized lipid coated $CaCO_3$ NPs loaded with a therapeutic peptide resulted higher apoptosis in lung cancer cell line as well as significant retardation in tumor growth with minimal side effect [61]. Si Chen et al. have prepared $CaCO_3$/DNA/DOX NPs by chemical coprecipitation for co-delivery of a p53 gene and DOX which have showed a higher cell inhibition and promoted tumor cell apoptosis more effectively [62]. Dong Zhao et al have prepared alginate/$CaCO_3$/DNA NPs by co-precipitation and loaded it with Dox to evaluate the gene and drug co-delivery ability and prepared nano-system showed enhanced tumor cell apoptosis compared to unmodified NPs [63]. Wei Cui et al have demonstrated that TRAIL/ALG-$CaCO_3$ loaded with DOX have good potential applications in the treatment of cancer [64]. Recently, Hanzhu Shi et al have prepared polyacrylic acid (PAA)/calcium carbonate ($CaCO_3$) NPs for Dox delivery using novel heat treatment based method [65]. Most of the literature ignored incorporating targeting either by ligands based or by incorporating MNPs. Magnetic targeting is simple and in expensive than complex ligands based targeting. Zhao Y et al. reported the fabrication of around 800 nm superparamagnetic $CaCO_3$ nanostructures for the co-delivery of DOX and Au–DNA NPs for magnetic control and therapy using a hectic multistage chemical process [66]. Kyung Hyun Min et al have prepared pH-Controlled Gas-Generating DOX-$CaCO_3$-MNPs nanosystem through a block copolymer templated in situ mineralization approach for triggered Dox release and ultrasound imaging [67]. Generating mesoporous nature in $CaCO_3$ NPs (by simple method using CTAB) will improve the loading capacity of drug. More ever all the proposed method for the preparation

of $CaCO_3$ NPs use some kind of chemical method and precursors. Waste Egg shell is natural, inexpensive, biocompatible source of $CaCO_3$. So, it was believed that development of mesoporous, biologically derived $CaCO_3$ based nanocarrier will be ideal platform due to its inherent biocompatibility (due to similarity with biominerals) and high drug loading (mesoporous nature) ability. In this work, novel mesoporous $CaCO_3$ based multifunctional $CaFe_2O_4$ NP impregnated meso$CaCO_3$ nanocomposite (meso$CaCO_3$@$CaFe_2O_4$ NC) have successfully been synthesized by environmental friendly biological route using waste egg shell, lemon juice, MNPs, CTAB and characterized for different physiochemical properties.

2.5 Multifunctional NZF@mSiO_2 and NZF@mSiO_2-CuS-PEG nanocomposites

As mentioned above pure mesoporous silica nanoparticle (MSN) based nanocarriers without MNP and surface functionalization lacks in tumour targeting ability and does not have control over drug release [47, 48]. Recently, mesoporous silica based magnetic nanocarriers are getting increasing attention in biomedical research such as, targeted drug delivery due to its biocompatibility, high surface area, and high porosity [68-72]. A primary aim of magnetic nanocarrier based drug delivery system is to develop a platform that effectively reduces systemic toxicity of drugs while retaining their pharmacological activity. Recently, anticancer activity of Ni-Zn ferrite was conducted and it was reported that Ni–Zn ferrites NPs have potential cytotoxicity against studied cancer cells- HT29, MCF-7, and HepG2 cells [38, 39]. In the present work, we have combined superparamagnetic NZF and MSN together in one entity to fabricate multifunctional nanocarrier for anticancer drug delivery application.

Imaging and photo irradiation involving Near-infrared light (NIR, $\lambda = 700 \sim 1100$ nm) has attracted superior attention due to its deep penetration and minimal absorption in tissues. CuS NPs have been reported as a new type of NIR based photothermal ablation agent for cancer treatment. The NIR absorption of CuS NP is based on the d-d transition of Cu^{2+} ions which is not affected by surrounding matrix unlike SPR based photothermal therapy using Au and Ag NPs, thus leading to higher photothermal ablation efficiency [73-76]. Low cost, d-d transition based NIR absorption ability, long term biocompatibility and a better tumor penetrating ability are advantages to the CuS NPs [77]. Higher NIR absorbance of CuS NP can enhance the efficiency to reduce the laser power for treatment. The combination of photothermal therapy, hyperthermia chemotherapy could have better synergistic therapeutic effects than any of the single treatments alone [78]. Song et al. have reported Cu_9S_5@mSiO_2−PEG core−shell nanocomposite for pH and NIR light triggered release of DOX [78]. The, same group in another

report have developed novel difunctional nanocomposite $HmSiO_2$-FA-CuS-PEG nanocomposites for targeted chemo-photothermal therapy. It involved conjugation of folic acid (as a targeting agent) and attachment CuS NPs on the surface of hollow mesoporous silica and loading of Dox [79]. L Wu et al have reported PEG-modified DOX loaded-MSN@CuS nanohybrids as efficient drug delivery carriers, which have combined PTT treatment with a controlled DOX release ability [77]. Chen et al. have prepared CuS@MSN core shell NPs based ^{64}Cu- CuS@MSN-TRC105 theranostic NPs by multistep surface engineering process. The CuS@MSN core shell NPs not only preserved the photothermal ablation property, but could load and release Dox [80]. Guixin Yang have CuS conjugated CuS NPs on the surface of UCNPs@$mSiO_2$ multi-modal imaging and combined chemo- and photothermal therapies [73]. All the above discussed nanosystems lack in magnetic targeting ability which is simple than antibody based targeting. Nanocomposite of only CuS and MNPs have been reported and they are versatile for magnetically guided photoinduced hyperthermia and imaging but without any porous carrier component they could lack in drug loading ability [81, 82]. There are very few report which have combined magnetic, mesoporous, and CuS component in single unit nanoparticle. Recently, Zhifang Gao et al have reported a new multifunctional nanoplatform (Fe_3O_4@$mSiO_2$-FA-CuS-PEG/Dox nanocomposite) for MRI and targeted chemo-photothermal therapy. In this (Fe_3O_4 NPs was used as a core of $mSiO_2$ and CuS, FA and PEG were conjugated on the surface $mSiO_2$ [83]. Bei Liu et have used CuS as core and prepared Cu_9S_5@$mSiO_2$@Fe_3O_4-PEG for magnetically targeted delivery of DOX combined MR imaging and chemo/photothermal [84]. Thus, incorporating NIR active CuS NPs in magnetic mesoporous silica (NZF@$mSiO_2$ NC) will provide a multifunctional system which can simultaneously deliver multitask such as chemotherapy, imaging, phototherapy etc. In this work, carboxylic functionalized CuS were embedded on the surface of amine functionalized NZF@$mSiO_2$ followed by coating with PEG to obtain a multifunctional NZF@$mSiO_2$-CuS-PEG nanocarriers which was loaded with anticancer drug 5 Fluorouracil (5Flu). Recently, it has been reported that the amine functionalization of silica enhanced loading capacity of 5Flu drug due to their similar hydrophilicity and opposite charges thus amine functionalized silica was used in this study [85].

2.6 Multifunctional NZF/$Zn_{0.95}Ni_{0.05}O$ and Cur loaded NZF/$Zn_{0.95}Ni_{0.05}O$-$mSiO_2$ nanocomposites

Magnetic-optical heterostructure nanosystem are finding several biomedical applications such as recyclable photocatalysis, (e.g. photo degradation of medical waste),

multimodal imaging, targeted drug delivery through harnessing of their optical and magnetic properties respectively [86]. These type of heterostructures have been proven to have a superior photocatalytic activity than single component based photocatalyst which can be used to degrade medical organic waste. Constant disposal of noxious organic pollutants from hospitals/textile/laboratory lead to unrealizable side effects, since the mineralization efficiency of these pollutants by conventional mineralization methods is inadequate[87]. The use of NPs as catalysts in organic transformations has attracted considerable interest in recent years, because of their larger surface area-to-volume ratio[88]. Among them multifunctional fluorescent magnetic nanocomposites have become the subject of intensive research due to their interesting multi physical-chemical properties and potential applications in photocatalysis, antimicrobial activities, magnetic resonance imaging (MRI), hyperthermia, bioseparation, drug delivery, and cell labeling [89-91]. ZnO is a well known photoluminescent photocatalyst with wide band gap (3.4 eV), and large excitonic binding energy (60 meV) at room temperature. Unfortunately, ZnO, being a wide band gap semiconductor, requires ultraviolet irradiation for its band gap excitation [87, 92]. Many commonly used photocatalysts have wide band gaps (>3.1 eV) and can absorb only small portion of the solar light (UV light). It is worth mentioning here that solar light contains ~50% visible light and only ~5% UV light. Thus, to utilize the maximum solar light a photocatalyst that can absorb visible solar energy should be used[93] [10]. The band gap of ZnO can be engineered by suitable doping in the ZnO lattice making them suitable for visible light absorption [94, 95]. However, recovery of these ZnO catalyst particles after the photocatalytic process is difficult. Fast recombination of the generated electron-hole pairs is another major drawback of pure semiconductor photocatalysts, which can be avoided by combining P-type and N-type semiconductors (by preparing heterostructures), as it facilitates charge migration[96-99].Thus commonly used non magnetic semiconductor photocatalyst possess three main limitations and those are less visible light activity, poor recovery, and fast recombination of the generated electron-hole pairs. Magnetic Ferrite NPs having band gap ~2eV offer several advantages including visible light absorption, magnetic separability, and enhanced photocatalytic efficiency due to the presence of extra catalytic sites in their crystal structures [100]. Independently ferrites have rarely been used in photolocatalysis due to its lower valence band potential and poor photocatalytic conversion efficiency[101]. Nanocomposite or heterostructure photocatalysts made up of semiconductor and magnetic materials, such as $ZnFe_2O_4$/ZnO, $CoFe_2O_4$/ZnO, Fe_2O_3/ZnO, Fe_3O_4/ZnO etc., are gaining increasing importance because of their recyclability and higher photocatalytic activity

than pure ferrites or ZnO[102]. Incorporation of ferrite in ZnO helps in improving the quantum yield of ZnO by slowing down the recombination of photogenerated electrons and holes[103]. Since pure ZnO is not suitable for absorption and utilization of visible region of the solar spectrum, in this study Ni doped ZnO ($Zn_{0.95}Ni_{0.05}O$) with a band gap of ~2.95 eV and $Ni_{0.5}Zn_{0.5}Fe_2O_4$ (band gap ~2.2eV) have been chosen to prepare nanophotocatalysts for visible light active, magnetically separable, and recyclable photocatalytic activity. In the present investigation, $Ni_{0.5}Zn_{0.5}Fe_2O_4/Zn_{0.95}Ni_{0.05}O$ nanocomposites (NZF@Zn NC) have been prepared, for the first time, using egg albumen as biotemplate, which is environment friendly and cost effective. No external surfactant or stabilizing agent has been used to prepare nanocomposites which are having varying degree of toxicity and are difficult to remove from nanoparticle surfaces even after repeated washing. Visible light absorption ability of $Zn_{0.95}Ni_{0.05}O$ could also provide optical imaging ability in NZF@Zn NC using light source of visible region. It is worthy to mention here that exposure to light source of UV region is harmful to body. The combination of ZnO which is having good optical properties with magnetic NZF NP provide an excellent magneto-optical nanocomposite (NZF@ZnO NC) which may find several biomedical applications ranging from multimodal imaging to drug delivery [104].

After successful preparation and characterization of magneto-optical NZF@Zn NC, it was used to prepared multifunctional NZF@Zn-mSiO_2 nano-system for delivery of Curcumin (Cur) which is well known anticancer agent. Even though curcumin is having excellent anticancer activity but due to its low water solubility or hydrophobic nature its practical uses in biomedicine is limited. Cur have been loaded in different hydrophilic carrier such mesoporous silica, polymers etc to avoid this problem and to avail its actual activity. A. Anitha et al have reported water-soluble O-carboxymethyl chitosan nanocarrier for the delivery of Cur to cancer cells but the polymer based nanocarrier may suffer leakage problem [105]. Hong Yan et al have prepared photothermal-responsive rotaxane-functionalized MSNPs-Cur and demonstrate photothermal controlled release of curcumin [106]. Siddharth Jambhrunkar et al. have observed that Mesoporous Silica NPs Enhance the Cytotoxicity of Curcumin Siddharth [107]. All the above discussed system lack in magnetic targeting and does not have semiconductor NPs based imaging ability. Faheem Muhammad et al have used ZnO nanolid on mesoporous silica and prepared ZnO@MSNs for pH responsive delivery of two hydrophobic drug (CUR-CPT-ZnO@MSNs formulations) [108]. This system lack in targeting ability and showed rapid Cur release, further loosely bounded ZnO lid may lose easily from

the surface. Murali M Yallapu et al have reported β-cyclodextrin (CD) and pluronic F68 polymer decorated IONP for Curcumin delivery but the system does not have mesoporous nature, QD based optical property and controlled release [109]. Recently, Peilin Huang at al. have prepared Cur loaded CD functionalized magnetic mesoporous silica as bifunctional pH responsive nanocarrier, but it does not have ZnO which may improve its multifunctionality [110]. In this work, we have prepared NZF@Zn embedded mesoporous silica (NZF@Zn-mSiO_2) nanocomposites which has magnetic, and optical properties along with drug loading ability, which could be used for multimodal imaging and drug delivery applications.

2.7 Multifunctional mSiO_2@AgNPs and mSiO_2@Ag-Fe_3O_4@P(Nipam) NC

The increase of infectious diseases and development of antibiotic resistance against conventional pharmaceutical antibiotics have encouraged researchers to search for new antimicrobial agents [111-113] [114]. Silver based materials are being investigated and used as an antimicrobial agent since long time because of their good antimicrobial properties [115]. Recently, silver nanoparticles (Ag NPs) have attracted lots of attention due to its strong antibacterial and antifungal activity than its bulk counterpart [116]. But, practical applications of Ag NPs are often limited by its surface oxidization and aggregation that reduces its antimicrobial activity. At small diameter, due to large surface to volume ratio and high surface energy, Ag NPs tend to agglomerate to minimize the surface energy, which diminish their antibacterial performance[117, 118]. This problem has been addressed by studying zeolite, titanium dioxide, activated carbon and silica as the silver-carrying antibacterial agents and such efforts have significantly improved the antimicrobial activity [119]. Among them mesoporous silica NPs (MSNs) are superior and well known for their biocompatibility, dispersibility, chemical stability and carriers for drug/gene/antimicrobial agent. Ag NPs are generally prepared by chemical synthesis processes involving the use of aggressive chemical reducing agents, capping agents, and organic solvents, which poses risks both from environmental or biological aspects (presence of toxic agent of NPs surface) [120]. Research groups have focused on developing more environmentally friendly methods, replacing the toxic reducing agents and stabilizer by bioorganic compounds[120-124]. Extracts from some plant leaves may act both as reducing and capping agents in Ag NPs preparation. Combinations of biomolecules such as enzymes/proteins, amino acids, polysaccharides, and vitamins having different functional groups (carboxyl & hydroxyl) present in these extracts work as reducing agent for Ag^+ [124]. In order to reduce the biological and environmental impact of the synthesis, in this work, green synthesis process using silver nitrate and leaf extract of *Azadirachta indica*,

commonly known as Neem, has been adopted for the synthesis of silver NPs. Every part of the Neem plant has been used as traditional medicines and leaf and seed extract of *Azadirachta indica* itself have shown good antimicrobial properties. The synthesis of NPs using bioreagents could lower the toxicity of the resulting NPs and the environmental impact of the byproducts [125]. Candida albicans is a diploid fungus that commonly causes infections, such as denture stomatitis, thrush, and urinary tract-infections, but can also cause more severe systemic infections in immunocompromised patients. Development of a suitable agent will be useful to play a significant role against this pathogenic fungus. Thus, this study has been designed to investigate the anticandidal activity of 'Ag nanoparticles embedded mesoporous silica nanocomposite' (denoted as "mSiO_2@Ag") against C. albicans 077. In this work, mSiO_2@Ag nanoparticles have successfully been synthesized and their different physico-chemical and anticandidal activities against C. albicans have been studied. Recently, some efforts have been made for the development of Ag-silica nanocomposites, but most of these studies have either concentrated on design of core-shell or post synthesis deposition of Ag NPs on silica sphere [126, 127] [128]. In both of these strategies antibacterial activity may not be fully utilized due to very slow release rate of Ag^+ ions (Ag wrapped in core) and quick consumption or chemical erosion of Ag NPs from silica surface (in case of post synthesis deposition of Ag NPs on SiO_2 sphere) [119]. Although few reports are available in the literature [113, 115, 116, 119, 126-128] on the synthesis of SiO_2–Ag NPs composite, their antifungal activity is not studied extensively. To the best of our knowledge antifungal activity of mSiO_2@Ag against C. Albicans has not been reported anywhere in the open literature. The mSiO_2 not only helps the AgNPs to disperse in aqueous solution, but also provides a good stability, long term antimicrobial activity by continuously release Ag ions (as bare Ag NPs may quickly be consumed) and good binding to microbial cells.

Magnetically responsive or separable antimicrobial materials can improve the antimicrobial effect and reduce the adverse side effect by targeted deliver antimicrobial agents, its magnetic separation after disinfection to reduce. Incorporation of Ag NPs, MNPs in the mSiO_2 nanocarriers and it subsequent surface coating with PNIPAM could give a multifunctional nanocomposite with magnetic, antibacterial, optical, drug loading and thermos-responsive properties which will enabled us to use it for targeted and magnetically recoverable smart antibacterial, imaging, tracking and chemo-photothermal therapy applications. Robert Prucek et al. have combined magnetic iron oxide NPs and antibacterial as well as optical silver NPs and prepared two binary nanocomposite of the Ag@Fe_3O_4 and g-Fe_2O_3@Ag type

employing polyacrylate acid as an effective linker. Properties of the present system (in term of colloidal and chemical stability, surface area, and loading ability) could be improved by incorporation Ag-Fe_3O_4 nanocomposite in mesoporous silica [129]. Few, magnetically separable antibacterial agent composed of Fe_3O_4, Ag and SiO_2 NPs with improve antibacterial activity have been recently reported but lack in porosity and thermoresponsiveness which will give temperature dependent release of antibacterial agents [130-132]. Recently, Erick Yu et al have reported a PNIPAM gated Fe_3O_4/mSiO_2 core shell NPs for the temperature triggered release of antibacterial lysozyme. They observed release of lysozyme at physiological temperature [133]. The above system does not used Ag NPs which could have improved its antibacterial and multifunctional properties. In order to expand the multifunctionality of mSiO_2-AgNPs based hybrid composites or to add magnetic controllability and thermoresponsive-ness to it, incorporation of Fe_3O_4 NPs and coating of P(Nipam) have been done to get mSiO_2@Ag-Fe_3O_4 and mSiO_2@Ag-Fe_3O_4@P(Nipam) respectively.

2.8 Mesoporous $CaFe_2O_4$ NPs (meso$CaFe_2O_4$ NPs)

Till date, most of the research have been focused on solid MNPs which does not provide porosity and enough surface area for loading and molecular targeting conjugation. This will ultimately lower the targeting and therapeutic efficiency of both drug and MNPs. Attachment of drug on the surface of solid MNP may not provide good stability to drug molecules and such drug easily can bind with various entities in blood and may not reach to the target site in sufficient amount. MNPs are generally being used as core in drug carrier materials such as in mesoporous silica or polymeric NPs to provide magnetic targeting. But, preparation process of these core shell type nanocomposite is very complex and required lots of optimizations and chemical steps. To solve these limitations, mesopores have been created in magnetic nanoparticles itself to obtain mesoporous magnetic nanoparticle[134-139]. Mesoporous magnetic nanoparticle shows high porosity, high surface area, high drug loading ability and high magnetic moment and good biocompatibility. Creation of mesoporous within magnetic nanoparticle itself will not only simplify the hectic synthesis process (required for heterostructure based mesoporous magnetic nanoparticles) but also provide good magnetic properties [134]. Recently, Weibing Zhang et al[135]have prepared Dox loaded porous clustered Fe_3O_4 NPs for destruction of prostate cancer cells by combination of PTT and chemotherapy. Ideas and findings of above cited many literatures have motivated us to use mesoporous magnetic nanoparticles specially calcium ferrite nanoparticles for drug delivery applications. In addition, the ferrites of calcium are expected to be more biocompatible than

Ni, Co based ferrite since calcium is inherently non-toxic [9]. In this work, different meso$CaFe_2O_4$ NPs were prepared by simple route using CTAB and oleic acid and characterized for different physiological properties. Prepared meso$CaFe_2O_4$ NPs was loaded with Dox and its release study was performed.

2.9 Objective of research

After a thorough critical review on the preparation of MNPs, multifunctional magnetic nanoparticle and their associated problems, the objectives of the present research have been identified.

The objectives of the present work are,

1) To prepare and characterize monodisperse magnetic nanoparticles of Fe_3O_4 (IO NPs), $CoFe_2O_4$ (CF NPs), $Ni_{0.5}Zn_{0.5}Fe_2O_4$ (NZF NPs) and $CaFe_2O_4$.
2) To study the structural, morphological, magnetic properties of above MNPs.
3) Preparation and characterization of albumen based multifunctional magnetic nanoparticles such as NZF@Alb, Fe_3O_4@Alb & CF@Alb NPs.
4) To prepare and characterize multifunctional $mSiO_2$-$CaFe_2O_4$@P(Nipam-Aa), meso$CaCO_3$@$CaFe_2O_4$ NC, NZF@$mSiO_2$, NZF@$mSiO_2$-CuS-PEG, NZF/$Zn_{0.95}Ni_{0.05}O$ NZF/$Zn_{0.95}Ni_{0.05}O$-$mSiO_2$ NCs and meso $CaFe_2O_4$ NPs
5) Preparation and characterization of multifunctional antimicrobial $mSiO_2$@AgNPs and $mSiO_2$@Ag-Fe_3O_4@P(Nipam) NC.
6) To study the structural, morphological, thermal, magnetic and drug loading/release properties and biocompatibility/cytotoxicity of prepared multifunctional nanoparticles.

The present investigation aims to develop some robust novel multifunctional nanoparticles or nanocarrier with excellent biocompatibility, good drug loading ability, high targeting ability and sustained & triggered release ability etc. The aim of the present research also includes development of novel multifunctional nanoparticles with good antimicrobial activity.

2.10 References

[1] Y. Tian, X. Jiang, X. Chen, Z. Shao, W. Yang, Doxorubicin-loaded magnetic silk fibroin nanoparticles for targeted therapy of multidrug-resistant cancer, Advanced materials 26(43) (2014) 7393-8.
[2] A.K. Gupta, M. Gupta, Synthesis and surface engineering of iron oxide nanoparticles for biomedical applications, Biomaterials 26(18) (2005) 3995-4021.
[3] Y.S. Kang, S. Risbud, J.F. Rabolt, P. Stroeve, Synthesis and Characterization of Nanometer-Size Fe3O4 and γ-Fe2O3 Particles, Chemistry of Materials 8(9) (1996) 2209-2211.
[4] H.Z. Shouheng Sun, David B. Robinson, Simone Raoux, Philip M. Rice, Shan X. Wang, and Guanxiong Li, Monodisperse MFe2O4 (M) Fe, Co, Mn) Nanoparticles, J. AM. CHEM. SOC 126 (2004,) 273-279.
[5] S. Sun, H. Zeng, J. Am. Chem. Soc. 124 (2002) 8204.

[6] J. Park, K. An, Y. Hwang, J.-G. Park, H.-J. Noh, J.-Y. Kim, J.-H. Park, N.-M. Hwang, T. Hyeon, Ultra-large-scale syntheses of monodisperse nanocrystals, 3 (2004) 891.
[7] Y. Deng, L. Wang, W. Yang, S. Fu, A. Elaïssari, Preparation of magnetic polymeric particles via inverse microemulsion polymerization process, Journal of Magnetism and Magnetic Materials 257(1) (2003) 69-78.
[8] M.Y. Rafique, L. Pan, Q.-u.-a. Javed, M.Z. Iqbal, L. Yang, Influence of NaBH4 on the size, composition, and magnetic properties of CoFe2O4 nanoparticles synthesized by hydrothermal method, Journal of Nanoparticle Research 14(10) (2012) 1189.
[9] L. Khanna, N.K. Verma, PEG/CaFe2O4 nanocomposite: Structural, morphological, magnetic and thermal analyses, Physica B: Condensed Matter 427 (2013) 68-75.
[10] K. Cho, X. Wang, S. Nie, Z. Chen, D.M. Shin, Therapeutic Nanoparticles for Drug Delivery in Cancer, Clinical Cancer Research 14(5) (2008) 1310.
[11] M.E. Davis, Z. Chen, D.M. Shin, Nanoparticle therapeutics: an emerging treatment modality for cancer, 7 (2008) 771.
[12] R.-M. Lu, Y.-L. Chang, M.-S. Chen, H.-C. Wu, Single chain anti-c-Met antibody conjugated nanoparticles for in vivo tumor-targeted imaging and drug delivery, Biomaterials 32(12) (2011) 3265-3274.
[13] Y. Ling, K. Wei, Y. Luo, X. Gao, S. Zhong, Dual docetaxel/superparamagnetic iron oxide loaded nanoparticles for both targeting magnetic resonance imaging and cancer therapy, Biomaterials 32(29) (2011) 7139-7150.
[14] S.K. Andrew, W.; George, C., Magnetic guidance of drug-carrying microspheres, Journal of Applied Physics , 49 (1978) 3578-3583.
[15] W. Lohcharoenkal, L. Wang, Y.C. Chen, Y. Rojanasakul, Protein Nanoparticles as Drug Delivery Carriers for Cancer Therapy, BioMed Research International 2014 (2014) 12.
[16] Y.H. Zhenglin Li , Tingting Jiang , Kenneth A. Howard , Yonggang Li , Xuelei Fan , Ye Sun , Flemming Besenbacher , and Miao Yu Human-serum-albumincoated Prussian blue nanoparticles as pH-/thermotriggered drug-delivery vehicles for cancer thermochemotherapy, Part. Part. Syst. Charact., 33 (2016) 53–62
[17] P. Ghosh, A. Singha Roy, S. Chaudhury, S.K. Jana, K. Chaudhury, S. Dasgupta, Preparation of albumin based nanoparticles for delivery of fisetin and evaluation of its cytotoxic activity, International Journal of Biological Macromolecules 86(Supplement C) (2016) 408-417.
[18] M. Karimi, S. Bahrami, S.B. Ravari, P.S. Zangabad, H. Mirshekari, M. Bozorgomid, S. Shahreza, M. Sori, M.R. Hamblin, Albumin nanostructures as advanced drug delivery systems, Expert Opinion on Drug Delivery 13(11) (2016) 1609-1623.
[19] A.O. Elzoghby, W.M. Samy, N.A. Elgindy, Albumin-based nanoparticles as potential controlled release drug delivery systems, Journal of Controlled Release 157(2) (2012) 168-182.
[20] S. Pulakkat, S.A. Balaji, A. Rangarajan, A.M. Raichur, Surface Engineered Protein Nanoparticles With Hyaluronic Acid Based Multilayers For Targeted Delivery Of Anticancer Agents, ACS Applied Materials & Interfaces 8(36) (2016) 23437-23449.
[21] Y. Takakura, T. Fujita, M. Hashida, H. Sezaki, Disposition Characteristics of Macromolecules in Tumor-Bearing Mice, Pharmaceutical Research 7(4) (1990) 339-346.
[22] S. Mura, J. Nicolas, P. Couvreur, Stimuli-responsive nanocarriers for drug delivery, 12 (2013) 991.
[23] Y.A. L. Wang, C. Yuan, H. Zhang, C. Liang, F. Ding, Q. Gao, D. Zhang,, GEM-loaded magnetic albumin nanospheres modified with cetuximab for simultaneous targeting, magnetic resonance imaging, and double-targeted thermochemotherapy of pancreatic cancer cells,,, International Journal of Nanomedicine 10 (2015) 2507–2519.
[24] C.E. Bunker, K.C. Novak, E.A. Guliants, B.A. Harruff, M.J. Meziani, Y. Lin, Y.-P. Sun, Formation of Protein−Metal Oxide Nanostructures by the Sonochemical Method: Observation of Nanofibers and Nanoneedles, Langmuir 23(20) (2007) 10342-10347.
[25] S.-M. Yu, A. Laromaine, A. Roig, Enhanced stability of superparamagnetic iron oxide nanoparticles in biological media using a pH adjusted-BSA adsorption protocol, Journal of Nanoparticle Research 16(7) (2014) 2484.
[26] H. Hao, Q. Ma, F. He, P. Yao, Doxorubicin and Fe3O4 loaded albumin nanoparticles with folic acid modified dextran surface for tumor diagnosis and therapy, Journal of Materials Chemistry B 2(45) (2014) 7978-7987.
[27] Z. Li, L. Qiang, S. Zhong, H. Wang, X. Cui, Synthesis and characterization of monodisperse magnetic Fe3O4@BSA core–shell nanoparticles, Colloids and Surfaces A: Physicochemical and Engineering Aspects 436(Supplement C) (2013) 1145-1151.
[28] M. Mikhaylova, D.K. Kim, C.C. Berry, A. Zagorodni, M. Toprak, A.S.G. Curtis, M. Muhammed, BSA Immobilization on Amine-Functionalized Superparamagnetic Iron Oxide Nanoparticles, Chemistry of Materials 16(12) (2004) 2344-2354.
[29] B. Zhang, Q. Li, P. Yin, Y. Rui, Y. Qiu, Y. Wang, D. Shi, Ultrasound-Triggered BSA/SPION Hybrid Nanoclusters for Liver-Specific Magnetic Resonance Imaging, ACS Applied Materials & Interfaces 4(12) (2012) 6479-6486.

[30] C.H. Yu, A. Al-Saadi, S.-J. Shih, L. Qiu, K.Y. Tam, S.C. Tsang, Immobilization of BSA on Silica-Coated Magnetic Iron Oxide Nanoparticle, The Journal of Physical Chemistry C 113(2) (2009) 537-543.
[31] Y. Wang, X. Wang, G. Luo, Y. Dai, Adsorption of bovin serum albumin (BSA) onto the magnetic chitosan nanoparticles prepared by a microemulsion system, Bioresource Technology 99(9) (2008) 3881-3884.
[32] I. Levy, I. Sher, E. Corem-Salkmon, O. Ziv-Polat, A. Meir, A.J. Treves, A. Nagler, O. Kalter-Leibovici, S. Margel, Y. Rotenstreich, Bioactive magnetic near Infra-Red fluorescent core-shell iron oxide/human serum albumin nanoparticles for controlled release of growth factors for augmentation of human mesenchymal stem cell growth and differentiation, Journal of Nanobiotechnology 13(1) (2015) 34.
[33] J. Xie, J. Wang, G. Niu, J. Huang, K. Chen, X. Li, X. Chen, Human serum albumin coated iron oxide nanoparticles for efficient cell labeling, Chemical communications 46(3) (2010) 433-435.
[34] M. Bellusci, A. La Barbera, L. Seralessandri, F. Padella, A. Piozzi, F. Varsano, Preparation of albumin-ferrite superparamagnetic nanoparticles using reverse micelles, Polymer International 58(10) (2009) 1142-1147.
[35] Z.Y. Wu, Y. Zou, Q.X. Liu, C.B. Ma, X.G. Tang, B.T. Chen, Preparation of Magnetic Ni0.5Co0.5Fe2O4 Nanoparticles and their Applications In Adsorption of Bovine Serum Albuminn, Integrated Ferroelectrics 142(1) (2013) 128-134.
[36] L.-H. Nie, F.-H. Bai, M.-F. Liu, J. Ning, B.-T. Chen, Z.-Y. Wu, Synthesis of monodispersed pH-sensitive Ni0.5Zn0.5Fe2O4 magnetic nanoparticles and the potential medical application of adsorption for bovine serum album, Integrated Ferroelectrics 168(1) (2016) 183-194.
[37] F.P. Seib, G.T. Jones, J. Rnjak-Kovacina, Y. Lin, D.L. Kaplan, pH-Dependent Anticancer Drug Release from Silk Nanoparticles, Advanced Healthcare Materials 2(12) (2013) 1606-1611.
[38] M.S. Al-Qubaisi, A. Rasedee, M.H. Flaifel, S.H. Ahmad, S. Hussein-Al-Ali, M.Z. Hussein, E.E. Eid, Z. Zainal, M. Saeed, M. Ilowefah, S. Fakurazi, N. Mohd Isa, M.E. El Zowalaty, Cytotoxicity of nickel zinc ferrite nanoparticles on cancer cells of epithelial origin, International journal of nanomedicine 8 (2013) 2497-508.
[39] M.S. Al-Qubaisi, A. Rasedee, M.H. Flaifel, S.H. Ahmad, S. Hussein-Al-Ali, M.Z. Hussein, Z. Zainal, F.H. Alhassan, Y.H. Taufiq-Yap, E.E. Eid, I.A. Arbab, B.A. Al-Asbahi, T.J. Webster, M.E. El Zowalaty, Induction of apoptosis in cancer cells by NiZn ferrite nanoparticles through mitochondrial cytochrome C release, International journal of nanomedicine 8 (2013) 4115-29.
[40] E.S. Taheri, M. Jahanshahi, M.T.H. Mosavian, Preparation, Characterization and Optimization of Egg Albumin Nanoparticles as Low Molecular-Weight Drug Delivery Vehicle, Particle & Particle Systems Characterization 29(3) (2012) 211-222.
[41] M. Qasim, K. Asghar, B.R. Singh, S. Prathapani, W. Khan, A.H. Naqvi, D. Das, Magnetically recyclable Ni0.5Zn0.5Fe2O4/Zn0.95Ni0.05O nano-photocatalyst: Structural, optical, magnetic and photocatalytic properties, Spectrochimica Acta Part A: Molecular and Biomolecular Spectroscopy 137(Supplement C) (2015) 1348-1356.
[42] G.V.N. Rathna, J.P. Jog, A.B. Gaikwad, Development of non-woven nanofibers of egg albumen-poly (vinyl alcohol) blends: influence of solution properties on morphology of nanofibers, Polym J 43(7) (2011) 654-661.
[43] S. Jana, S. Manna, A.K. Nayak, K.K. Sen, S.K. Basu, Carbopol gel containing chitosan-egg albumin nanoparticles for transdermal aceclofenac delivery, Colloids and Surfaces B: Biointerfaces 114(Supplement C) (2014) 36-44.
[44] D.S. Aniesrani Delfiya, K. Thangavel, D. Amirtham, Preparation of Curcumin Loaded Egg Albumin Nanoparticles Using Acetone and Optimization of Desolvation Process, The Protein Journal 35(2) (2016) 124-135.
[45] K. Rani, Preparation of Egg Albumin Nanoparticles (EANPs) by Using Toluene-Butanol Desolvation Method, International Journal of Pharmaceutical and Chemical Sciences 5 (2016) 128-131.
[46] J. L. Tucker & M. M. Faul, Industrial research: Drug companies must adopt green chemistry, , Nature, 534, (2016) 27-29.
[47] R.E. Yanes, F. Tamanoi, Development of mesoporous silica nanomaterials as a vehicle for anticancer drug delivery, Therapeutic delivery 3(3) (2012) 389-404.
[48] S. Angelos, E. Johansson, J.F. Stoddart, J.I. Zink, Mesostructured Silica Supports for Functional Materials and Molecular Machines, Advanced Functional Materials 17(14) (2007) 2261-2271.
[49] X. Yang, H. Hong, J.J. Grailer, I.J. Rowland, A. Javadi, S.A. Hurley, Y. Xiao, Y. Yang, Y. Zhang, R.J. Nickles, W. Cai, D.A. Steeber, S. Gong, cRGD-functionalized, DOX-conjugated, and 64Cu-labeled superparamagnetic iron oxide nanoparticles for targeted anticancer drug delivery and PET/MR imaging, Biomaterials 32(17) (2011) 4151-4160.
[50] N.S. Satarkar, J.Z. Hilt, Magnetic hydrogel nanocomposites for remote controlled pulsatile drug release, Journal of Controlled Release 130(3) (2008) 246-251.
[51] T. Saitoh, K. Asano, M. Hiraide, Removal of phenols in water using chitosan-conjugated thermo-responsive polymers, Journal of hazardous materials 185(2) (2011) 1369-1373.

[52] F.-H. Chen, L.-M. Zhang, Q.-T. Chen, Y. Zhang, Z.-J. Zhang, Synthesis of a novel magnetic drug delivery system composed of doxorubicin-conjugated Fe3O4 nanoparticle cores and a PEG-functionalized porous silica shell, Chemical communications 46(45) (2010) 8633-8635.
[53] S. Mura, J. Nicolas, P. Couvreur, Stimuli-responsive nanocarriers for drug delivery, Nat Mater 12(11) (2013) 991-1003.
[54] B. Chang, X. Sha, J. Guo, Y. Jiao, C. Wang, W. Yang, Thermo and pH dual responsive, polymer shell coated, magnetic mesoporous silica nanoparticles for controlled drug release, Journal of materials chemistry 21(25) (2011) 9239-9247.
[55] C. Liu, J. Guo, W. Yang, J. Hu, C. Wang, S. Fu, Magnetic mesoporous silica microspheres with thermo-sensitive polymer shell for controlled drug release, Journal of materials chemistry 19(27) (2009) 4764-4770.
[56] S. Sharma, A. Verma, B.V. Teja, G. Pandey, N. Mittapelly, R. Trivedi, P.R. Mishra, An insight into functionalized calcium based inorganic nanomaterials in biomedicine: Trends and transitions, Colloids and Surfaces B: Biointerfaces 133(Supplement C) (2015) 120-139.
[57] Y. Ueno, H. Futagawa, Y. Takagi, A. Ueno, Y. Mizushima, Drug-incorporating calcium carbonate nanoparticles for a new delivery system, Journal of Controlled Release 103(1) (2005) 93-98.
[58] X.w. He, T. Liu, Y.x. Chen, D.j. Cheng, X.r. Li, Y. Xiao, Y.l. Feng, Calcium carbonate nanoparticle delivering vascular endothelial growth factor-C siRNA effectively inhibits lymphangiogenesis and growth of gastric cancer in vivo, Cancer Gene Ther 15(3) (2008) 193-202.
[59] X. Ying, C. Shan, K. Jiang, Z. Chen, Y. Du, Intracellular pH-sensitive delivery CaCO3 nanoparticles templated by hydrophobic modified starch micelles, RSC Advances 4(21) (2014) 10841-10844.
[60] J. Wang, J.-S. Chen, J.-Y. Zong, D. Zhao, F. Li, R.-X. Zhuo, S.-X. Cheng, Calcium Carbonate/Carboxymethyl Chitosan Hybrid Microspheres and Nanospheres for Drug Delivery, The Journal of Physical Chemistry C 114(44) (2010) 18940-18945.
[61] S.K. Kim, M.B. Foote, L. Huang, Targeted delivery of EV peptide to tumor cell cytoplasm using lipid coated calcium carbonate nanoparticles, Cancer Letters 334(2) (2013) 311-318.
[62] S. Chen, D. Zhao, F. Li, R.-X. Zhuo, S.-X. Cheng, Co-delivery of genes and drugs with nanostructured calcium carbonate for cancer therapy, RSC Advances 2(5) (2012) 1820-1826.
[63] D. Zhao, R.-X. Zhuo, S.-X. Cheng, Alginate modified nanostructured calcium carbonate with enhanced delivery efficiency for gene and drug delivery, Molecular BioSystems 8(3) (2012) 753-759.
[64] W. Cui, Y. Cui, J. Zhao, J. Li, Fabrication of tumor necrosis factor-related apoptosis inducing ligand (TRAIL)/ALG modified CaCO3 as drug carriers with the function of tumor selective recognition, Journal of Materials Chemistry B 1(9) (2013) 1326-1332.
[65] H. Shi, L. Li, L. Zhang, T. Wang, C. Wang, D. Zhu, Z. Su, Designed preparation of polyacrylic acid/calcium carbonate nanoparticles with high doxorubicin payload for liver cancer chemotherapy, CrystEngComm 17(26) (2015) 4768-4773.
[66] Y. Zhao, Y. Lu, Y. Hu, J.-P. Li, L. Dong, L.-N. Lin, S.-H. Yu, Synthesis of Superparamagnetic CaCO3 Mesocrystals for Multistage Delivery in Cancer Therapy, Small 6(21) (2010) 2436-2442.
[67] K.H. Min, H.S. Min, H.J. Lee, D.J. Park, J.Y. Yhee, K. Kim, I.C. Kwon, S.Y. Jeong, O.F. Silvestre, X. Chen, Y.-S. Hwang, E.-C. Kim, S.C. Lee, pH-Controlled Gas-Generating Mineralized Nanoparticles: A Theranostic Agent for Ultrasound Imaging and Therapy of Cancers, ACS Nano 9(1) (2015) 134-145.
[68] J. Kim, H.S. Kim, N. Lee, T. Kim, H. Kim, T. Yu, I.C. Song, W.K. Moon, T. Hyeon, Multifunctional Uniform Nanoparticles Composed of a Magnetite Nanocrystal Core and a Mesoporous Silica Shell for Magnetic Resonance and Fluorescence Imaging and for Drug Delivery, Angewandte Chemie 120(44) (2008) 8566-8569.
[69] J. Kim, J.E. Lee, J. Lee, J.H. Yu, B.C. Kim, K. An, Y. Hwang, C.-H. Shin, J.-G. Park, J. Kim, T. Hyeon, Magnetic Fluorescent Delivery Vehicle Using Uniform Mesoporous Silica Spheres Embedded with Monodisperse Magnetic and Semiconductor Nanocrystals, Journal of the American Chemical Society 128(3) (2006) 688-689.
[70] J.E. Lee, N. Lee, T. Kim, J. Kim, T. Hyeon, Multifunctional Mesoporous Silica Nanocomposite Nanoparticles for Theranostic Applications, Accounts of Chemical Research 44(10) (2011) 893-902.
[71] W.-H. Chen, G.-F. Luo, Q. Lei, F.-Y. Cao, J.-X. Fan, W.-X. Qiu, H.-Z. Jia, S. Hong, F. Fang, X. Zeng, R.-X. Zhuo, X.-Z. Zhang, Rational design of multifunctional magnetic mesoporous silica nanoparticle for tumor-targeted magnetic resonance imaging and precise therapy, Biomaterials 76(Supplement C) (2016) 87-101.
[72] Alvarez-Berr, #xed, M.P. os, N. Sosa-Cintron, M. Rodriguez-Lugo, R. Juneja, J.L. Vivero-Escoto, Hybrid Nanomaterials Based on Iron Oxide Nanoparticles and Mesoporous Silica Nanoparticles: Overcoming Challenges in Current Cancer Treatments, Journal of Chemistry 2016 (2016) 15.
[73] G. Yang, R. Lv, F. He, F. Qu, S. Gai, S. Du, Z. Wei, P. Yang, A core/shell/satellite anticancer platform for 808 NIR light-driven multimodal imaging and combined chemo-/photothermal therapy, Nanoscale 7(32) (2015) 13747-13758.
[74] L. Guo, I. Panderi, D.D. Yan, K. Szulak, Y. Li, Y.-T. Chen, H. Ma, D.B. Niesen, N. Seeram, A. Ahmed, B. Yan, D. Pantazatos, W. Lu, A Comparative Study of Hollow Copper Sulfide Nanoparticles and Hollow Gold Nanospheres on Degradability and Toxicity, ACS Nano 7(10) (2013) 8780-8793.

[75] Z. Zha, S. Wang, S. Zhang, E. Qu, H. Ke, J. Wang, Z. Dai, Targeted delivery of CuS nanoparticles through ultrasound image-guided microbubble destruction for efficient photothermal therapy, Nanoscale 5(8) (2013) 3216-3219.
[76] Y. Li, W. Lu, Q. Huang, C. Li, W. Chen, Copper sulfide nanoparticles for photothermal ablation of tumor cells, Nanomedicine 5(8) (2010) 1161-1171.
[77] W. Lingjie, W. Ming, Z. Yongyi, Z. Da, Z. Aixian, L. Xiaolong, L. Jingfeng, Multifunctional PEG modified DOX loaded mesoporous silica nanoparticle@CuS nanohybrids as photo-thermal agent and thermal-triggered drug release vehicle for hepatocellular carcinoma treatment, Nanotechnology 26(2) (2015) 025102.
[78] G. Song, Q. Wang, Y. Wang, G. Lv, C. Li, R. Zou, Z. Chen, Z. Qin, K. Huo, R. Hu, J. Hu, A Low-Toxic Multifunctional Nanoplatform Based on Cu9S5@mSiO2 Core-Shell Nanocomposites: Combining Photothermal-and Chemotherapies with Infrared Thermal Imaging for Cancer Treatment, Advanced Functional Materials 23(35) (2013) 4281-4292.
[79] X. Liu, F. Fu, K. Xu, R. Zou, J. Yang, Q. Wang, Q. Liu, Z. Xiao, J. Hu, Folic acid-conjugated hollow mesoporous silica/CuS nanocomposites as a difunctional nanoplatform for targeted chemo-photothermal therapy of cancer cells, Journal of Materials Chemistry B 2(33) (2014) 5358-5367.
[80] F. Chen, H. Hong, S. Goel, S.A. Graves, H. Orbay, E.B. Ehlerding, S. Shi, C.P. Theuer, R.J. Nickles, W. Cai, In Vivo Tumor Vasculature Targeting of CuS@MSN Based Theranostic Nanomedicine, ACS Nano 9(4) (2015) 3926-3934.
[81] Q. Tian, J. Hu, Y. Zhu, R. Zou, Z. Chen, S. Yang, R. Li, Q. Su, Y. Han, X. Liu, Sub-10 nm Fe3O4@Cu2–xS Core–Shell Nanoparticles for Dual-Modal Imaging and Photothermal Therapy, Journal of the American Chemical Society 135(23) (2013) 8571-8577.
[82] Z.-C. Wu, W.-P. Li, C.-H. Luo, C.-H. Su, C.-S. Yeh, Rattle-Type Fe3O4@CuS Developed to Conduct Magnetically Guided Photoinduced Hyperthermia at First and Second NIR Biological Windows, Advanced Functional Materials 25(41) (2015) 6527-6537.
[83] Z. Gao, X. Liu, G. Deng, F. Zhou, L. Zhang, Q. Wang, J. Lu, Fe3O4@mSiO2-FA-CuS-PEG nanocomposites for magnetic resonance imaging and targeted chemo-photothermal synergistic therapy of cancer cells, Dalton Transactions 45(34) (2016) 13456-13465.
[84] B. Liu, X. Zhang, C. Li, F. He, Y. Chen, S. Huang, D. Jin, P. Yang, Z. Cheng, J. Lin, Magnetically targeted delivery of DOX loaded Cu9S5@mSiO2@Fe3O4-PEG nanocomposites for combined MR imaging and chemo/photothermal synergistic therapy, Nanoscale 8(25) (2016) 12560-12569.
[85] X. She, L. Chen, C. Li, C. He, L. He, L. Kong, Functionalization of Hollow Mesoporous Silica Nanoparticles for Improved 5-FU Loading, Journal of Nanomaterials 2015 (2015) 9.
[86] N.-H. Cho, T.-C. Cheong, J.H. Min, J.H. Wu, S.J. Lee, D. Kim, J.-S. Yang, S. Kim, Y.K. Kim, S.-Y. Seong, A multifunctional core–shell nanoparticle for dendritic cell-based cancer immunotherapy, 6 (2011) 675.
[87] P. Sathishkumar, N. Pugazhenthiran, R.V. Mangalaraja, A.M. Asiri, S. Anandan, ZnO supported CoFe2O4 nanophotocatalysts for the mineralization of Direct Blue 71 in aqueous environments, Journal of hazardous materials 252-253(Supplement C) (2013) 171-179.
[88] K.K. Senapati, C. Borgohain, P. Phukan, Synthesis of highly stable CoFe2O4 nanoparticles and their use as magnetically separable catalyst for Knoevenagel reaction in aqueous medium, Journal of Molecular Catalysis A: Chemical 339(1) (2011) 24-31.
[89] A. Ito, M. Shinkai, H. Honda, T. Kobayashi, Medical application of functionalized magnetic nanoparticles, Journal of Bioscience and Bioengineering 100(1) (2005) 1-11.
[90] J.A. Khan, M. Qasim, B.R. Singh, S. Singh, M. Shoeb, W. Khan, D. Das, A.H. Naqvi, Synthesis and characterization of structural, optical, thermal and dielectric properties of polyaniline/CoFe2O4 nanocomposites with special reference to photocatalytic activity, Spectrochimica Acta Part A: Molecular and Biomolecular Spectroscopy 109(Supplement C) (2013) 313-321.
[91] A. Roychowdhury, S.P. Pati, A.K. Mishra, S. Kumar, D. Das, Magnetically addressable fluorescent Fe3O4/ZnO nanocomposites: Structural, optical and magnetization studies, Journal of Physics and Chemistry of Solids 74(6) (2013) 811-818.
[92] L. Sun, R. Shao, L. Tang, Z. Chen, Synthesis of ZnFe2O4/ZnO nanocomposites immobilized on graphene with enhanced photocatalytic activity under solar light irradiation, Journal of Alloys and Compounds 564(Supplement C) (2013) 55-62.
[93] E. Casbeer, V.K. Sharma, X.-Z. Li, Synthesis and photocatalytic activity of ferrites under visible light: A review, Separation and Purification Technology 87(Supplement C) (2012) 1-14.
[94] A. Bouaoud, A. Rmili, F. Ouachtari, A. Louardi, T. Chtouki, B. Elidrissi, H. Erguig, Transparent conducting properties of Ni doped zinc oxide thin films prepared by a facile spray pyrolysis technique using perfume atomizer, Materials Chemistry and Physics 137(3) (2013) 843-847.
[95] J.K. Salem, T.M. Hammad, R.R. Harrison, Synthesis, structural and optical properties of Ni-doped ZnO micro-spheres, Journal of Materials Science: Materials in Electronics 24(5) (2013) 1670-1676.

[96] L. Huang, F. Peng, H. Wang, H. Yu, Z. Li, Preparation and characterization of Cu2O/TiO2 nano–nano heterostructure photocatalysts, Catalysis Communications 10(14) (2009) 1839-1843.
[97] H.G. Kim, P.H. Borse, W. Choi, J.S. Lee, Photocatalytic Nanodiodes for Visible-Light Photocatalysis, Angewandte Chemie International Edition 44(29) (2005) 4585-4589.
[98] E.S. Kim, N. Nishimura, G. Magesh, J.Y. Kim, J.-W. Jang, H. Jun, J. Kubota, K. Domen, J.S. Lee, Fabrication of CaFe2O4/TaON Heterojunction Photoanode for Photoelectrochemical Water Oxidation, Journal of the American Chemical Society 135(14) (2013) 5375-5383.
[99] H.G. Kim, P.H. Borse, J.S. Jang, E.D. Jeong, O.-S. Jung, Y.J. Suh, J.S. Lee, Fabrication of CaFe2O4/MgFe2O4 bulk heterojunction for enhanced visible light photocatalysis, Chemical communications (39) (2009) 5889-5891.
[100] R. Dom, R. Subasri, K. Radha, P.H. Borse, Synthesis of solar active nanocrystalline ferrite, MFe2O4 (M: Ca, Zn, Mg) photocatalyst by microwave irradiation, Solid State Communications 151(6) (2011) 470-473.
[101] S.H. Xu, D.L. Feng, W.F. Shangguan, J. Phys. Chem. C 113 (2009) 2463-2467.
[102] R.Y. Hong, S.Z. Zhang, G.Q. Di, H.Z. Li, Y. Zheng, J. Ding, D.G. Wei, Preparation, characterization and application of Fe3O4/ZnO core/shell magnetic nanoparticles, Materials Research Bulletin 43(8) (2008) 2457-2468.
[103] C. Borgohain, K.K. Senapati, K.C. Sarma, P. Phukan, A facile synthesis of nanocrystalline CoFe2O4 embedded one-dimensional ZnO hetero-structure and its use in photocatalysis, Journal of Molecular Catalysis A: Chemical 363-364(Supplement C) (2012) 495-500.
[104] Z.-Y. Zhang, H.-M. Xiong, Photoluminescent ZnO Nanoparticles and Their Biological Applications, Materials 8(6) (2015).
[105] A. Anitha, S. Maya, N. Deepa, K.P. Chennazhi, S.V. Nair, H. Tamura, R. Jayakumar, Efficient water soluble O-carboxymethyl chitosan nanocarrier for the delivery of curcumin to cancer cells, Carbohydrate Polymers 83(2) (2011) 452-461.
[106] H. Yan, C. Teh, S. Sreejith, L. Zhu, A. Kwok, W. Fang, X. Ma, K.T. Nguyen, V. Korzh, Y. Zhao, Functional Mesoporous Silica Nanoparticles for Photothermal-Controlled Drug Delivery In Vivo, Angewandte Chemie International Edition 51(33) (2012) 8373-8377.
[107] S. Jambhrunkar, S. Karmakar, A. Popat, M. Yu, C. Yu, Mesoporous silica nanoparticles enhance the cytotoxicity of curcumin, RSC Advances 4(2) (2014) 709-712.
[108] F. Muhammad, A. Wang, M. Guo, J. Zhao, W. Qi, G. Yingjie, J. Gu, G. Zhu, pH Dictates the Release of Hydrophobic Drug Cocktail from Mesoporous Nanoarchitecture, ACS Applied Materials & Interfaces 5(22) (2013) 11828-11835.
[109] M.M. Yallapu, S.F. Othman, E.T. Curtis, N.A. Bauer, N. Chauhan, D. Kumar, M. Jaggi, S.C. Chauhan, Curcumin-loaded magnetic nanoparticles for breast cancer therapeutics and imaging applications, International journal of nanomedicine 7 (2012) 1761-1779.
[110] P. Huang, B. Zeng, Z. Mai, J. Deng, Y. Fang, W. Huang, H. Zhang, J. Yuan, Y. Wei, W. Zhou, Novel drug delivery nanosystems based on out-inside bifunctionalized mesoporous silica yolk-shell magnetic nanostars used as nanocarriers for curcumin, Journal of Materials Chemistry B 4(1) (2016) 46-56.
[111] J.D.D. Pitout, The latest threat in the war on antimicrobial resistance, The Lancet Infectious Diseases 10(9) (2010) 578-579.
[112] P.-R. Hsueh, New Delhi Metallo-β-lactamase-1 (NDM-1): An Emerging Threat Among Enterobacteriaceae, Journal of the Formosan Medical Association 109(10) (2010) 685-687.
[113] D.V. Quang, P.B. Sarawade, A. Hilonga, J.-K. Kim, Y.G. Chai, S.H. Kim, J.-Y. Ryu, H.T. Kim, Preparation of silver nanoparticle containing silica micro beads and investigation of their antibacterial activity, Applied Surface Science 257(15) (2011) 6963-6970.
[114] J.A. Khan, M. Qasim, B.R. Singh, W. Khan, D. Das, A.H. Naqvi, Polyaniline/CoFe2O4 nanocomposite inhibits the growth of Candida albicans 077 by ROS production, Comptes Rendus Chimie 17(2) (2014) 91-102.
[115] K. Nischala, T.N. Rao, N. Hebalkar, Silica–silver core–shell particles for antibacterial textile application, Colloids and Surfaces B: Biointerfaces 82(1) (2011) 203-208.
[116] D.V. Quang, P.B. Sarawade, A. Hilonga, S.D. Park, J.-K. Kim, H.T. Kim, Facile route for preparation of silver nanoparticle-coated precipitated silica, Applied Surface Science 257(9) (2011) 4250-4256.
[117] C.-N. Lok, C.-M. Ho, R. Chen, Q.-Y. He, W.-Y. Yu, H. Sun, P.K.-H. Tam, J.-F. Chiu, C.-M. Che, Silver nanoparticles: partial oxidation and antibacterial activities, JBIC Journal of Biological Inorganic Chemistry 12(4) (2007) 527-534.
[118] Y.K.T.a.J.M.S. Sukdeb Pal, Does the Antibacterial Activity of Silver Nanoparticles Depend on the Shape of the Nanoparticle? A Study of the Gram-Negative Bacterium Escherichia coli, 73 (2007) 1712-1720.
[119] Y. Tian, J. Qi, W. Zhang, Q. Cai, X. Jiang, Facile, One-Pot Synthesis, and Antibacterial Activity of Mesoporous Silica Nanoparticles Decorated with Well-Dispersed Silver Nanoparticles, ACS Applied Materials & Interfaces 6(15) (2014) 12038-12045.

[120] B. Hu, S.-B. Wang, K. Wang, M. Zhang, S.-H. Yu, Microwave-Assisted Rapid Facile "Green" Synthesis of Uniform Silver Nanoparticles: Self-Assembly into Multilayered Films and Their Optical Properties, The Journal of Physical Chemistry C 112(30) (2008) 11169-11174.
[121] E. Filippo, A. Serra, A. Buccolieri, D. Manno, Green synthesis of silver nanoparticles with sucrose and maltose: Morphological and structural characterization, Journal of Non-Crystalline Solids 356(6) (2010) 344-350.
[122] R. Lu, D. Yang, D. Cui, Z. Wang, L. Guo, Egg white-mediated green synthesis of silver nanoparticles with excellent biocompatibility and enhanced radiation effects on cancer cells, International journal of nanomedicine 7 (2012) 2101-2107.
[123] Q. Sun, X. Cai, J. Li, M. Zheng, Z. Chen, C.-P. Yu, Green synthesis of silver nanoparticles using tea leaf extract and evaluation of their stability and antibacterial activity, Colloids and Surfaces A: Physicochemical and Engineering Aspects 444(Supplement C) (2014) 226-231.
[124] V.K. Sharma, R.A. Yngard, Y. Lin, Silver nanoparticles: Green synthesis and their antimicrobial activities, Advances in Colloid and Interface Science 145(1) (2009) 83-96.
[125] O.V. Kharissova, H.V.R. Dias, B.I. Kharisov, B.O. Pérez, V.M.J. Pérez, The greener synthesis of nanoparticles, Trends in Biotechnology 31(4) (2013) 240-248.
[126] M. Liong, B. France, K.A. Bradley, J.I. Zink, Antimicrobial Activity of Silver Nanocrystals Encapsulated in Mesoporous Silica Nanoparticles, Advanced materials 21(17) (2009) 1684-1689.
[127] L. Rocks, K. Faulds, D. Graham, Rationally designed SERS active silica coated silver nanoparticles, Chemical communications 47(15) (2011) 4415-4417.
[128] G. Gu, J. Xu, Y. Wu, M. Chen, L. Wu, Synthesis and antibacterial property of hollow SiO2/Ag nanocomposite spheres, Journal of Colloid and Interface Science 359(2) (2011) 327-333.
[129] R. Prucek, J. Tuček, M. Kilianová, A. Panáček, L. Kvítek, J. Filip, M. Kolář, K. Tománková, R. Zbořil, The targeted antibacterial and antifungal properties of magnetic nanocomposite of iron oxide and silver nanoparticles, Biomaterials 32(21) (2011) 4704-4713.
[130] X. Zhang, H. Niu, J. Yan, Y. Cai, Immobilizing silver nanoparticles onto the surface of magnetic silica composite to prepare magnetic disinfectant with enhanced stability and antibacterial activity, Colloids and Surfaces A: Physicochemical and Engineering Aspects 375(1) (2011) 186-192.
[131] H.H. Park, S. Park, G. Ko, K. Woo, Magnetic hybrid colloids decorated with Ag nanoparticles bite away bacteria and chemisorb viruses, Journal of Materials Chemistry B 1(21) (2013) 2701-2709.
[132] S.-S. Chen, H. Xu, H.-J. Xu, G.-J. Yu, X.-L. Gong, Q.-L. Fang, K.C.-F. Leung, S.-H. Xuan, Q.-R. Xiong, A facile ultrasonication assisted method for Fe3O4@SiO2-Ag nanospheres with excellent antibacterial activity, Dalton Transactions 44(19) (2015) 9140-9148.
[133] E. Yu, I. Galiana, R. Martínez-Máñez, P. Stroeve, M.D. Marcos, E. Aznar, F. Sancenón, J.R. Murguía, P. Amorós, Poly(N-isopropylacrylamide)-gated Fe3O4/SiO2 core shell nanoparticles with expanded mesoporous structures for the temperature triggered release of lysozyme, Colloids and Surfaces B: Biointerfaces 135(Supplement C) (2015) 652-660.
[134] K. Asghar, M. Qasim, G. Dharmapuri, D. Das, Investigation on a smart nanocarrier with a mesoporous magnetic core and thermo-responsive shell for co-delivery of doxorubicin and curcumin: a new approach towards combination therapy of cancer, RSC Adv. 7(46) (2017) 28802-28818.
[135] W. Zhang, X. Zheng, S. Shen, X. Wang, Doxorubicin-loaded magnetic nanoparticle clusters for chemo-photothermal treatment of the prostate cancer cell line PC3, Biochemical and Biophysical Research Communications 466(2) (2015) 278-282.
[136] J. Liu, Z. Sun, Y. Deng, Y. Zou, C. Li, X. Guo, L. Xiong, Y. Gao, F. Li, D. Zhao, Highly water-dispersible biocompatible magnetite particles with low cytotoxicity stabilized by citrate groups, Angewandte Chemie 48(32) (2009) 5875-9.
[137] S. Xuan, F. Wang, J.M.Y. Lai, K.W.Y. Sham, Y.-X.J. Wang, S.-F. Lee, J.C. Yu, C.H.K. Cheng, K.C.-F. Leung, Synthesis of Biocompatible, Mesoporous Fe3O4 Nano/Microspheres with Large Surface Area for Magnetic Resonance Imaging and Therapeutic Applications, ACS Applied Materials & Interfaces 3(2) (2011) 237-244.
[138] X. Liu, Q. Hu, Z. Fang, Q. Wu, Q. Xie, Carboxyl Enriched Monodisperse Porous Fe3O4 Nanoparticles with Extraordinary Sustained-Release Property, Langmuir 25(13) (2009) 7244-7248.
[139] S. Zhang, W. Wu, X. Xiao, J. Zhou, F. Ren, C. Jiang, Preparation and characterization of spindle-like Fe3O4 mesoporous nanoparticles, Nanoscale Research Letters 6(1) (2011) 89.

CHAPTER 3: EXPERIMENTAL WORK

Chapter 3

Experimental work

In this chapter details of synthesis and various experimental techniques carried out in this work are reported in detail.

3.1 Materials:

All reagents used in this study were of analytical grade. $FeCl_3.6H_2O$, and $CoCl_2.4H_2O$ were purchased from the Fisher Scientific. NaOH, $NaBH_4$ and Hydrazine Hydrate were obtained from SRL India. Zinc nitrate (>98% $Zn(NO_3)_2.6H_2O$), nickel nitrate (>98% $Ni(NO_3)_2.6H_2O$), iron nitrate (>98% $Fe(NO_3)_3.9H_2O$), doxorubicin hydrochloride (DOX, 98%), 3-(4,5-dimethylthiazol-2-yl)-2,5-diphenyltetrazolium bromide (MTT), Tetraethyl orthosilicate (TEOS, 99.99%), NIPAM from Sigma Aldrich and citric acid, ammonia, phosphate buffer saline (PBS), citrate buffer, DMSO, silver nitrate (99%) from SRL, India were used in this study without any purification. Egg white was obtained from fresh hen egg available in the market. Cetyltrimethylammonium bromide($C_{19}H_{42}BrN$) and aqueous ammonia were obtained from SDFCL and ethanol (99.9%) was procured from Hangzhou China.

3.2 Preparation of samples

3.2.1 Synthesis of different MNPs

Various synthesis methods have been used for the preparation of Fe_3O_4 (IO NPs), $CoFe_2O_4$ (CF NPs), $Ni_{0.5}Zn_{0.5}Fe_2O_4$ (NZF NPs) and $CaFe_2O_4$ NPs such as modified coprecipitation, high-temperature decomposition of organic precursors, and auto-combustion etc. [1-3,4].

3.2.1.1 Synthesis of Fe_3O_4 NPs by precipitation method

Two different size of Fe_3O_4 NPs were prepared using $FeCl_3$, $NaBH_4$, hydrazine hydrate, NaOH and oleic acid[5]. In typical synthesis procedure, first, 100 ml of 0.3 M $FeCl_3$ solution was prepared in ethanol. Then certain amount of $NaBH_4$ in 100 ml water was poured to the above salt solution. Then, 5ml hydrazine hydrate, 2 gm NaOH (in 50 ml water) and 5 ml oleic acid were added one by one. Obtained blackish brown color Fe_3O_4 NP was separated, washed and dried at 100 ^oC. Preparation of Fe_3O_4 NP was carried out twice, using 0.5 gm (IO-1) and 1 gm (IO 2) $NaBH_4$ and fixing other condition same.

3.2.1.2 Synthesis of $CoFe_2O_4$ (CF NPs) by coprecipitation method

CF NPs were prepared by co-precipitation of Fe^{3+} and Co^{2+} (2:1 molar ratio) in presence of $NaBH_4$, hydrazine hydrate NaOH and oleic acid. First, $FeCl_3$ and $CoCl_2$ in 2:1 molar ratio, were dissolved in 100 ml of ethanol. Then certain amount of $NaBH_4$ in 100 ml water was added to the Fe^{3+} and Co^{2+} solution. The 5ml hydrazine hydrate, 2 gm NaOH (in 50 ml water) and 5 ml oleic acid were added one by one. Precipitated black color CF NPs was separated from water, rinsed with water and dried at 100 ^oC. Preparation of CF NPs was carried out twice, using 0.5 gm (CF1) and 1 gm (CF2) $NaBH_4$ and fixing other condition same.

3.2.1.3 Preparation of $Ni_{0.5}Zn_{0.5}Fe_2O_4$ nanoparticle (NZF NP) by auto combustion method

NZF NP was prepared by gel-combustion method [6, 7]. In typical synthesis procedure, nickel nitrate, zinc nitrate and iron nitrate with a molar ratio of 1:1:4 were magnetically stirred to dissolve in 100 ml of water. Citric acid was added to the above nitrate precursor solution with citric acid: nitrate molar ratio of 1:1. The resultant sol was continuously stirred at 90 ^oC for 1 hour to evaporate excess water and to get viscous gel formed. The gel so formed was subjected to heating at 300 ^oC that has resulted in self ignited combustion reaction. Obtained powder was grounded in mortar and pestle and calcined to get reddish brown NZF NPs.

3.2.1.4 Synthesis of $CaFe_2O_4$ NP by auto combustion method

$CaFe_2O_4$ NP was prepared following the same gel combustion method as of NZF NP using 1:2 molar ratio of calcium nitrate and iron nitrate. Metal nitrates in 100 ml of water were stirred at 90 ^oC for 1 hour to get viscous gel and the mixture was then heated at 300 ^oC to initiate combustion reaction. After combustion, the powder was grounded and calcined at 300 ^OC to get reddish $CaFe_2O_4$ NP.

3.2.1.5 Synthesis of Fe_3O_4 NP by high temperature decomposition method

Well crystalline, monodispersed Fe_3O_4 NPs were prepared by high temperature decomposition Iron acetylacetonate in boiling dibenzyl ether in presence of 1,2-decanediol, oleic acid and oleylamine [2, 3]. In a typical synthesis procedure, Iron acetylacetonate (1.41 gm), 1,2-decanediol (4 gm), oleic acid (3.78 ml) and oleylamine (3.94 ml) were mixed 40 ml in dibezyl ether. Then the mixture was stirred at 200 ^oC for 30 hours and the temperature was raised to the 300^oC and further stirred at same temperature for 30 minute which has resulted formation of blackish Fe_3O_4 NPs.

3.2.2 Synthesis of NZF@Alb & NZF@Alb-Dox NPs and Fe_3O_4@Alb & CF@Alb NPs

3.2.2.1 Preparation of NZF@Alb and NZF@Alb-Dox Nanoparticles:

To prepare NZF@Alb NPs, firstly required quantity of prepared NZF NPs was dispersed in 8 ml of water by bath ultra-sonication. 2 ml of freshly extracted egg albumen was added drop-wise to the above dispersion with continuous ultra-sonication. Obtained NZF and albumen mixture was further sonicated for 30 minutes and then subjected to magnetic stirring for 4 hours. Resultant albumen coated NZF NPs (NZF@Alb NPs) were magnetically separated and stored for characterization. Dox loaded NZF@Alb NPs (NZF@Alb-Dox NPs) were obtained by in situ incorporation of doxorubicin in albumen matrix during NZF@Alb NPs formation. NZF@Alb-Dox NPs were prepared by following almost similar procedure of NZF@Alb NPs but with extra addition of doxorubicin in starting aqueous dispersion of NZF NPs. Obtained NZF@Alb-Dox NPs were magnetically separated and rinsed twice with DI water to remove excess physically adsorbed Dox on surface of the nanoparticles. Finally, NZF@Alb-Dox NPs were stored in dark. Supernatant having unloaded free Dox was also collected and stored for further use[8].

3.2.2.2 Preparation of Fe_3O_4@Alb, Fe_3O_4@Alb-Dox and CF@Alb NP Nanoparticles

Fe_3O_4@Alb NP was synthesized by ultrasonication and stirring of aqueous mixture of Fe_3O_4 NPs and hen egg albumen[5]. First stable aqueous dispersion of Fe_3O_4 NP was obtained by ultrasonication. Then dropwise albumen was added to the above dispersion during sonication. The mixture was finally stirred for few hours. Obtained Fe_3O_4@Alb NP was separated by magnet and stored in glass vial. Fe_3O_4@Alb-Dox NP were obtained by stirring the aqueous dispersion of Fe_3O_4@Alb NP and Dox at room temperature. CF@Alb NP was fabricated by ultrasonication and stirring of aqueous mixture of CF NPs and egg albumen as described above for NZF@Alb and Fe_3O_4@Alb NP.

3.2.3 Synthesis of $mSiO_2$, MPS modified $mSiO_2$ NPs and multifuntional $mSiO_2$-$CaFe_2O_4$@P (Nipam-Aa) NC

$mSiO_2$ NPs was prepared using CTAB as a template via the simple Stober method which involve hydrolysis and condensation of TEOS. Formation process of $mSiO_2$ NPs and MPS modified $mSiO_2$ NPs is shown in figure 3.1. First, 1 gm of CTAB and 0.3 gm NaOH were

dissolved by sonication in 480 ml of water. Then the mixture was stirred at 80 ^{o}C on 500 rpm for 15 minutes to get uniform mixing. 10 ml of TEOS was then drop wise added to the above mixture. Mixture was further stirred 24 hours to get milky solution. Obtained silica-CTAB complex was centrifuged and washed several times with water and ethanol. The silica-CTAB complex was dried at 100 ^{o}C. Silica-CTAB complex was calcined at 600 ^{o}C for 2 hours to get mesoporous silica NPs ($mSiO_2$ NPs). MPS modified $mSiO_2$ NPs was prepared by stirring already prepared $mSiO_2$ NPs with MPS in ethanol. For that, 200 mg of $mSiO_2$ NPs was dispersed in 50 ml of EtOH by sonication for 30 minutes. The mixture was then transfer to the magnetic stirring and 0.5 ml of MPS was added to the above mixture. The mixture was stirred at 40 ^{o}C for 12 hours to get MPS modified $mSiO_2$ NPs (MPS- $mSiO_2$ NPs). The MPS- $mSiO_2$ NPs was separated and washed multiple time.

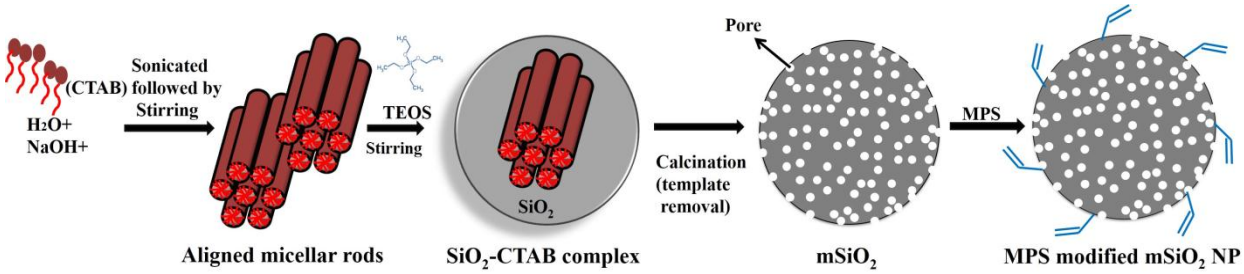

Figure. 3.1. Synthesis process of $mSiO_2$ NPs and MPS modified $mSiO_2$ NPs.

$mSiO_2$-CF@P(Nipam-Aa) nanocomposites were synthesized by copolymerization of NIPAM and Acrylic acid monomer on the surface of $mSiO_2$ NPs, in the presence of $CaFe_2O_4$ NPs, crosslinker (MBA) and oxidizer (KPS). In typical synthesis procedure, 200 mg of MPS modified $mSiO_2$ NPs, 50 mg of $CaFe_2O_4$ NPs, 147 mg of NIPAM, 16.45 mg of Acrylic acid (Aa), 10.26 mg of MBA and 16 mg of SDS were added in 50 ml of water. The resulting mixture was stirred for 30 min at 70 ^{o}C. After getting homogenous mixture, 30 mg of KPS in 10 ml of water was added to the mixture. The reaction mixture was allowed to stir for another 8 hours at 70 ^{o}C. Finally, obtained product was magnetically separated and washed several times with water and ethanol. Product was dried at RT to get powdered nanocomposite. Obtained P(Nipam-Aa) coated and $CaFe_2O_4$ embedded mesoporous silica nanocomposite was named as $mSiO_2$-$CaFe_2O_4$@ P(Nipam-Aa) nanocomposite. Namely, $mSiO_2$-CF@P(Nipam-Aa)-1 and $mSiO_2$-CF@P(Nipam-Aa)-2 nanocomposites have been prepared using bare $mSiO_2$ NPs and MPS modified $mSiO_2$ NPs respectively. In both the cases same synthesis process was used.

$mSiO_2$-$CaFe_2O_4$@ P(Nipam-Aa)-Dox was obtained by stirring (150 rpm) the mixture of $mSiO_2$-$CaFe_2O_4$@ P(Nipam-Aa)-2 and Dox in 4 ml 7.4 PBS.

3.2.4 Synthesis of multifuntional mesoCaCO$_3$@CaFe$_2$O$_4$ and mesoCaCO$_3$@CaFe$_2$O$_4$-Dox

$CaFe_2O_4$ NP impregnated mesoCaCO$_3$ nanocomposite (mesoCaCO$_3$@$CaFe_2O_4$ NC) have successfully been synthesized by environmental friendly biological route using waste egg shell, lemon juice, $CaFe_2O_4$ NP, and cetyltrimethylammonium bromide (CTAB). First, $CaFe_2O_4$ NP was prepared by auto-combustion method. To prepare mesoCaCO$_3$@$CaFe_2O_4$ NC, first $CaFe_2O_4$ NP, CTAB, and lemon juice were mixed in water by sonication and stirring. Then the suspension of powdered egg shell was drop wise added to the above mixture while stirring. The mixture was left on magnetic stirrer to complete the reaction. Obtained brown precipitate was centrifuge, washed and dried at room temperature. Finally, the obtained intermediated compound was calcined at 500 ^oC for 2 hours to get mesoCaCO$_3$@$CaFe_2O_4$ NC. Pure mesoporous $CaCO_3$ (mesoCaCO$_3$) was also synthesized following the similar process without addition of $CaFe_2O_4$ NP. mesoCaCO$_3$@$CaFe_2O_4$-Dox was obtained by stirring (150 rpm) the aqueous dispersion (4 ml water) of mesoCaCO$_3$@$CaFe_2O_4$ NC and Dox in dark for 48 hours. The loaded mesoCaCO$_3$@$CaFe_2O_4$-Dox was washed several times to remove excess of drugs molecules on the surface of nanocarriers.

3.2.5 Synthesis of multifuntional NZF@mSiO$_2$ and NZF@mSiO$_2$-CuS-PEG

3.2.5.1 Synthesis of NZF@mSiO$_2$ NP

NZF@$mSiO_2$ were prepared by sol gel method [9] and NZF@$mSiO_2$-CuS-PEG was prepared by simple ultrasonication and stirring assisted deposition. $Ni_{0.5}Zn_{0.5}Fe_2O_4$ nanoparticles were synthesized using gel-combustion method. NZF@$mSiO_2$ nanocarrier was synthesized by in situ deposition of silica by hydrolysis-condensation of TEOS in presence of $Ni_{0.5}Zn_{0.5}Fe_2O_4$ nanoparticles and CTAB template. For the synthesis of NZF@$mSiO_2$ nanocarrier, first colloidal NZF NPs were prepared by dispersing proper amount of $Ni_{0.5}Zn_{0.5}Fe_2O_4$ NPs and CTAB in an alkaline mixture of water. The dispersion was then stirred at 50^oC. Then, 2.5 mL TEOS was added drop wise to the above dispersion and was stirred for another 12 h at room temperature. Obtained product was magnetically isolated, washed, dried and calcined at 500 ^oC.

3.2.5.2 Synthesis of CuS NP:

CuS NP was prepared using copper nitrate, tri-sodium citrate and sodium sulfide. First, 0.4 gm of copper nitrate was dissolved in 60 ml of water resulting blue color solution. Then,

20 ml aqueous solution of tri-sodium citrate was added to the above solution and stirred for another 30 minutes. After that, 5 ml of sodium sulfide aqueous solution was added and the temperature was raised to the 120 ^{o}C while the stirring for 30 minutes. Then, the temperature was reduced to zero ^{o}C and stirring was stopped. The obtained green color carboxylic functionalized CuS was centrifuged, washed and stored in water.

3.2.5.3 Synthesis of NZF@mSiO$_2$-CuS-PEG

For the preparation of NZF@mSiO$_2$-CuS-PEG, the prepared NZF@mSiO$_2$ NP was first functionalized with amine group using APTES. For this, 100 mg NZF@mSiO$_2$ NP, 1 ml water, 1 ml APTES in 30 ml ethanol were stirred at 60 ^{o}C for 3 hours. Then, the obtained NZF@mSiO$_2$-NH$_2$ NP was magnetically separated and dispersed in water. Carboxyl group functionalized CuS NP was separately prepared and used. NZF@mSiO$_2$-CuS NP was obtained by mixing and ultrasonicating the aqueous dispersion of NZF@mSiO$_2$-NH$_2$ NP and carboxyl group functionalized CuS NP. Further, 50 mg PEG was added to the mixture of NZF@mSiO$_2$-NH$_2$ and CuS (e.i. NZF@mSiO$_2$-CuS NP) during the sonication and further stirred for few hours to get NZF@mSiO$_2$-CuS-PEG NP. The obtained NZF@mSiO$_2$-CuS-PEG NP was magnetically separated, washed and stored. 5 Flu loaded NZF@mSiO$_2$-CuS-PEG NP (NZF@mSiO$_2$-CuS-PEG-5Flu NP) was obtained by stirring NZF@mSiO$_2$-CuS-PEG NP with aqueous solution of 5Flu at pH 7.4. 5 Flu and NZF@mSiO$_2$-CuS-PEG NP were dispersed in 5 ml mixture of water PBS (4.5 ml water and 0.5 ml PBS) by sonication for 15 minutes. Then the mixture was transferred to the magnetic stirrer and stirred further for 48 hours to obtained NZF@mSiO$_2$-CuS-PEG-5Flu NP. Loaded NP was washed several times to remove excess of drugs molecules on the surface of nanocarriers.

3.2.6 Synthesis of multifuntional NZF@Zn$_{0.95}$Ni$_{0.05}$O and NZF@Zn$_{0.95}$Ni$_{0.05}$O-mSiO$_2$

3.2.6.1 Synthesis of NZF@Zn$_{0.95}$Ni$_{0.05}$O NC

The synthesis procedure of Ni$_{0.5}$Zn$_{0.5}$Fe$_2$O$_4$@Zn$_{0.95}$Ni$_{0.05}$O nanocomposites involved a twostep process. In first step, dispersion of albumen coated Ni$_{0.5}$Zn$_{0.5}$Fe$_2$O$_4$ nanoparticles, which served as seeding materials, was prepared. In second step, Zn$_{0.95}$Ni$_{0.05}$O coated Ni$_{0.5}$Zn$_{0.5}$Fe$_2$O$_4$ nanoparticles, were synthesized using a precipitation method. The typical synthesis procedure is as below. In a beaker, appropriate amount of Ni$_{0.5}$Zn$_{0.5}$Fe$_2$O$_4$ nanoparticles were dispersed in 20 ml of water. Then, 30 ml of freshly extracted egg white was added to the above dispersion (beaker 1). In another beaker, appropriate amount of Zn(NO$_3$)$_2$.6H$_2$O, Ni(NO$_3$)$_2$.6H$_2$O were dissolved in 50 ml water (beaker 2). Both beakers were sonicated for 15 minutes to ensure proper mixing. Aqueous metal nitrate solution of beaker 2,

was added drop wise to the stable dispersion of $Ni_{0.5}Zn_{0.5}Fe_2O_4$ (NZF) in beaker 1 with continuous stirring for 30 minutes. Then 2-3 ml of ammonia was added in the resultant mixture. A brown color precipitate was obtained in the beaker. Obtained brown color precipitate was centrifuged, washed for several times with alcohol & water and dried at 50^oC. The dried NZF@Zn precursor was further calcined at 600^oC for 3 hours. Pure $Zn_{0.95}Ni_{0.05}O$ nanoparticles were prepared by the same method excluding the addition of ferrite nanoparticles. Different ferrite-zinc oxide nanocomposites were prepared by adding different percentages of ferrite ($Ni_{0.5}Zn_{0.5}Fe_2O_4$) nanoparticles such as 15%, 40% and 60% with $Zn_{0.95}Ni_{0.05}O$ nanoparticles and named as 15%NZF@Zn, 40%NZF@Zn and 60%NZF@Zn respectively. Obtained nanocomposites were kept in glass vials at room temperature for characterization.

3.2.6.2 Synthesis of multifuntional NZF@$Zn_{0.95}Ni_{0.05}O$-$mSiO_2$ NC

NZF@$Zn_{0.95}Ni_{0.05}O$-$mSiO_2$ (NZF@Zn-$mSiO_2$ NC) was prepared using CTAB as a soft template and TEOS as silica source via the simple Stober method. For the synthesis of NZF@Zn-$mSiO_2$ nanocarrier, first colloidal dispersion of NZF@Zn NP was obtained by stirring NZF@Zn NP and CTAB in an alkaline mixture of water. For this, 1 gm of CTAB and 0.3 gm NaOH were used. Then the mixture was stirred at 80 ^oC on 500 rpm for 15 minutes to get uniform mixing. Then, TEOS was drop wise added to the above mixture. The mixture was further stirred for 24 hours to get NZF@Zn-$mSiO_2$-CTAB intermediate complex. Obtained intermediate product was centrifuged and washed several times with water and ethanol and then dried at 100 ^oC. It was calcined at 500 ^oC for 2 hours to get NZF@Zn-$mSiO_2$ NC.

3.2.7 Synthesis of Ag NP, $mSiO_2$@AgNPs and multifuntional $mSiO_2$@Ag-Fe_3O_4@P(Nipam) NC

3.2.7.1 Preparation of Ag Nanoparticles:

Azadirachta indica (also known as Neem) leaves were collected and washed with water. Leaf extract was then prepared by taking 10 gm of leaf in 100 mL MQ water. Before decanting, the mixture was boiled for 10 min, till the colour changes from clear transparent to dark yellow indicating extraction. For synthesis of silver nanoparticles (Ag NPs), 5 mL of obtained leaf extract was added drop-wise into 25 mL of 1mM aqueous solution of $AgNO_3$ with constant stirring at room temperature for 30 minutes. The synthesis of Ag NPs indicated the change in color from yellowish to brown and finally to dark brown due to excitation of surface plasmon resonance. The Ag NPs were collected by centrifuging at 5500 rpm for 15 min and dried under vacuum.

3.2.7.2 Preparation of $mSiO_2$@AgNPs

The preparation of $mSiO_2$@Ag was done by the condensation of TEOS in presence of Ag NPs and CTAB [10]. For the synthesis of $mSiO_2$@Ag, first colloidal Ag nanoparticles were obtained by dispersing Ag NPs with CTAB in alkaline mixture of water and alcohol. Ag embedded mesoporous silica nanosphere was prepared by hydrolysis and condensation of TEOS in water-alcohol mixture containing CTAB and Ag NPs. In the typical synthesis procedure, 15 ml of pre-synthesized Ag NPs, 1.5 ml of aqueous NH_3, 20 ml ethanol and 0.5 gm of CTAB were added to the 60 ml of water. The resulting suspension was sonicated for 15 minutes. The resulting suspension was transferred to the magnetic stirrer and stirred for 10 minutes at 50 ^oC followed by addition of 5ml TEOS drop wise for about 30 minutes. Afterward the suspension was stirred for 24 hours at room temperature. Resulting white precipitate was centrifuged and washed for two times with water and alcohol and then dried in oven. Finally, the powder was calcined at 600^oC for 2 hours to remove CTAB templates resulting in mesoporous silica [11].

Anticandidal activity of $mSiO_2$@Ag:

The agar disc diffusion assay was carried out by following process. Briefly, 5 mL mid-log phase grown culture of *Candida albicans* 077 was centrifuged at 4000 rpm for 5 min. Then the pellet was rinsed with 1 × PBS and re-suspended in 500 µL normal saline solution (NSS). 100µL of the suspended cells were spread uniformly on sabouraud dextrose agar plates and the plates were incubated at 37 ^0C for 30 min. The seeded petri plates were used for the loading of the various concentrations of $mSiO_2$@AgNPs (0, 2 and 8 µg/mL) onto the filter paper discs. The Petri plates were incubated at 37 ^0C for 40 h, after that zone of inhibition were obtained by finding the diameter of *C. albicans* 077 cells disappearance.

3.2.7.3 Preparation of multifuntional $mSiO_2$@Ag-Fe_3O_4@P(Nipam)

First, $mSiO_2$-Ag-Fe_3O_4 was prepared by simple sol gel process using AgNPs, Fe_3O_4 NPs, TEOS, and CTAB (as a template). Calcination of CTAB containing $mSiO_2$-Ag-Fe_3O_4 was done to remove the CTAB template. After preparation and characterization of $mSiO_2$-Ag-Fe_3O_4, it was used to prepare $mSiO_2$@Ag-Fe_3O_4@P(Nipam) NC by in situ coating of P(Nipam) on the surface of $mSiO_2$@Ag-Fe_3O_4 in the presence of oxidizer and crosslinker. In typical procedure, $mSiO_2$-Ag-Fe_3O_4, NIPAM, MBA, SDS were mixed well in 50 ml of water by stirring at ~70 ^oC. Then, ~1.2 µl TEMED and 10 mg KPS (in 1 ml water) were added to the above mixture. The mixture was further stirred at 70^oC for 5 hours to obtained $mSiO_2$@Ag-

Fe_3O_4@P(Nipam) NC. Obtained mSiO_2@Ag-Fe_3O_4@P(Nipam) NC product was centrifuged, washed and stored in glass vial.

3.2.8 Synthesis of MesoCaFe_2O_4 NPs and MesoCaFe_2O_4-Dox NPs

meso$CaFe_2O_4$ NPs were prepared by simple coprecipitation route followed by calcination. Calcination has resulted in the generation of mesopores via the removal of template as well as phase formation of meso$CaFe_2O_4$ NPs. Two different, meso$CaFe_2O_4$-1 and meso$CaFe_2O_4$-2 NPs were prepared using oleic acid and CTAB respectively. Meso$CaFe_2O_4$-1 NPs was prepared by coprecipitation method using $FeCl_3$, $CaCl_2$, $NaBH_4$, hydrazine hydrate, NaOH and oleic acid. In typical synthesis procedure, first, solution of $FeCl_3$ and $CaCl_2$ was prepared in ethanol. Then certain amount of $NaBH_4$ solution was poured to the above salt solution while stirring on 80 ^oC. Then, the hydrazine hydrate and NaOH solutions were added. Then 10 ml oleic acid was added to the above precipitating mixture. Obtained brown color product was separated and dried at 100 ^oC. Finally, the product was calcined at 400 ^oC and 600 ^oC for removal of template and to obtain meso$CaFe_2O_4$-1(400) and meso$CaFe_2O_4$-1(600). To obtain mesoporous calcium ferrite using CTAB as template (meso$CaFe_2O_4$-2 NPs), first 0.5 gm CTAB was mixed in aqueous solution of hydrazine and NaOH which has resulted formation of aligned micellar rods into the solution. Then, salt solution (50 ml) of Iron and Calcium was dropped in the above mixture containing soft template of CTAB. CTAB micellar rods formed in the alkaline aqueous medium acted as soft template. Coprecipitation of Fe and Ca precursor on these templates have resulted in the formation of intermediate $CaFe_2O_4$-CTAB complex. Obtained $CaFe_2O_4$-CTAB complex was dried at 100 ^oC. Further, calcination of this intermediate $CaFe_2O_4$-CTAB complex have resulted in the formation of meso$CaFe_2O_4$-2 NPs via the removal of CTAB. meso$CaFe_2O_4$-2-Dox NP was obtained by stirring (150 rpm) the aqueous dispersion (4 ml water) of meso$CaFe_2O_4$-2 and Dox in dark for 48 hours at pH 8. The loaded meso$CaFe_2O_4$-2-Dox NP was washed several times to remove excess of Dox molecules on the surface of nanocarriers.

3.3 Drug loading and in vitro release study

3.3.1 Drug loading study

Drug loaded nanocarriers were obtained by stirring (at 150 rpm) the mixture (~4 ml water) of nanocarriers and drug in 4 ml of liquid medium in dark. Then, the loaded nanocarriers were washed several times to remove excess of drugs molecules on the surface of nanocarriers. The amount of loaded drug was quantified by subtracting the amount of free drug in supernatant

from the total drug. A UV–Vis spectrophotometer was used to determine the amount of unloaded free drug present in the supernatant. The absorbances of the supernatant and pure drug were measured at absorption maxima of drug (at 480 nm for Dox). A standard calibration curve of concentration vs. absorbance was plotted for this purpose. Drug loading efficiency (LE) and loading capacity (LC) of nanoparticle were estimated from the following equations,

Loading efficiency = (Total amount loaded Drug / Total amount of taken Dox) X 100…. (1)

Loading capacity = (Total amount of loaded Drug / amount of nanoparticle) X 100 ……. (2)

where, Total amount of loaded Drug = Total amount taken Drug – amount of Drug in supernatant……. (3)

3.3.2 In vitro release study:

In vitro release studies of drug from nanocarriers were carried out by using dialysis bag diffusion method. The pH dependent release studies of drug from nanocarriers were carried out at 37 ^{o}C in two different buffers (citrate buffer and Phosphate buffer saline) of pH 5 (mimicking cancer cell pH especially for microenvironment in endosomes and lysosomes) [12] and pH 7.4 (mimicking blood plasma pH) [12]. The temperature dependent in vitro release studies of drug from thermos-responsive nanocarriers were carried out at two different temperature at 25 ^{o}C and 40 ^{o}C i.e above and below the LCST of polymers used. In typical procedure, drug loaded nanocarriers in 0.5ml buffer were placed in dialysis bag (molecular weight cut off of 14 kDa.) sealed from one end and there after other end of the dialysis bag was also sealed. Dialysis bag with drug loaded nanocarriers was then immersed into buffer solution (0.1M) in a beaker and continuously stirred at 150 rpm in dark. For release study of hydrophobic drug like Curcumin ~0.2 wt% surfactant (SDS) was also added to the buffer solution. The dialysis bag acts as a donor compartment, and the beaker with buffer solution (release medium) acts as the receptor compartment. Fixed amount aliquots were withdrawn from release medium after appropriate regular time interval and equal amounts of fresh buffer were added to maintain the sink condition throughout the experiment. Each withdrawn sample was subjected to UV-Vis spectrophotometer to monitor the amount of drug released. The concentration of the solution (release media) was determined by measuring the absorbance at λ_{max} of drug (480 nm for Dox). To study the zero order, first order, Higuchi and Korsmeyer–Peppas release kinetics, data obtained from in vitro drug release studies were plotted as cumulative amount of drug released versus time, log cumulative percentage of drug remaining vs. time, cumulative percentage drug

release versus square root of time, and log cumulative percentage drug release versus log time, respectively.

3.4 MTT assay:

In order to elucidate biocompatibility of the prepared nanoparticles and blank nanocarriers, MTT Assay was performed against the normal cells. The in vitro cytocompatibility assay of blank nanoparticles were carried out against RAW 264.7 cells (normal cells). For checking the dose dependent response, RAW 264.7 cells were incubated with different ranges of concentration varying from 5 to 1000 μg/ml of NPs. In typical procedure, 100 μL media with RAW 264.7 cells were seeded onto the 96 well plates (~5×10^3 cells) and incubated in 5% CO_2 atmosphere at 37 ^oC for 24 hours. Then different concentrations of NPs suspension in media were added to cells and further incubated for 24h at 37 ^oC and 5% CO_2. Then, 20 μL of MTT dye (5 mg/ml in 1X PBS) was added into each well and further incubated for 4 hours. Then, the media was carefully removed, and 100 μL of DMSO was added into each well. Plate was gently shaken for few minutes to dissolve formed formazan and the absorbance was recorded at 570 nm with a microplate reader. Each experiment was conducted thrice in order to minimize experimental errors. Untreated cells in the medium were considered as control. Cell viability (%) was determined using the optical density at 570 nm relative to a control (untreated) value using the following equation,

Cell viability (%) = Absorbance of treated culture × 100/ Absorbance of control culture …… (4)

The in vitro anticancer activity of drug loaded nanocarriers were studied against the cancerous Hela cells and also compared with activity of pure drugs. The in vitro cytotoxicity of the plain NPs, free Dox, and loaded NPs against HeLa cells were carried out by MTT assay in the same above-mentioned way. Dose range of free Dox was chosen 0.1, 1, 5, 10, 20 and 40 μg/ml. In order to get contribution from plain NPs on cell inhibition same dose as of loaded NPs have been tested for plain NPs.

3.5 Characterizations of samples:

Structural, morphological, thermal, magnetic properties and drug loading/release behavior have been studied by using different techniques. The phase composition and crystalline structure of the prepared NPs and nanocomposites were studied by XRD (Bruker D8 Advance X-ray Diffractometer) with θ–2θ geometry, using Cu Kα radiation in the 2θ rang

10 to 80^{o}. The phase composition of samples was also studied by selected area electron diffraction (SAED) pattern. Particle sizes and morphologies of samples were analyzed by using Transmission electron microscopy (FEI Tecnai T20G2 S TWIN TEM) and field emission scanning electron microscopy (Carl Zeiss Ultra 55 FESEM). A pinch of NPs was dispersed in 2 ml of DI water and a drop of this suspension was placed on a carbon coated copper grid and the grid was examined under TEM. For FESEM analysis, a pinch of powdered NPs was placed on the carbon tape pasted on the stub followed by coating with gold for 90 seconds to avoid any charging effect. The compositional analysis of the sample was carried out by EDS (Energy dispersive X-ray) performed by a Horiba Energy Dispersive X-ray Micro-analyzer attached to a Hitachi S-3400N Scanning Electron Microscope. The structure and major functional groups present on the prepared NPs and nanocomposites were determined using Fourier transformed infrared (FT-IR) spectroscopy. Perkin-Elmer 2000 FT-IR spectrometer was used to obtain the FTIR spectra from 400 to 4000 cm^{-1} by KBr pellet method. Thermogravimetric analysis (TGA) of samples were performed by Mettler Toledo TGA/SDTA 851e module under N_2 atmosphere from 50 to 1000 ^{o}C at a heating rate of 10 ^{o}C/min. The magnetic properties of NPs and nanocomposites were conducted using a Lakeshore (Model 7407) Vibrating Sample Magnetometer (VSM) in magnetic fields up to 1.5 T at ambient temperature (298 K). Electronic absorption properties of samples were studied by Perkin Elmer Lambda 35 UV-VIS spectrophotometer. UV–vis studies were performed at room temperature in the range 200–800 nm.

3.6 References

[1] Y.S. Kang, S. Risbud, J.F. Rabolt, P. Stroeve, Synthesis and Characterization of Nanometer-Size Fe3O4 and γ-Fe2O3 Particles, Chemistry of Materials 8(9) (1996) 2209-2211.
[2] H.Z. Shouheng Sun, David B. Robinson, Simone Raoux, Philip M. Rice, Shan X. Wang, and Guanxiong Li, Monodisperse MFe2O4 (M) Fe, Co, Mn) Nanoparticles, J. AM. CHEM. SOC 126 (2004,) 273-279.
[3] S. Sun, H. Zeng, J. Am. Chem. Soc. 124 (2002) 8204.
[4] M. Qasim, K. Asghar, B.R. Singh, S. Prathapani, W. Khan, A.H. Naqvi, D. Das, Magnetically recyclable Ni0.5Zn0.5Fe2O4/Zn0.95Ni0.05O nano-photocatalyst: Structural, optical, magnetic and photocatalytic properties, Spectrochimica Acta Part A: Molecular and Biomolecular Spectroscopy 137(Supplement C) (2015) 1348-1356.
[5] K.A. M Qasim, Dibakar Das, Facile Synthesis of Fe3O4 and multifunctional Fe3O4@Albumen Nanoparticles for Biomedical Application, AIP Proceedings 1832, (2017) 050116.
[6] k.A. Mohd Qasim, Braj Raj Singh, Sateesh Prathapani, Wasi Khan, A.H. Naqvi Dibakar Das, Magnetically recyclable Ni0.5Zn0.5Fe2O4/Zn0.95Ni0.05O nano-photocatalyst: Structural, optical, magnetic and photocatalytic properties, Spectrochimica Acta Part A: Molecular and Biomolecular Spectroscopy 137 (2015) 1348–1356
[7] J.A. Khan, M. Qasim, B.R. Singh, S. Singh, M. Shoeb, W. Khan, D. Das, A.H. Naqvi, Synthesis and characterization of structural, optical, thermal and dielectric properties of polyaniline/CoFe2O4 nanocomposites with special reference to photocatalytic activity, Spectrochimica Acta Part A: Molecular and Biomolecular Spectroscopy 109 (2013) 313-321.

[8] M. Qasim, K. Asghar, G. Dharmapuri, D. Das, Investigation of novel superparamagnetic Ni0.5Zn0.5Fe2O4@albumen nanoparticles for controlled delivery of anticancer drug, Nanotechnology 28(36) (2017) 365101.
[9] M. Qasim, K. Asghar, D. Das, Synthesis and Characterization of Ni0.5Zn0.5Fe2O4@mSiO2 Core Shell Nanocarrier for Drug Delivery Applications, in: M.A. Meyers, H.A.C. Benavides, S.P. Brühl, H.A. Colorado, E. Dalgaard, C.N. Elias, R.B. Figueiredo, O. Garcia-Rincon, M. Kawasaki, T.G. Langdon, R.V. Mangalaraja, M.C.G. Marroquin, A. da Cunha Rocha, J.M. Schoenung, A. Costa e Silva, M. Wells, W. Yang (Eds.), Proceedings of the 3rd Pan American Materials Congress, Springer International Publishing, Cham, 2017, pp. 47-54.
[10] M. Qasim, R.S. Braj, A.H. Naqvi, P. Paik, D. Das, Silver nanoparticles embedded mesoporous SiO 2 nanosphere: an effective anticandidal agent against Candida albicans 077, Nanotechnology 26(28) (2015) 285102.
[11] Q. He, J. Zhang, J. Shi, Z. Zhu, L. Zhang, W. Bu, L. Guo, Y. Chen, The effect of PEGylation of mesoporous silica nanoparticles on nonspecific binding of serum proteins and cellular responses, Biomaterials 31(6) (2010) 1085-1092.
[12] Y. Tian, X. Jiang, X. Chen, Z. Shao, W. Yang, Doxorubicin-loaded magnetic silk fibroin nanoparticles for targeted therapy of multidrug-resistant cancer, Advanced materials 26(43) (2014) 7393-8.

CHAPTER 4: RESULTS AND DISCUSSION

Chapter 4

Results and Discussion

Chapter 4 is divided into eight sections. Section 4.1 describes the synthesis and characterizations of different types of magnetic nanoparticles, Section 4.2 describes the results on albumen coated different magnetic nanoparticles, Section 4.3 describes the results on Multifunctional $mSiO_2$-CF@P(Nipam-Aa) nanocomposites, Section 4.4 describes the results on mesoCaCO3@$CaFe_2O_4$ NC, Section 4.5 describes the results on multifunctional NZF@$mSiO_2$ and NZF@$mSiO_2$-CuS-PEG NPs, Section 4.6 describes the results on multifunctional NZF/$Zn_{0.95}Ni_{0.05}O$ and NZF/$Zn_{0.95}Ni_{0.05}O$-$mSiO_2$-Cur NCs, Section 4.7 describes the results on multifunctional $mSiO_2$@AgNPs and $mSiO_2$@Ag-Fe_3O_4@P(Nipam)NCs, and Section 4.8 describes the results on mesoCaFe_2O_4-Dox NPs.

Section 4.1: Synthesis and characterization of different magnetic nanoparticles (MNPs)

In this section, synthesis and characterizations of different types magnetic nanoparticles such as Fe_3O_4 (IO NPs), $CoFe_2O_4$(CF NPs), $Ni_{0.5}Zn_{0.5}Fe_2O_4$ (NZF NP), and $CaFe_2O_4$ nanoparticles will be discussed.

Multi-functional magnetic nanocomposites have been widely studied because of their potential in drug delivery, bioimaging and clinical applications [1, 2]. Different types of magnetic nanoparticles (MNPs) are being used to prepare multifunctional magnetic nanocarriers. Among them spinel ferrites based magnetic nanoparticles (such as Fe_3O_4 NPs, $CoFe_2O_4$ NPs NZF, and $CaFe_2O_4$ nanoparticles etc.) have shown remarkably good magnetic properties that offer a broad range of biomedical applications [1]. Fe_3O_4 NPs are most commonly used as magnetic component in nanocarrier development due to its good magnetic (superparamagnetic) and inherent biocompatibility. $CoFe_2O_4$ nanoparticles (CF NPs) have shown very high saturation magnetization, excellent stability, high magnetocrystalline anisotropy, and high coercivity which make them a suitable candidate for many biomedical applications, such as hyperthermia, MRI, and targeted drug delivery. Calcium is one of the major element of body and inherently nontoxic in nature thus ferrite of calcium could be a good MNP for biomedical applications. Magnetic nanoparticles can be prepared by several chemical

methods such as sol-gel, co-precipitation, thermal decomposition, hydrothermal synthesis, micro-emulsion, and sonochemical etc. [3, 4]. Even though thermal decomposition method can produce highly monodispersed and crystalline MNPs but they are hydrophobic in nature and require further surfactant based processing [5]. Monodisperse MNPs can be prepared by micro-emulsion method but very less yield and less crystallinity are its major drawbacks [6]. Among the different methods, coprecipitation method is generally used to prepare hydrophilic magnetic nanoparticle. Low crystallinity and broad size distribution are drawback of this method that require further processing of prepared samples. Thus, despite lots of research in the fields of preparation of nanocrystalline magnetic nanoparticles, it is still difficult and hectic to prepare a well crystalline, monodispersed, biocompatible and hydrophilic magnetic nanoparticle. Use of suitable chemical and controlled synthesis parameters could overcome these problems. M.Y. Rafique et.al have showed that $NaBH_4$ have significant effect on the particle size, composition, and magnetic properties of $CoFe_2O_4$ NPs [7]. Particles size, morphology and crystallinity of magnetic nanoparticles is dependent on its synthesis procedure, precursors concentration, calcination time etc. The magnetic properties of magnetic particles are governed by particle size, crystallinity and distributions of metal ions and all these are related with synthesis route. Well crystalline and monodispersed CF NPs and IO NPs have been prepared using $NaBH_4$, hydrazine hydrate, NaOH and oleic acid during co-precipitation. Well crystalline superparamagnetic NZF and $CaFe_2O_4$ nanoparticles were prepared by auto combustion method.

4.1.1 Synthesis and characterization of Fe_3O_4 nanoparticles:

Well crystalline two different sizes of Fe_3O_4 NPs have been synthesized by a simple precipitation method [8] which is well known to produce hydrophilic NPs. Oleic acid was used as capping agent to keep particles size smaller. Use of additional $NaBH_4$, hydrazine hydrate than only NaOH, have resulted well crystalline monodispersed Fe_3O_4 NPs at lower temperature without any calcination. It is worthy to mention that conventional coprecipitation method required calcination and particles sorting process. Two different sizes of Fe_3O_4 nanoparticles have successfully been synthesized by varying reaction conditions. In other word, preparation of Fe_3O_4 NP was carried out twice, using 0.5 gm (IO-1) and 1 gm (IO 2) $NaBH_4$ and fixing other condition same. Effect of reducing agent on IO particles size and morphology has been studied.

Powder XRD patterns of both prepared IO1 and IO2 Fe_3O_4 NPs are shown in Fig.1 (a) and (b) respectively. Both samples show diffraction peaks centered around, 2Ɵ 30, 36, 37, 43,

53, 57, and 63^{o} which can be assigned to reflections obtained from (220), (311), (222), (400), (422), (511), and (440), planes, respectively, of crystalline Fe_3O_4 NPs. The observed diffraction pattern correlates well with characteristics diffraction pattern of the spinel cubic structure of Fe_3O_4 (space group: Fd3 m (227), JCPDS card No. 88315)[8]. The crystallite sizes of IO1 and IO2 Fe_3O_4 NPs were estimated from most intense diffraction peak (311) using the Debye–Scherrer equation and were found to be 9 and 18 nm respectively. It is observed that concentration of $NaBH_4$ has immense effect on crystallite size [7]. Diffraction peaks of IO1 sample were observed to be broader than IO2 which is due to the smaller size. Increase in the crystallinity of the sample with increase in the $NaBH_4$ concentration has been observed. The increase in the crystallite size can be attributed to the increased amount of $NaBH_4$[7]. The lattice constant of IO1 and IO2 were estimated to be 8.38 and 8.37 Å which match well with the standard value.

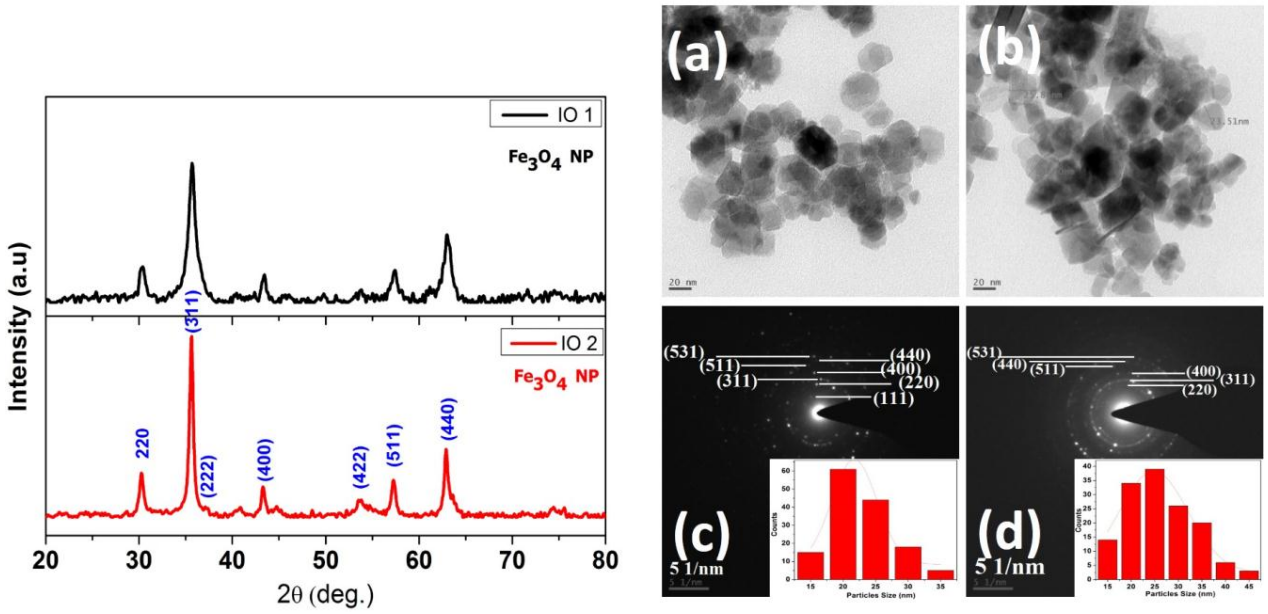

Figure 4.1.1. XRD pattern of IO1 and IO2 NPs (left). TEM images of IO1(a) and IO2 (b) Fe_3O_4 NPs with corresponding SAED (c & d) patterns with particles size distribution (inset).

Fig.4.1.1 (a) and (b) (right side) show TEM images of samples IO1 and IO2 Fe_3O_4 NPs respectively. Their corresponding SAED patterns and particles size distribution are shown in figure 1 (c & d) and (inset of c & d). IO 1 NPs shows spherical to hexagonal morphology where as IO2 NP does not has a regular morphology. Particles diameter IO1 and IO2 NPs are found to be 22 nm and 27 nm respectively. This increment in the particles size in case of IO1 can be attributed to the increased amount of $NaBH_4$. Uncontrolled rapid nucleation and subsequent fast particle growth rate could have caused increased in the particles size at high doses of

$NaBH_4$. Similar behavior was also observed earlier for cobalt ferrite NPs with increased amount $NaBH_4$ [7]. The SAED pattern of both samples (Fig. 4.1.1 (c &d)) show distinct dotted ring pattern, which confirms the polycrystalline nature of both NPs. Obtained SAED patterns have shown characteristic rings of cubic system and were indexed estimating d-spacing from rings (JCPDS card No. 88315). Thus, SAED results also confirm successful formation of Fe_3O_4 NPs. Gaussian particles size distribution was observed in both cases and the particles size distribution of IO1 is found narrower than IO2 NPs. IO1 NP was found to be relatively more uniform and monodispersed than IO2 NP. Thus, the IO1 NP was selected for fabrication of Fe_3O_4@Alb NP.

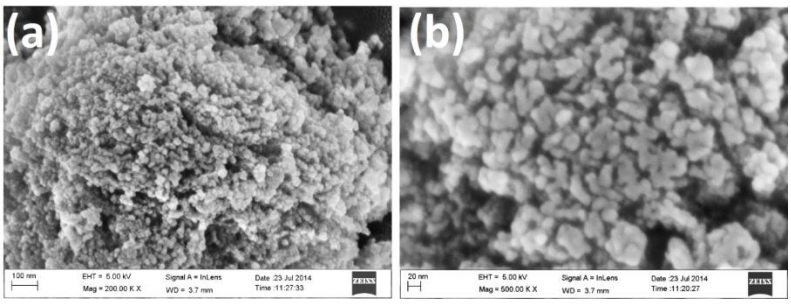

Figure 4.1.2. FESEM images of IO1 NP at low (a) and high (b) magnifications.

Figure 4.1.2 (a-b) show FESEM image of IO 1 NP at low (a) and high (b) magnifications It was found that Fe_3O_4 NPs are nearly spherical in shape with mean particle diameter of 22 nm. Particles are uniform in size and monodispersed in nature. Individual NP can be seen in both the micrographs. In conclusion, two different size of Fe_3O_4 NPs were prepared by changing the reaction parameter and characterized by for its structural and morphological properties.

4.1.2 Synthesis and characterization of $CoFe_2O_4$ nanoparticles:

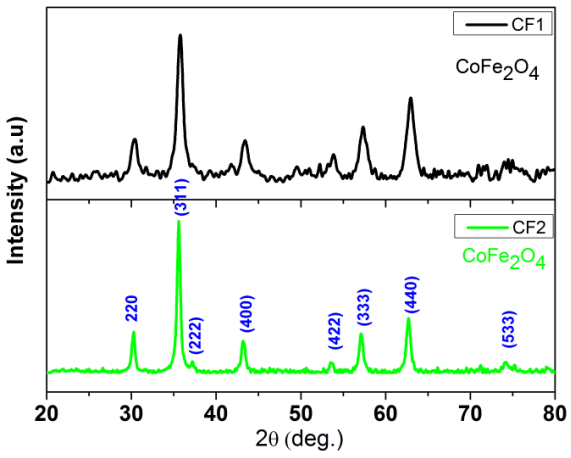

Figure 4.1.3. XRD pattern of CF1 and CF2 NPs.

Similar to the Fe_3O_4 NPs, two different sizes of $CoFe_2O_4$ nanoparticles have successfully been synthesized by varying reaction conditions in coprecipitation method. Preparation of CF1 and CF2 NPs was carried out using 0.5 gm and 1 gm $NaBH_4$ respectively. XRD patterns of CF1 and CF2 NPs are shown in fig 4.1.3. Both the samples show formation of single phase spinel cubic $CoFe_2O_4$ nanoparticles. The appeared diffraction patterns are well matching with the standard diffraction pattern of spinel cubic $CoFe_2O_4$. The average crystallite size of CF1 and CF2, estimated by Debye Debye–Scherrer equation were found to be 8 nm and 15 nm, respectively. Peaks of CF1 are broader than CF2 due to its smaller size. Increase in the crystallinity of the sample with increase in the $NaBH_4$ concentration has been observed. The increase in the crystallite size can be attributed to the increased amount of $NaBH_4$ [2]. TEM micrographs of both CF1 and CF2, $CoFe_2O_4$ NPs are shown in Fig. 4.1.4 (a) and (b) respectively with corresponding particles size distribution (c & d) and SAED patterns (e & f). Particles size CF1 and CF2 NPs are found to be 11 nm and 15 nm respectively. Particles are found to be nearly spherical in shape. The particles size distribution of CF1 is found narrower than CF2 NPs. The increase in the particles size in case of CF1 can be attributed to the increased amount of $NaBH_4$. Uncontrolled rapid nucleation and subsequent fast particle growth rate could have caused increased in the particles size at high doses of $NaBH_4$. This phenomenon of increase in the particles size with increase in $NaBH_4$ was also observed earlier for same ferrite NPs [7]. Polycrystalline natures of both samples were also revealed by SAED analysis (Fig. 4.1.4 (e &f)) which have shown characteristic dotted ring pattern of spinel cubic $CoFe_2O_4$ NPs. Appeared rings were indexed estimating their d-spacing and comparing with standard data (JCPDF No. 22-1086). Thus, SAED results also confirm successful formation of CF NPs. Figure 4.1.5 (a) and (b) show HRTEM micrographs of CF1 and CF2 NPs. Appearance of well-ordered atomic planes on particles confirmed its well crystalline nature. In addition, appearance of atomic planes on one single particles only in one direction suggested that the particle is made up of a single crystallite. Closeness of particles size estimated by TEM and crystallite size estimated by XRD, also support this observation. d-spacing of atomic plane was estimated and it was confirmed that particle was $CoFe_2O_4$ as it was well matching with d-spacing of $CoFe_2O_4$ (Fig. 4.1.5 (c, d)). Figure (c) and (d) are enlarge HRTEM image of marked region in (a) and (b) respectively which clearly show ordered (220) atomic planes of CF NPs.

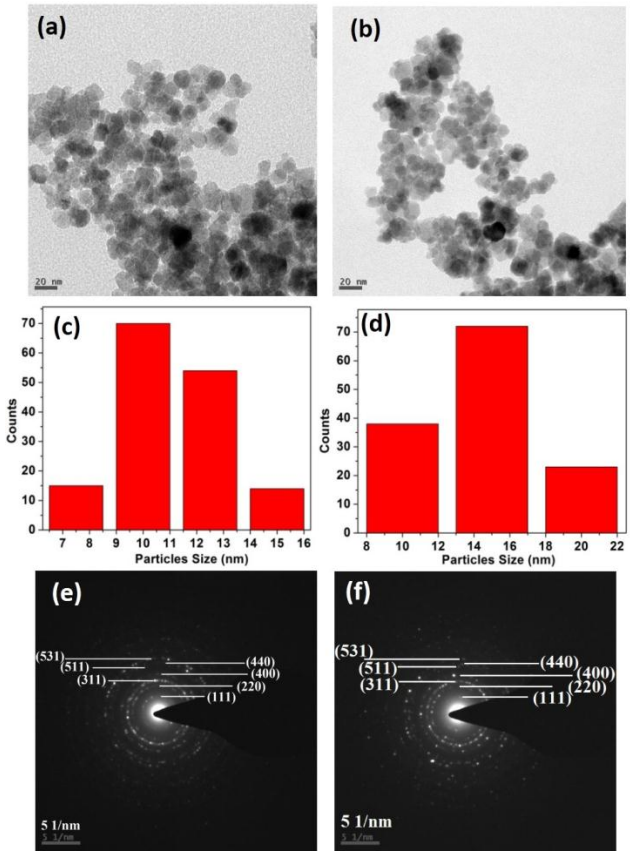

Figure 4.1.4. TEM micrographs of CF1 (a) and CF2 (b) NPs with corresponding Particle size distribution (c & d) and SAED pattern (e & f).

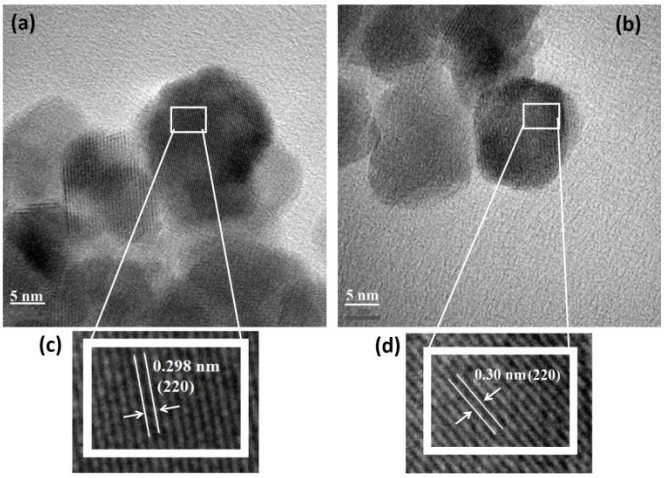

Figure 4.1.5. HRTEM micrographs of CF1 (a) and CF2 (b) NPs. Figure (c) and (d) are enlarge image of marked region.

4.1.3 Synthesis and characterization of Fe_3O_4 nanoparticles by High Temperature decomposition method: Well crystalline, monodispersed Fe_3O_4 NPs were prepared by High temperature decomposition of Iron acetylacetonate in boiling phenyl ether in presence of 1,2-hexadecanediol, oleic acid and oleylamine [5]. Figure 4.1.6 shows low and high magnification

TEM micrograph of Fe_3O_4 NPs prepared by high temperature decomposition method. NPs are found to highly monodispersed in size and shape. The particles size was found to be ~8 nm. The prepared sample was observed to be highly hydrophobic in nature. Indexed SAED pattern of prepared Fe_3O_4 NPs suggest well poly-crystalline nature of the sample with spinel cubic structure (JCPDS card No. 88315).

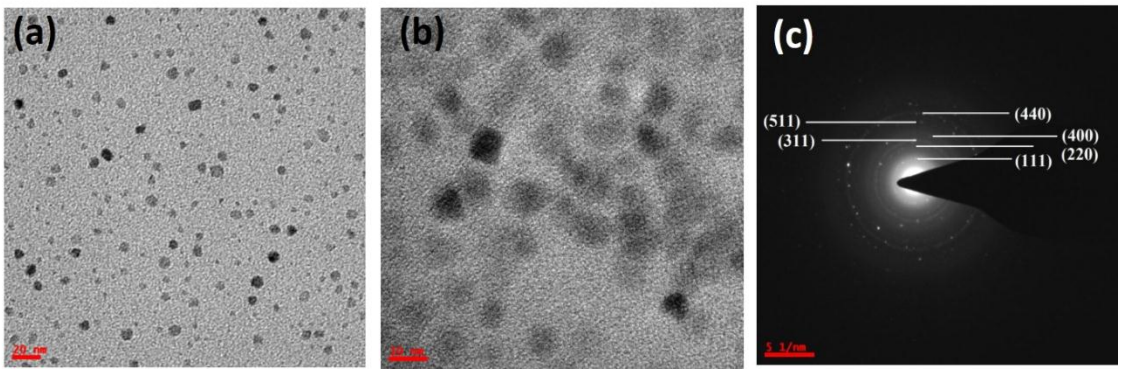

Figure 4.1.6. Low (a) and high (b) magnification TEM micrograph of Fe_3O_4 NPs prepared by High temperature decomposition method. Indexed SAED pattern of corresponding Fe_3O_4 NPs.

4.1.4 Synthesis and characterization of NZF nanoparticles:

NZF NP was prepared by auto combustion method [9] [10]. XRD pattern of NZF NP is shown in the figure 4.1.7 (a). The XRD patterns of NZF nanoparticles show the sharp diffraction peaks of (220), (311), (222), (400), (422), (511) and (440) planes at 2 Θ 30°, 35°, 43°, 53°, 57°, and 62°. These observed characteristic peaks confirmed the spinel cubic structure of the crystalline NZF (JCPDS card No. 520278). The crystallite size of NZF NP was estimated to be ~15 nm. Figure 4.1.7 (b) and (c) shows TEM micrograph and corresponding particles size distribution. Particles are observed to be spherical with mean size of ~21 nm. Indexed SAED pattern of NZF NP confirmed its poly-crystalline nature with spinel cubic structure as it has shown doted ring pattern. Indexing was done estimating the d spacing of each ring and comparing with standard d spacing. FESEM image of NZF with corresponding particles size distribution is shown in figure 4.1.7 (e) and (f) respectively. FESEM analysis also showed formation of nearly spherical particle of size ~22 nm (e &f).

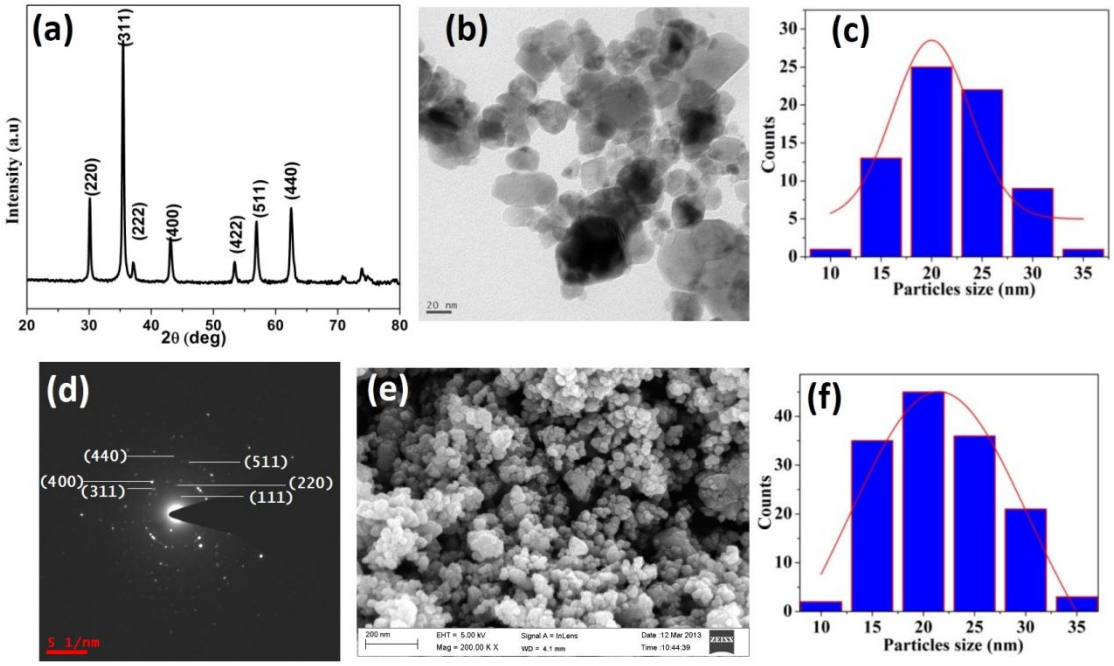

Figure 4.1.7. XRD pattern (a) and TEM micrograph (b) of NZF NP with particles size distribution and Indexed SAED pattern (d). FESEM micrograph (e) with corresponding particles size distribution (f).

4.1.5 Synthesis and characterization of $CaFe_2O_4$ nanoparticles:

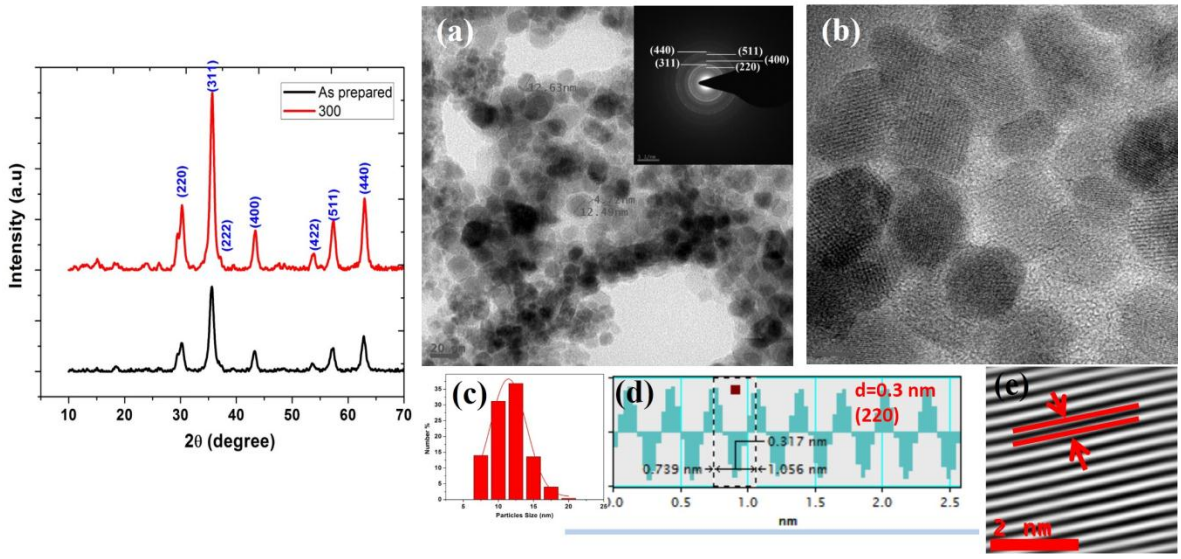

Figure 4.1.8. XRD pattern of as prepared and calcined $CaFe_2O_4$ NP (left side). TEM (a) and HRTEM (b) images of $CaFe_2O_4$ NP with SAED pattern (inset of (a)), particles size distributions (c). Line profile through atomic plane and IFFT image are shown in (d) and (e) respectively.

Even though the ferrite of transition metal such as Ni, Mn, Co, Zn show excellent magnetic properties, but they cannot be used after a certain dose due to their toxicity. This raises question on their biocompatibility and effective use in biological applications. MNP of

calcium are expected to be more suitable and biocompatible as calcium is biocompatible and nontoxic [11]. XRD patterns of as prepared and calcined $CaFe_2O_4$ NP are shown in fig. 4.1.8, which show the characteristic sharp diffraction peaks of (220), (311), (222), (400), (422), (511) and (440) planes of spinel cubic $CaFe_2O_4$ nanoparticles. The appeared diffraction patterns are well matching with the standard diffraction pattern of spinel cubic $CaFe_2O_4$ [12]. The average crystallite size of as prepared and calcined $CaFe_2O_4$, estimated by Debye–Scherrer equation were found to be 9 nm and 10 nm, respectively. TEM and HRTEM images of $CaFe_2O_4$NP with particles size distributions, line profile through atomic plane and IFFT image are shown in Figure 4.1.8. (a), (b), (c) (d) and (e) respectively. TEM image shows formation of monodispersed, spherical $CaFe_2O_4$NP of size 11 nm. Indexed SAED pattern $CaFe_2O_4$ NP shown in inset of (a) confirmed successful formation of polycrystalline spinel cubic $CaFe_2O_4$ NP. HRTEM and IFFT of HRTEM shows presence of highly ordered atomic plane which suggest well crystalline nature of $CaFe_2O_4$NP. The d-spacing (0.3 nm) obtained by line profile is indexed to (220) plane of spinel cubic structure.

4.1.6 Conclusions:

Two different sizes of Fe_3O_4 NPs and $CoFe_2O_4$ NPs were prepared by changing the reaction parameter in simple coprecipitation route and characterized by for its structural and morphological properties. Particles were found to well crystalline and monodispersed in nature. Present method resulted well crystalline monodispersed Fe_3O_4 NPs and $CoFe_2O_4$ NPs at lower temperature without any calcination. The particles size was found to be in between ~10-30 nm. Well crystalline superparamagnetic NZF and $CaFe_2O_4$ NPs were prepared by auto combustion method. Particles sizes of NZF and $CaFe_2O_4$ NPs were found to be 21 and 10 nm respectively. Well crystalline and monodispersed Fe_3O_4 NP of size ~8 nm was also prepared by High temperature decomposition.

4.1.7 References

[1] C. Fang, M. Zhang, Multifunctional Magnetic Nanoparticles for Medical Imaging Applications, Journal of materials chemistry 19 (2009) 6258-6266.
[2] S.K. Yen, P. Padmanabhan, S.T. Selvan, Multifunctional iron oxide nanoparticles for diagnostics, therapy and macromolecule delivery, Theranostics 3(12) (2013) 975-992.
[3] A.K. Gupta, M. Gupta, Synthesis and surface engineering of iron oxide nanoparticles for biomedical applications, Biomaterials 26(18) (2005) 3995-4021.
[4] Y.Y.a.M.R. M. Faraji, Magnetic Nanoparticles: Synthesis, Stabilization, Functionalization, Characterization, and Applications, J. Iran. Chem. Soc., Vol. 7, No. 1, March 2010, pp. 1-37. 7(1) (2010) 1-37.
[5] H.Z. Shouheng Sun, David B. Robinson, Simone Raoux, Philip M. Rice, Shan X. Wang, and Guanxiong Li, Monodisperse MFe2O4 (M) Fe, Co, Mn) Nanoparticles, J. AM. CHEM. SOC 126 (2004,) 273-279.
[6] Y. Deng, L. Wang, W. Yang, S. Fu, A. Elaïssari, Preparation of magnetic polymeric particles via inverse microemulsion polymerization process, Journal of Magnetism and Magnetic Materials 257(1) (2003) 69-78.

[7] M.Y. Rafique, L. Pan, Q.-u.-a. Javed, M.Z. Iqbal, L. Yang, Influence of NaBH4 on the size, composition, and magnetic properties of CoFe2O4 nanoparticles synthesized by hydrothermal method, Journal of Nanoparticle Research 14(10) (2012) 1189.
[8] K.A. M Qasim, Dibakar Das, Facile Synthesis of Fe3O4 and multifunctional Fe3O4@Albumen Nanoparticles for Biomedical Application, AIP Proceedings 1832, (2017) 050116.
[9] M. Qasim, K. Asghar, G. Dharmapuri, D. Das, Investigation of novel superparamagnetic Ni0.5Zn0.5Fe2O4@albumen nanoparticles for controlled delivery of anticancer drug, Nanotechnology 28(36) (2017) 365101.
[10] M. Qasim, K. Asghar, B.R. Singh, S. Prathapani, W. Khan, A.H. Naqvi, D. Das, Magnetically recyclable Ni0.5Zn0.5Fe2O4/Zn0.95Ni0.05O nano-photocatalyst: Structural, optical, magnetic and photocatalytic properties, Spectrochimica Acta Part A: Molecular and Biomolecular Spectroscopy 137(Supplement C) (2015) 1348-1356.
[11] L. Khanna, N.K. Verma, PEG/CaFe2O4 nanocomposite: Structural, morphological, magnetic and thermal analyses, Physica B: Condensed Matter 427 (2013) 68-75.
[12] A. Samariya, S.N. Dolia, A.S. Prasad, P.K. Sharma, S.P. Pareek, M.S. Dhawan, S. Kumar, Size dependent structural and magnetic behaviour of CaFe2O4, Current Applied Physics 13(5) (2013) 830-835.

Section 4.2: Albumen based magnetic nanoparticles (NZF@Alb & NZF@Alb-Dox NPs and Fe_3O_4@Alb & CF@Alb NPs)

This section describes the preparation and characterization of albumen based multifuctional magnetic nanoparticles such as, NZF@Alb & NZF@Alb-Dox NPs. The section also includes results and discussion on Fe_3O_4@Alb & CF@Alb NPs.

4.2.1 Superparamagnetic $Ni_{0.5}Zn_{0.5}Fe_2O_4$@Alb NP for controlled delivery of anti-cancer drug

In the present work, the merit of superparamagnetic $Ni_{0.5}Zn_{0.5}Fe_2O_4$ and albumen nanoparticle have been combined together to fabricate multifunctional nanoparticles for tumour diagnosis and therapy[1]. In this study, $Ni_{0.5}Zn_{0.5}Fe_2O_4$@Egg albumen (NZF@Alb) core-shell nanoparticles have been prepared by green and simple method using inexpensive chicken egg albumen and have been characterized for different physiochemical properties. The structural, thermal and magnetic properties of the prepared core-shell nanoparticles have been investigated by XRD, FTIR, TGA, HRTEM, FESEM, and VSM techniques. Doxorubicin, as model anticancer drug, has been loaded in albumen matrix of NZF@Alb to get NZF@Alb-Dox and its release behavior has been studied at pH 7.4 and 5. Biocompatibility of the NZF and NZF@Alb nanoparticles was confirmed by in vitro cytocompatibility assay (MTT assay) against RAW 264.7 cells (normal cells). The in vitro cytotoxicity test of the blank NZF@Alb NPs, free Dox, and NZF@Alb-Dox NPs against HeLa cells were carried out by MTT assay.

4.2.1.1 Preparation of NZF@Alb and NZF@Alb-Dox NPs

In the present work, superparamagnetic, multifunctional NZF@Alb and NZF@Alb-Dox NPs have been prepared by two step processes for tumor diagnosis and therapy. First, superparamagnetic NZF NPs were prepared by gel combustion method [2]. Using prepared NZF NPs, Dox and freshly extracted egg albumen NZF@Alb-Dox NPs were prepared. NZF@Alb NPs were also prepared by the same procedure except addition of Dox. Schematic of steps involved in preparation of NZF@Alb-Dox and NZF@Alb NPs with plausible formation mechanism are shown in figure 4.2.1. Egg albumen contains different types of proteins such as ~60% ovalbumin, ~12% Ovotransferrin, and ~11% Ovomucoid [3]. These proteins have polar-COOH (hydrophilic) and nonpolar-alkyl (hydrophobic) groups. When NZF NPs are sonicated along with albumen these polymeric proteins wrap the surface of NPs via

hydrophobic or electrostatic interactions. A large number of negatively charged carboxylic groups present in albumen will bind with the positively charged surface metal ions to give a core shell type albumen coated NZF NPs. Ovotransferrin is well known for its iron binding property. Iron binding capacity may also provide affinity toward iron of NZF NPs and help in deposition of ovotransferrin on NZF NPs surface leading to formation of NZF@Alb NPs. Dox molecules have been loaded in albumen matrix via electrostatic interaction between positively charge amine groups of Dox and negatively charge carboxylic groups of albumen. The heating process can induce albumen denaturation and gelation which can result in nucleation and precipitation of albumen on NZF NPs. The various functional groups which are present in albumen are –SH, –OH, –COOH and $–NH_2$. The sulfhydryl groups in albumen form covalent disulfide (S–S) bonds at 70–80 ^oC leading to irreversible gel formation [4]. Very high acoustic energy and heat generated during ultrasonication will cause gelation of albumins on the surface of NZF NPs and result in the formation of spherical particles (NZF@Alb NPs) via heterogeneous nucleation of albumen on NZF NPs surface [5, 6]. High speed collisions between the albumen and NZF NPs during ultrasonication could also result in embedding of NZF NPs within the albumin matrix. Thus, present method does not require any extra gelation agent for formation of albumin based magnetic NPs. For preparation of NZF@Alb-Dox, positively charged Dox (pKa 8.3) and NZF NPs were dispersed in water, where part of Dox was adsorbed on the surface of NZF NPs via electrostatic attractions as NZF NPs have negatively charged carboxylate groups (citrate) on its surface [6]. Presence of citrate groups on the surface of NZF NPs was confirmed by FTIR and TGA analysis. Drop-wise addition of albumen, while ultra-sonication, to the above mixture of NZF-Dox resulted in formation of NZF@Alb-Dox. Negatively charged albumen (iso-electric point ~5) will favorably be adsorbed on the surface of slightly positively charged NZF NPs due to partial decoration of Dox molecules and positively charged surface metal ions of NZF (Fe^{3+}, Ni^{2+} and Zn^{2+}) [3] [5]. Electrostatic and /or hydrophobic interaction among NZF, Dox, and albumen possibly played a major role in the formation of NZF@Alb-Dox. Prepared nanocomposites were found to be stable in aqueous media due to hydrophilic nature and electrostatic repulsive force between negatively charged coated albumen. Detailed physiochemical properties of NZF@Alb and NZF@Alb-Dox NPs are explained in the subsequent sections below.

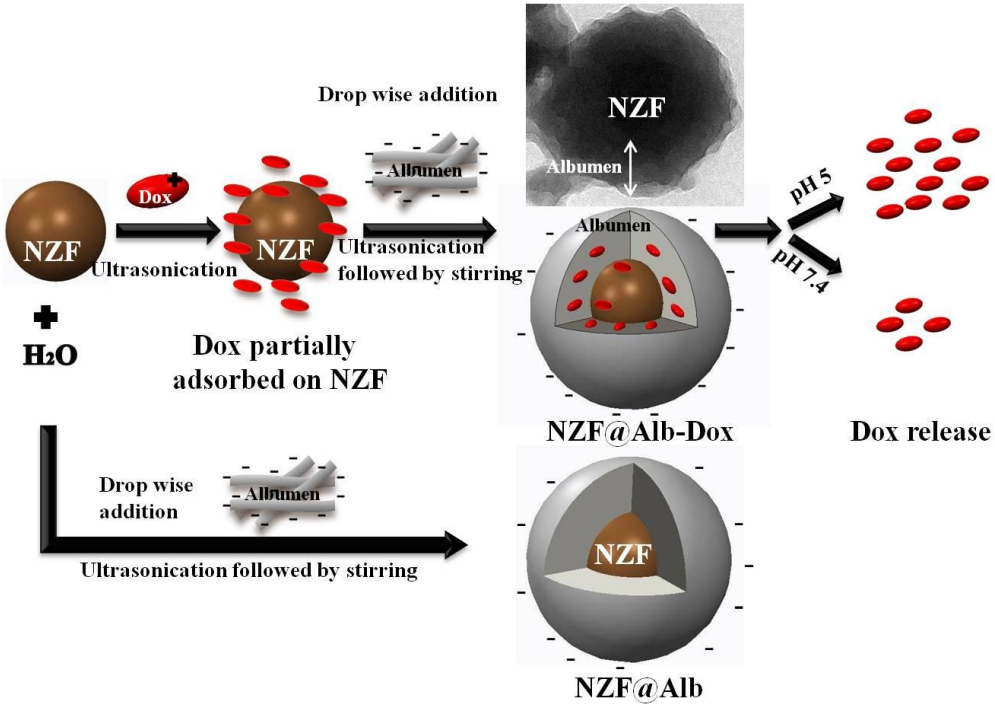

Figure 4.2.1. Schematic illustration of formation of NZF@Alb and NZF@Alb-Dox NPs. DOX is partly adsorbed on the surface of NZF NPs and then encapsulated in the albumen matrix during the gelation process. The diagram is not drawn to scale. pH dependent Dox release behavior from NZF@Alb-Dox NPs is also illustrated.

4.2.1.2 Structural analysis by XRD

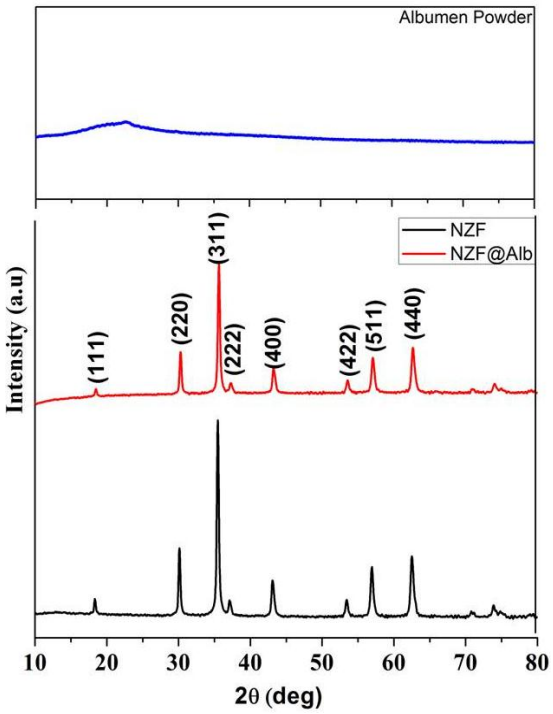

Figure 4.2.2. XRD patterns of powdered albumen, $Ni_{0.5}Zn_{0.5}Fe_2O_4$ and NZF@Alb nanoparticles.

The phase and crystalline structure of powdered albumen, NZF and NZF@Alb NPs were evaluated by powder X-ray diffraction (XRD) using CuKα radiation (CuKα= 1.540598 Å) at room temperature. Powder XRD patterns of Albumen, NZF and NZF@Alb NZF NPs are shown in Figure 4.2.2. NZF and NZF@Alb samples show diffraction peaks centered around 2Θ, 18.3, 30.1, 35.5, 37.1, 43.1, 53.4, 56.9, 62.5, and 73.9^o which can be assigned to reflections obtained from (111), (220), (311), (222), (400), (422), (511), (440), and (533) planes, respectively, of crystalline $Ni_{0.5}Zn_{0.5}Fe_2O_4$ NPs [2]. The observed diffraction patterns match with the characteristics diffraction pattern of the cubic spinel structure of $Ni_{0.5}Zn_{0.5}Fe_2O_4$ [space group: Fd3 m (227), JCPDS card No. 520278]. Presence of the characteristic diffraction peaks of cubic $Ni_{0.5}Zn_{0.5}Fe_2O_4$ phase structure in XRD pattern of NZF@Alb NPs confirms that the structure of NZF nanocrystals does not change with albumen coating. In other word, the surface modification of NZF NPs with albumen and modification process does not adversely affect the crystal structure of magnetic NZF phase [7]. NZF@Alb NPs shows similar XRD pattern, except the weaker intensities of the diffraction peaks compared to those of pure NZF NPs, which might be attributed to the coating of albumen shell on the surface of NZF NPs [8]. No diffraction peak of albumen was observed in XRD pattern of NZF@Alb NPs, suggesting the amorphous nature of the albumen coating. It is noteworthy to mention here that normally three main types of secondary structure of natural protein are well distinguishable and those are α helix(crystalline), β sheet (crystalline) and disordered conformation random globules (amorphous) [9]. XRD pattern of pure dried albumen shows presence of a low intensity broad hump in between 2Θ = 14 to 30 degree and centered at ~23^o, which suggests its nearly amorphous or very poorly ordered nature (due to the presence of few α helix and β sheet form). This broad peak, having d spacing of 3.8Å (at 23^o), could be assigned to the semicrystalline protein (d spacing ~3.5 Å) [9, 10]. The broad hump at 23^{o,} which was observed in XRD pattern of dried albumen powder is not observed in case of NZF@Alb NPs. This low intensity hump may have been relatively suppressed in the presence of high intensity peaks of well crystalline NZF NPs. High sonication energy, continuous stirring and incorporation of NZF in albumen matrix during preparation of NZF@Alb NPs may have reoriented ordered protein macromolecular chains and thus distorted the ordering (α helix and β sheet form) of protein molecule resulting in the loss of crystallinity (amouphous disordered conformation of random globules). No impurity peak is detected in the XRD patterns of both samples. The average crystallite size of NZF NPs was estimated from the full width at half maximum (FWHM) of the corresponding diffraction peak using the Debye–Scherrer equation, $D = 0.9k/\beta\cos\Theta$, where

k is the wavelength of X-ray (Cu Kα = 1.540598 Å), β is the broadening of the diffraction line measured at half of its maximum intensity in radians and Θ is the Bragg's diffraction angle. The average crystallite size of NZF NPs in pure phase and in nanocomposites was found to be ~21 nm. Lattice constant of NZF NPs, estimated from the Powder Xray software, was found to be ~8.4 Å. Similar XRD patterns for BSA-Fe_3O_4 nanocomposites have been reported earlier [8] [11].

4.2.1.3 Structural and morphological analysis by FESEM and HRTEM

Particle size and morphology of NZF and NZF@Alb NPs have been studied using FESEM and TEM. The FESEM images of NZF (a) and NZF@Alb (c) with corresponding EDS spectra (b and d) are shown in figure 4.2.3. It has been observed from FESEM images that NZF NPs are nearly spherical in shape with mean particle sizes ~ 22 nm. The particle sizes of NZF NPs have a Gaussian distribution and are shown in the insets of figure 4.2.3(a). Particles having spherical morphology and relatively bigger in size than pure NZF NPs have been observed from the FESEM image of NZF@Alb NPs as shown in figure 4.2.3(c). The bigger particle sizes of NZF@Alb NPs compared to those of pure NZF NPs could be due to the coating of albumen around the surface of NZF NPs. In case of nanocomposite two ranges of particles sizes were observed, i.e. smaller one from 35-50 nm and bigger one from 100-150 nm. It can be observed from the FESEM image that these bigger NZF@Alb NPs are formed by the aggregation of many smaller NZF@Alb NPs. However, the observed aggregate particles sizes do not exceed the useful range for biomedical applications. The EDS spectra of NZF NPs (Fig. 4.2.3(b)) show only the presence of Fe, Ni, Zn, and O in stoichiometric ratio, without any impurity peak, confirming the purity of the phases. Appearance of all elements of NZF with few additional elements such as carbon and calcium etc. in EDS spectra of NZF@Alb NPs confirm the formation of nanocomposite. It is noteworthy to mention that egg albumen contains different types of biologically useful important minerals and outer egg shell is made up of calcium carbonate.

Particles size of NZF NPs and coating of NZF NP with albumen was further confirmed by TEM and HRTEM analysis. Figure 4.2.4(a) shows TEM image of pure NZF NPs with corresponding particles size distribution. From the TEM micrograph, the average size of NZF NPs was estimated to be ~ 20 nm and the shape of the NPs was observed to be spherical (figure 4.2.4(a)). The value obtained is in good agreement with size obtained from FESEM and XRD, indicating that the nanoparticles consist of single crystallite. TEM micrographs of NZF@Alb NPs are shown in figures 4.2.4(b) (at relatively low magnification) and 4.2.4 (c) (at high

magnification). Coating of albumen (grey color) on NZF NPs (black) is clearly visible in these low and high magnification TEM micrographs of NZF@Alb NPs. Average particle size of NZF and NZF@Alb NPs are found to be ~22 nm and ~100 nm respectively. Thickness of albumen coating is found to be in the range of 10-15 nm. HRTEM images of two different NZF@Alb NPs are shown in figure 4.2.4 (d & e). HRTEM of core region of NZF@Alb NPs shows presence of highly ordered atomic plane whose d spacing matches well with that of crystalline NZF, thus confirming the NZF core. Shell region does not show any ordered arrangement of atoms indicating amorphous nature of coated albumen (figure 4.2.4e).

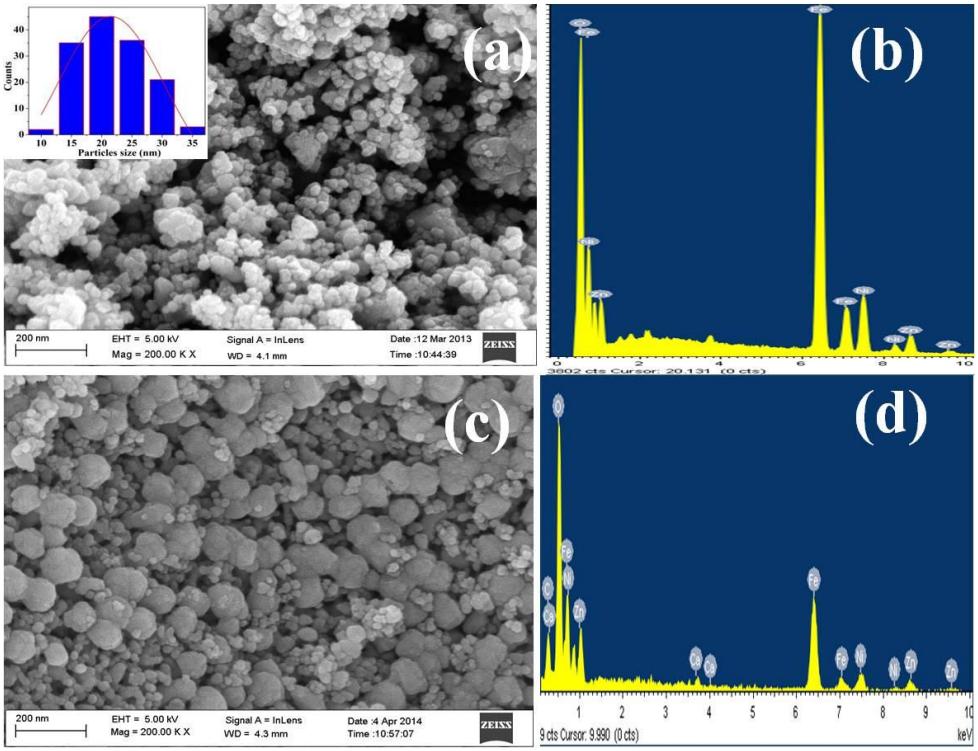

Figure 4.2.3. FESEM micrographs of NZF (a), NZF@Alb (c) nanoparticles with corresponding EDS spectra (b, d). Inset of Fig (a) shows particles size distribution histogram of NZF nanoparticles.

For better clarity and understanding inverse fast Fourier Transformation (IFFT) of HRTEM image of selected core region (figure 4.2.4 (d & e)) has been carried out and obtained IFFT images are shown in inset of figure 4.2.4 (d & e). The IFFT image in the inset of figure 4.2.4 (d) clearly shows presence of well-ordered atoms and atomic planes with d spacing of 0.29 nm that is (220) plane of NZF [2]. The IFFT image in the inset of figure 4.2.4(e) also shows presence of well-ordered atomic planes with d spacing of 0.48 nm that can be assigned to the (111) plane of NZF. d-spacing was obtained by line profile method and a line profile graph of the IFFT image of figure 4.2.4 (e) is shown in figure 4.2.4 (h). Thus, from TEM and HRTEM

analysis it can be concluded that crystalline NZF NPs are well coated with amorphous albumen layer.

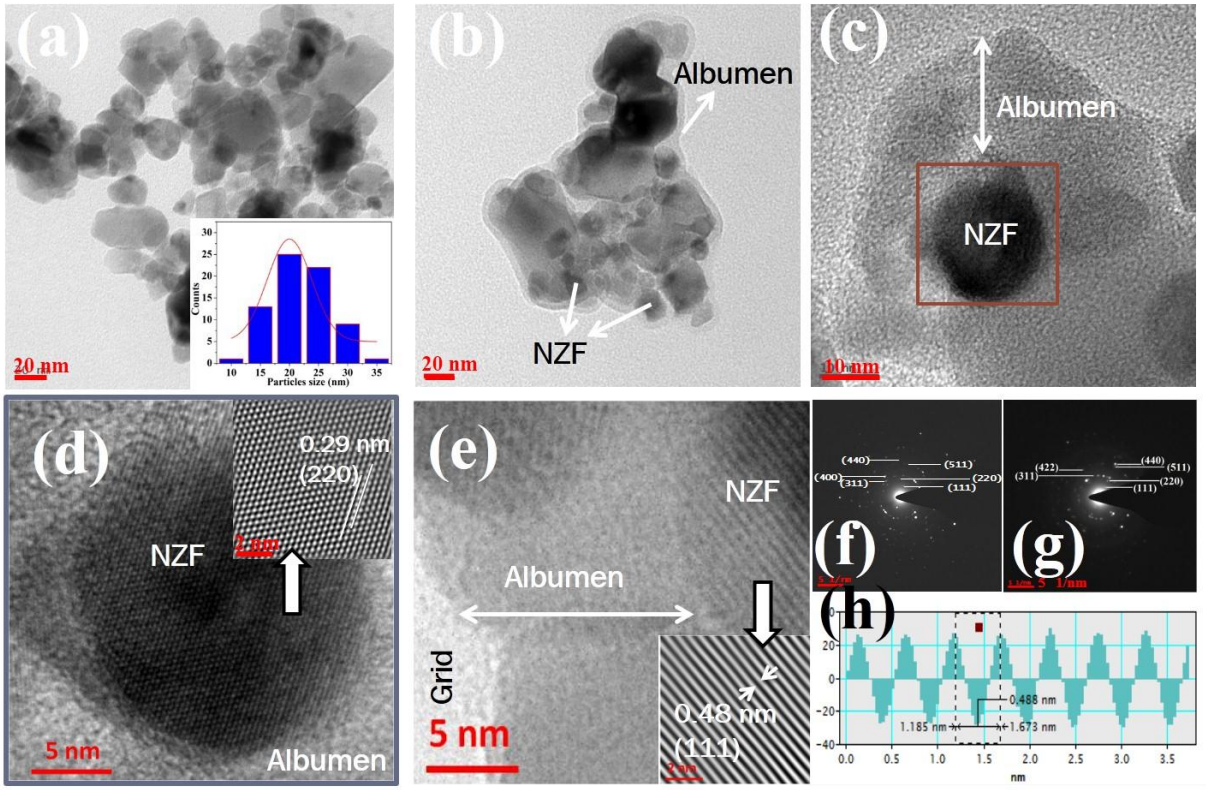

Figure 4.2.4. TEM images of NZF (a) and NZF@Alb (b-c) nanoparticles. Inset of Figure a shows particles size distribution histogram of NZF nanoparticles. HRTEM images of two different NZF@Alb NP with corresponding IFFT images (inset) of core region are shown in figure (d & e). Indexed SAED pattern of NZF and NZF@Alb nanoparticles are shown in figure (f) and (g) respectively. Line profile graph though atomic planes in IFFT image (inset of (e)) is shown in figure (h).

Figure 4.2.4(f) and (g) shows the indexed selected area electron diffraction (SAED) patterns of NZF and NZF@Alb NPs, respectively. The SAED patterns of both NZF and NZF@Alb NPs show distinct dotted ring pattern, which confirm the polycrystalline nature of both the samples. Obtained SAED patterns were indexed for cubic system by estimating the d-spacing from the ring pattern and compared with the standard value. Appearance of ring patterns of NZF in the SAED pattern of NZF@Alb NPs confirmed the formation of nanocomposite. It can also be concluded that coating process and coating of albumen on the surface of NZF NPs does not change the crystalline nature of magnetic NZF component.

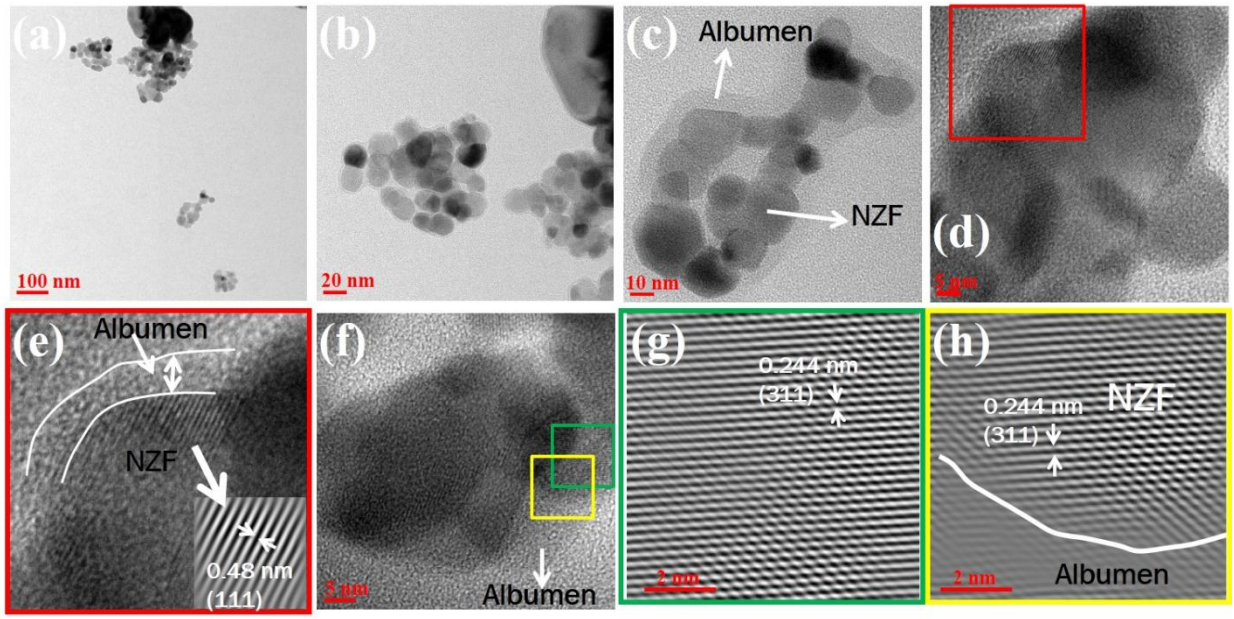

Figure 4.2.5. TEM micrographs of NZF@Alb-Dox nanoparticles at different magnification scales, 100 nm (a), 20 nm (b), 10 nm (c) and 5 nm (d). HRTEM image of the red-framed square in (d) to show lattice fringes of crystalline NZF NPs as shown in figure (e). IFFT from the core region indicated by arrow in (e) is shown in the inset of (e). HRTEM image of other NZF@Alb-Dox nanoparticle is shown in figure (f). Figures (g) and (h) show IFFT images of green and yellow framed squares in (f) respectively.

TEM analysis of NZF@Alb-Dox NPs also has been carried out and TEM micrographs at different magnifications are shown in figure 4.2.5 (a-d). It was observed that many smaller NZF NPs aggregated within the albumen matrix to form spherical morphology of size ~ 100 nm. Similar to the NZF@Alb NPs, in case of NZF@Alb-Dox NPs also, coating of albumen (grey color) on NZF NPs (black) is very clearly seen in the TEM micrographs of NZF@Alb-Dox NPs. Thickness of albumen coating was found to be ~ 12-17 nm. Figure 4.2.5(e) shows HRTEM image of red framed square region of figure 4.2.5(d) and Figure 4.2.5(f) shows HRTEM image of another NZF@Alb-Dox NP. Coating of amorphous albumen on crystalline NZF NPs can very clearly be seen in HRTEM images (Figure 4.2.5(e-f). IFFT image (inset of figure 4.2.5(e) of core region (indicated by arrow) shows presence of highly ordered lattice plane with the d-spacing of 0.48 nm ((111) plane of NZF) confirming that core particles are NZF NPs. For better clarity and understanding of the amorphous coating on crystalline core, IFFT of two regions, crystalline core and both core and shell region, have been carried out and are shown in figure 4.2.5g & h, respectively. These two regions are selected from figure 4.2.5(f) and marked with green and yellow square, respectively. Appearances of only highly ordered atomic planes in figure 4.2.5(g) and highly ordered atomic planes with relatively blur region in

figure 4.2.5 (h) confirm that crystalline NZF NPs is coated with amorphous albumen. d-spacing of theses atomic plane is found to be 0.244 nm, which corresponds to the (311) plane of cubic NZF NPs. These observations are consistent with XRD results, which also indicated presence of amorphous albumen in NZF@Alb NPs. Similar TEM results for BSA coated MNPs were earlier reported by few researchers [11]. Interestingly, both NZF@Alb and NZF@Alb-Dox NPs synthesized in this investigation does not only display simple core-shell morphology but also show a rich interaction and good contact between the protein and the magnetic nanoparticles.

4.2.1.4 Thermal analysis

To confirm the albumen coating on NZF NPs, to quantify the weight percent of NZF & albumen in nanocomposite and to investigate the thermal stability of prepared nanosystems thermal analyses were carried out. TGA and DTG of albumen, NZF, and NZF@Alb NPs are shown in figure 4.2.6 (a) and (b) respectively. Appearance of similar degradation pattern in TGA and DTG curves of NZF@Alb as of pure albumen confirms the presence of albumen in NZF@Alb NPs. For better understanding of TGA curve the temperature range has been divided into three ranges, i.e 50-150, 150-500 and 500-950 ^{o}C. In the first range (50-150 ^{o}C) all the samples show ~ 3-6 % weight loss, which can be attributed to the loss of physically adsorbed water on the surface of nanoparticles. In the second range (150-500 ^{o}C) major weight losses were observed in all samples and it can be attributed to the loss of organic citrate and albumen from NZF and NZF@Alb NPs respectively [8]. In this range about 35% and 63.3% weight losses were observed for NZF@Alb and pure albumen, respectively. In the third range (500-950 ^{o}C) relatively lower weight loss than second range has been observed and this may be attributed to the loss of higher molecular weight organic species and decompositions of carbonates such as, calcium carbonate [8]. It was assumed that available calcium in albumen would have formed calcium carbonate in the presence of evolved CO_2 during burning of organic matrix. Presence of calcium in egg albumen was also observed in EDX analysis. In the last range ~17% and 27% weight losses were observed for NZF@Alb and pure albumen, respectively. Total weight losses for NZF, NZF@Alb and pure albumen were found to be 11.8 %, 58%, and 97.3% respectively. Weight % of albumen in NZF@Alb NPs was estimated to be ~40%. Thus, prepared NZF@Alb NPs were found to be thermally stable till 250 ^{o}C with slight weight loss due to physically adsorbed water molecules.

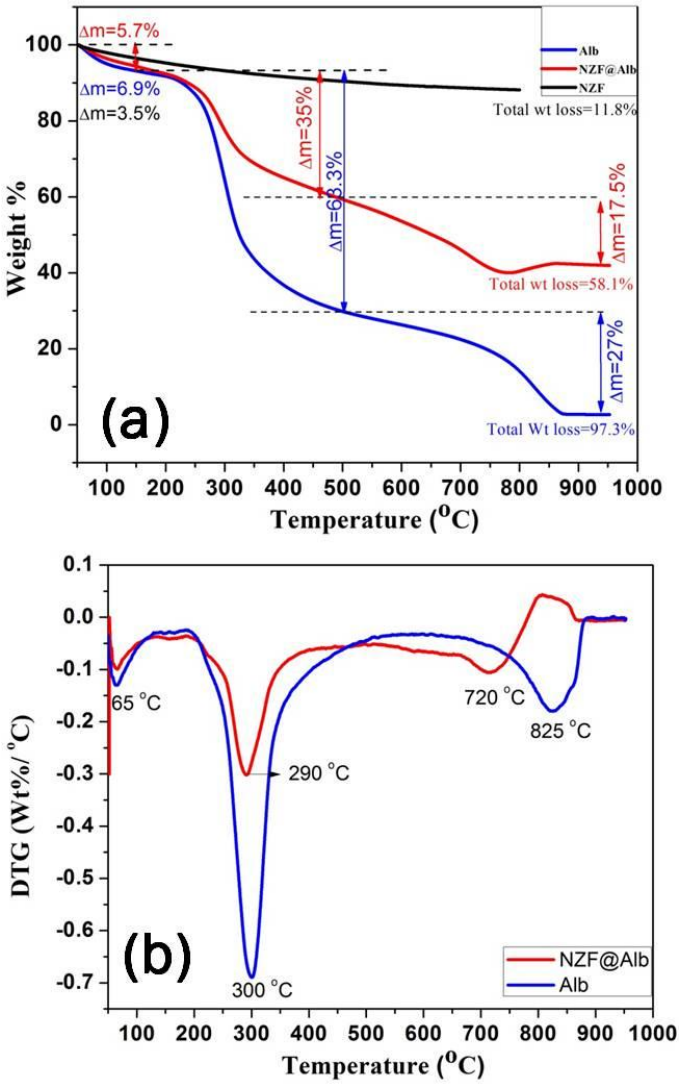

Figure 4.2.6. TGA (a) and DTG (b) curves of albumen, NZF and NZF@Alb nanoparticles.

DTG curves of NZF@Alb NPs and pure albumen show almost similar behavior with one major peak centered at 300 ºC (Figure 4.2.6(b)). This peak can be assigned to the loss of organic albumen [12]. Two more peaks with relatively smaller intensities also have been observed in DTG curves of both NZF@Alb and pure albumen. Peaks centered at 65ºC can be assigned to loss of water molecules and other peak which appeared above 700 ºC (at 825 ºC for pure albumen and at 720 ºC for NZF@Alb) can be due to the loss of higher molecular weight organic species or decompositions of carbonates [13]. The peaks around 300 & 825 ºC in pure albumen have slightly shifted to lower temperatures at 290 & 720 ºC, respectively, for NZF@Alb NPs. This shifting could be due to the presence of NZF NPs, which could have catalyzed the thermal decomposition process resulting in decomposition at relatively lower temperature.

4.2.1.5 Magnetic Properties

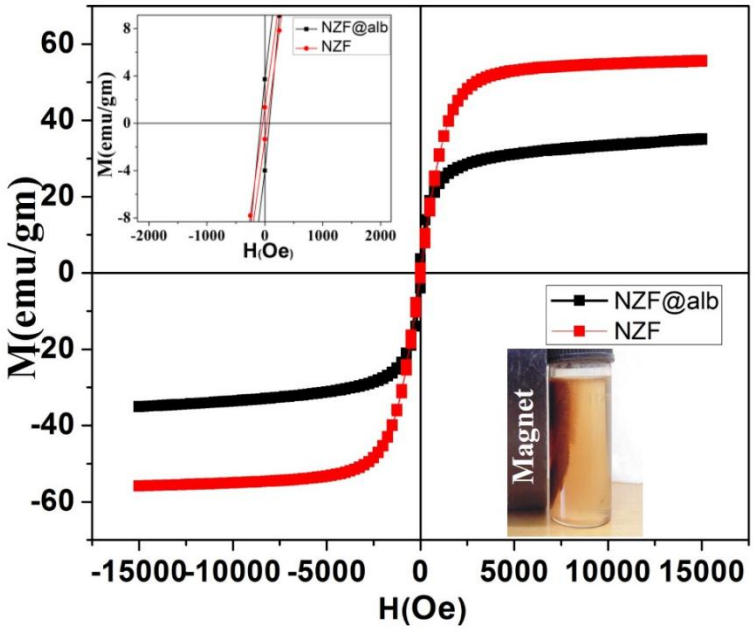

Figure 4.2.7. Room temperature (M-H) curves of NZF and NZF@Alb nanoparticles. Inset figure in second quadrant shows enlarge M-H curves. Inset digital photograph in the fourth quadrant shows magnetic controllability of aqueous NZF@Alb NP.

The field dependent magnetic behaviors of NZF and NZF@Alb NPs are shown in figure 4.2.7. Various magnetic properties including saturation magnetization (M_s), remanent magnetization (M_R) and coercivity (H_c) have been obtained from the M-H curve. Saturation magnetization (M_s) value of magnetic material determines its response towards external magnetic field. The M_s values for NZF and NZF@Alb NPs were found to be 56 and 36 emu/gm respectively. Relatively lower content of NZF in NZF@Alb than pure NZF sample is the reason for observed smaller M_s value of NZF@Alb than NZF NPs. Obtained M_s value (36 emu/gm) of NZF@Alb NPs is sufficient for magnetically guided drug delivery application. Both the samples were found to be super-paramagnetic in nature with very low remanent magnetization and coercivity. The superparamagnetic nature of prepared samples is due to very small and single domain (magnetic) equivalent particle size of NZF NPs (22 nm). TEM and XRD results have shown prepared NZF NPs were made up of single crystal. When the size of magnetic particles come down to single domain (magnetic) size then thermal vibration surpass the energy barrier for its spin reversal leading to superparamagnetic behavior [2]. Remanent magnetizations of NZF and NZF@Alb NPs are found to be 1.35 and 3.70 emu/gm respectively. The coercivity values are 36 and 77 Oe for NZF and NZF@Alb NPs, respectively. The slight increase in coercivity for the NZF@Alb NPs could be attributed to domain wall pining by the

non-magnetic albumen. Magnetic controllability of NZF@Alb NPs has also been demonstrated and shown as a digital image in the inset of figure 4.2.7. It was observed that NZF@Alb NPs can be easily magnetically controlled by applying an external magnetic field.

4.2.1.6 FTIR analysis

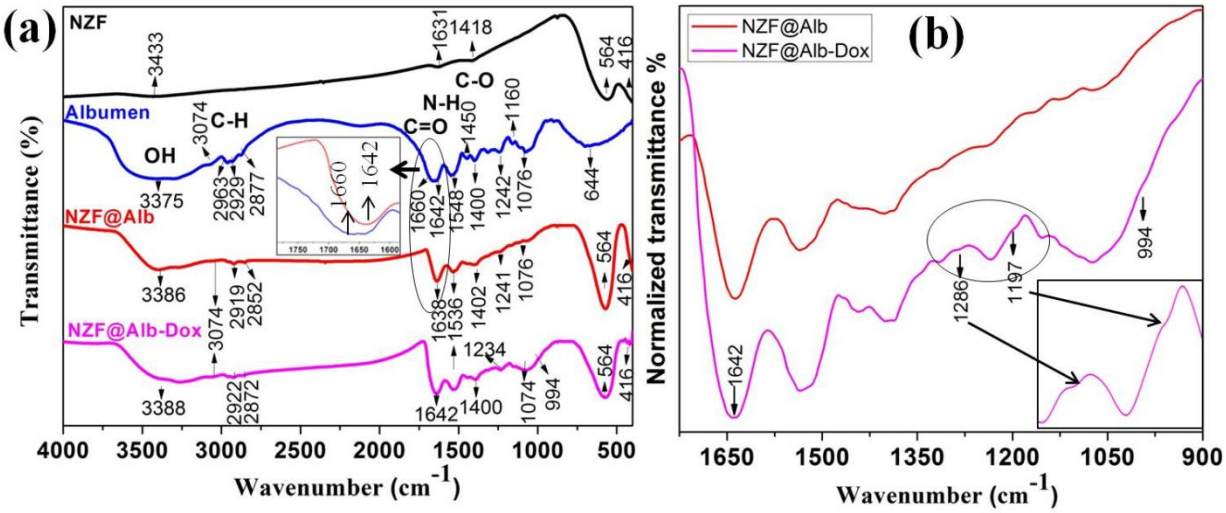

Figure 4.2.8. (a) FTIR spectra of NZF, albumen, NZF@Alb and NZF@Alb-Dox nanoparticles. Inset of figure (a) shows enlarge indicated 1600-1750 bands of albumen and NZF@Alb (b) FTIR spectra of NZF@Alb and NZF@Alb-Dox nanocomposite between wavenumber 900-1700 cm^{-1}. Inset of figure (b) shows enlarge spectra of indicated circled region.

In order to investigate the chemical structure of NZF@Alb-Dox NPs and to investigate available functional groups FTIR analysis was carried out. FTIR results were also used to support the coating of albumen on NZF NPs and loading of Dox in NZF@Alb-Dox. FT-IR spectra of NZF, Albumen, NZF@Alb and NZF@Alb-Dox NPs are shown in figure 4.2.8(a). The IR spectra of NZF NPs shows two principle absorption bands in the wavelength range 400-600 cm^{-1}, the first band is around 416 cm^{-1} and the second around 564 cm^{-1}. These two vibration bands can be attributed to the intrinsic lattice vibrations of octahedral and tetrahedral coordination complexes in the spinel structure, respectively [2]. Two additional bands at 1631 and 1418 cm^{-1} may be due to the undecomposed citrate on the surface of NZF NPs and could be assigned to the stretching and bending vibration of C=O and C-O respectively. The characteristic absorption bands of albumen at 1642 (& 1660) and 1548 cm^{-1} were attributed to Amide I and Amide II bond of protein molecules and originated from -C=O stretching vibration and –N-H bending vibration coupled with C-N stretching, respectively [8] [4]. Absorption bands of albumen at 1600-1700 cm^{-1} (1642 & 1660 cm^{-1}) are directly related to the protein

backbone conformations and have been used for studying protein secondary structures [6]. Appearance of bands of same intensities at 1660 and 1642 cm^{-1} indicated the equal presence of α helix (crystalline) and random (amorphous) secondary structure in dried albumen sample (inset of figure 4.2.8a) [14]. XRD pattern of the dried albumen powder also suggests partial crystalline nature of the sample. The spectra of pure albumen showed many other important peaks, at 3375 and 3074 cm^{-1} due to -OH stretching vibration with contribution from –NH stretching of the secondary amide, at 2929 and 2963 cm^{-1} due to –CH stretching, at 2877 cm^{-1} due to –SH stretching, at 1400 cm^{-1} due to carboxylate C-O bending vibration, at 1450 cm−1 due to amine III, at 1242 cm−1 due to C-O-H stretching, at 1160 cm^{-1} due to C-N stretching, and at 1076 cm^{-1} due to C-O stretching vibration [4, 15, 16]. A peak due to plane wagging was observed at 644 cm^{-1} and it can be assign to the out of plane N-H bending [10]. In IR spectra of NZF@Alb and NZF@Alb-Dox NPs nearly all absorption bands of albumen and NZF have been observed. Simultaneous appearance of characteristic bands of both albumen (1000-1700 cm^{-1}) and NZF (400-600 cm^{-1}) in FTIR spectra of NZF@Alb confirmed successful formation of the nanocomposite. In case of NZF@Alb NPs appearance of only one band at 1638 cm^{-1} and disappearance of band of crystalline α helix at 1660 cm^{-1} suggested increased randomness and irregular structures of coated albumen (inset of figure 4.2.8a). This phenomenon can be attributed to the electrostatic interaction of albumen with the nanoparticles and high ultra-sonication energy could have caused reorientation of the albumen chains. HRTEM and XRD pattern of NZF@Alb nanocomposite also suggested amorphous nature of coated albumen. Relatively lower fraction of crystalline β-sheet in BSA in Fe_3O_4/BSA nanocomposite has also been observed by Tian et al using FTIR [6]. In IR spectra of NZF@Alb-Dox nanocomposite main band of Dox (1640 cm^{-1}, C=O) has overlapped with the main band of albumen (1642 cm^{-1}) resulting in relatively intense and broader band [17]. Figure 4.2.8(b) shows absorption bands of NZF@Alb and NZF@Alb-Dox NPs with a normalized intensity between 900-1700 cm^{-1}. Increase in intensity and broadening of bands between 1000-1700 cm^{-1} and appearance of new bands of Dox at 1286 cm^{-1} (skeleton vibration of Dox), 1197 cm^{-1} (asymmetric stretching of C-O-C) and 994 cm^{-1} (stretching vibration of C-O)) confirmed Dox loading in NZF@Alb-Dox (figure 8(b)) [18]. The N–H wag bands of pure Dox, which normally appears at 870 cm−1 and 805 cm^{-1} [19], diminished in the FTIR spectrum of NZF@Alb-Dox. From this FTIR result, it can be inferred that attachment of DOX to the NZF@Alb NPs occurs via the interaction of $–NH_2$ of DOX with –COOH groups of albumen [1].

4.2.1.7 Doxorubicin (Dox) loading study

Due to the good anticancer activity of clinically accepted Dox, their loading and release behaviors had widely been studied in vitro or in vivo. Herein, Dox was chosen to load in NZF@Alb NPs due to many of its suitable and favorable properties such as, excellent anticancer activity against variety of cancer cells, clinical acceptance, opposite charge (positive at pH ~7.4, pKa value 8.3) to that of albumen carrier (negative at pH~7.4, Zeta Potential ~ -23.3 mV, isoelectric point of albumen ~5) and hydrophilic nature (doxorubicin hydrochloride) etc. [6, 11]. Hydrophilic nature of Dox could ensure its good miscibility in hydrophilic albumen matrix, which is expected to lead good compatibility of Dox with albumen nanocarrier. Albumin proteins have been proven to be a suitable and compatible carrier for Dox and several researches, using albumin as Dox's carrier, have successfully been conducted [11, 20]. Encouraging results of these studies show compatibility of Dox with albumin carriers and also motivated us to use Dox as anticancer agent to be loaded in NZF@Alb NPs.

In this work, Dox loaded NZF@Alb NPs (NZF@Alb-Dox NP) was obtained by the in situ incorporation method, where the drug is loaded at the time of preparation of the nanocarriers. UV-Vis absorption spectra of total Dox and free Dox remained in the supernatant are shown in figure 4.2.9(a). Almost complete suppression of the Dox peak (~480 nm) in UV-Vis absorption spectra of supernatant suggested that most of the Dox molecules have been loaded in the nanocarrier. Electrostatic interaction between negatively charged albumen and positively charged Dox (at pH 7.4) could have resulted in excellent loading of Dox in albumen. To support this explanation, surface charge of NZF@Alb NPs at pH 7.4 was studied by Zeta Potential measurement and shown in figure 4.2.9(f). The Zeta Potential value of NZF@Alb NPs was found to be ~ -23.3 mV, which confirmed negative charge on its surface. The excellent loading behavior of Dox in NZF@Alb and appearance of peak of Dox in UV-Vis absorption spectra of NZF@Alb-Dox suggested Dox compatibility with nanocarrier. Dox encapsulation efficiency and encapsulation capacity of nanocarrier were estimated to be ~90 % and ~5 % (50 ng Dox /μg particle), respectively. Similar results were also reported by other researchers for similar kind of systems [6] [11]. Loading of Dox was also confirmed by UV-Vis absorption spectra of NZF@Alb-Dox (figure 4.2.9(b)). Appearance of a hump of Dox in between 480-510 nm confirmed the presence of Dox in NZF@Alb-Dox NPs. Pure Dox has an absorption peak centered at ~480 nm (inset of figure 9(b)). Digital images (figure 4.2.9(b)) show the physical appearance of aqueous NZF@Alb and NZF@Alb-Dox NPs at the same concentration (~0.25mg/ml). Difference in their colors can be observed clearly. Incorporation

of Dox (red color) in NZF@Alb (brown color) has resulted in reddish brown colored NZF@Alb-Dox NPs. All the quantifications of Dox loading and release studies were done using a standard calibration curve (y = 0.01336x + 0.01192, R^2 = 0.999) shown in figure 4.2.9(c).

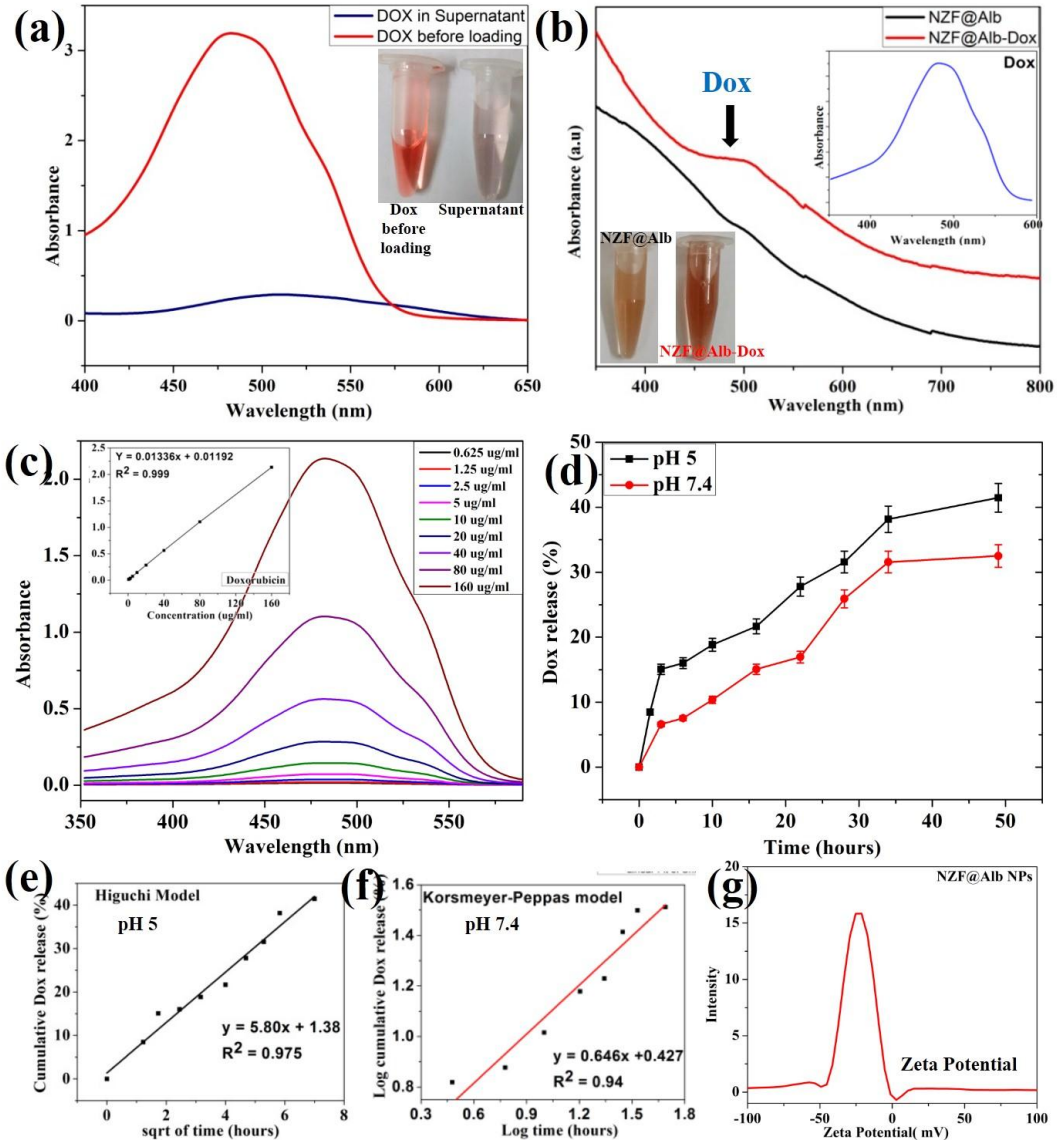

Figure 4.2.9. (a) UV-Vis absorption spectra and digital photographs of Dox before loading and free Dox in supernatant. (b) UV-vis absorption spectra of NZF@Alb and NZF@Alb-Dox. Inset of (b) shows UV-vis absorption spectra of pure Dox. Digital images shown in (b) show the physical appearance of aqueous dispersion of NZF@Alb and NZF@Alb-Dox NPs at same concentration of nanoparticles (~0.25mg/ml). (c) UV-vis absorption spectra of different known concentration Dox with corresponding standard calibration. Time dependent Dox released behavior from NZF@Alb-Dox at pH5 (black) and pH 7(red). Plots of Dox release data fitted to Higuchi (pH 5) and Korsmeyer-Peppas (pH 7.4) kinetic models are shown in (e) and (f) respectively. (g) Zeta Potential result of NZF@Alb NP dispersed in PBS of pH 7.4.

Table 1. Release kinetic parameters of Dox released from NZF@Alb-Dox at pH 5 and 7.4.

Dox release at	Zero-order		First-order		Higuchi		Korsemeyer-Peppas	
	K_0	R^2	K_1	R^2	K_H	R^2	n	R^2
pH 5	0.764	0.889	0.010	0.930	5.799	0.975	0.424	0.951
pH 7.4	0.688	0.924	0.008	0.931	5.085	0.925	0.646	0.938

4.2.1.8 In vitro release study of Dox:

Besides drug loading, time-dependent release is the other important parameter for drug efficacy and delivery in a sustained and controlled manner. In vitro release behavior of Dox from NZF@Alb-Dox NPs was investigated under various environmental pH values and are demonstrated in figure 4.2.9(d). The release studies were carried out at 37 ^oC in two different buffers of pH 5 (mimicking cancer cell pH, especially for microenvironment in endosomes and lysosomes) and pH7.4 (blood plasma). A sustained and pH dependent release of Dox from NZF@Alb-Dox NPs was observed. It was observed that low environment pH accelerates the DOX release. 15 mg of NZF@Alb-Dox (5% Dox content) was used for release study. In first 10 hours at pH 5.0 (18.8 % of loaded Dox) the Dox release % was considerably higher than those at pH 7.4 (10.4 % of loaded Dox). After 24 hours, the Dox release % at pH 5 and 7 were noted to be 29 and 20 % of total loaded Dox. After 50 hours of incubation the Dox release % at pH 5 and 7 were found to be 41.5 % (~311µg) and 32.5 % (~244 µg) of total loaded Dox in NZF@Alb-Dox. Very controlled and sustained release of drug from nano-carrier is desired for anticancer drug delivery applications. Obtained Dox release profile (gradual increment with time) and nearly 29 % release in first 24 hours show its sustained release behavior, which is better than reported result (~40-45% Dox release in ~24 hours) for similar kind of system (Dox-BSA-Fe_3O_4-DEX-FA) [11]. Sustained release behavior of Dox could be attributed to the good electrostatic interaction between $–NH_2$ of Dox and –COOH groups of albumen at tested pH. Relatively fast Dox release at lower pH (pH 5) than pH 7 can be attributed to a relatively weak electrostatic interaction between albumen matrix and Dox molecules at lower pH value (pH 5). In other words, pH-dependent release behavior of Dox from NZF@Alb-Dox NPs is due to electrostatic interactions between Dox and albumen, which is also in agreement with other

reports [6] [20]. Negatively charged carboxyl groups of albumen could bind positively charged amino groups of Dox (pKa 8.3)) via electrostatic attractions. Albumin protein, having isoelectric point around pH ~5, remains negatively charge at pH 7.4 [20]. The electrostatic interactions between Dox and albumen became weak due to protonation of albumen at lower pH resulting relatively faster release of Dox from NZF@Alb-Dox NPs. The sudden increase in the Dox release % within first one hour could be attributed to the loosely and physically adsorbed Dox molecules on the surface of NZF@Alb NPs. These pH-responsive NZF@Alb-Dox NPs may reduce the unwanted release of Dox during its transportation in the blood circulation system and improve the effective release inside tumor cells (magnetic targeting), thus reduced side effects and improved efficacy of Dox is anticipated. Release kinetics of drug from a reservoir is generally interpreted using different mathematical models. Thus, release kinetics of Dox from NZF@Alb-Dox at pH 5 and pH 7.4 were analyzed using zero order, first order, Higuchi and Korsmeyer–Peppas models and obtained parameters (R^2, K_0, K_1, K_H, and *n*) are shown in table 1. Experimental release data were fitted to these models and best fitted model was identified by the best correlation coefficient (R^2). It was observed that release data at pH 5 and 7 were fitted well with the Higuchi and Korsmeyer–Peppas models, respectively. Release data fitted with Higuchi (pH 5) and Korsmeyer–Peppas (pH 7.4) models are shown in figure 4.2.9 (e) and (f) respectively. Higuchi model suggests that at pH 5 Dox is released by diffusion controlled process according to Fick's Law. In case of Korsmeyer–Peppas model the value of *n* suggests the involved release mechanisms, $n \leq 0.5$ indicates Fickian diffusion and $n > 0.5$ indicates anomalous diffusion (in case of thin coating). The mentioned range of n values and corresponding drug release mechanism slightly differ for different geometries (such as film, cylindrical, and sphere). For sphere, $n \leq 0.43$ indicates Fickian diffusion and n in the range of $0.43 < n < 0.85$ suggests the mechanism is non-Fickian diffusion or anomalous diffusion [21] [22, 23]. Thus, it is imperative that at pH 5 (n = 0.424), Dox release mechanism was via Fickian diffusion, whereas at pH 7.4 (n = 0.646), it was via anomalous or non Fickian diffusion process. This could be explained in terms of reduced electrostatic interaction between Dox and albumen at lower pH. In the absence of electrostatic interaction at pH 5, Dox could have released through diffusion controlled process. Anomalous diffusion of Dox at pH 7.4 could be attributed to many factors such as, good electrostatic interaction between Dox and albumen, swelling and erosion of albumin matrix etc. The Zero order kinetic model does not fit well with the experimental data however, first order kinetic model has shown better fitting than zero order kinetic model.

4.2.1.9 Biocompatibility and anticancer activity by MTT assay

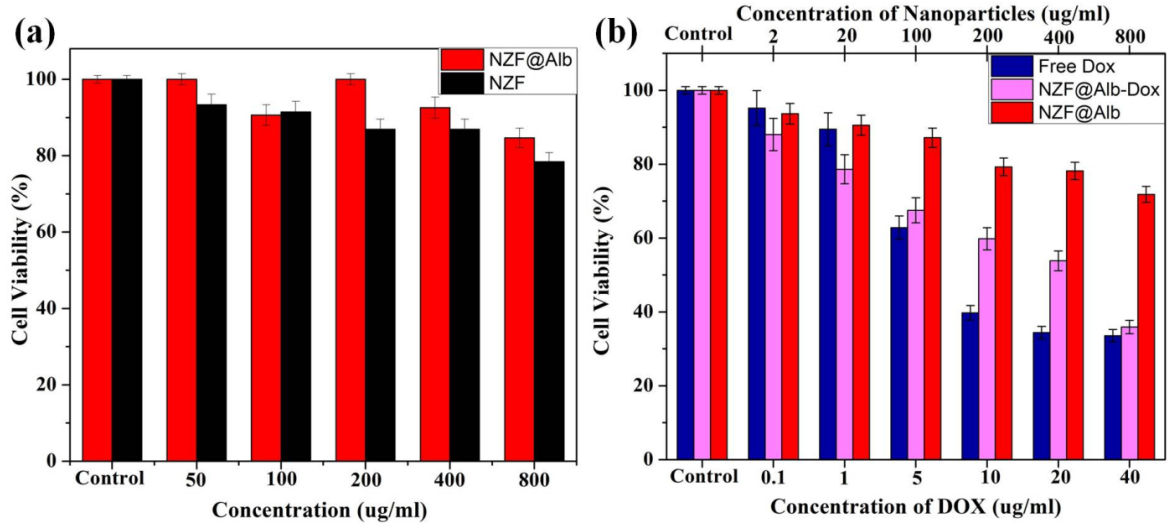

Figure 4.2.10. (a) Cell viabilities measured by MTT assay of RAW 264.7 cells treated with different concentrations of the NZF and NZF@Alb NPs. (b) Growth inhibition results or cytotoxicity assay for Hela cells treated with free Dox, plain NZF@Alb NPs and NZF@Alb-Dox NPs with different concentrations. The concentration of NZF@Alb NPs against Hela cells is shown on the upper x axis of (b).

Biocompatibility of the NZF and NZF@Alb NPs were confirmed by in vitro cytocompatibility assay (MTT assay) against RAW 264.7 cells (normal cells). The results of in vitro cytocompatibility assay are shown in figure 4.2.10(a). A dose dependant response was observed for both the NZF and NZF@Alb NPs. Both the samples were found to be biocompatible in nature with a minimal cells inhibition even at very high doses. A good cell viabilities i.e 87% and 93% for NZF and NZF@Alb NPs, respectively, were observed at high dose (400µg/ml). It means only 13% and 7% cell inhibition have occurred for NZF and NZF@Alb NPs, respectively, at 400µg/ml NPs dose. For the maximum tested dose (800µg/ml) the cell viability for NZF and NZF@Alb NPs were found to be ~85% and 88%, respectively, which suggested biocompatible nature of both the samples. A relatively improved biocompatibility of NZF@Alb NPs than bare NZF NPs was observed and could be attributed to the coating of NZF with biocompatible albumen. Thus, MTT assay confirmed that prepared NZF@Alb NP was biocompatible and nontoxic to tested normal cells even at concentration of 800µg/ml. Hela cells were also used to evaluate in vitro anticancer activity of NZF@Alb-Dox NPs. The in vitro cytotoxicity of the plain NZF@Alb NPs, free Dox, and NZF@Alb-Dox NPs against HeLa cells were carried out by MTT assay and obtained comparative results are shown in figure 4.2.10(b). Dox dose concentrations were chosen as 0.1, 1, 5, 10, 20 and 40µg/ml for

both free Dox and loaded Dox. In order to study contribution from NZF@Alb NPs on cell inhibition, killing effect of NZF@Alb NPs also has been tested and compared. In general, the cytotoxicities for NZF@Alb NPs, free Dox, and NZF@Alb-Dox NPs against HeLa cells were all dose dependent. A moderate toxicity toward Hela cells has been observed for NZF@Alb NPs. A considerable cell inhibition (28.4%) at 800µg/ml has been observed for NZF@Alb NPs. IC_{50} (i.e inhibitory concentration required to kill 50% of cells) value of NZF@Alb NPs was not observed in the tested concentration range. In a recent study, Al-Qubaisi et al have concluded that NZF have potential cytotoxicity against studied cancer cells- HT29, MCF-7, and HepG2 cells [24]. They have shown that NZF induce glutathione depletion in cancer cells, which results in increased production of reactive oxygen species and eventually death of cancer cells [25]. In the present case NZF@Alb NPs does not show much toxicity toward Hela cell due to coating of biocompatible albumen on NZF NPs. Soft and superparamagnetic nature of NZF NPs retained its importance due to good magnetic controllability. Free Dox shows slow inhibition rate upto 1µg/ml (10.4%) and then shows fast killing rate till 10 µg/ml resulting in ~60 % inhibition, there after inhibitions rate become nearly constant. In case of free Dox maximum killing was found to be ~66.2% at highest given Dox dose (40µg/ml). IC_{50} for free Dox was found to be 10µg/ml. In case of NZF@Alb-Dox a linear dose dependent cell inhibition was observed. IC_{50} value of loaded Dox in NZF@Alb-Dox was found to be 20µg/ml. Maximum cell inhibition (at 40µg/ml) for free Dox and NZF@Alb-Dox were found to 66.2 and 64.3 %, respectively, after 24 hours incubation. The NZF@Alb-Dox showed decreased cytotoxicity than free Dox for the same concentration of Dox. However, free Dox lacks in having magnetic tumor-targeting ability, which can lead to severe side effects. Less cytotoxicity of NZF@Alb-Dox than free Dox could be explained by taking the slow release rate into account in the following ways. It may be due to very slow release of loaded Dox from nanocarrier than diffusion of free Dox molecules. In other words, due to very slow release rate a large proportion of Dox molecules were still within the NZF@Alb-Dox (after 24 hours incubation), which results in a lower actual Dox concentration in the test medium of NZF@Alb-Dox than that of free DOX [26]. Similar observations were also made by earlier researchers [11] [26]. As mentioned above (in the Dox release study section) that only 29% (pH 5) of loaded Dox was released within the 24 hours of incubation. It means actual dose encountered by the cells are approximately 29% of given dose after 24 hours incubation. MTT assay against Hela cells has shown a promising anticancer activity of NZF@Alb-Dox. It is suggested that NZF@Alb based nano-formulations, which possess efficient anti-cancer activity

together with low systemic toxicity, can act as ideal nanocarrier for the targeted parceling of anticancer drugs.

A novel, multifunctional, pH responsive, water dispersible and magnetically guidable NZF@Alb and NZF@Alb-Dox NPs have been successfully prepared by simple and eco-friendly method using inexpensive chicken egg albumen and have been characterized for different physiochemical properties.

4.2.2 Development of multifunctional Fe_3O_4@Alb nanoparticle for anticancer drug delivery

4.2.2.1 Synthesis of Fe_3O_4@Alb Nanocomposite

Preparation of Fe_3O_4@Alb NP was carried out by similar method as used in case of NZF@Alb NP i.e an environment friendly ultrasonication method [1, 27]. Formation of Fe_3O_4@Alb NP is shown figure 4.2.11. Similar formation mechanism as of NZF@Alb NP could be explained for the formation of Fe_3O_4@Alb NP. Gelation of albumen and rapid collision during ultrasonication resulted deposition of albumen on Fe_3O_4 NPs. It is worthy to mention that ultrasonication produced very high localized heat and energy which was sufficient to initiate chemical interaction between NPs and albumen molecules. Fe_3O_4@Alb NP was characterized for its different physicochemical properties and loaded with Dox. Its anticancer activity was studied against Hela cells by MTT assay.

4.2.2.2) Structural and morphological characterization of Fe_3O_4@Alb Nanocomposite

Figure 4.2.12 shows XRD pattern of Fe_3O_4 NPs and Fe_3O_4@Alb NP. Characteristic diffraction peaks of spinel cubic Fe_3O_4 NP have been observed in both sample which confirm formation of nanocomposite. It can also be concluded that coating of albumen does not disturb crystalline structure of Fe_3O_4 NP. No sharp diffraction peaks of albumen have been observed due to its amorphous nature. The intensity of diffraction peaks of Fe_3O_4@Alb NP is relatively reduced as compared to the Fe_3O_4 NPs. It could be due the incorporation of Fe_3O_4 NPs in amorphous albumen matrix. The crystallite size of Fe_3O_4 NPs in Fe_3O_4@Alb NP was found to be ~9 nm. Similar XRD patterns for BSA-Fe_3O_4 nanocomposites have been reported earlier [8, 11].

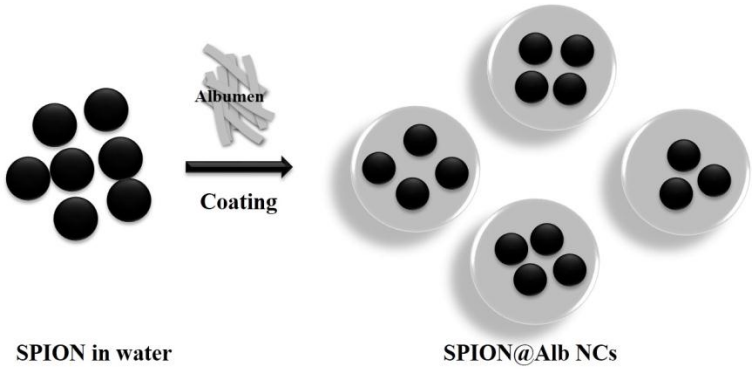

Figure 4.2.11. Formation process of Fe_3O_4@Alb NP.

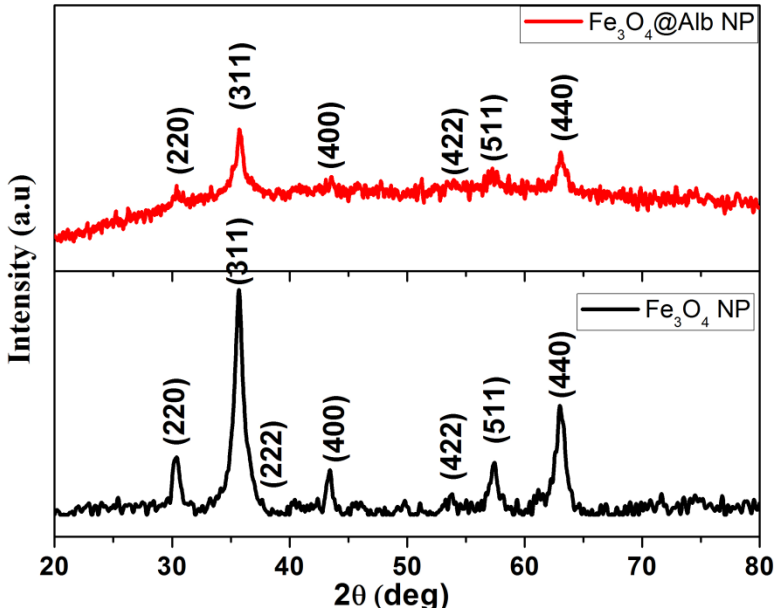

Figure 4.2.12. XRD pattern of Fe_3O_4 NPs and Fe_3O_4@Alb NP

For biological application specially for drug delivery, magnetic nanoparticle should be hydrophilic, biocompatible and colloidally stable. This can be obtained by surface engineering or core shell nanocomposite formation and thus by coating with albumen [6, 15] [28]. Incorporation of magnetic nanoparticles in albumen will provide magnetic targeting ability to nanocarrier [6]. Thus Fe_3O_4@Alb NP were prepared and characterized for different physico-chemical properties. TEM analysis of Fe_3O_4@Alb NP was performed to confirm its formation, particles size as well as morphology.

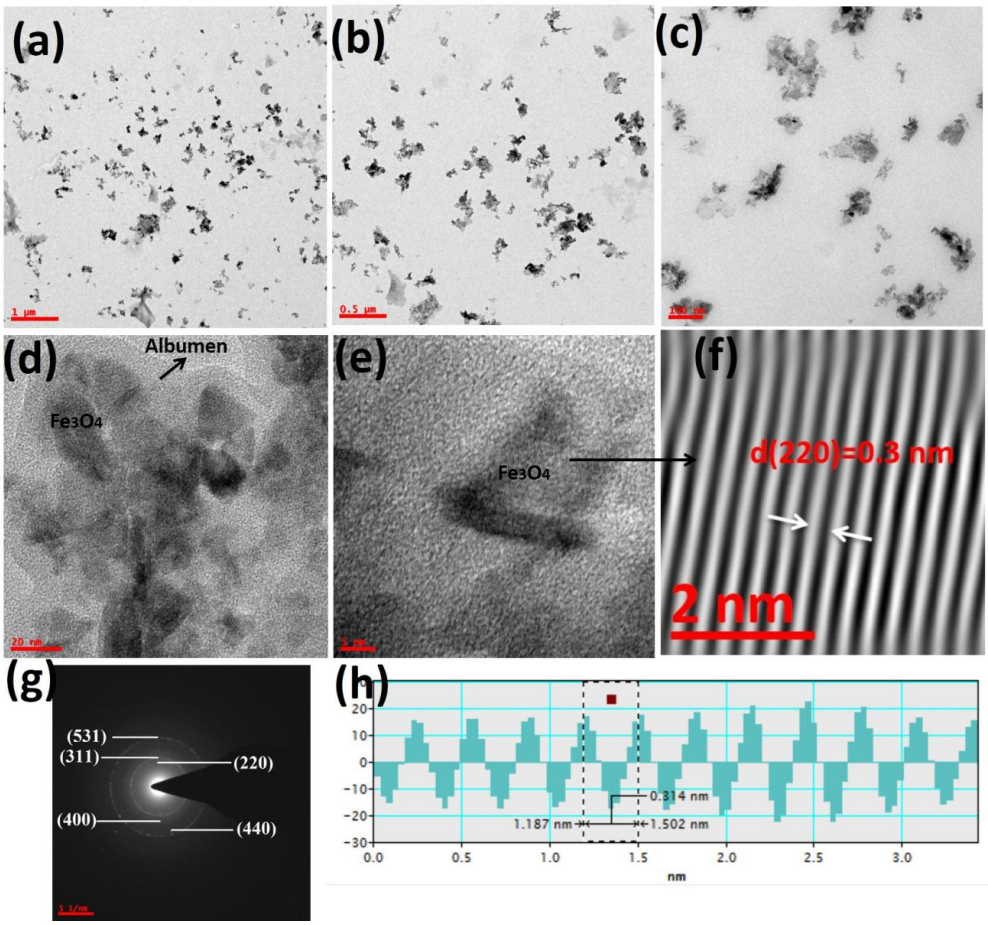

Figure 4.2.13. TEM images of Fe_3O_4@Alb NPs at low to high magnifications (a-d). HRTEM image of Fe_3O_4@Alb NP showing crystalline Fe_3O_4 NPs coated with amorphous albumen (d-e). IFFT image of indicated region of (e) is shown in (f). Indexed SAED pattern of Fe_3O_4@Alb NP. Line profile through atomic planes is shown in (h).

TEM images of Fe_3O_4@Alb NP at different magnifications (low to high) are shown in figure 4.2.13(a-d). Particles size of Fe_3O_4@Alb NP was found to vary between ~ 60-180 nm with average particle size of 119 nm. No specific shape and morphologies were observed. The surface of Fe_3O_4@Alb NP was observed to be very rough that may due to the irregular shape of particles. It can be observed that Fe_3O_4@Alb NP is composed of many smaller IO NPs embedded in albumen matrix. The covering albumen (grey color) on IO NPs (black dots) can very clearly be seen in the high magnification images (fig. 4.2.13 (d & e)). It can be observed that many IO NP are aggregated and covered with continuous albumen layer. HRTEM image of Fe_3O_4@Alb NP shows crystalline IO NPs are embedded in albumen matrix. The presence of amorphous albumen on the surface of crystalline IO NPs are shown in figure 4.2.13(d and e). The presence of well-ordered atomic planes with the d-spacing of Fe_3O_4 NP on the surface of smaller particle confirm that those are IO NPs and suggest its well crystalline nature IFFT image of indicated region of (e) is shown in (f) which clearly showed well-ordered atomic

plane with the d-spacing of 0.3 nm that is (220) plane of IO NPs. Indexed SAED pattern of Fe_3O_4@Alb NP is shown in (g) and appearance of characteristic ring pattern of spinel cubic IO NPs confirmed formation of nanocomposite. From the SAED and XRD result of Fe_3O_4@Alb NP, it was also observed that coating of albumen of surface of IO NP does not alter crystalline nature of magnetic component. Line profile through atomic planes of figure (f), which was used to estimated d-spacing is shown in (h).

4.2.2.3 FTIR analysis of blank and Dox loaded NPs

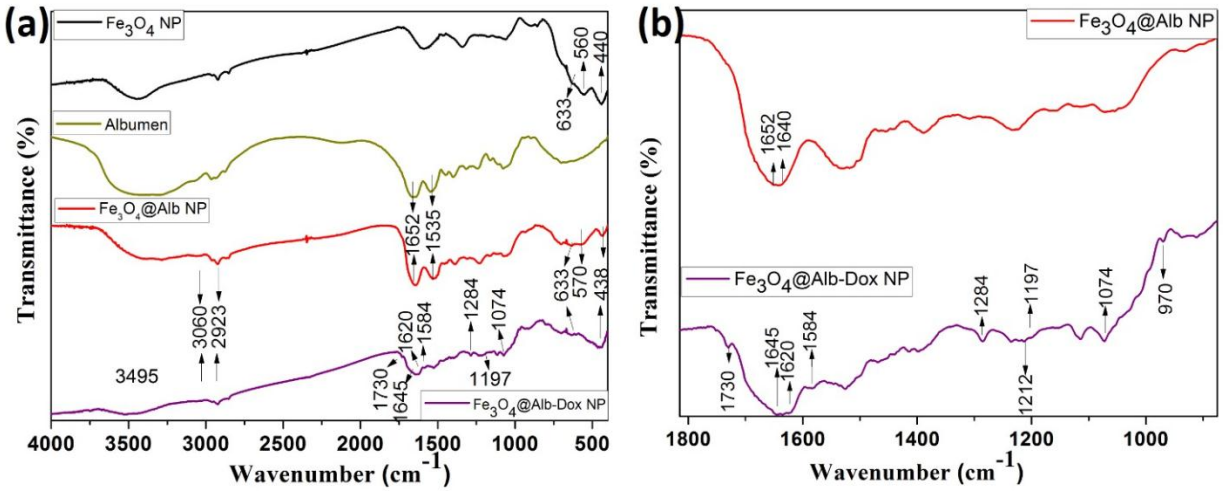

Figure 4.2.14. (a) FTIR spectra of bare Fe_3O_4 NP, albumen, Fe_3O_4@Alb NP and Fe_3O_4@Alb-Dox NP. (b) Enlarge FTIR spectra of Fe_3O_4@Alb NP and Fe_3O_4@Alb-Dox NP in the range of 900-1800.

To study the anticancer drug loading ability of Fe_3O_4@Alb NP, Dox as model drug has been loaded to get Fe_3O_4@Alb-Dox NP. Formation of IO NPs and Fe_3O_4@Alb NP and loading of Dox in Fe_3O_4@Alb NP were further confirmed by FTIR analysis. Figure 4.2.14(a) shows FTIR spectra of bare Fe_3O_4 NP, albumen, Fe_3O_4@Alb NP and Fe_3O_4@Alb-Dox NP. In FTIR spectra of Fe_3O_4 NP, emergence of characteristic band of spinel cubic Fe_3O_4 at 440 and 560 cm^{-1} confirmed its successful formation. These bands can be assign to the lattice vibrations of octahedral and tetrahedral sites in the Fe_3O_4, respectively. FTIR spectra of Fe_3O_4@Alb NP show characteristic band of both spinel cubic Fe_3O_4 and albumen which confirmed successful formation of nanocomposite. The characteristic bands of albumen at 1652 and 1535 cm^{-1} were attributed to Amide I and Amide II bond of protein molecules[4, 8]. The bands at ~2920 cm^{-1} and 3200-3600 cm^{-1} of pure albumen and Fe_3O_4@Alb NP can be assigned to the -OH with contribution from N-H and -C-H stretching vibration in albumen. For better visualization of bands enlarge FTIR spectra of Fe_3O_4@Alb NP and Fe_3O_4@Alb-Dox NP in the range of 900-

1800 is shown in figure 4.2.14(b). In case of Dox loaded sample Fe_3O_4@Alb-Dox NP the major band at 1645 become asymmetric due to the coupling of band of Dox (1620 & 1640) and albumen (1652) [18]. Several other characteristic bands of Dox also have been observed in the FTIR spectra of Fe_3O_4@Alb-Dox NP such as 1730, 1584, 1284, 1212, 1197 and 970 cm^{-1} etc. Thus, FTIR analysis also confirm formation of nanocomposite and Dox loading in nanocomposite[18].

4.2.2.4 Thermal analysis

TGA was used to study the thermal properties Fe_3O_4 and Fe_3O_4@Alb NP and TGA results are shown in figure 4.2.15. Amount of albumen in Fe_3O_4@Alb NP were also estimated using the degradation pattern. Bothe the samples show ~ 5-6% weight loss in the range of 50-150 ^oC and this was due to the loss of adsorbed water. The TGA results of bare Fe_3O_4 NPs does not show much degradation in between 150-600 ^oC with the loss of ~7 %. This very little weight loss can be attributed to oleic acid on the surface of Fe_3O_4 NPs. Thus, prepared Fe_3O_4 NPs was found to well stable in the tested temperature rang with the total weight of only 10-12%. Fe_3O_4@Alb NP was found to be stable upto 200 ^oC with very little weight loss of 6 % that can be assigned to the loss of adsorbed water molecules. Very fast degradation of albumen take place at around 250-300 ^oC. The total weight in case Fe_3O_4@Alb NP was found to be ~50%. Thus, TGA analysis also suggested presence of albumen in the nanocomposite and confirmed formation of Fe_3O_4@Alb NP.

4.2.2.5 Magnetic Properties

Figure 4.2.16(a) shows room temperature M-H curve of bare Fe_3O_4 and Fe_3O_4@Alb NP in the range of 1.5 Tesla. Different magnetic data such saturation magnetization (M_s), remanent magnetization (M_R) and coercivity (H_c) value were noted for the M-H curve. It was observed that both the sample are having superparamagnetic nature with negligible coercivity and remanant magnetization. High M_s value of magnetic nanocarrier reflect its high magnetic controllability. The Ms value of Fe_3O_4 and Fe_3O_4@Alb NP were found to be ~55.5 and ~25.7 emu/gm. Enlarge M-H graph of Fe_3O_4 and Fe_3O_4@Alb NP in figure 4.2.16(b) show negligible coercivity and remanant magnetization value. The coercivity and remnant magnetization of both the samples were found to be in between 20-21 Oe and 0.8-1.1 emu/gm respectively. The decrease of M_s value of Fe_3O_4@Alb NP than bare Fe_3O_4 is due the presence of nonmagnetic albumen in the sample. Superparamagnetic nature of samples is due the ultra-small size of

Fe_3O_4 NP where thermal vibration can cause spin reversal or randomization of spin. Smaller size and superparamagnetic nature and Dox loading ability make this nanocomposite very suitable for targeted drug delivery application where it can be magnetically targeted to the specific site and deliver loaded drug. Superparamagnetic nature is suitable for drug delivery application as particles remains in completely demagnetized without magnetic field and get magnetized in magnetic field. Demagnetized form of the particle remains in non-aggregated state (no magnetic attraction) and give stable suspension which is important for smooth flow in biological system.

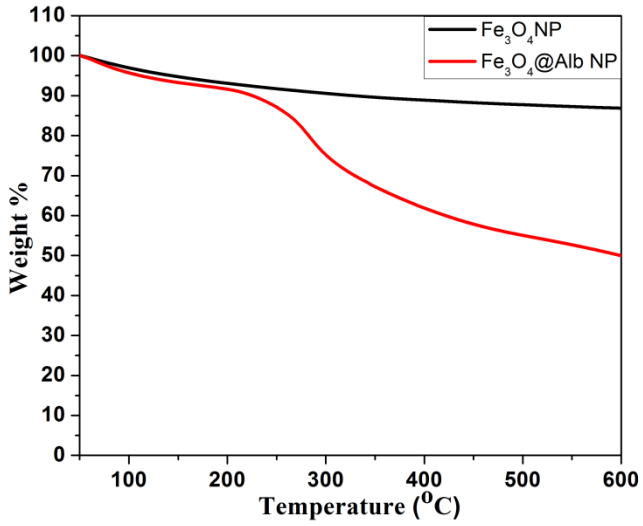

Figure 4.2.15. TGA results of bare Fe_3O_4 and Fe_3O_4@Alb NP.

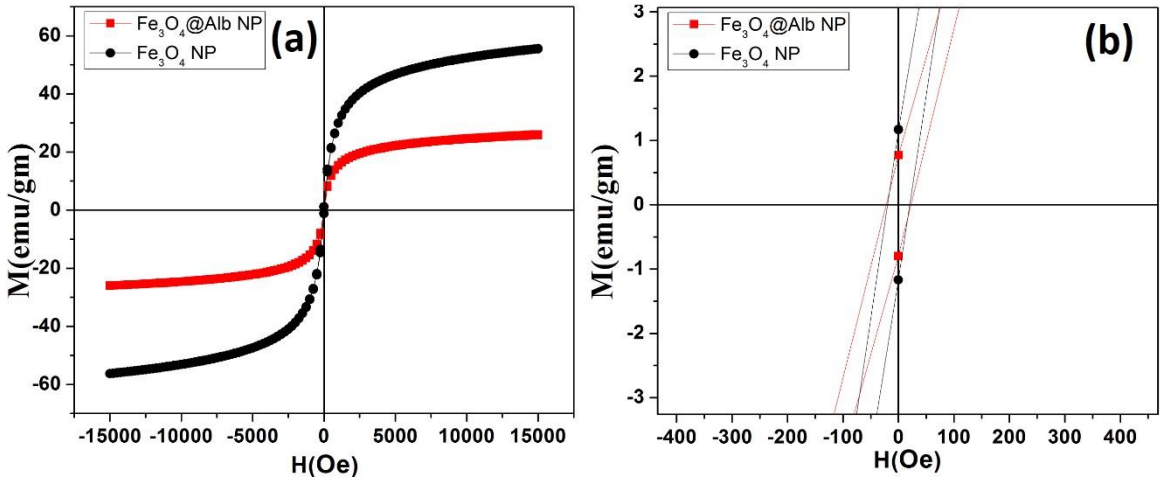

Figure 4.2.16. (a) Room Temperature M-H curve of bare Fe_3O_4 and Fe_3O_4@Alb NP. (b) Enlarge M-H graph of Fe_3O_4 and Fe_3O_4@Alb NP to show coercivity and remanant magnetization value.

4.2.2.6 Anticancer activity of Dox loaded Fe_3O_4@Alb NP

Anticancer activity of Dox loaded Fe_3O_4@Alb NP was studied against the Hela cell by MTT assay. Figure 4.2.17. shows cell viability of Hela cell treated with different concentration of Fe_3O_4@Alb-Dox NP after 24 hours of incubation. Dox dose amount were selected as 0.1, 1, 10, 20 and 40µg/ml. 40 % cell inhibition was observed at very low dose of loaded Dox i.e. 1 ug/ml. A dose dependent cell inhibition was observed. Highest cell inhibition was observed to be ~53% at highest given dose (40µg/ml). The IC_{50} value was found to be somewhere between 20-40 ug/ml of loaded Dox. Thus, MTT assay result suggest a promising anticancer activity of Fe_3O_4@Alb-Dox NP.

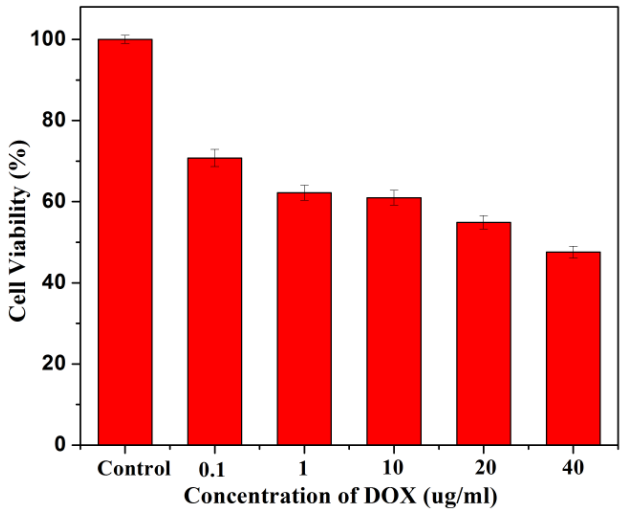

Figure 4.2.17. Cell viability of Hela cell treated with different concentration of Fe_3O_4@Alb-Dox NP after 24 hours of incubation.

Thus, the obtained results suggested the successfully formation of Fe_3O_4@Alb NP and Fe_3O_4@Alb-Dox NP. This biocompatible, hydrophilic, inexpensive and magnetically targetable Fe_3O_4@Alb NP could be very useful for hyperthermia and anticancer targeted drug delivery application.

4.2.3 Synthesis and characterization of $CoFe_2O_4$@Albumen nanoparticle

4.2.3.1 Preparation of CF@Alb NP

First, well crystalline $CoFe_2O_4$ nanoparticles (CF NPs) have been synthesized by a simple coprecipitation method. Formation of CF@Alb NP has taken placed in similar way as discussed in case of NZF@Alb and Fe_3O_4@Alb NP by environment friendly ultrasonication method (fig.4.2.18).

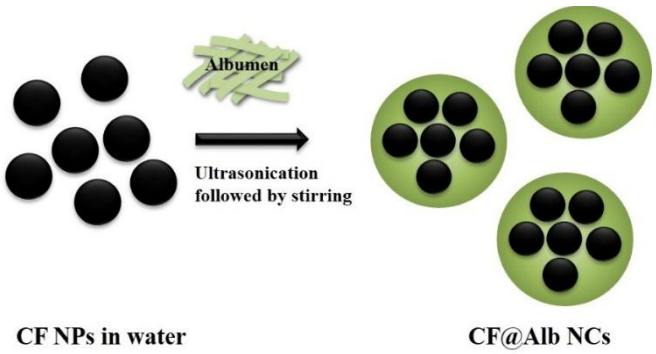

Figure 4.2.18. Formation process of CF@Alb NP.

4.2.3.2 Structural analysis

Figure 4.2.18 shows formation of CF@Alb NP. Figure 4.2.19 shows XRD pattern of CF NPs and CF@Alb NP. Both the samples show characteristic diffraction peaks of spinel cubic $CoFe_2O_4$. The XRD pattern of CF@Alb NP confirm presence of CF NPs in nanocomposite. The intensity of diffraction peaks of CF@Alb NP is relatively reduced as compared to the CF NPs. It could be due the incorporation of CF NPs in amorphous albumen matrix. Due to amorphous nature of albumen no sharp diffraction has been observed.

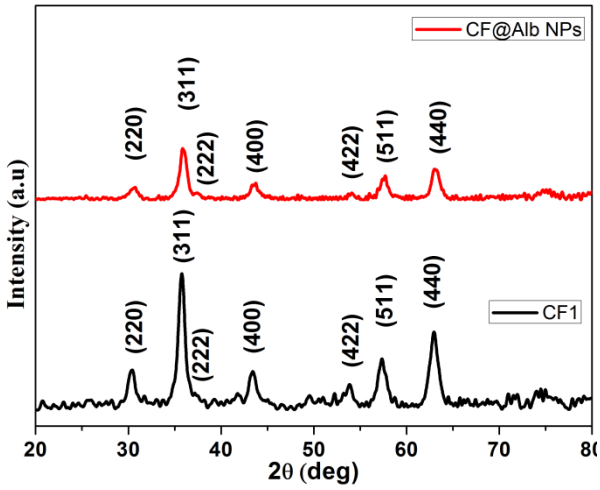

Figure 4.2.19. XRD pattern of CF NPs and CF@Alb NP.

4.2.3.3 Particles size, structure and Morphology by TEM

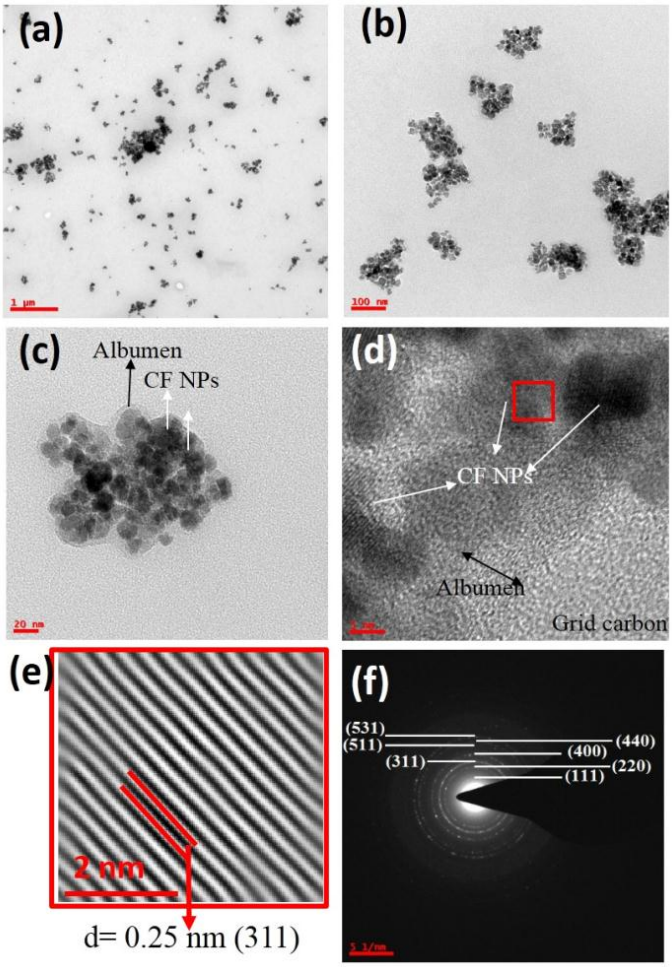

Figure 4.2.20. TEM micrographs of CF@Alb NP at different magnifications (a-c). HRTEM image of CF@Alb NP showing crystalline CF NPs coated with amorphous albumen. IFFT image of framed (red) region of (d) is shown in (e). Indexed SAED pattern of CF@Alb NP.

Coating of magnetic nanoparticles with albumen gives hydrophilic, biocompatible and colloidally stable nanoparticles. Presence of magnetic nanoparticles in albumen will provide magnetic targeting ability to nanocarrier. Formation of CF@Alb NP and its particles size as well as morphology were studied by TEM analysis. TEM micrographs of CF@Alb NP at different magnifications are shown in figure 4.2.20(a-d). Particles size of CF@Alb NP was found to lie between ~ 80-130 nm. Average particle size CF@Alb NP was estimated to be 106 nm. It can be observed that CF@Alb NP is composed of many smaller CF NPs embedded in albumen matrix. The shape of CF@Alb NP was found to vary from spherical to irregular shape. The covering of albumen (grey color) on CF NPs (black dots) can very clearly be seen in the high magnification images (fig. 4.2.20 (c & d)). HRTEM image of CF@Alb NP shows crystalline CF NPs are embedded in albumen matrix. The amorphous coating of albumen and

crystalline CF NPs are indicated by arrow in figure 4.2.20 (d). The presence of well-ordered atomic planes on the CF NPs suggest its well crystalline nature. IFFT image of framed (red) region of (d) is shown in (e) which clearly showed well-ordered atomic plane (311) of CF NPs with the d-spacing of 0.25 nm. Indexed SAED pattern of CF@Alb NP is shown in (f) and appearance of characteristic ring pattern of spinel cubic CF NPs confirmed formation of nanocomposite. From the SAED and XRD result of CF@Alb NP, it can also be inferred that coating of albumen does not affect crystal structure of CF NPs.

4.2.3.4 FTIR analysis

Chemical structure and formation of CF NPs and CF@Alb NP were confirmed by FTIR analysis. FTIR spectra of bare CF NPs, CF@Ab NP and pure albumen are shown in figure 4.2.21. Appearance of characteristic band of spinel cubic $CoFe_2O_4$ at 420 and 580 cm^{-1} confirmed its successful formation. These bands can be assign to the lattice vibrations of octahedral and tetrahedral sites in the $CoFe_2O_4$, respectively [2]. Simultaneous appearance of characteristic band of both spinel cubic $CoFe_2O_4$ and albumen in FTIR spectra of CF@Alb NP confirmed its successful formation. The characteristic bands of albumen at 1652 and 1535 cm^{-1} were attributed to Amide I and Amide II bond of protein molecules. The bands at ~2920 cm^{-1} and 3200-3600 cm^{-1} of pure albumen and CF@Alb NP can be assigned to the -OH with contribution from N-H and -C-H stretching vibration in albumen.

4.2.3.5 Thermal analysis

Thermal stability CF NPs and amount of albumen in CF@Alb NP were studied by TGA analysis. The TGA results of bare CF NPs and CF@Alb NP are shown in figure 4.2.22. CF NPs does not show much degradation upto 600 ^oC. This very little weight loss can be attributed to the adsorbed water and oleic acid. Thus, CF NPs was found to stable in the tested temperature rang. CF@Ab NP was found to be stable upto 200 ^oC with very little weight loss that can be assigned to the loss of water molecules. Very fast degradation of albumen take place at around 300 ^oC. The total weight in case CF@Alb NP was found to be ~42%. Thus, TGA analysis also suggested presence of albumen in the nanocomposite.

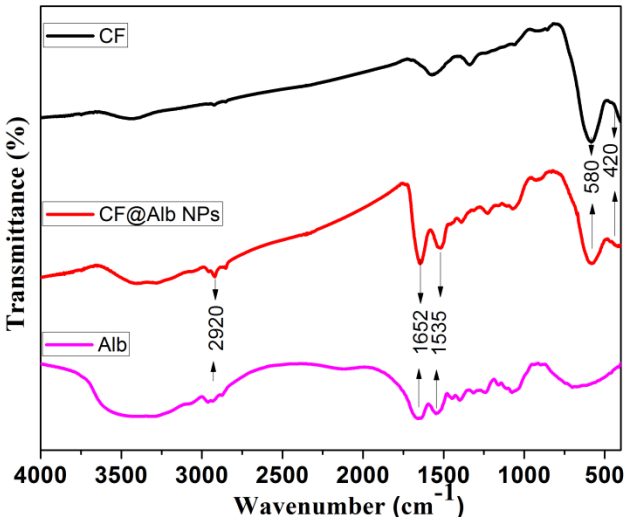

Figure 4.2.21. FTIR spectra of bare CF NPs and CF@Ab NP and pure Albumen.

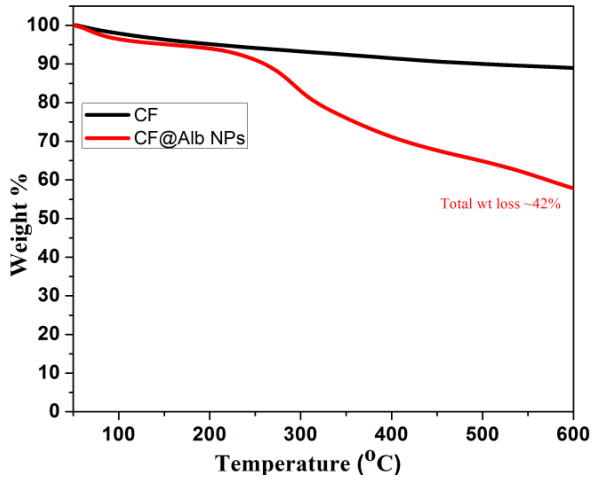

Figure 4.2.22. TGA results of bare CF NPs and CF@Alb NP.

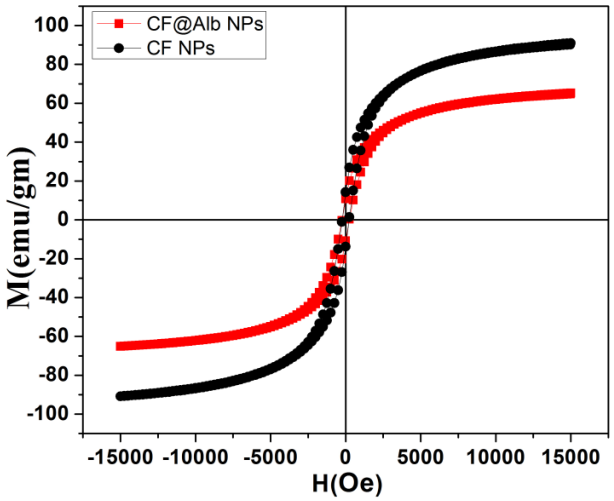

Figure 4.2.23. Room Temperature M-H curve of bare CF NPs and CF@Alb NP.

4.2.3.6 Magnetic properties

RT M-H curve of bare CF NPs and CF@Alb NP are shown in figure 4.2.23. Bulk $CoFe_2O_4$ is well known for its very high magnetization value and coercivity. It was observed that both the sample are having very high magnetization value which reflect its magnetic controllability. The Ms value of CF NPs and CF@Alb NP were found to be ~88 and ~64 emu/gm. The coercivity and remnant magnetization of both the samples were found to be in between 230-240 Oe and 11-14 emu/gm respectively. Smaller size and suitable amount of coercivity make this nanocomposite very suitable for hyperthermia application where heat energy will be generated due to hysteresis loss. Very high value of coercivity (of bulk) is not suitable for biomedical application as it results in aggregation of particles due to magnetic attraction which may cause blockage in biological system. This biocompatible, hydrophilic CF@Ab NP could be very useful for hyperthermia based cancer treatment due its suitable magnetic nature.

4.2.4 Conclusions

Novel, multifunctional, pH responsive and magnetically guidable, water dispersible NZF@Alb, NZF@Alb-Dox NPs, Fe_3O_4@Alb NP, Fe_3O_4@Alb-Dox NP, and CF@Ab NP have been successfully prepared by simple and eco-friendly method using inexpensive chicken egg albumen. Different physiochemical properties of prepared nanosystems have been studied using XRD, HRTEM, FESEM, FTIR, TGA, and VSM techniques. NZF@Alb NPs and Fe_3O_4@Alb NP were found to be superparamagnetic in nature. Magnetic property of CF@Alb shows its suitability for hyperthermia based cancer treatment. All the nano-systems were found to be biocompatible in nature. Average particles size of NZF@Alb, Fe_3O_4@Alb NP and CF@Alb were found to be in between 100-120 nm. Beside high loading efficiency, in Vitro Dox release studies from NZF@Alb-Dox NPs have shown a sustained and pH dependent Dox release profile. In vitro anticancer activity of NZF@Alb-Dox and Fe_3O_4@Alb-Dox NPs against HeLa cells were also carried out by MTT assay and both have shown a promising anticancer activity. So, in light of the obtained results, it is suggested that this scalable and pH responsive albumen based magnetic nanoformulation would have potential application in targeted and controlled delivery of anticancer drugs for cancer treatment. Thus, this type of nano-formulations which possess efficient anti-cancer activity, together with low systemic toxicity would be very useful where targeted and pH dependent delivery of hydrophilic anticancer drug are required. Other potential biomedical applications of the prepared nano-formulations could be in the field of hyperthermia and MRI.

4.2.4 References

[1] M. Qasim, K. Asghar, G. Dharmapuri, D. Das, Investigation of novel superparamagnetic Ni0.5Zn0.5Fe2O4@albumen nanoparticles for controlled delivery of anticancer drug, Nanotechnology 28(36) (2017) 365101.
[2] M. Qasim, K. Asghar, B.R. Singh, S. Prathapani, W. Khan, A.H. Naqvi, D. Das, Magnetically recyclable Ni0.5Zn0.5Fe2O4/Zn0.95Ni0.05O nano-photocatalyst: Structural, optical, magnetic and photocatalytic properties, Spectrochimica Acta Part A: Molecular and Biomolecular Spectroscopy 137(Supplement C) (2015) 1348-1356.
[3] A.A.C. C, Albumen protein and functional properties of gelation and foaming Sci. Agric. (Piracicaba, Braz.) 63 (2006) 291-298.
[4] G.V.N. Rathna, J.P. Jog, A.B. Gaikwad, Development of non-woven nanofibers of egg albumen-poly (vinyl alcohol) blends: influence of solution properties on morphology of nanofibers, Polym J 43(7) (2011) 654-661.
[5] H. Hao, Q. Ma, C. Huang, F. He, P. Yao, Preparation, characterization, and in vivo evaluation of doxorubicin loaded BSA nanoparticles with folic acid modified dextran surface, International Journal of Pharmaceutics 444(1) (2013) 77-84.
[6] Y. Tian, X. Jiang, X. Chen, Z. Shao, W. Yang, Doxorubicin-loaded magnetic silk fibroin nanoparticles for targeted therapy of multidrug-resistant cancer, Advanced materials 26(43) (2014) 7393-8.
[7] J. Wang, X. He, L. Chen, Y. Zhang, Boronic acid functionalized magnetic nanoparticles synthesized by atom transfer radical polymerization and their application for selective enrichment of glycoproteins, RSC Advances 6(52) (2016) 47055-47061.
[8] Z. Li, L. Qiang, S. Zhong, H. Wang, X. Cui, Synthesis and characterization of monodisperse magnetic Fe3O4@BSA core–shell nanoparticles, Colloids and Surfaces A: Physicochemical and Engineering Aspects 436(Supplement C) (2013) 1145-1151.
[9] E.S. Sashina, A.M. Bochek, N.P. Novoselov, D.A. Kirichenko, Structure and solubility of natural silk fibroin, Russian Journal of Applied Chemistry 79(6) (2006) 869-876.
[10] M. Bellusci, A. La Barbera, L. Seralessandri, F. Padella, A. Piozzi, F. Varsano, Preparation of albumin-ferrite superparamagnetic nanoparticles using reverse micelles, Polymer International 58(10) (2009) 1142-1147.
[11] H. Hao, Q. Ma, F. He, P. Yao, Doxorubicin and Fe3O4 loaded albumin nanoparticles with folic acid modified dextran surface for tumor diagnosis and therapy, Journal of Materials Chemistry B 2(45) (2014) 7978-7987.
[12] M. Mikhaylova, D.K. Kim, C.C. Berry, A. Zagorodni, M. Toprak, A.S.G. Curtis, M. Muhammed, BSA Immobilization on Amine-Functionalized Superparamagnetic Iron Oxide Nanoparticles, Chemistry of Materials 16(12) (2004) 2344-2354.
[13] Y. Gao, L. Liu, Z. Zhang, Mechanical performance of nano-CaCO3 filled polystyrene composites, Acta Mechanica Solida Sinica 22(6) (2009) 555-562.
[14] S.S.A.a.P.M.H. Furlan P Y, FTIR-ATR Study of pH Effects on Egg Albumin Secondary Structure, Spectrosc. Lett. 40 (2007) 475-482.
[15] S. Jana, S. Manna, A.K. Nayak, K.K. Sen, S.K. Basu, Carbopol gel containing chitosan-egg albumin nanoparticles for transdermal aceclofenac delivery, Colloids and Surfaces B: Biointerfaces 114(Supplement C) (2014) 36-44.
[16] Y.C. Chen, H.C. Yu, C.Y. Huang, W.L. Chung, S.L. Wu, Y.K. Su, Nonvolatile bio-memristor fabricated with egg albumen film, Scientific reports 5 (2015) 10022.
[17] S.P. Victor, W. Paul, M. Jayabalan, C.P. Sharma, Supramolecular hydroxyapatite complexes as theranostic near-infrared luminescent drug carriers, CrystEngComm 16(38) (2014) 9033-9042.
[18] S. Li, Y. Ma, X. Yue, Z. Cao, Z. Dai, One-pot construction of doxorubicin conjugated magnetic silica nanoparticles, New Journal of Chemistry 33(12) (2009) 2414-2418.
[19] S. Kayal, R.V. Ramanujan, Doxorubicin loaded PVA coated iron oxide nanoparticles for targeted drug delivery, Materials Science and Engineering: C 30(3) (2010) 484-490.
[20] B. Xia, W. Zhang, J. Shi, S.-j. Xiao, A novel strategy to fabricate doxorubicin/bovine serum albumin/porous silicon nanocomposites with pH-triggered drug delivery for cancer therapy in vitro, Journal of Materials Chemistry B 2(32) (2014) 5280-5286.
[21] J. Siepmann, N.A. Peppas, Modeling of drug release from delivery systems based on hydroxypropyl methylcellulose (HPMC), Advanced Drug Delivery Reviews 48(2) (2001) 139-157.
[22] K. Asghar, M. Qasim, G. Dharmapuri, D. Das, Investigation on a smart nanocarrier with a mesoporous magnetic core and thermo-responsive shell for co-delivery of doxorubicin and curcumin: a new approach towards combination therapy of cancer, RSC Adv. 7(46) (2017) 28802-28818.
[23] N.A. Wilson, M. Blenner, A. Guiseppi-Elie, Polyplex Formation Influences Release Mechanism of Mono- and Di-Valent Ions from Phosphorylcholine Group Bearing Hydrogels, Polymers 6(9) (2014).

[24] M.S. Al-Qubaisi, A. Rasedee, M.H. Flaifel, S.H. Ahmad, S. Hussein-Al-Ali, M.Z. Hussein, E.E. Eid, Z. Zainal, M. Saeed, M. Ilowefah, S. Fakurazi, N. Mohd Isa, M.E. El Zowalaty, Cytotoxicity of nickel zinc ferrite nanoparticles on cancer cells of epithelial origin, International journal of nanomedicine 8 (2013) 2497-508.
[25] M.S. Al-Qubaisi, A. Rasedee, M.H. Flaifel, S.H. Ahmad, S. Hussein-Al-Ali, M.Z. Hussein, Z. Zainal, F.H. Alhassan, Y.H. Taufiq-Yap, E.E. Eid, I.A. Arbab, B.A. Al-Asbahi, T.J. Webster, M.E. El Zowalaty, Induction of apoptosis in cancer cells by NiZn ferrite nanoparticles through mitochondrial cytochrome C release, International journal of nanomedicine 8 (2013) 4115-29.
[26] K. Qiu, C. He, W. Feng, W. Wang, X. Zhou, Z. Yin, L. Chen, H. Wang, X. Mo, Doxorubicin-loaded electrospun poly(l-lactic acid)/mesoporous silica nanoparticles composite nanofibers for potential postsurgical cancer treatment, Journal of Materials Chemistry B 1(36) (2013) 4601-4611.
[27] K.A. M Qasim, Dibakar Das, Facile Synthesis of Fe3O4 and multifunctional Fe3O4@Albumen Nanoparticles for Biomedical Application, AIP Proceedings 1832, (2017) 050116.
[28] Y.H. Zhenglin Li , Tingting Jiang , Kenneth A. Howard , Yonggang Li , Xuelei Fan , Ye Sun , Flemming Besenbacher , and Miao Yu Human-serum-albumincoated Prussian blue nanoparticles as pH-/thermotriggered drug-delivery vehicles for cancer thermochemotherapy, Part. Part. Syst. Charact., 33 (2016) 53–62

Section 4.3: Thermo-responsive multifunctional $mSiO_2$-$CaFe_2O_4$@P(Nipam-Aa) nanocomposites

In this section synthesis and characterization of mesoporous silica ($mSiO_2$) based multifunctional $mSiO_2$-CaF_2O_4@P(Nipam-Aa) NC will be discussed.

The use of smart and stimuli responsive drug nanocarrier in drug delivery is getting increasing attention [1]. Among them temperature responsive multifunctional mesoporous nanocarriers are most promising [2, 3]. Incorporation of magnetic nanoparticles (MNPs) within these smart nanocarriers not only provide magnetic targetability but also facilitate imaging and hyperthermia based heating ability [4]. Here, $CaFe_2O_4$ NP was used as MNP due to its biocompatible nature [5]. Namely, $mSiO_2$-$CaFe_2O_4$@P(Nipam-Aa)-1, and $mSiO_2$-$CaFe_2O_4$@P(Nipam-Aa)-2 nanocomposites have been prepared by in situ coating of polymer on bare $mSiO_2$ NPs and MPS modified $mSiO_2$ NPs respectively in the presence of oxidizer, cross linker and $CaFe_2O_4$ NPs. The prepared $mSiO_2$-$CaFe_2O_4$@P(Nipam-Aa) NC was characterized thoroughly for different physicochemical properties using various characterization techniques. Dox was loaded as model anticancer drug and loading and release behavior have been studied. Prepared nanocarrier was found to be biocompatible against the normal cells (RAW 264.7). Anticancer activity of Dox loaded nanocarrier ($mSiO_2$-$CaFe_2O_4$@P(Nipam-Aa)-Dox) was studied against Hela cells.

4.3.1 Synthesis of $mSiO_2$ NPs, MPS modified $mSiO_2$ NPs and $mSiO_2$-$CaFe_2O_4$ @P(Nipam-Aa) nanocomposites

First $mSiO_2$ and $CaFe_2O_4$ NPs were synthesized separately. $mSiO_2$ NPs was prepared by hydrolysis and condensation of TEOS in the presence of soft template of CTAB and subsequent removal of template by calcination. The formation mechanism of $mSiO_2$ NPs is shown in figure 3.1 of chapter 3. First aligned micellar rod of CTAB was obtained in the alkaline water. Addition of TEOS in reaction medium resulted in deposition of silica on the aligned micellar rod which acted as nucleation site. Further removal of CTAB by calcination resulted in the formation of mesoporous silica. The surface of $mSiO_2$ NPs was further modified with MPS to get -C=C bond on the surface which can covalently bind with P(Nipam-Aa) polymer [3]. Namely, $mSiO_2$-$CaFe_2O_4$@P(Nipam-Aa)-1, and $mSiO_2$-$CaFe_2O_4$@P(Nipam-Aa)-2 nanocomposites have been prepared using bare $mSiO_2$ NPs and MPS modified $mSiO_2$

NPs respectively. Formation process of $mSiO_2$-CF@P(Nipam-Aa) nanocomposite is shown in the figure 4.3.1. $mSiO_2$-$CaFe_2O_4$@P(NIPAM-Aa) nanocarrier were prepared by in situ coating of polymer on the surface of MPS modified mesoporous silica in the presence of oxidizer, crosslinker and $CaFe_2O_4$ NPs (CF NPs). The C=C bond on the surface of $mSiO_2$ nanoparticles facilitated the coating of P(NIPAM-Aa) on the silica surface via the covalent bonding. Stirring of MPS modified $mSiO_2$ NPs, $CaFe_2O_4$ NPs, NIPAM, Acrylic acid (Aa), MBA and SDS resulted formation of homogeneous mixture in water. Addition of oxidizer (KPS) initiated the copolymerization of NIPAM and Aa on the surface of $mSiO_2$ NPs [2, 4].

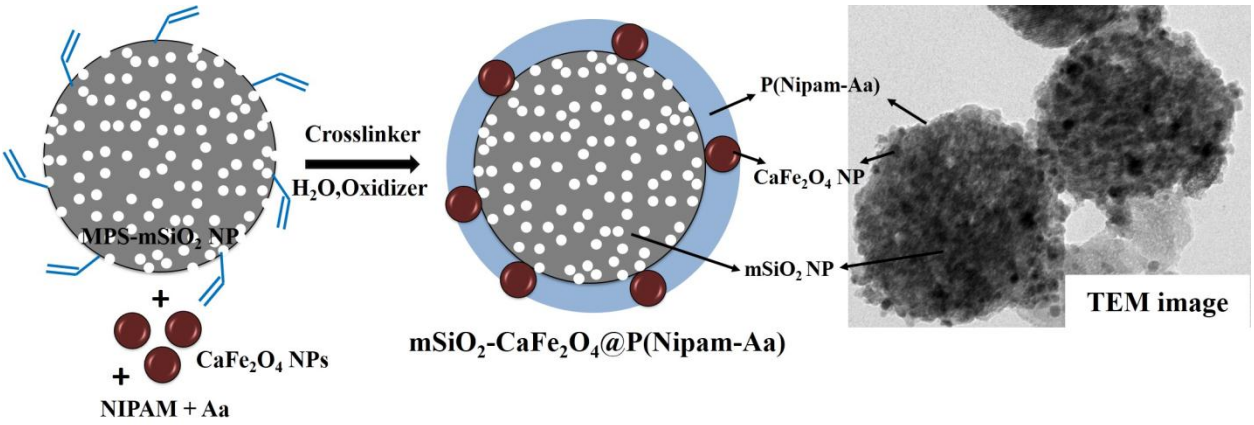

Figure 4.3.1. Schematic illustration of the formation process of $mSiO_2$-$CaFe_2O_4$@P(Nipam-Aa) nanocomposite.

4.3.2 Crystalline structure (wide angle XRD)

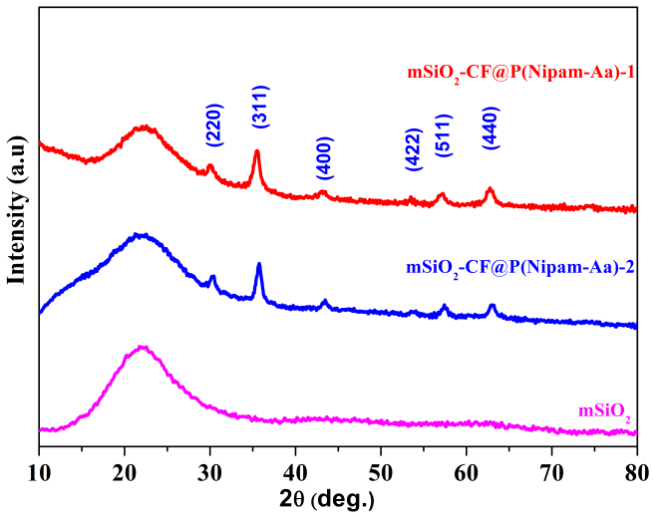

Figure 4.3.2. XRD pattern of $mSiO_2$-$CaFe_2O_4$@P(Nipam-Aa)-1, $mSiO_2$-$CaFe_2O_4$@P(Nipam-Aa)-2 nanocomposite and $mSiO_2$ NPs.

The crystalline structure as well as formation of $mSiO_2$-$CaFe_2O_4$@P(Nipam-Aa)-1 and $mSiO_2$-$CaFe_2O_4$@P(Nipam-Aa)-2 nanocomposite was confirmed by x-ray diffraction (XRD). Figure 4.3.2 shows XRD pattern of $mSiO_2$-$CaFe_2O_4$@P(Nipam-Aa)-1, $mSiO_2$-$CaFe_2O_4$@P(Nipam-Aa)-2 nanocomposite and $mSiO_2$ NPs. XRD pattern of $mSiO_2$ NPs shows amorphous nature of $mSiO_2$ NPs with a broad peak at 23°. No sharp diffraction peaks were observed in case of $mSiO_2$ NPs. XRD pattern of $mSiO_2$-$CaFe_2O_4$@P(Nipam-Aa)-1 and $mSiO_2$-$CaFe_2O_4$@P(Nipam-Aa)-2 nanocomposite showed similar diffraction pattern with a broad peak at 23° and many sharp diffraction peaks at 30°, 36°, 43°, 53°, 57°, and 63°. The broad peak and sharp diffraction peaks were attributed to the presence of amorphous silica and polycrystalline $CaFe_2O_4$ NPs respectively [6]. The sharp diffraction peaks of (220), (311), (400), (422), (511) and (440) planes at 2Θ 30°, 36°, 43°, 53°, 57°, and 63° respectively can be assigned to the Fe_3O_4 type spinel cubic $CaFe_2O_4$ NPs (JCPDS cards No. 88-315). Appearance of all characteristic peaks of $CaFe_2O_4$ NPs and broad amorphous peak of $mSiO_2$ NPs in XRD pattern of $CaFe_2O_4$@P(Nipam-Aa)-1, $mSiO_2$-$CaFe_2O_4$@P(Nipam-Aa)-2 nanocomposite confirms the successful formation of the sample [6]. No characteristic diffraction peaks of P(Nipam-Aa) have been observed in the XRD pattern of $CaFe_2O_4$@P(Nipam-Aa)-1 and $mSiO_2$-$CaFe_2O_4$@P(Nipam-Aa)-2 due to its amorphous nature. The crystallite size of $CaFe_2O_4$ NPs was found to be 14 nm.

4.3.3 Low angle XRD analysis

Mesoporous structure of prepared samples was studied using Low angle XRD, TEM and HRTEM analysis. Figure 4.3.3 shows low angle XRD pattern of $mSiO_2$ NPs, and $mSiO_2$-$CaFe_2O_4$@P(Nipam-Aa)-1, $mSiO_2$-$CaFe_2O_4$@P(Nipam-Aa)-2 nanocomposite. Three diffraction peaks in the 2 Θ range of 2-10° were observed in all the samples which can be assigned to the (100), (110) and (200) planes of highly ordered 2D hexagonal symmetry of meso-structure of $mSiO_2$ [3]. Thus, appearance of these characteristic peaks of mesostructured suggested the successful formation of mesoporous silica as well as successful formation of mesoporous nanocomposite. Appearance of characteristic peaks of mesoporous $mSiO_2$ NPs in the low angle XRD pattern of nanocomposite suggested that mesoporous nature of $mSiO_2$ NPs does not disturbed due to the coating of polymer. The pore diameter is generally estimated using (100) d spacing. The d-spacing of (100) plane were found to be 3.6, 3.4 and 3.4 nm for $mSiO_2$ NPs, $mSiO_2$-$CaFe_2O_4$@P(Nipam-Aa)-1, and $mSiO_2$-$CaFe_2O_4$@P(Nipam-Aa)-2 nanocomposite respectively.

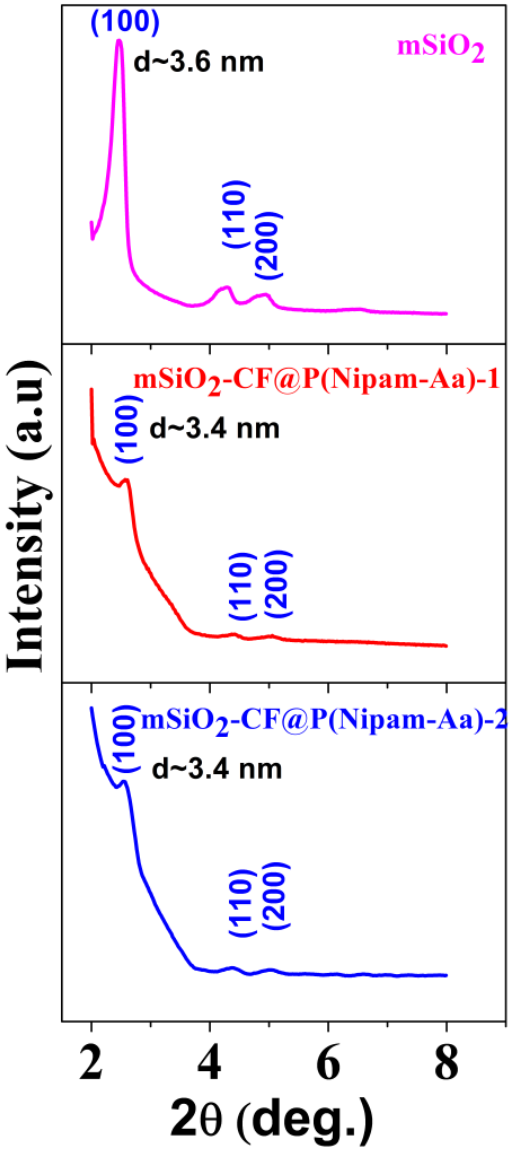

Figure 4.3.3. Low angle XRD pattern of $mSiO_2$ NPs, and $mSiO_2$-$CaFe_2O_4$@P(Nipam-Aa)-1, $mSiO_2$-$CaFe_2O_4$@P(Nipam-Aa)-2 nanocomposite.

4.3.4) TEM and HRTEM analysis

Particles size, morphology and mesoporous structure of $mSiO_2$ NPs, $mSiO_2$-$CaFe_2O_4$@P(Nipam-Aa)-1, $mSiO_2$-$CaFe_2O_4$@P(Nipam-Aa)-2 nanocomposite were studied by TEM and FESEM analysis. TEM images at different magnification of $mSiO_2$ NP are shown in figure 4.3.4 (a-c). Particles size of $mSiO_2$ NP is found to be ~250 nm with hexagonal shape. Particles are found to be uniform in size and shape. Mesoporous nature of the $mSiO_2$ NP can very clearly been observed in the TEM images. Pore and pore channels are highly ordered in nature. Figure 4.3.4 (c) (in which particles pores channels were parallel to the electron bean) shows presence of hexagonally arranged pores of diameter ~3.7 nm. Thus, it can be inferred

that these hexagonally arranged pore channels are formed via the hexagonally aligned micellar rod and its subsequent removal. Presence of hexagonally arranged pore channels were also confirmed by FFT and IFFT analysis. FFT diffraction pattern clearly show a characteristic diffraction of hexagonal arrangement. In addition, the IFFT image of selected region (bottom of (c)) also shows presence of ordered pore in better and with more clarity. Thus, TEM analysis also confirmed formation of mesoporous silica nanoparticles.

Coating of polymer on $mSiO_2$ NP and embedding of CF NPs in polymer layer were confirmed by TEM analysis. TEM images at different magnification of $mSiO_2$-$CaFe_2O_4$@P(Nipam-Aa)-1 nanocomposite are shown in figure 4.3.5 (a-f). It can be observed that a thin layer of polymer is coated around $mSiO_2$ NP and $CaFe_2O_4$ NPs (CF NPs) can also be seen embedded in the surrounding polymer layer. The thickness of the film is found to 10-20 nm and not uniform in nature. The distribution of $CaFe_2O_4$ NPs on $mSiO_2$ NP surface was observed to be random in nature. The non-uniformity of polymer layer and particles distribution may be due to the use of non-MPS modified $mSiO_2$ NPs. Particles size of $CaFe_2O_4$@P(Nipam-Aa)-1 nanocomposite is found to be ~280 nm with spherical to hexagonal in shape. Particles are found to be nearly uniform in size and shape. Mesoporous nature of the $mSiO_2$ NP did not destroyed due to coating of polymer (and coating processes) and its mesoporous channels can very clearly be observed in the TEM images (Fig. 4.3.5c-d). Figure 4.3.5 (c-d) shows $mSiO_2$ NP pores channels perpendicular to the electron beam. Pore channels were found highly ordered in nature with d spacing of ~3.5 nm. Embedding of $CaFe_2O_4$ NPs of 10-15 nm in polymer coating on the surface of $mSiO_2$ NPs is shown in (e). HRTEM analysis of these embedded NPs confirmed that these are $CaFe_2O_4$ NPs as its d spacing is well matching with d spacing of $CaFe_2O_4$ (Fig (f)). The d spacing of particle was found to be ~0.3 nm which was indexed to the (220) plane of spinel cubic $CaFe_2O_4$ NPs (IFFT image shown in inset of (f)). The polymer coated around the $mSiO_2$ and $CaFe_2O_4$ NPs are found to be amorphous in nature as it did not show any ordering in HRTEM image (f). Thus, TEM and HRTEM analysis show that $mSiO_2$ NPs was coated with polymer and embedded with $CaFe_2O_4$ NPs so it confirmed the formation of $mSiO_2$-$CaFe_2O_4$@P(Nipam-Aa)-1 nanocomposite. The further confirmation about the presence of polycrystalline $CaFe_2O_4$ NPs in nanocomposite was done though SAED analysis. The indexed SAED pattern of $mSiO_2$-$CaFe_2O_4$@P(Nipam-Aa)-1 nanocomposite is shown in inset of (e). Appearance of characteristic ring pattern of spinel cubic system with some blur region (around center) suggested presence of polycrystalline $CaFe_2O_4$ NPs and amorphous silica and polymer in nanocomposite. TEM images at different

magnification of $mSiO_2$-$CaFe_2O_4$@P(Nipam-Aa)-2 nanocomposite (prepared using MPS modified $mSiO_2$ NPs) are shown in figure 4.3.6 (a-c). It can be observed that polymer is well coated around $mSiO_2$ NP and $CaFe_2O_4$ NPs (~10-15 nm) are uniformly embedded in the surrounding polymer layer. It was also observed that density of $CaFe_2O_4$ NPs and coating of polymer on the surface of $mSiO_2$ NPs is more as compare to $mSiO_2$-$CaFe_2O_4$@P(Nipam-Aa)-1. Particles size of $CaFe_2O_4$@P(Nipam-Aa)-2 nanocomposite is found to be ~330 nm with spherical in shape. Particles were found to be uniform in size and shape. In this case also, mesoporous nature of the $mSiO_2$ NP did not destroyed due to coating of polymer and its mesoporous channels with d spacing of 3.5 nm can very clearly be seen in the TEM images (inset of Fig. 4.3.6b). TEM micrograph of a single $mSiO_2$-$CaFe_2O_4$@P(Nipam-Aa)-2 nanocomposite showing coating of polymer on the surface of $mSiO_2$ NPs is shown in (d). Appearance of rough and wavy surface of nanocomposite than bare silica is due to polymer coating and presence of $CaFe_2O_4$ NPs. Light grew materials on silica is polymer layer. HRTEM images (e & f) of embedded $CaFe_2O_4$ NPs with corresponding IFFT image of selected region of HRTEM image (inset of f) confirmed that the embedded particles of size ~10-15 nm are $CaFe_2O_4$ NPs. HRTEM and its IFFT very clearly shows presence of crystalline $CaFe_2O_4$ NPs on the surface of $mSiO_2$ NPs. The d spacing of particle was found to be ~0.25 nm which was indexed to the (311) plane of spinel cubic CF NPs (IFFT image shown in inset of (f)). The thickness of the film is found to 20-30 nm. The distribution of $CaFe_2O_4$ NPs on $mSiO_2$ NP surface was observed to be uniform in nature than $CaFe_2O_4$@P(Nipam-Aa)-1 nanocomposite. Thus, TEM and HRTEM analysis confirmed successful formation of polymer coated and $CaFe_2O_4$ NPs embedded $mSiO_2$ NPs ($mSiO_2$-$CaFe_2O_4$@P(Nipam-Aa)-1 nanocomposite). Figure 4.3.7 shows HRTEM images of surface pore channels of $mSiO_2$ NPs (a), $mSiO_2$-$CaFe_2O_4$@P(Nipam-Aa)-1(b), and $mSiO_2$-$CaFe_2O_4$@P(Nipam-Aa)-2 nanocomposite (b). In case of nanocomposites coating of polymer can clearly be seen (b and c) however the surface around pore channels of bare $mSiO_2$ NPs are clear and smoother. The surface of nanocomposites is relatively rough due to coating of polymer.

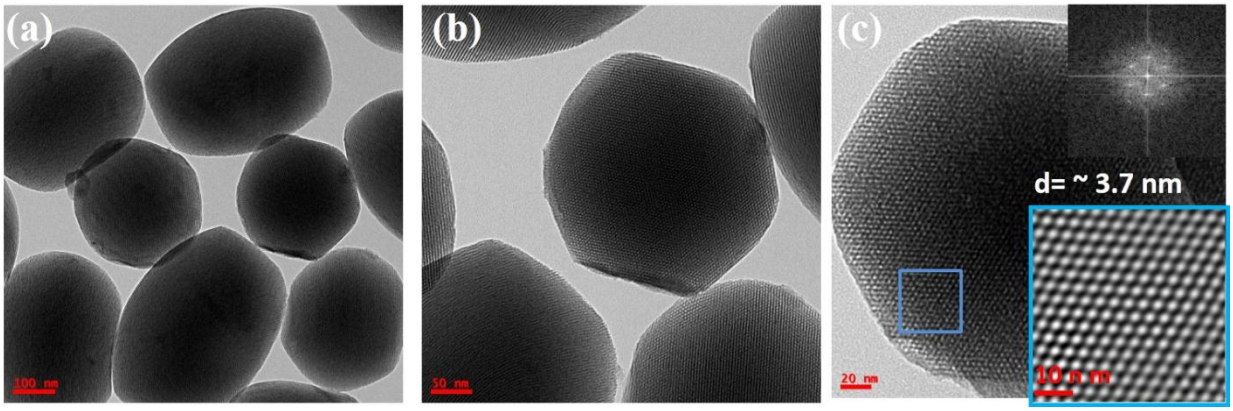

Figure 4.3.4. TEM micrograph of $mSiO_2$ NPs at difference magnification (a-c). HRTEM micrograph of a particles with incident electron beam perpendicular to pores channels of $mSiO_2$ (c). Top and bottom inset image of figure (c) shows FFT and IFFT images of selected region.

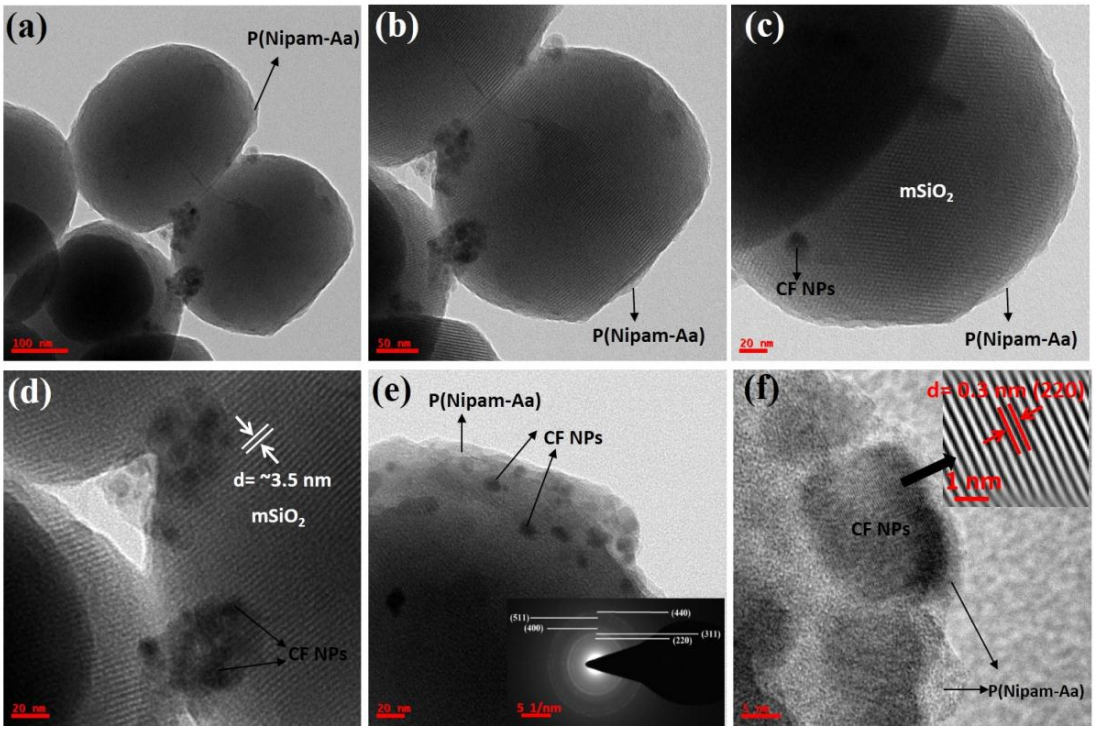

Figure 4.3.5. TEM micrographs at different magnification (low to high) of $mSiO_2$-$CaFe_2O_4$@P(Nipam-Aa)-1 nanocomposite (a-c). Presence of $CaFe_2O_4$ NPs in polymer coating on the surface of $mSiO_2$ NPs is shown in (d and e). HRTEM image of embedded CF NPs with corresponding IFFT image (f). indexed SAED pattern of $mSiO_2$-$CaFe_2O_4$@P(Nipam-Aa)-1 nanocomposite is shown in inset of (e).

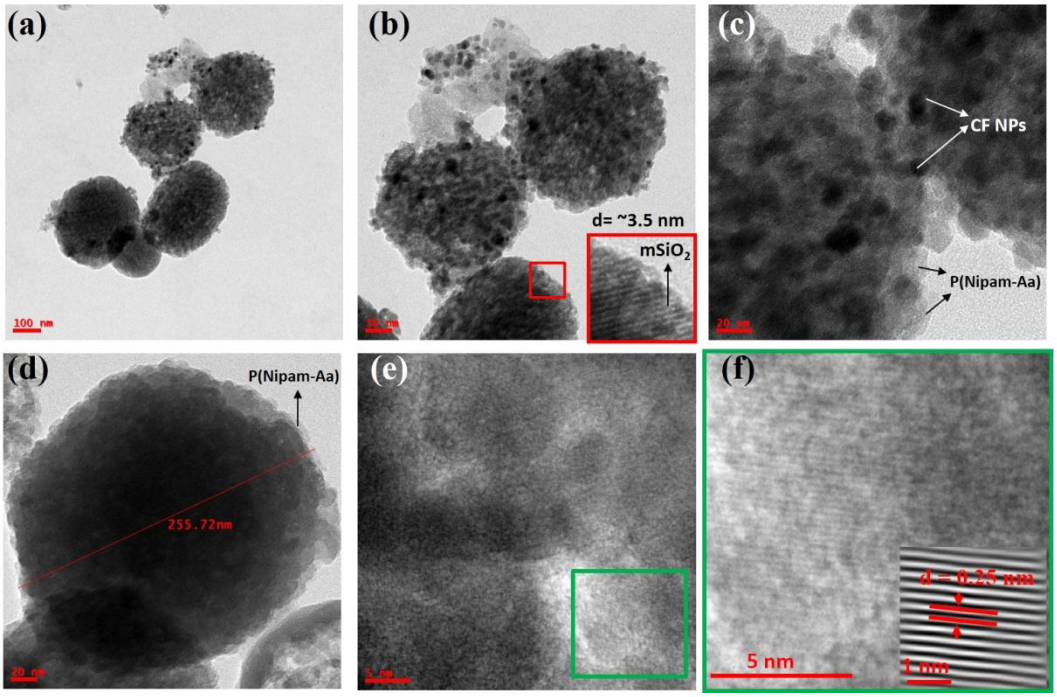

Figure 4.3.6. TEM micrographs at different magnification (low to high) of $mSiO_2$-$CaFe_2O_4$@P(Nipam-Aa)-2 nanocomposite (a-c). TEM micrograph of a single $mSiO_2$-$CaFe_2O_4$@P(Nipam-Aa)-2 nanocomposite showing coating of polymer on the surface of $mSiO_2$ NPs (d). HRTEM images (e & f) of embedded CF NPs with corresponding IFFT image of selected region of HRTEM image (inset of f).

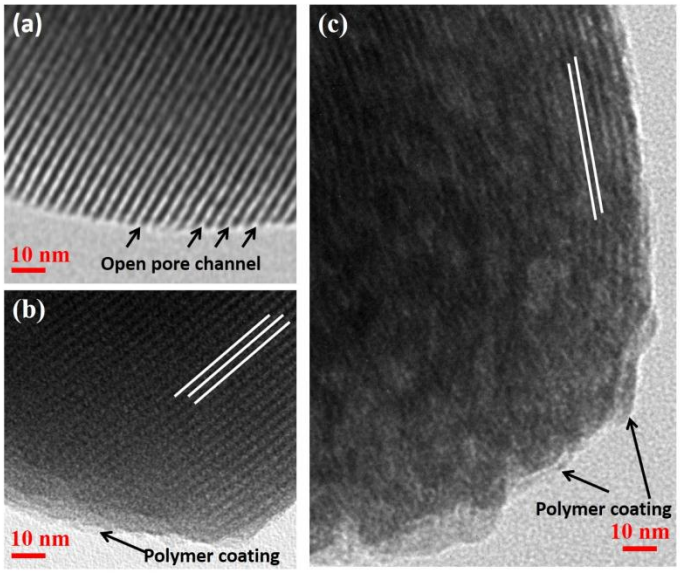

Figure 4.3.7. HRTEM images showing surface of $mSiO_2$ NPs, $mSiO_2$-$CaFe_2O_4$@P(Nipam-Aa)-1, and $mSiO_2$-$CaFe_2O_4$@P(Nipam-Aa)-2 nanocomposite.

4.3.5 FESEM analysis

Figure 4.3.8 shows FESEM micrographs at different magnifications of $mSiO_2$ NPs (a-b), $mSiO_2$-$CaFe_2O_4$@P(Nipam-Aa)-1 (c-d), and $mSiO_2$-$CaFe_2O_4$@P(Nipam-Aa)-2(e-f)

nanocomposite. Particles size, morphology and surface topography of the $mSiO_2$-$CaFe_2O_4$@P(Nipam-Aa)-1 (c-d), and $mSiO_2$-$CaFe_2O_4$@P(Nipam-Aa)-2 have been examined. Particles size of $mSiO_2$ NP is found to be ~250 nm with spherical to hexagonal shape. Particles are found to be uniform and monodispersed in size and shape. In case of bare $mSiO_2$ NPs the surface of the particles is found to be smooth. It was observed from the FESEM images of $mSiO_2$-$CaFe_2O_4$@P(Nipam-Aa)-1 NC that the embedding of $CaFe_2O_4$ NPs is not uniform and no much differences in surface structure than bare $mSiO_2$ NP was observed. In case of $mSiO_2$-$CaFe_2O_4$@P(Nipam-Aa)-2 NC well embedding of $CaFe_2O_4$ NPs on the surface of $mSiO_2$ NP was observed. Particles were found to be nearly spherical in shape with monodispersed and uniform in size. Rough surface topography of the $mSiO_2$-$CaFe_2O_4$@P(Nipam-Aa)-2 NC than bare silica is due to polymer coating and presence of $CaFe_2O_4$ NPs. Presence of embedded $CaFe_2O_4$ NP of very small size (~10-15 nm) can be seen in the inset of figure 4.3.8 (e). Particles size of the $mSiO_2$-$CaFe_2O_4$@P(Nipam-Aa)-1 and $mSiO_2$-$CaFe_2O_4$@P(Nipam-Aa)-2 NC were found to be in between 280-350 nm.

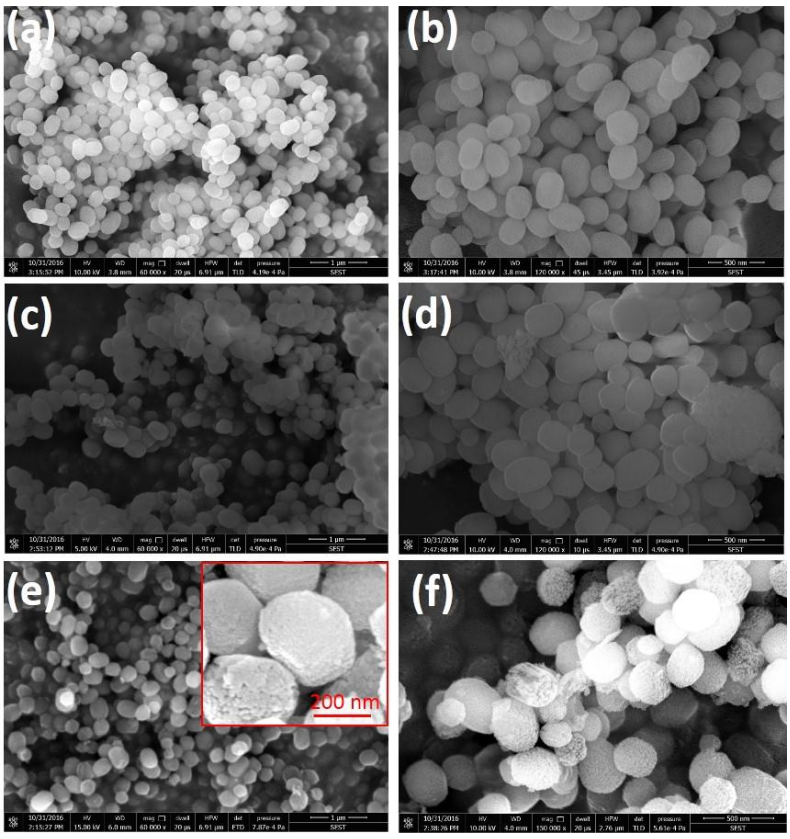

Figure 4.3.8. FESEM micrographs at different magnifications of $mSiO_2$ NPs (a-b), $mSiO_2$-$CaFe_2O_4$@P(Nipam-Aa)-1 (c-d), and $mSiO_2$-$CaFe_2O_4$@P(Nipam-Aa)-2(e-f) nanocomposite. Inset of (e) shows surface topography of $mSiO_2$-$CaFe_2O_4$@P(Nipam-Aa)-2.

4.3.6 TGA and DTG analysis

Thermal properties of nanocomposite and presence of polymer on the surface of mesoporous silica were analyzed by TGA and DTG analysis. Thermal degradation behavior of $mSiO_2$ NPs, $mSiO_2$-$CaFe_2O_4$@P(Nipam-Aa)-1, and $mSiO_2$-$CaFe_2O_4$@P(Nipam-Aa)-2 nanocomposite are shown in figure 4.3.9. Weight loss of ~5-10 % from the all sample below 200 ^oC can be attributed to the loss of physically adsorbed water molecules. In case of $mSiO_2$ NPs minimum total weight loss (~17%) was observed and this can be attributed to the loss of water and hydroxyl groups from the silica NPs. Both the nanocomposite has shown ~ 17 % weight upto 350 ^oC which could be due to the loss of water and different function groups. $mSiO_2$-$CaFe_2O_4$@P(Nipam-Aa)-1 nanocomposites shows a slow degradation behavior upto 350 ^oC which became slightly fast on further increase in the temperature. The $mSiO_2$-$CaFe_2O_4$@P(Nipam-Aa)-1 nanocomposites has shown ~14% weight loss in between 350-1000 ^oC. In case of $mSiO_2$-$CaFe_2O_4$@P(Nipam-Aa)-2 nanocomposites a slow degradation behavior was observed upto 350 ^oC and there after a rapid degradation was noticed upto 600 ^oC. The $mSiO_2$-$CaFe_2O_4$@P(Nipam-Aa)-2 nanocomposites has shown ~36.5% weight loss in between 350-1000 ^oC. For both the nanocomposite weight loss in between ~350-1000 ^oC could be attributed to the loss of P(Nipam-Aa) polymer. The degradation temperature of P(Nipam-Aa) polymer was found to ~400 ^oC. In case of $CaFe_2O_4$@P(Nipam-Aa)-1 and $mSiO_2$-$CaFe_2O_4$@P(Nipam-Aa)-2 nanocomposite the total weight loss was found to be 31 % and 53.5 %. Relatively more weight loss in case of $mSiO_2$-$CaFe_2O_4$@P(Nipam-Aa)-2 nanocomposite can be attributed to the presence of more amount polymer due to its favored coating via MPS modified $mSiO_2$ NPs than bare $mSiO_2$ NPs. The weight % of P(Nipam-Aa) in $mSiO_2$-$CaFe_2O_4$@P(Nipam-Aa)-1 and $mSiO_2$-$CaFe_2O_4$@P(Nipam-Aa)-2 nanocomposite were estimated to be ~14 % and 36% respectively. DTG result of $mSiO_2$-$CaFe_2O_4$@P(Nipam-Aa)-2 nanocomposite is shown in figure 4.3.10 which shows a major degradation peak of centered at 405 ^oC. The peak at ~405 ^oC can be attributed to the loss of P(Nipam-Aa) from $mSiO_2$-$CaFe_2O_4$@P(Nipam-Aa)-2 nanocomposite. Peaks below 200 ^oC can be due to the loss of water molecules.

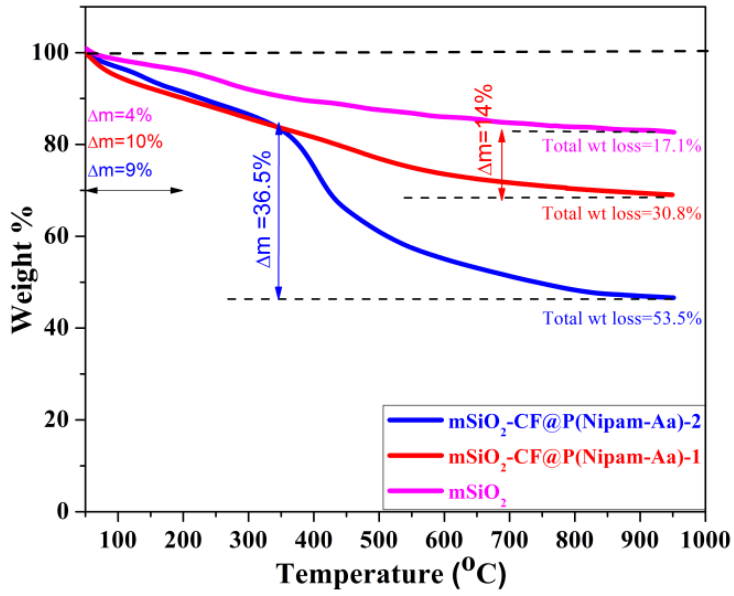

Figure 4.3.9. TGA degradation behavior of $mSiO_2$ NPs, $mSiO_2$-$CaFe_2O_4$@P(Nipam-Aa)-1, and $mSiO_2$-$CaFe_2O_4$@P(Nipam-Aa)-2 nanocomposite.

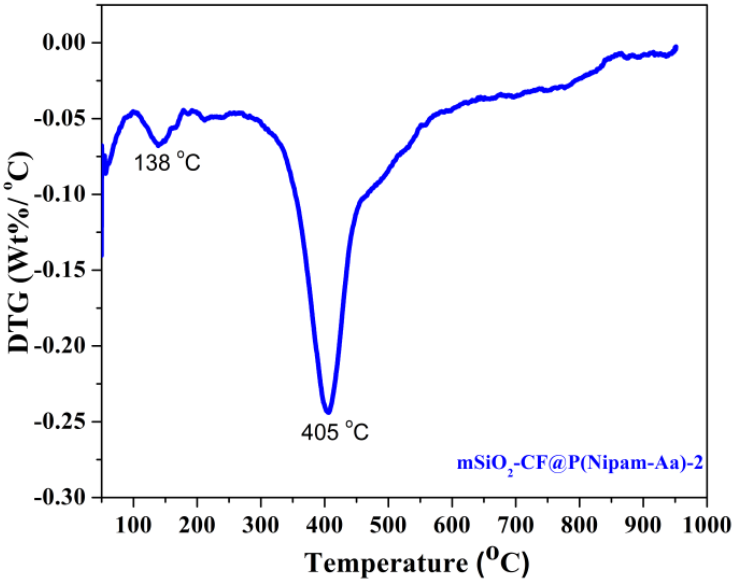

Figure 4.3.10. DTG result of $mSiO_2$-$CaFe_2O_4$@P(Nipam-Aa)-2 nanocomposite

4.3.7 LCST determination using DSC

Lower critical solution temperature (LCST) of pure P(NIPAM) and $mSiO_2$-$CaFe_2O_4$@P(Nipam-Aa)-2 was analyzed by DSC measurement and obtained DSC curve are shown in the figure 4.3.11. The LCST of thermos-responsive polymer shows its phase transition temperature as polymer convert to hydrophobic above LCST and become hydrophilic below LCST. Having LCST below body temperature pure PNIPAM is not suitable for

nanocarrier development [3]. The LCST of PNIPAM can be enhanced by addition suitable hydrophilic group such as carboxylic group [7]. Pure P(NIPAM) has showed a sharp endothermic peak at about 33 ^{o}C which is characteristic of linear PNIPAM. In Case of $mSiO_2$-$CaFe_2O_4$@P(Nipam-Aa)-2, the endothermic phase transition was observed at about 37.5 ^{o}C. However, the endothermic peak in case of nanocomposite is not much sharp which may due to the less amount of polymer $mSiO_2$-$CaFe_2O_4$@P(Nipam-Aa)-2 nanocomposite. Thus, The LCST of pure linear P(NIPAM) and $mSiO_2$-$CaFe_2O_4$@P(Nipam-Aa)-2 were found to 33 and 37.5 ^{o}C respectively. The observed endothermic peaks can be attributed to the breakage of hydrogen bond between polymer and water molecules [8]. This increase in the LCST is due the incorporation of carboxyl group (acrylic acid) in the PNIPAM chains [2].

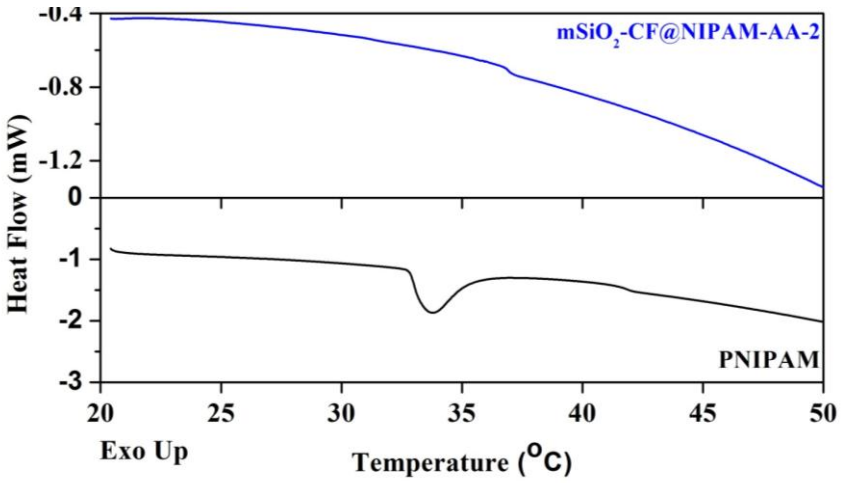

Figure 4.3.11. DSC curve of PNIPAM and $mSiO_2$-$CaFe_2O_4$@P(Nipam-Aa)-2.

4.3.8 VSM analysis

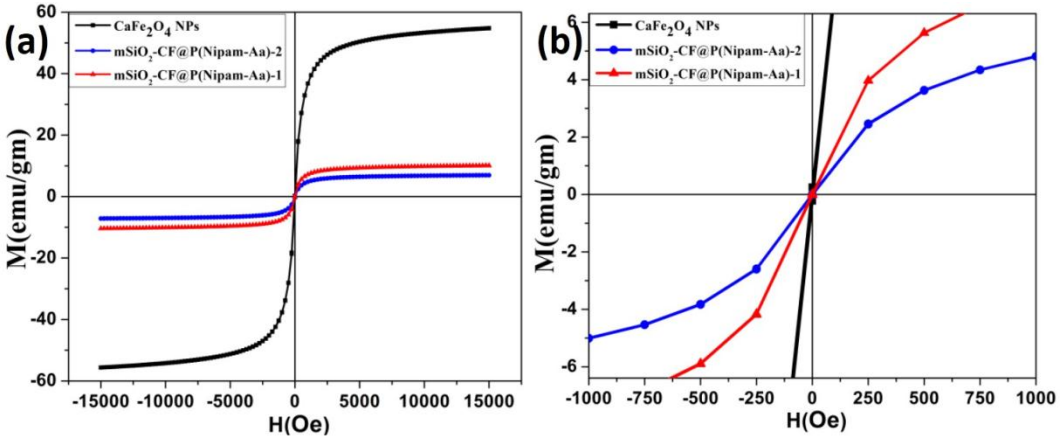

Figure 4.3.12. (a) M-H curve of $CaFe_2O_4$ NPs, $mSiO_2$-$CaFe_2O_4$@P(Nipam-Aa)-1 and $mSiO_2$-$CaFe_2O_4$@P(Nipam-Aa)-2 with corresponding enlarge (b) M-H curve.

Magnetic properties of $CaFe_2O_4$ NPs, $mSiO_2$-$CaFe_2O_4$@P(Nipam-Aa)-1 and $mSiO_2$-$CaFe_2O_4$@P(Nipam-Aa)-2 were studied by VSM analysis and obtained Room Temperature M-H curves are shown figure 4.3.12(a-b). All the samples were found to be superparamagnetic nature with the negligible coercivity and Mr values. Ms value of $CaFe_2O_4$ NPs, $mSiO_2$-$CaFe_2O_4$@P(Nipam-Aa)-1 and $mSiO_2$-$CaFe_2O_4$@P(Nipam-Aa)-2 were found to be ~54.7, ~10 and ~7 emu/g respectively. Enlarge M-H graph is shown in figure 4.3.12(b) to show M_R and coercivity values. The coercivity values of $CaFe_2O_4$ NPs was found to be 3.2 Oe where as in case of nanocomposites ($mSiO_2$-$CaFe_2O_4$@P(Nipam-Aa)-1 and $mSiO_2$-$CaFe_2O_4$@P(Nipam-Aa)-2), it was found to be in between ~1.41 to 1.44 Oe. This slight decrease in the coercivity may be attributed to the discrete distribution of MNPs in polymer on the surface of $mSiO_2$ NPs which allows them for very easy magnetization and demagnetization. The Ms value of nanocarrier represent its magnetic targeting ability and it is proportionally dependent on the amount of magnetic component in the nanocarriers. In the present case, the obtained Ms values of the prepared $mSiO_2$-$CaFe_2O_4$@P(Nipam-Aa)-1 and $mSiO_2$-$CaFe_2O_4$@P(Nipam-Aa)-2 nanocomposites are sufficient for drug delivery applications. The M_R value of $CaFe_2O_4$ NPs, $mSiO_2$-$CaFe_2O_4$@P(Nipam-Aa)-1 and $mSiO_2$-$CaFe_2O_4$@P(Nipam-Aa)-2 were found to be 0.23, 0.025 and 0.014 emu/g, respectively. The superparamagnetic nature of samples can be attributed to the very small size of $CaFe_2O_4$ NP.

4.3.9 FTIR analysis

Further formation of $mSiO_2$-$CaFe_2O_4$@P(Nipam-Aa)-2 nanocomposite and loading Dox were confirmed by FTIR analysis. Figure 4.3.13(a) shows FTIR spectra of $mSiO_2$-$CaFe_2O_4$@P(Nipam-Aa)-2 and $mSiO_2$-$CaFe_2O_4$@P(Nipam-Aa)-Dox NCs. FTIR spectra of $mSiO_2$-$CaFe_2O_4$@P(Nipam-Aa)-2 nanocomposite shows presence of characteristic peak of $CaFe_2O_4$ NPs, SiO_2, and P(Nipam-Aa) which confirm successful formation of $mSiO_2$-$CaFe_2O_4$@P(Nipam-Aa)-2 NC. Band at 592 cm^{-1} in FTIR spectra of $mSiO_2$-$CaFe_2O_4$@P(Nipam-Aa)-2 NC can be attributed to the $CaFe_2O_4$ NPs whereas bands at 464, 807, and 1080 cm^{-1} were arisen from silica matrix [9]. Characteristic bands of polymer (P(Nipam-Aa)) were observed at 1720 cm^{-1} (stretching of C=O), 1640 cm^{-1} (stretching vibration of C=O from amide I), 1542 cm^{-1} (secondary amide N-H), and 1406 cm^{-1} (deformation of methyl group $(CH_3)_2$) [7]. Appearance of new characteristic band of Dox in the FTIR spectra of $CaFe_2O_4$@P(Nipam-Aa)-Dox NC confirmed loading of Dox in nanocomposite. In other word, FTIR spectra of Dox loaded nanocomposites shows all

characteristic bands of nanocomposites with new characteristic bands of Dox. It was observed that the band at 1720 cm^{-1} of blank $CaFe_2O_4$@P(Nipam-Aa)-become relatively intense and broader for the $CaFe_2O_4$@P(Nipam-Aa)-Dox NC, which is due to the coupling with the band of Dox at 1730 cm^{-1}. Similar observation was made for the band at 1640 which is due to the band of Dox at 1640 cm^{-1}(figure 4.3.13b). Characteristic bands of Dox were observed at 1730 cm^{-1} (stretching of carbonyl group at keto position), 1640 cm^{-1} (C=O), 1620 cm^{-1} (N-H), and 1583 cm^{-1} (stretching vibration of two carbonyl of anthracene ring) [10]. The other band around 2900 and 3400 cm^{-1} in both the samples can be assigned to the C-H and O-H (with contribution of N-H) respectively. The intensity of these two bands has also increased in case of Dox loaded sample due the presence of more corresponding (-NH_2, -OH) groups in the sample. Thus, FTIR analysis also suggest successful formation of nanocomposites as well as loading of Dox in nanocomposite.

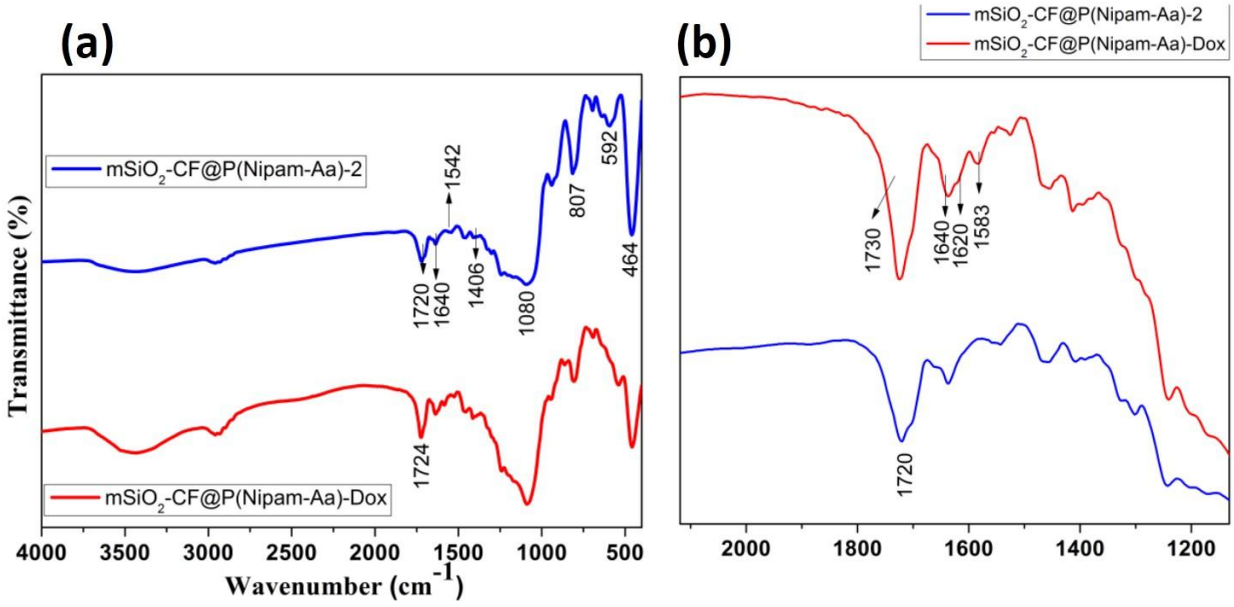

Figure 4.3.13. (a) FTIR spectra of $mSiO_2$-$CaFe_2O_4$@P(Nipam-Aa)-2 nanocomposite and $mSiO_2$-$CaFe_2O_4$@P(Nipam-Aa)-Dox NC. Figure (b) shows enlarge FTIR spectra of $mSiO_2$-$CaFe_2O_4$@P(Nipam-Aa)-2 nanocomposite and $mSiO_2$-$CaFe_2O_4$@P(Nipam-Aa)-Dox NC with a normalized transmittance.

4.3.10 Dox loading and release study

Figure 4.3.14. (a) shows UV-Vis absorption spectra of Dox before loading and Dox remained in supernatant. The inset of (a) shows individual UV-Vis absorption spectra of free Dox in supernatant. Drastic reduction in the absorption intensity of Dox in supernatant than initial Dox suggest very high loading efficiency. Loading capacity and loading efficiency were

found to be ~6 and 98%. Figure 4.3.14(b) shows UV-Vis absorption spectra of $mSiO_2$-$CaFe_2O_4$@P(Nipam-Aa)-2 nanocomposite and $mSiO_2$-$CaFe_2O_4$@P(Nipam-Aa)-Dox NC. Both the samples show similar absorption spectra except an additional peak of Dox in case of $mSiO_2$-$CaFe_2O_4$@P(Nipam-Aa)-Dox NC. Appearance of characteristic absorption peak of Dox at ~500 nm wavelength in the UV-Vis absorption spectra of $mSiO_2$-$CaFe_2O_4$@P(Nipam-Aa)-Dox NC also confirmed loading of Dox in $mSiO_2$-$CaFe_2O_4$@P(Nipam-Aa)-NC. Electrostatic attraction between negative charges of nanocarriers (OH and Si-O^- on SiO_2, COOH on polymer) and positive charge of Dox(NH_2) at loading pH 7.4 could have facilitated the excellent loading of Dox in nanocomposites [11] [12] [13] [10].

In vitro release study Dox from $mSiO_2$-$CaFe_2O_4$@P(Nipam-Aa)-Dox NC were carried out at below and above LCST temperature in PBS medium. Figure 4.3.15 (a) and (b) show time dependent UV-Vis absorption spectra of Dox in release medium released at 25 ^oC and 40 ^oC, respectively. Increase in the absorption intensity of Dox peak with time can be observed in both the cases. In vitro Dox release profiles from $mSiO_2$-$CaFe_2O_4$@P(Nipam-Aa)-Dox NC are shown in figure 4.3.15 (c). A sustained and temperature dependent release of Dox was observed which is very important for controlled drug delivery applications. It was observed that the Dox release is approximately twofold higher above LCST temperature. For the first 24 hours, 16 % and 9 % Dox were observed for the 40 and 25 ^oC respectively. After 60 hours of incubation, only ~28 % and ~14 % Dox were observed for the 40 and 25 ^oC respectively which shows sustained release behavior. Figure 4.3.15 (d) Temperature dependent Dox release mechanism from $mSiO_2$-$CaFe_2O_4$@P(Nipam-Aa)-Dox NC. Above LCST, the thermos-responsive polymer on the surface of $mSiO_2$ get shrink leaving the pores of mSiO2 opened, which allow release of loaded Dox to release medium and below LCST polymer remains in swollen state which keeps the pores closed [4].

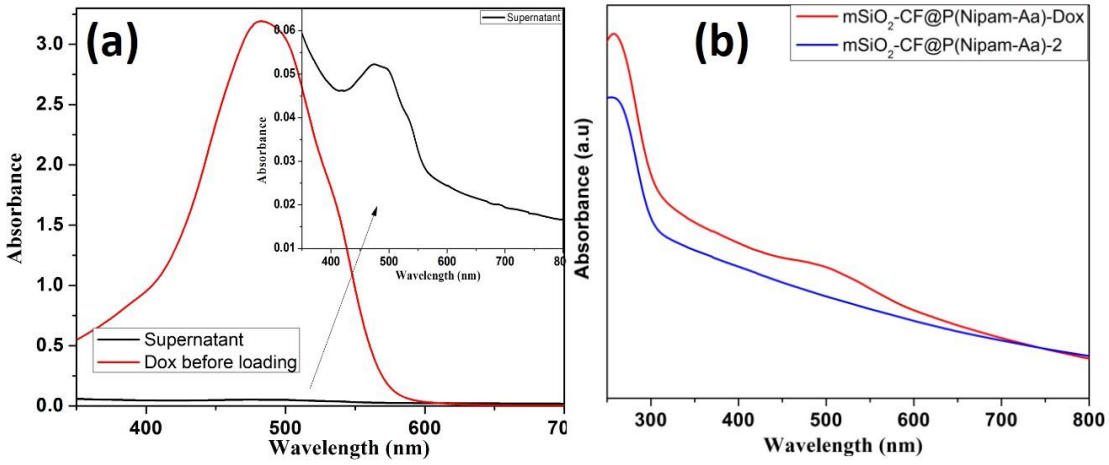

Figure 4.3.14. (a) UV-Vis absorption spectra of both Dox before loading and free Dox in supernatant. The inset of (a) shows individual UV-Vis absorption spectra of free Dox in supernatant. (b) UV-Vis absorption spectra of $mSiO_2$-$CaFe_2O_4$@P(Nipam-Aa)-2 nanocomposite and $mSiO_2$-$CaFe_2O_4$@P(Nipam-Aa)-Dox NC.

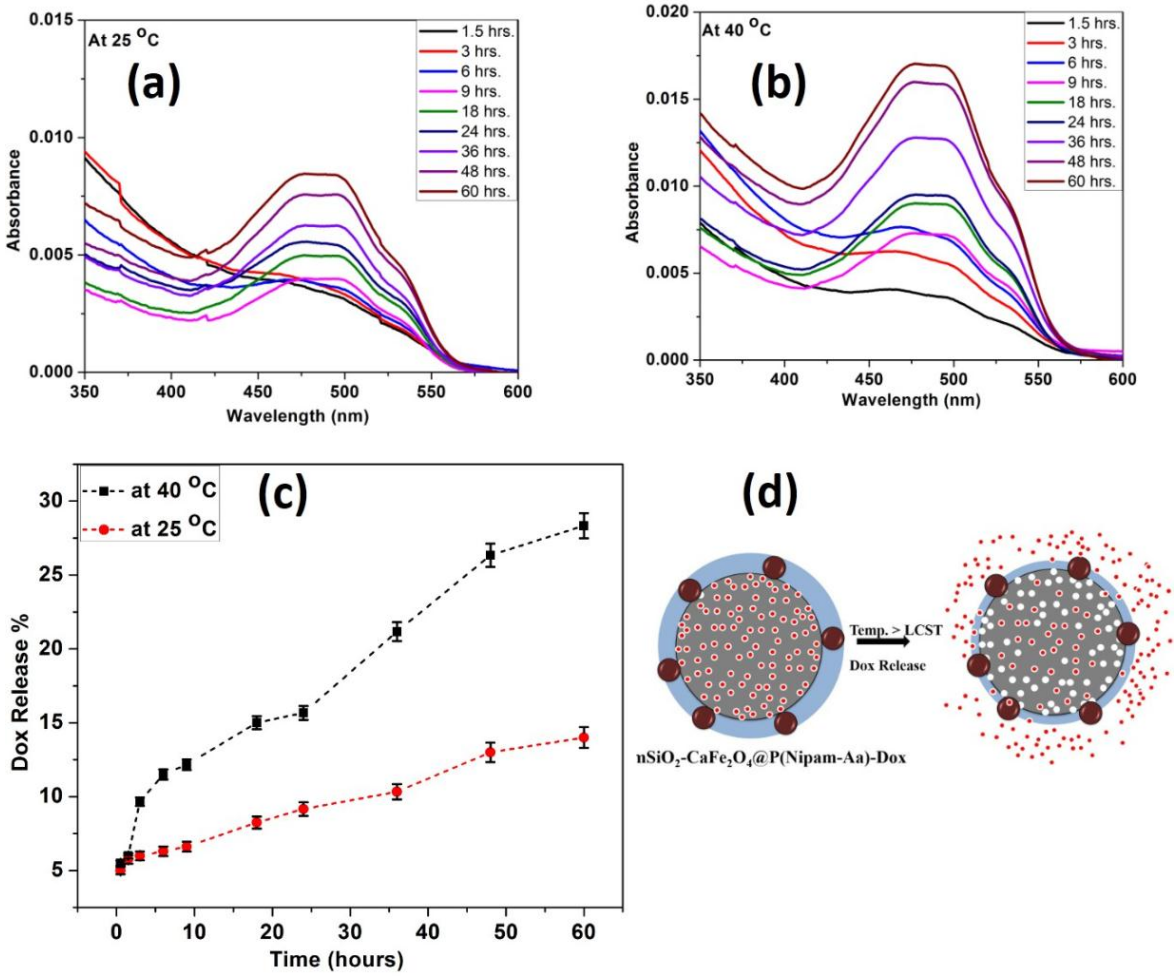

Figure 4.3.15. (a) UV-Vis absorption spectra of Dox in release medium with time released at 25 °C. (b) UV-Vis absorption spectra of Dox in release medium with time released at 40 °C. (c) In Vitro Dox release behavior from $mSiO_2$-$CaFe_2O_4$@P(Nipam-Aa)-Dox NC at 25 and 40 °C in PBS. (d) Temperature dependent Dox release mechanism from $mSiO_2$-$CaFe_2O_4$@P(Nipam-Aa)-Dox NC

4.3.11 In vitro biocompatibility of blank NCs and cytotoxicity of Dox loaded NCs

Biocompatibility of prepared $mSiO_2$-$CaFe_2O_4$@P(Nipam-Aa) was studied by MTT assay against normal cells (RAW 264.7 cells) and obtained cell viabilities are shown in figure 16 (a). Very high cell viabilities (~ 85%) upto high dose (800 µg/ml) of $mSiO_2$-$CaFe_2O_4$@P(Nipam-Aa) was observed that confirm biocompatible nature of $mSiO_2$-$CaFe_2O_4$@P(Nipam-Aa) on normal cells. Anticancer activity of $mSiO_2$-$CaFe_2O_4$@P(Nipam-Aa)-Dox NC was also studied by MTT assay against cancerous Hela cell line. Cell inhibition of Hela cells incubated with free Dox, $mSiO_2$-$CaFe_2O_4$@P(Nipam-Aa)-Dox NC with different concentrations are shown in figure 16 (b). $mSiO_2$-$CaFe_2O_4$@P(Nipam-Aa)-Dox NC has shown a high killing effect on Hela cells even better than free Dox upto 5µg/ml concentration. There after inhibition became slower. The IC_{50} of free Dox and loaded Dox were found to be 10 and ~5 µg/ml. The maximum cell killing (at 40µg/ml) of free Dox and $CaFe_2O_4$@P(Nipam-Aa)-Dox NC were found to be ~69 and ~67 respectively. Thus, the $CaFe_2O_4$@P(Nipam-Aa)-Dox NC has shown improved anticancer activity than free Dox and also has magnetic targeting ability. It is worthy to mention that the free Dox molecules lacks in targeting ability which cause severe side effect on normal body parts.

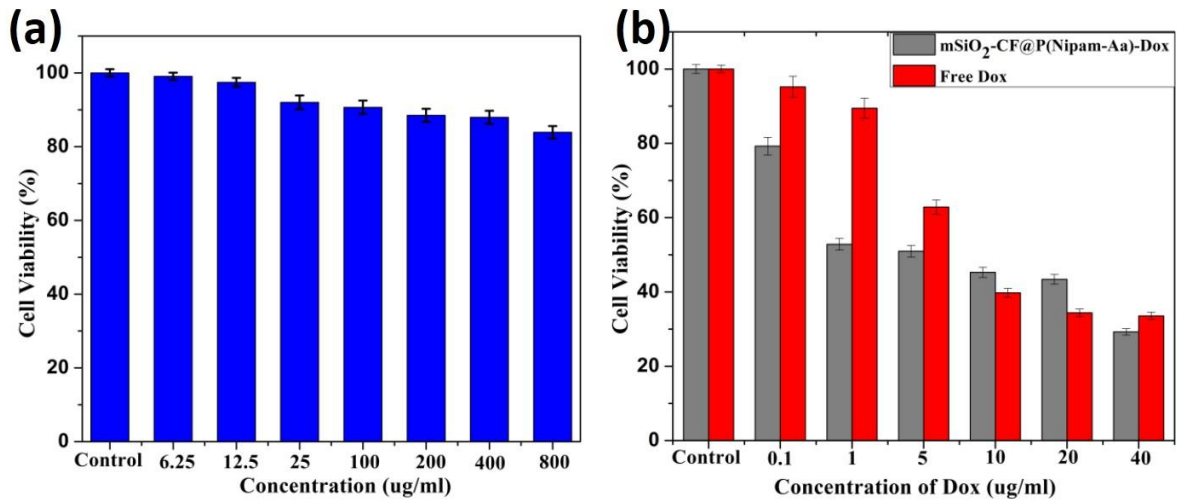

Figure 4.3.16. (a) Cell viabilities of RAW 264.7 cells treated with different dose of $mSiO_2$-$CaFe_2O_4$@P(Nipam-Aa) after 24hour incubation. (b) Cell inhibition of Hela cells treated with free Dox, blank $mSiO_2$-$CaFe_2O_4$@P(Nipam-Aa)-and $mSiO_2$-$CaFe_2O_4$@P(Nipam-Aa)-Dox NC with different concentrations.

4.3.12 Conclusions

Multifunctional thermos-responsive $mSiO_2$-$CaFe_2O_4$@P(Nipam-Aa) nanocomposites have been successfully prepared. The prepared $mSiO_2$-$CaFe_2O_4$@P(Nipam-Aa) NC was characterized thoroughly for different physicochemical properties and plausible formation mechanism has been proposed. Particles size of $CaFe_2O_4$ NPs and $mSiO_2$-$CaFe_2O_4$@P(Nipam-Aa) NC were found to be ~10 and ~330 nm, respectively. Powder XRD, TEM, SAED, TGA and FTIR analyses confirmed embedding of $CaFe_2O_4$ NPs and coating of P(Nipam-Aa) on surface of $mSiO_2$ NPs. All samples were found to be super-paramagnetic in nature. It was also observed that MPS modification on $mSiO_2$ surface, improve the coating of P(Nipam-Aa) polymer on surface of $mSiO_2$. $mSiO_2$-$CaFe_2O_4$@P(Nipam-Aa) has shown excellent Dox loading ability and also has demonstrated sustained and temperature dependent release of Dox. $mSiO_2$-$CaFe_2O_4$@P(Nipam-Aa) was found to be biocompatible to normal cells. An enhanced anticancer activity than free Dox against Hela cells was observed. Thus, obtained results suggest prepared smart thermo-responsive nanocarrier could have potential application in targeted and controlled drug delivery.

4.3.13 References

[1] S. Mura, J. Nicolas, P. Couvreur, Stimuli-responsive nanocarriers for drug delivery, Nat Mater 12(11) (2013) 991-1003.
[2] B. Chang, X. Sha, J. Guo, Y. Jiao, C. Wang, W. Yang, Thermo and pH dual responsive, polymer shell coated, magnetic mesoporous silica nanoparticles for controlled drug release, Journal of materials chemistry 21(25) (2011) 9239-9247.
[3] C. Liu, J. Guo, W. Yang, J. Hu, C. Wang, S. Fu, Magnetic mesoporous silica microspheres with thermo-sensitive polymer shell for controlled drug release, Journal of materials chemistry 19(27) (2009) 4764-4770.
[4] K. Asghar, M. Qasim, G. Dharmapuri, D. Das, Investigation on a smart nanocarrier with a mesoporous magnetic core and thermo-responsive shell for co-delivery of doxorubicin and curcumin: a new approach towards combination therapy of cancer, RSC Adv. 7(46) (2017) 28802-28818.
[5] L. Khanna, N.K. Verma, PEG/CaFe2O4 nanocomposite: Structural, morphological, magnetic and thermal analyses, Physica B: Condensed Matter 427 (2013) 68-75.
[6] A. Samariya, S.N. Dolia, A.S. Prasad, P.K. Sharma, S.P. Pareek, M.S. Dhawan, S. Kumar, Size dependent structural and magnetic behaviour of CaFe2O4, Current Applied Physics 13(5) (2013) 830-835.
[7] X. Hu, X. Hao, Y. Wu, J. Zhang, X. Zhang, P.C. Wang, G. Zou, X.-J. Liang, Multifunctional hybrid silica nanoparticles for controlled doxorubicin loading and release with thermal and pH dually response, Journal of materials chemistry. B, Materials for biology and medicine 1(8) (2013) 1109-1118.
[8] M. Schönhoff, A. Larsson, P.B. Welzel, D. Kuckling, Thermoreversible Polymers Adsorbed to Colloidal Silica: A 1H NMR and DSC Study of the Phase Transition in Confined Geometry, The Journal of Physical Chemistry B 106(32) (2002) 7800-7808.
[9] M. Jang, J.K. Park, E.W. Shin, Lanthanum functionalized highly ordered mesoporous media: implications of arsenate removal, Microporous and Mesoporous Materials 75(1) (2004) 159-168.
[10] S. Li, Y. Ma, X. Yue, Z. Cao, Z. Dai, One-pot construction of doxorubicin conjugated magnetic silica nanoparticles, New Journal of Chemistry 33(12) (2009) 2414-2418.
[11] W.Y. Qian, D.M. Sun, R.R. Zhu, X.L. Du, H. Liu, S.L. Wang, pH-sensitive strontium carbonate nanoparticles as new anticancer vehicles for controlled etoposide release, International journal of nanomedicine 7 (2012) 5781-92.
[12] S. Kayal, R.V. Ramanujan, Doxorubicin loaded PVA coated iron oxide nanoparticles for targeted drug delivery, Materials Science and Engineering: C 30(3) (2010) 484-490.
[13] S.P. Victor, W. Paul, M. Jayabalan, C.P. Sharma, Supramolecular hydroxyapatite complexes as theranostic near-infrared luminescent drug carriers, CrystEngComm 16(38) (2014) 9033-9042.

Section 4.4: $CaFe_2O_4$ NPs impregnated mesoporous $CaCO_3$ based multifunctional Nanocarrier (meso$CaCO_3$@$CaFe_2O_4$ NC) prepared by green route

In this section synthesis and characterization of novel mesoporous $CaCO_3$ based multifunctional $CaFe_2O_4$ NP impregnated meso$CaCO_3$ nanocomposite (meso$CaCO_3$@$CaFe_2O_4$ NC) for delivery of anticancer drug will be discussed.

Mesoporous magnetic nanoparticles are widely studied for their biomedical applications such as in magnetic bioseparation, cell labelling, and magnetically controlled transport of anti-cancer drugs [1-5]. The ferrites of Ni, Mn, Co, Zn although possess good magnetic properties, their inherent toxicity after certain amount reduces their reliability. This, raises worries on their biocompatibility and their effectiveness for biomedical applications. The use of biocompatible and biodegradable carrier in biomedicine is getting significant priority over conventional synthetic carriers. Ferrites of calcium are expected to be more biocompatible since calcium is inherently non-toxic [6]. $CaCO_3$ has shown promising potential for the development of smart carriers for anticancer drugs because of 1) cost effectiveness, 2) naturally existence in living creatures and even in human body, 3) ideal biocompatibility, 4) biodegradability, 5) pH-sensitive properties, and 6) chemical stability[7]. $CaCO_3$ is one of the most common inorganic material of the nature. $CaCO_3$ is the main component of shells of marine organisms, snails, pearls, and eggshells. $CaCO_3$ and MNPs based nano-carriers are receiving increasing consideration because of their inherent biocompatibility and magnetic controllability, respectively. In this work, novel mesoporous $CaCO_3$ based multifunctional $CaFe_2O_4$ NP impregnated meso$CaCO_3$ nanocomposite (meso$CaCO_3$@$CaFe_2O_4$ NC) have successfully been synthesized by environmental friendly biological route using waste egg shell, lemon juice, $CaFe_2O_4$ NP, CTAB and characterized for different physiochemical properties. A detailed mechanism of formation of meso$CaCO_3$@$CaFe_2O_4$ NC from bulk egg shell has been proposed. The structure and morphology of meso$CaCO_3$@$CaFe_2O_4$ NC were characterized by XRD, HRTEM and BET. Powder XRD, TEM, SAED, FTIR and energy dispersive spectroscopic (EDS) analyses confirmed coexistence of $CaFe_2O_4$ NP and $CaCO_3$ phases in the nanocomposite. Magnetic measurements (M-H curve) show $CaFe_2O_4$ NP and meso$CaCO_3$@$CaFe_2O_4$ NC to be super-paramagnetic in nature. Drug loading and release behavior of meso$CaCO_3$@$CaFe_2O_4$ NC were studied using doxorubicin as the anticancer drug.

Biocompatibility and cyto-toxicity of bare carriers and drug loaded carrier were studied by MTT assay. Obtained results suggest prepared nano formulation could have potential application in targeted drug delivery. The use of biocompatible and biodegradable meso$CaCO_3$@$CaFe_2O_4$ NC, developed through a green chemistry route, in nanomedicine will be cheaper and environmental friendly.

4.4.1 Synthesis of meso$CaCO_3$@$CaFe_2O_4$ NC

As we know, nanocarrier developed using only single materials such as $CaCO_3$, SiO_2 and polymer lacks in tumor targeting ability. Targeting ability to the nanocarrier can be introduced by surface functionalization with antibody or by simply incorporating MNP within NC. Waste egg shell could be good and inexpensive source of $CaCO_3$. In this work, egg shell derived $CaCO_3$ based multifunctional magnetic mesoporous nanocarrier have been developed by green route using lemon juice and egg shell. Step wise formation process of $CaFe_2O_4$ NP impregnated meso$CaCO_3$ nanocomposite (meso$CaCO_3$@$CaFe_2O_4$ NC) is shown in the schematic 4.4.1. meso$CaCO_3$@$CaFe_2O_4$ NC was prepared by green route using waste egg shell, lemon juice, $CaFe_2O_4$ NP, and CTAB. $CaFe_2O_4$ NP of size ~10 nm was prepared by auto-combustion method. The whole synthesis process of mesoporous $CaCO_3$ involve conversion of egg shell to calcium citrate with help of citric acid of lemon juice on the surface CTAB template and further decomposition of calcium citrate and template to mesoporous $CaCO_3$. Initially, sonication and stirring of $CaFe_2O_4$ NP, CTAB, and lemon juice in water have resulted in the formation aligned micellar rod of CTAB holding $CaFe_2O_4$ NP. On addition of egg shell, the citric acid present in the lemon juice reacted with it to give calcium citrate which deposited on the soft template holding $CaFe_2O_4$ NP. Further calcination of this intermediated complex (i.e. calcium citrate on CTAB and $CaFe_2O_4$) result in the formation of $CaFe_2O_4$ NP impregnated meso$CaCO_3$ nanocomposite (meso$CaCO_3$@$CaFe_2O_4$ NC). As removal of CTAB template result in the generation of mesoporous structure in $CaCO_3$. In the absence of $CaFe_2O_4$ NP and following the same process pure meso$CaCO_3$ NP was prepared. In this first calcium citrate was deposited on the CTAB templet giving calcium citrate based intermediate compound and calcination of this intermediated compound resulted in the formation of pure meso$CaCO_3$ NP. To validate the above discussed formation mechanism of meso$CaCO_3$ NP and meso$CaCO_3$@$CaFe_2O_4$ NC, TGA, FTIR, and TEM analysis of intermediate compound, meso$CaCO_3$, and meso$CaCO_3$@$CaFe_2O_4$ NC were carried out and all these techniques have

confirmed the formation of calcium citrate intermediate compound and its transformation to $CaCO_3$ on calcination.

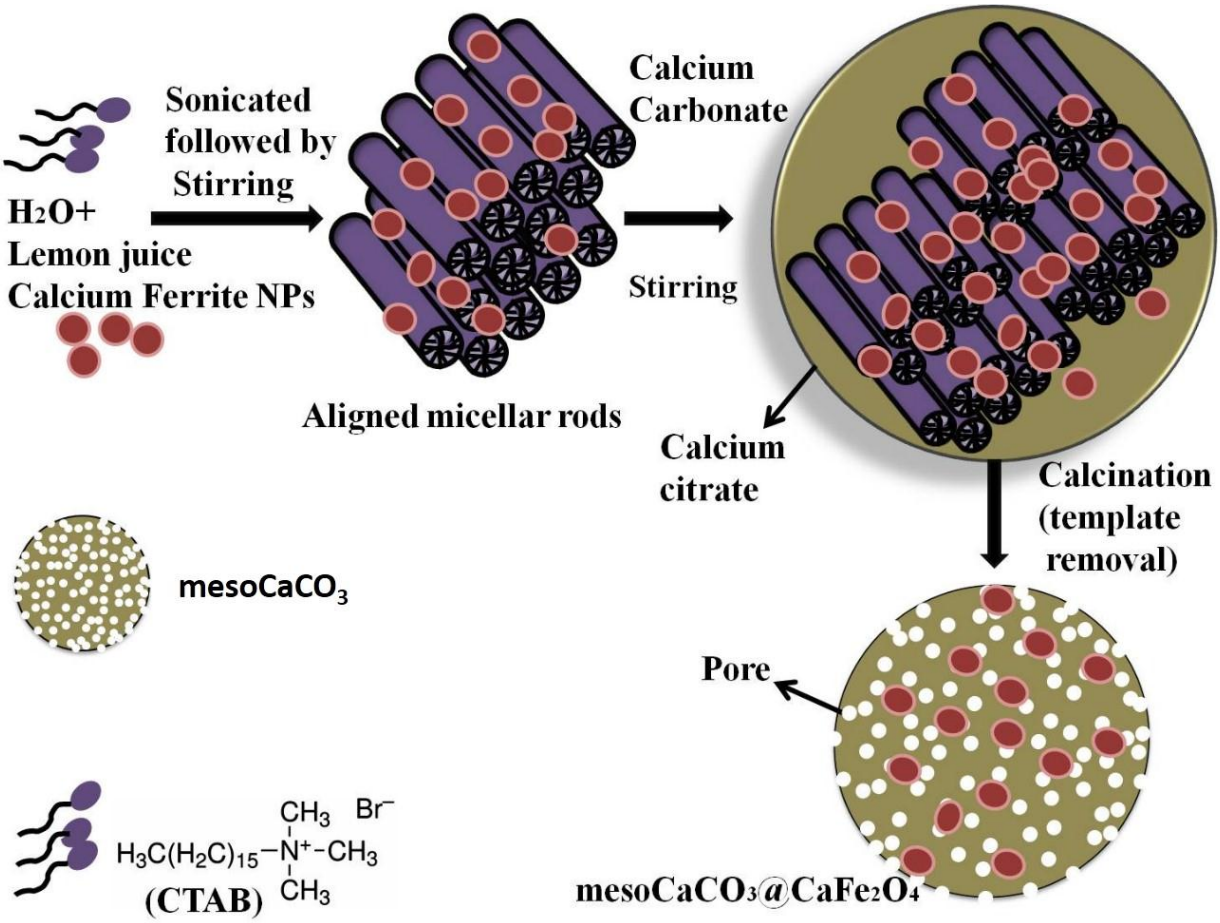

Schematic 4.4.1. Step wise formation process of $CaFe_2O_4$ NP impregnated mesoCaCO$_3$ nanocomposite (mesoCaCO$_3$@$CaFe_2O_4$ NC).

4.4.2 TGA analysis

TGA graph of intermediate compound, mesoCaCO$_3$, and mesoCaCO$_3$@$CaFe_2O_4$ NC are shown in figure 4.4.1(a & b). TGA of intermediate compound shown in figure 4.4.1(a) shows characteristic degradation pattern of calcium citrate which confirmed the formation of calcium citrate from the egg shell and citric acid. Little weight loss of 10% in the range of 50-130 ^oC from the intermediate compound is assigned to the dehydration of hydrated calcium citrate and formation of anhydrous calcium citrate. The weight loss of ~44 % in the range of 130-485 ^oC is due to the decomposition of CTAB and anhydrous calcium citrate associated with the formation of $CaCO_3$. The formation of mesoCaCO$_3$ occurred at 466 ^oC (in between 440-485 ^oC) due to complete decomposition of calcium citrate and CTAB. After that, formed mesoCaCO$_3$ remained stable up-to 630 ^oC with minute weight loss of ~3%. After this stage

decomposition of mesoCaCO$_3$ took place in between 630-700 ^oC (centered at 670 ^oC) with the weight loss of 20% resulting in formation of CaO which remained stable up-to tested temperature (950 ^oC). The observed results are consistent with the earlier report [8]. As formation temperature of $CaCO_3$ was observed to be 466 ^oC, thus, in this study calcination of intermediate compound were carried out at 500 ^oC. TGA graph of mesoCaCO$_3$, and mesoCaCO$_3$@CaFe$_2$O$_4$ NC (figure 4.4.1b) show characteristic degradation behavior of $CaCO_3$ which confirm successful formation of mesoCaCO$_3$ base system. In addition, appearance of similar degradation behavior of mesoCaCO$_3$, and mesoCaCO$_3$@CaFe$_2$O$_4$ also suggested successful formation of mesoCaCO$_3$ based nanocomposite. Formation of $CaCO_3$ was also confirmed by XRD analysis. Up-to 550 ^oC, a little weight loss of 12 and 17 % have been observed from mesoCaCO3, and mesoCaCO$_3$@CaFe$_2$O$_4$ respectively which could be due the loss adsorbed water and remained organic species. Decomposition of $CaCO_3$ to CaO in mesoCaCO$_3$, and mesoCaCO$_3$@CaFe$_2$O$_4$ occurred in between 560-684 ^oC (at ~668 ^oC) and 540-665 ^oC, with the weight of 43% and 34% respectively. Above this temperature (~700 ^oC) no further weight loss was observed for the both the sample because of stable nature of formed CaO. DTG graph of mesoCaCO$_3$ shown in inset of (b) shows single peak at 668 ^oC which can be assigned to the decomposition of $CaCO_3$.

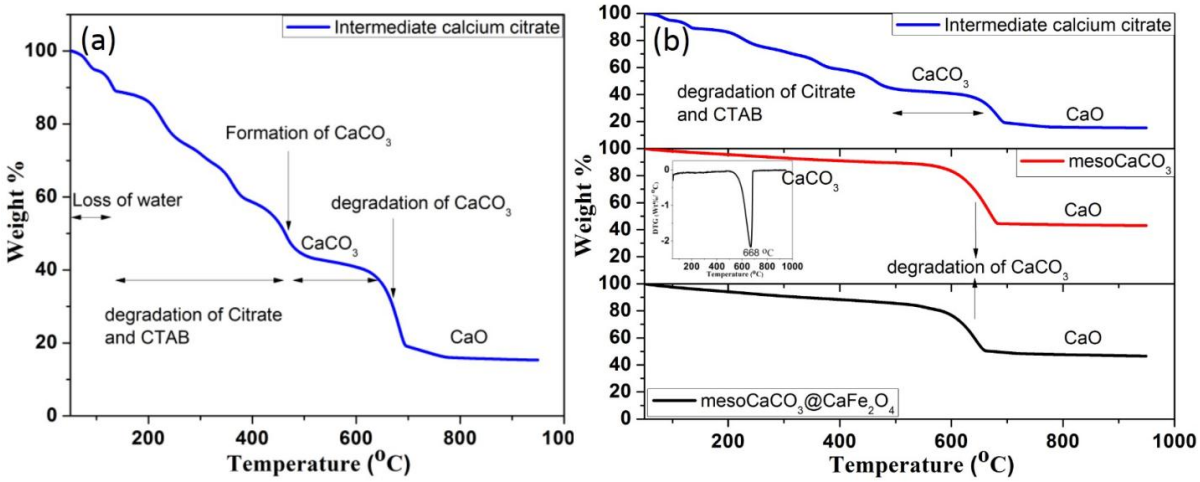

Figure 4.4.1. TGA graph of intermediate compound (a). TGA graph of intermediate compound, mesoCaCO$_3$, and mesoCaCO$_3$@CaFe$_2$O$_4$ NC (b).

4.4.3 XRD analysis

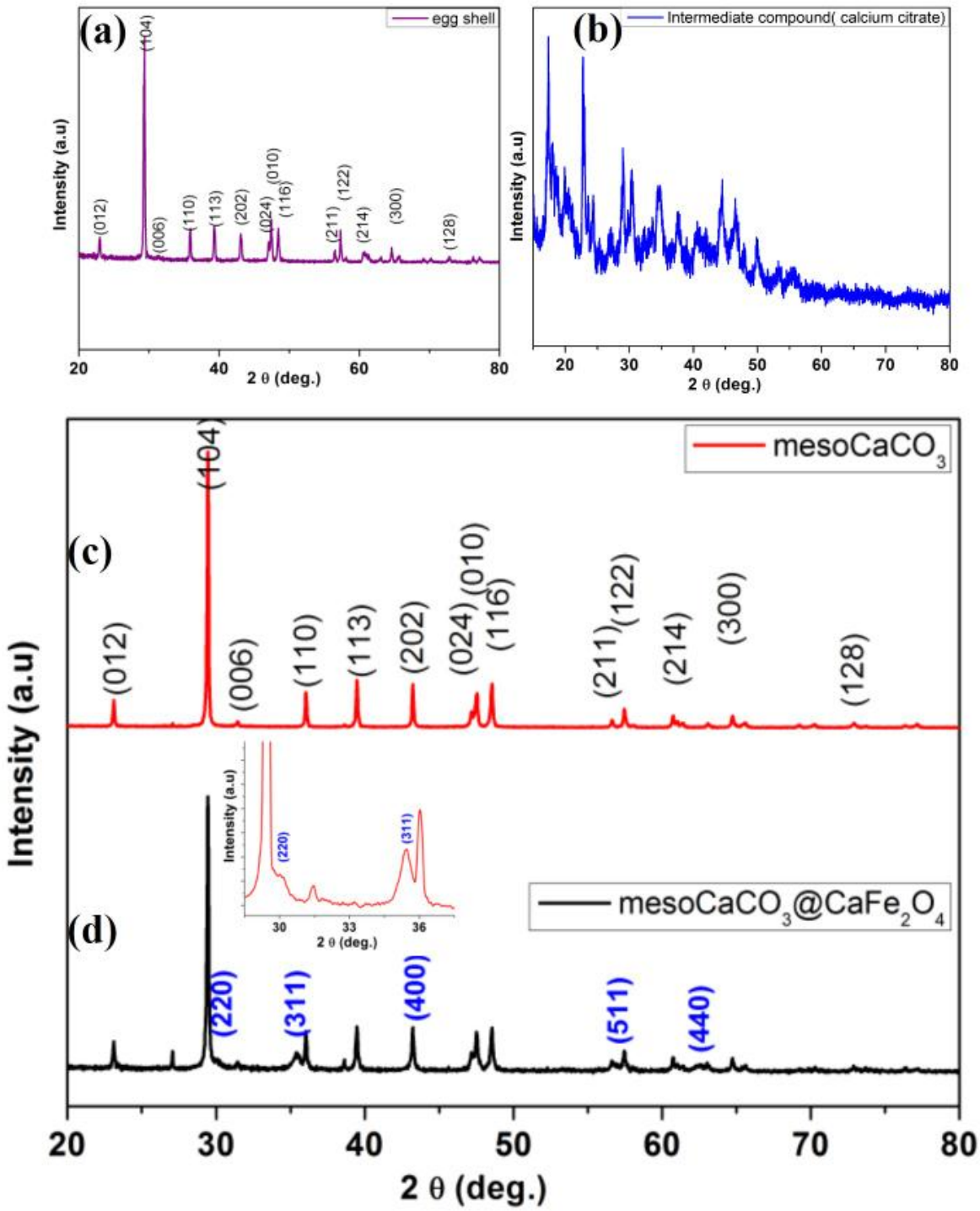

Figure 4.4.2. Wide angle XRD patterns of powdered egg shell (a), pure intermediate compound (b), mesoCaCO$_3$(c) and mesoCaCO$_3$@CaFe$_2$O$_4$ (d) NPs. Inset of (d) shows enlarge pattern in range of mesoCaCO$_3$@CaFe$_2$O$_4$ in 2Θ range 28-37^o.

The crystalline structure as well as formation of calcium citrate, mesoCaCO$_3$ and mesoCaCO$_3$@CaFe$_2$O$_4$ was confirmed by x-ray diffraction (XRD). To support the above

explained mechanism XRD pattern of powdered egg shell, pure intermediate compound, meso$CaCO_3$ and meso$CaCO_3$@$CaFe_2O_4$ NC have been obtained and shown in figure 4.4.2(a-d). The XRD pattern of raw powdered egg shell (fig. 4.4.2a) shows presence of well crystalline $CaCO_3$, as only characteristic diffraction peaks of rhombohedral $CaCO_3$ were observed without any impurity phases. These peaks are well matching with the standard diffraction pattern (PDF Number: 01-085-1108). The XRD pattern of intermediate compound shows characteristic diffraction pattern of calcium citrate (fig. 4.4.2b) [8] [9]. Disappearance of peaks of $CaCO_3$ and appearance of new characteristic peaks of calcium citrate confirmed that chemical reaction has occurred between egg shell and citric acid to form calcium citrate. In short, egg shell reacted with citric acid of lemon juice and converted to the calcium citrate. Further calcination of intermediate compound has resulted in the formation of meso$CaCO_3$. XRD pattern of meso$CaCO_3$ (fig. 4.4.2c) shows presence of characteristic peaks of rhombohedral $CaCO_3$ without any impurity phase [[10]]. These peaks are well matching with the standard diffraction pattern (PDF Number: 01-085-1108). Thus, XRD analysis confirmed successful formation of meso$CaCO_3$ from calcium citrate. Appearance of characteristic diffraction peaks of both component, meso$CaCO_3$ and $CaFe_2O_4$, in XRD pattern of meso$CaCO_3$@$CaFe_2O_4$ NC (fig. 4.4.2d) confirmed successful formation on nanocomposite[11]. Crystallite size of $CaFe_2O_4$ in nanocomposite was found to be 14 nm. Crystallite sizes of $CaCO_3$ in raw egg shell, in pure meso$CaCO_3$ and in nanocomposite were estimated to be 35 nm, 70 nm and 57 nm respectively.

4.4.4 Meso-structure analysis by low angle XRD and BET:

Mesoporous structure of prepared samples was studied using Low angle XRD and BET analysis. Low angle XRD patterns of pure intermediate calcium citrate (i.e calcium citrate without $CaFe_2O_4$ NP), composite intermediate calcium citrate (i.e calcium citrate with $CaFe_2O_4$ NP), meso$CaCO_3$ NP and meso$CaCO_3$@$CaFe_2O_4$ NC are shown in figure 4.4.3 (a), (b), (c) and (d) respectively. Presence of three diffraction peaks in the 2 Θ range of 2-10^o were observed in both un-calcined samples ((a) and (b)) that can be assigned to the (100), (110) and (200) planes of highly ordered 2D hexagonal symmetry of meso-structure. Thus, formation of mesoporous structure in intermediate compound is confirmed by low angle XRD. Low angle XRD pattern of meso$CaCO_3$ NP and meso$CaCO_3$@$CaFe_2O_4$ NC show presence of only one diffraction pattern which was assigned to the (100) plane. This disappearance of two small peaks can be assigned to the loss of some orderness in mesoporous structure. Rearmament of atoms during the calcination process could have caused dis-orderness in the mesostructure of meso$CaCO_3$.

The d-spacing of (100) plane was found to be ~4.4 nm which is representative of pore diameter[12]. The unit cell parameter was found to be ~5.1 nm. Presence of (100) reflection in low angle XRD pattern mesoCaCO$_3$ NP and mesoCaCO$_3$@CaFe$_2$O$_4$ NC confirmed their mesoporous nature. Further confirmation of mesoporous nature was made by BET and HRTEM analysis.

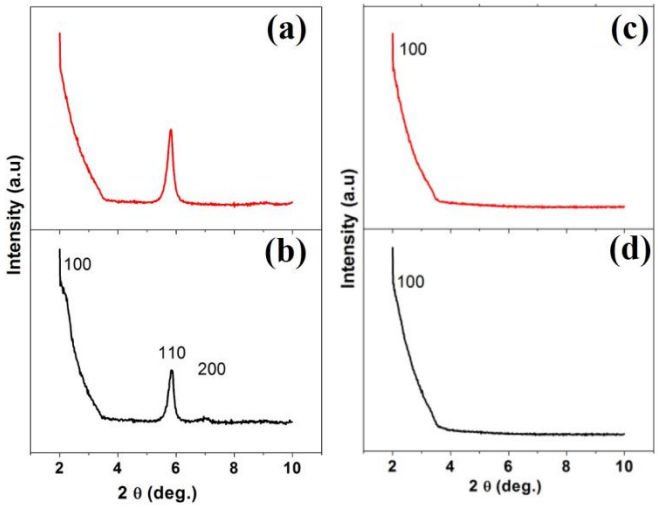

Figure 4.4.3. Low angle XRD patterns of pure intermediate calcium citrate (a), composite intermediate calcium citrate (b) mesoCaCO$_3$(c) and mesoCaCO$_3$@CaFe$_2$O$_4$ (d) NPs.

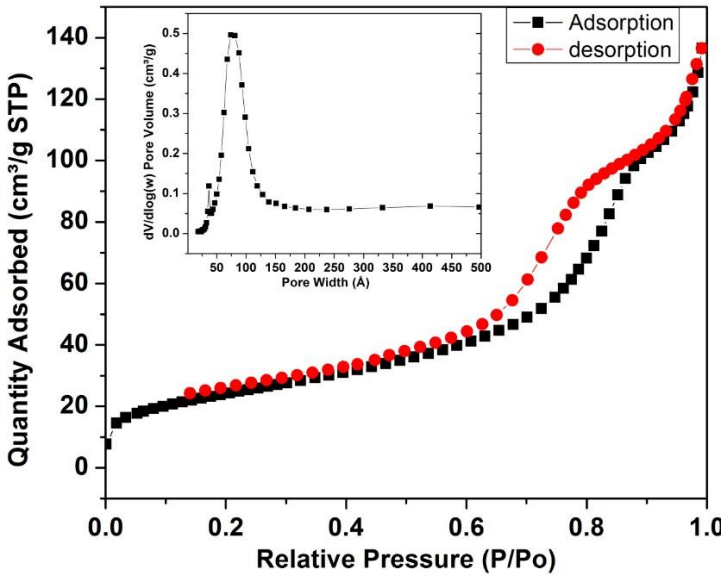

Figure 4.4.4. N$_2$ adsorption and desorption isotherm of the mesoCaCO$_3$@CaFe$_2$O$_4$ NC. Inset figure shows pore size distribution obtained from desorption isotherm.

The BET result of mesoCaCO$_3$@CaFe$_2$O$_4$ NC which is shown in figure 4.4.4 show mesoporous nature of mesoCaCO$_3$@CaFe$_2$O$_4$ NC. N$_2$ adsorption desorption isotherm was used to study surface area and mesostructure of the mesoCaCO$_3$@CaFe$_2$O$_4$ NC. Presence of

hysteresis in N_2 adsorption and desorption isotherm is characteristic feature of mesoporous structure. Type IV isotherm with H1 hysteresis loop was observed which is symbolic of mesoporous structure meso$CaCO_3$@$CaFe_2O_4$ NC [13]. Capillary condensation of N_2 gas in the mesopores has resulted the rapid increase in adsorption isotherm in between 0.5 to 0.9 P/Po [12]. The BET and Langmuir specific surface area were found to be 87 and 134 m^2/g respectively. The obtained specific surface area is higher than that of reported such system[14] [10] [15, 16]. Inset of figure 4.4.4 shows pore size distribution graph which was obtained from desorption isotherm using BJH method. The pore size distribution was found to be narrower and with uniform pores. Presence of single peak indicate monodispersed nature of pores. The pore diameter was found to be in between 3-12 nm which centered at 9 nm.

4.4.5 Particles size, shape and morphology by TEM and FESEM

TEM analysis of intermediate stage nanocomposites (as prepared nanocomposites) was also carried out to find out its shape, morphology, particles size and to know formation mechanism of final nanocomposite. TEM images of intermediate nanocomposite compound (calcium citrate-$CaFe_2O_4$) at different magnifications is shown in figure 4.4.5 (a-c). It is observed that the intermediate particles of size 150-250 nm are well embedded with smaller (~10-15 nm) $CaFe_2O_4$ NPs. It was also observed that formed calcium citrate intermediate is mesoporous in nature. Mesoporous nature of calcium citrate intermediate was also shown by low angle XRD analysis. Particles size, morphology and mesoporous structure of meso$CaCO_3$ NP and meso$CaCO_3$@$CaFe_2O_4$ NC were studied by FESEM and TEM analysis. Figure 4.4.6 (a) and (b) show FESEM images of meso$CaCO_3$ NP and meso$CaCO_3$@$CaFe_2O_4$ NC respectively. In both the cases particles size is found to be ~150-200 nm with the spherical to irregular morphology. Embedding of smaller $CaFe_2O_4$ NPs on the bigger meso$CaCO_3$ particles can easily be seen in the FESEM image of meso$CaCO_3$@$CaFe_2O_4$ NC.

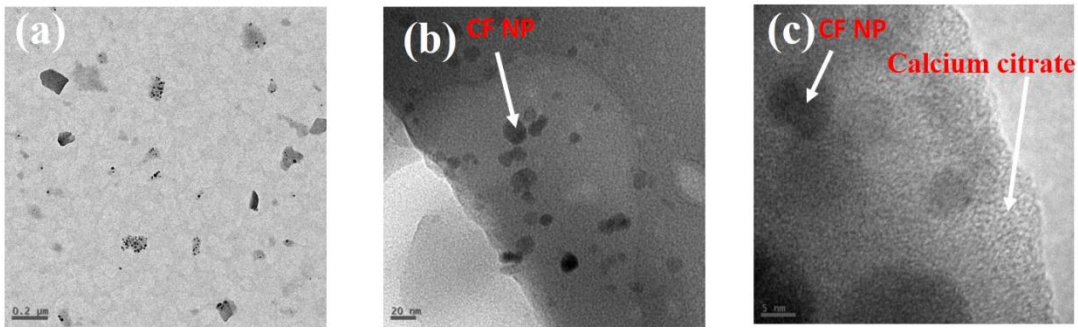

Figure 4.4.5. TEM images of intermediate nanocomposite compound (calcium citrate-$CaFe_2O_4$) at different magnifications(a-c).

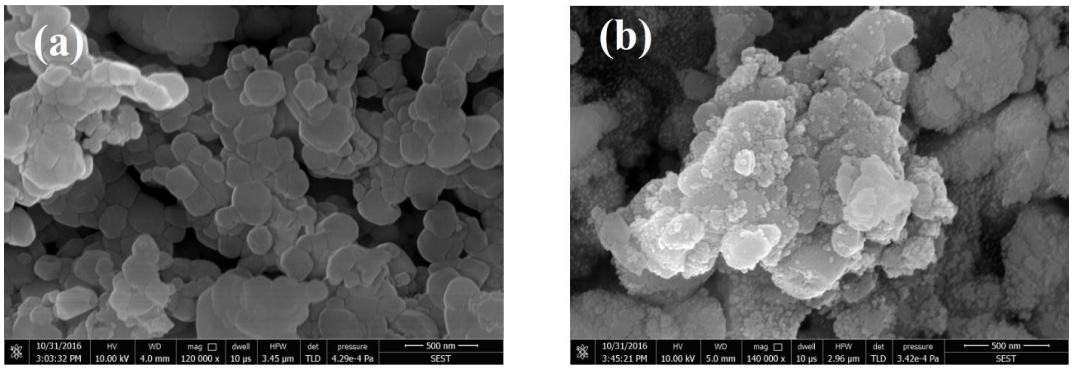

Figure 4.4.6. FESEM of meso$CaCO_3$ NP and meso$CaCO_3$@$CaFe_2O_4$ NC.

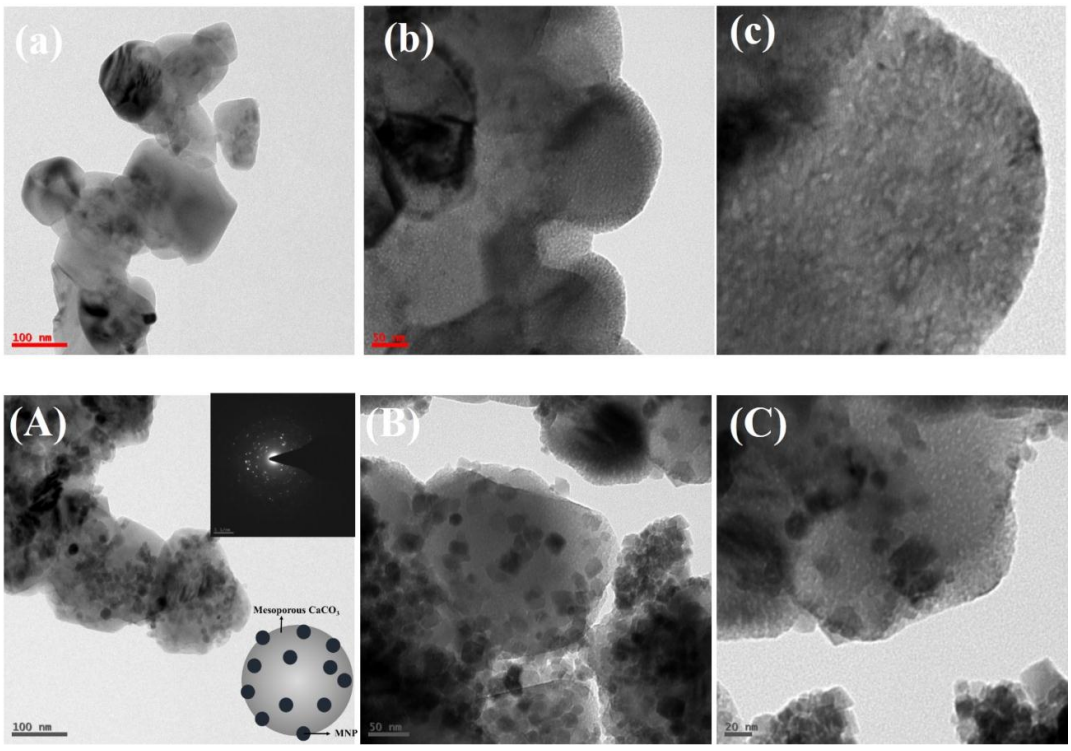

Figure 4.4.7. TEM images of meso$CaCO_3$ (a-c) and meso$CaCO_3$@$CaFe_2O_4$ NC (A-C). Inset of (A) shows SAED of meso$CaCO_3$@$CaFe_2O_4$ NC.

TEM images at different magnification of mesoCaCO$_3$ (a-c) and mesoCaCO$_3$@CaFe$_2$O$_4$ NPs (A-C) are shown in figure 4.4.7. Particles size of mesoCaCO$_3$ (a-c) is found to be ~150 nm with spherical to irregular shape. Pore on the surface of mesoCaCO$_3$ can be seen in the TEM images (b and c). In case of mesoCaCO$_3$@CaFe$_2$O$_4$ NC similar particles size (~150) and morphology was observed. It was observed from TEM image that calcium ferrite NPs of size ~10-15 nm are well embedded in mesoporous CaCO$_3$ nanosphere. Pore size was found to be ~3-10 nm. Appearance of diffraction pattern of both calcium ferrite and CaCO$_3$ in SAED pattern of nanocomposite also confirms successful formation of nanocomposite (inset of A). HRTEM and EDS analysis of samples were also carried out to confirm embedding of CaFe$_2$O$_4$ NPs and mesoporous nature of mesoCaCO$_3$.

4.4.6 HRTEM and EDS analysis

Figure 4.4.8(a-c) shows HRTEM analysis of mesoCaCO$_3$@CaFe$_2$O$_4$ NC. Presence of pore in the HRTEM images is clearly visible and absence of lattice fringes in the pore region confirm it to be pores. The d-spacing of embedded particles was estimated and it is well matches with the standard d-spacing of CaFe$_2$O$_4$ NP. The d-spacing of matrix mesoCaCO$_3$ was also estimated and it is well matching with standard value. The estimated d-spacing of CaFe$_2$O$_4$ NP and mesoCaCO$_3$ were found to be 0.25 nm and 0.44 nm which were indexed to (311) plane of spinel cubic system and (012) plane of rhombohedral CaCO$_3$ respectively (PDF Number: 01-085-1108) [11]. Presence of well-ordered atomic plane of CaFe$_2$O$_4$ NP is shown in figure 4.4.8(c) which suggested that crystalline structure of CaFe2O4 NP have not changed during the synthesis process. Figure 4.4.8 (d) and (e) show EDS spectra of mesoCaCO$_3$ and mesoCaCO$_3$@CaFe$_2$O$_4$ NC respectively. EDS spectra of mesoCaCO$_3$ NP has shown presence of elemental peaks of those only elements present in CaCO$_3$ whereas EDS spectra of mesoCaCO$_3$@CaFe$_2$O$_4$ NC has shown presence of all elemental peaks of both mesoCaCO$_3$ and CaFe$_2$O$_4$ confirming confirmed coexistence of both component. Thus, TEM, HRTEM and EDS analysis confirmed coexistence of CaFe$_2$O$_4$ NP and mesoCaCO$_3$ and formation of mesoCaCO$_3$@CaFe$_2$O$_4$ NC.

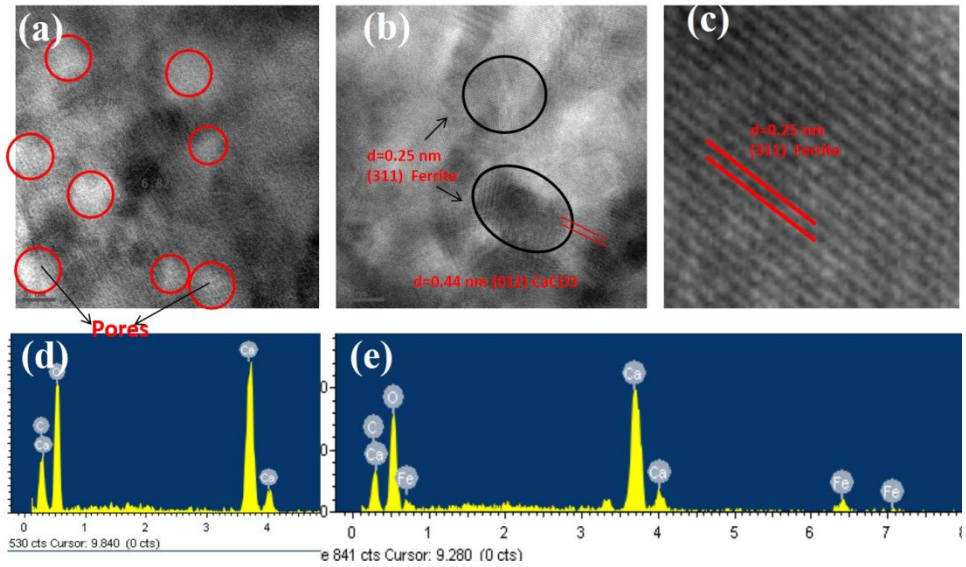

Figure 4.4.8. HRTEM images of mesoCaCO$_3$@CaFe$_2$O$_4$ NC (a-c). EDS spectra of mesoCaCO$_3$ NP(d) and mesoCaCO$_3$@CaFe$_2$O$_4$ NC(e).

4.4.7) Magnetic properties:

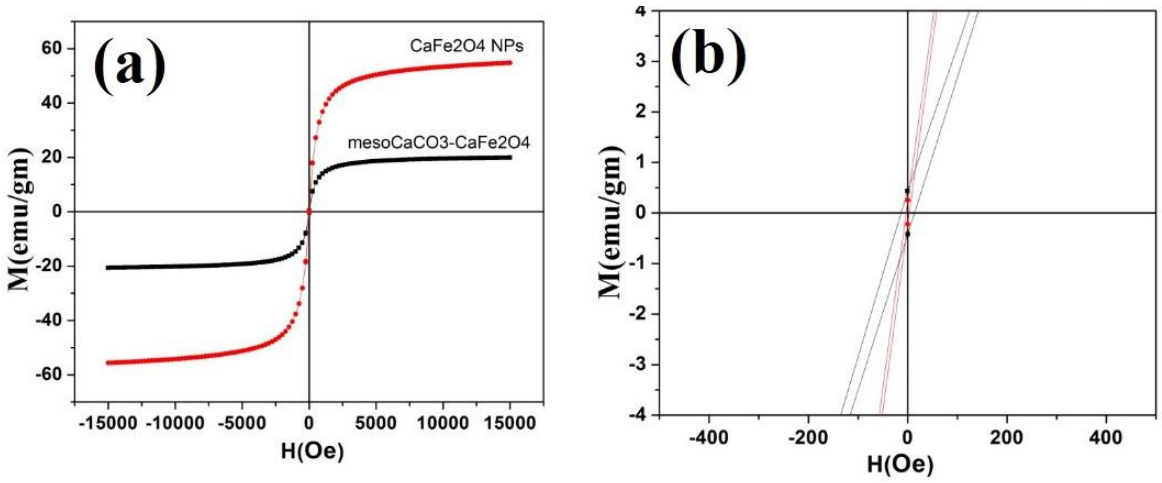

Figure 4.4.9. (a) M-H curve of CaFe$_2$O$_4$ and mesoCaCO$_3$@CaFe$_2$O$_4$ NC with corresponding enlarge M-H curve (b).

Magnetic properties of CaFe$_2$O$_4$ NP and mesoCaCO$_3$@CaFe$_2$O$_4$ NC were studied by vibrating sample magnetometry (VSM) technique and obtained RT M-H curve are shown in figure 4.4.9. M-H curve of CaFe$_2$O$_4$ NP and mesoCaCO$_3$@CaFe$_2$O$_4$ NC shows superparamagnetic nature with negligible remnant magnetization and coercivity. The M_S value of pure CaFe$_2$O$_4$ nanoparticles and nanocomposites are found to 54.7 and 20 emu/g respectively. Reduction in the Ms value of mesoCaCO$_3$@CaFe$_2$O$_4$ NC than pure CaFe$_2$O$_4$ NP is due to the presence of nonmagnetic mesoCaCO$_3$ [17]. The M_S value of magnetic nanoparticle represents its magnetic

controllability and obtained Ms value of meso$CaCO_3$@$CaFe_2O_4$ NC is sufficient to be used for targeted drug delivery application. The M_R value were found to be 0.23 and 0.43emu/g for pure $CaFe_2O_4$ and nanocomposite respectively. The coercivity value were found to be 3.2 and 13 Oe for pure $CaFe_2O_4$ and nanocomposite respectively. Enlarge M-H graph is shown in figure 4.4.9(b) to show M_R and coercivity value. The superparamagnetic nature of samples can be attributed to the very small size of $CaFe_2O_4$ NP.

4.4.8 FTIR analysis of blank nanoparticles and Dox loaded nanoparticles

An anticancer drug Doxorubicin (Dox) was loaded in meso$CaCO_3$@$CaFe_2O_4$ NC and drug loading was confirmed two different technique such as FTIR and UV-Vis spectroscopy [18]. Both the results confirmed successful loading of Dox in meso$CaCO_3$@$CaFe_2O_4$ NC. The Dox loaded meso$CaCO_3$@$CaFe_2O_4$ NC was named as meso$CaCO_3$@$CaFe_2O_4$-Dox NC. Further, formation of intermediate calcium citrate, meso$CaCO_3$ NP, meso$CaCO_3$@$CaFe_2O_4$ NC and meso$CaCO_3$@$CaFe_2O_4$-Dox NC were also supported by FTIR analysis. The FTIR spectra of intermediate calcium citrate, meso$CaCO_3$ NP, meso$CaCO_3$@$CaFe_2O_4$ NC and meso$CaCO_3$@$CaFe_2O_4$-Dox NC are shown in figure 4.4.10(a-c). FTIR spectra of intermediate calcium citrate and meso$CaCO_3$ NP show characteristic bands of calcium citrate and $CaCO_3$. These bands are well matching with the reported spectra of calcium citrate and $CaCO_3$ [10]. In case of meso$CaCO_3$ NP the major bands observed at 714, 875, 1061, 1432, 1797, and 2515 cm^{-1} etc. [10]. FTIR spectra of meso$CaCO_3$@$CaFe_2O_4$ NC shows characteristic bands of both $CaFe_2O_4$ and $CaCO_3$. The band between 400-600 cm^{-1} in FTIR spectra of meso$CaCO_3$@$CaFe_2O_4$ NC can be assign to the $CaFe_2O_4$ NP and the other bands at 713, 875, 1432, 1798, and 2514 cm^{-1} was arises from meso$CaCO_3$. [19] [6, 20] [10]. Thus, appearance of characteristic band of both $CaFe_2O_4$ and $CaCO_3$ in the FTIR spectra of meso$CaCO_3$@$CaFe_2O_4$ NC confirmed successful formation of meso$CaCO_3$@$CaFe_2O_4$ NC. FTIR spectra of meso$CaCO_3$@$CaFe_2O_4$-Dox NC shows characteristic bands of both component of nanocarrier ($CaFe_2O_4$ and $CaCO_3$) with characteristic band of Dox. Appearance of few new characteristic bands of Dox in FTIR spectra of Dox loaded meso$CaCO_3$@$CaFe_2O_4$ NC confirmed loading of Dox in mesoporous nanocarrier. Enlarge FTIR spectra of meso$CaCO_3$@$CaFe_2O_4$-Dox NC in range 950-1850 and 2750-3250 cm^{-1} are shown in figure 4.4.10 (b) and (c) to show presence of characteristic bands of Dox. The bands at 1720, 1645, 1615, 1579, 1287, 1212, 3019, and 3062 cm^{-1} (figure 4.4.10 (b) and (c)) in in FTIR spectra of meso$CaCO_3$@$CaFe_2O_4$-Dox NC can

be attributed to the presence of Dox [21] [22]. Thus, FTIR spectra also confirmed successful formation of nanocomposites and loading of Dox in the nanocomposites.

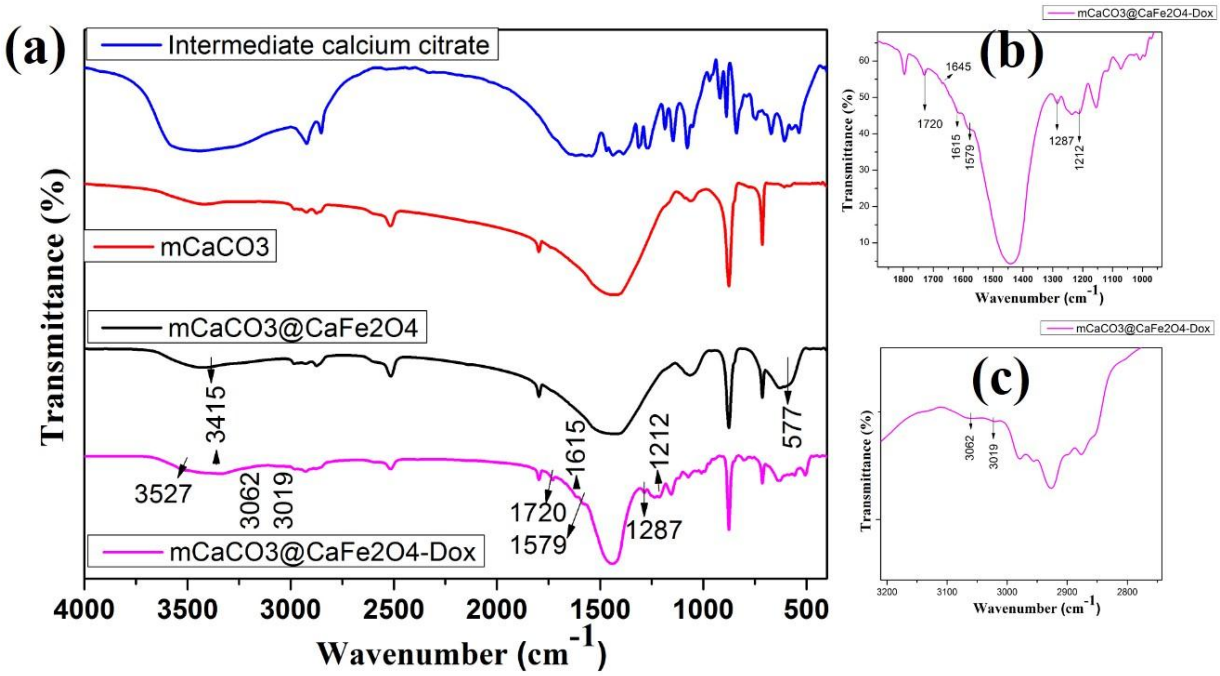

Figure 4.4.10. (a) FTIR spectra of intermediate calcium citrate, meso$CaCO_3$ NP, meso$CaCO_3$@$CaFe_2O_4$ NC and meso$CaCO_3$@$CaFe_2O_4$-Dox NC. (b) and (c) show enlarge FTIR spectra of meso$CaCO_3$@$CaFe_2O_4$-Dox NC in range 950-1850 and 2750-3250 cm^{-1}.

4.4.9 Dox loading and release study by UV-Vis absorption spectroscopy:

The amount of Dox loaded in nanocarrier was estimated by UV-Vis absorption spectroscopy technique, by subtracting the amount of Dox remained in supernatant form the initials Dox taken. Figure 4.4.11. (a) shows UV-Vis absorption spectra of Dox before loading and Dox remained in supernatant. Drastic reduction in the absorption intensity of Dox in supernatant than initial Dox suggested very high loading efficiency [14]. Loading capacity and loading efficiency were found to be ~4 and 95%. Figure 4.4.11(b) shows UV-Vis absorption spectra of meso$CaCO_3$@$CaFe_2O_4$-Dox NC with UV-Vis absorption spectra of pure Dox (in Inset of (b). Appearance of characteristic absorption peak of Dox at ~500 nm wavelength in the UV-Vis absorption spectra of meso$CaCO_3$@$CaFe_2O_4$-Dox NC also confirmed loading of Dox in meso$CaCO_3$@$CaFe_2O_4$ NC. A standard calibration curve between absorbance and different known concentration of Dox was plotted to monitor amount of Dox by using UV-Vis absorption spectra. Figure 4.4.12 shows UV-Vis absorption spectra of different known concentration of Dox with corresponding standard calibration curve. A linear behavior ($y = 0.01336x + 0.01192$, $R^2 = 0.999$) was obtained [23].

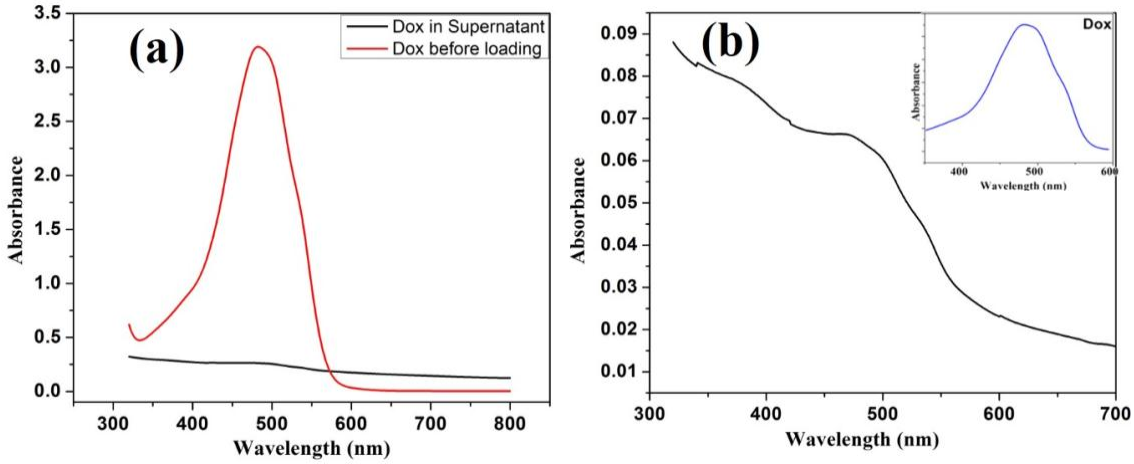

Figure 4.4.11. (a) UV-Vis absorption spectra of Dox before loading and remained Dox in supernatant. (b) UV-Vis absorption spectra of meso$CaCO_3$@$CaFe_2O_4$-Dox NC. Inset of (b) shows UV-Vis absorption spectra of pure Dox.

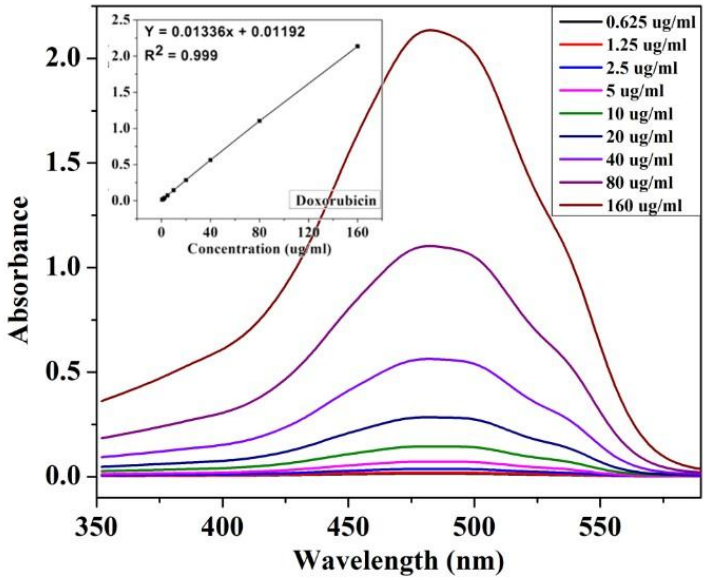

Figure 4.4.12. UV-Vis absorption spectra of different known concentration of Dox with corresponding standard calibration curve.

After successful loading of Dox in meso$CaCO_3$@$CaFe_2O_4$ NC and its confirmation, in vitro release study Dox from meso$CaCO_3$@$CaFe_2O_4$-Dox NC were carried out at two different pH values. pH 5 and 7.4 was selected for this purpose mimicking cancerous cell pH and blood plasma pH value. A sustained and pH dependent release of Dox was observed (figure 4.4.13). It was observed that lower pH accelerates the Dox release. For the first 8 hours, 18 % and 8 % Dox were observed for the pH 5 and 7.4 respectively which is almost double release rate at lower pH in starting hours. After that the release rate becomes slower for both the cases.

Increased release rate at lower pH (pH5) may be due enhanced solubility of Dox and dissolution of $CaCO_3$ matrix at lower pH [14] [24].

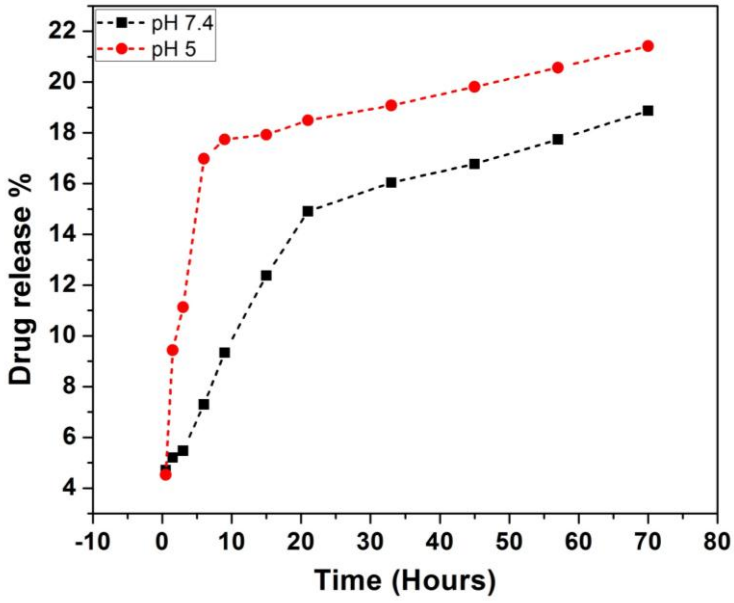

Figure 4.4.13. In vitro release profile Dox from mesoCaCO$_3$@CaFe$_2$O$_4$-Dox NC.

4.4.10 MTT assay against normal and cancerous cells

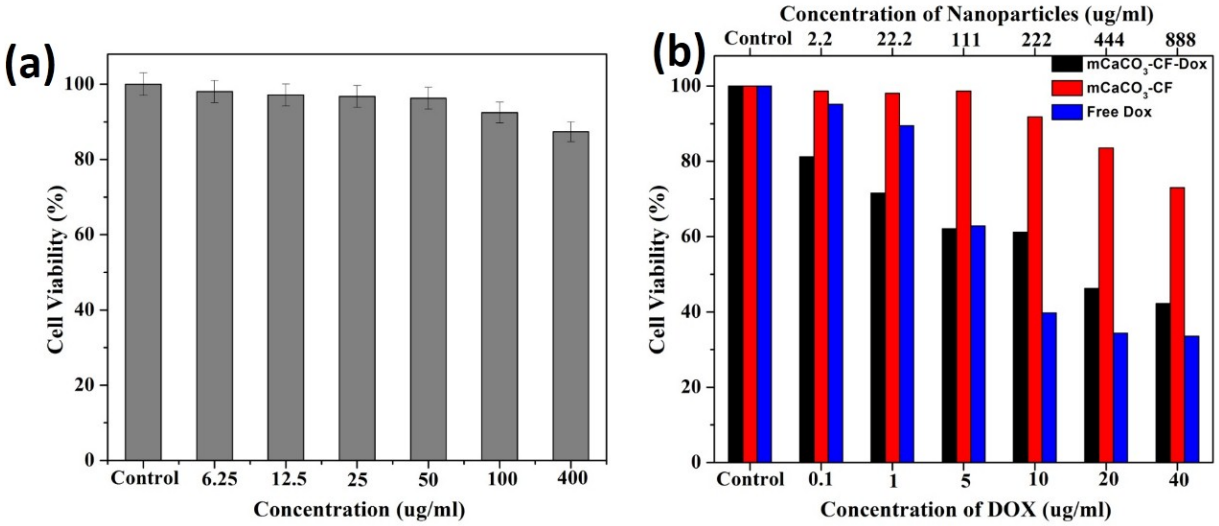

Figure 4.4.14. (a) Cell viabilities obtained by MTT assay of RAW 264.7 cells incubated with different amount of mesoCaCO$_3$@CaFe$_2$O$_4$. (b) Cell inhibition of Hela cells incubated with free Dox, plain mesoCaCO$_3$@CaFe$_2$O$_4$ and mesoCaCO$_3$@CaFe$_2$O$_4$-Dox NC with different concentrations.

Biocompatibility of prepared mesoCaCO$_3$@CaFe$_2$O$_4$ NC was studied by MTT assay against normal cells. Cell viabilities obtained by MTT assay of RAW 264.7 cells incubated with different amount of mesoCaCO$_3$@CaFe$_2$O$_4$ are shown in figure 4.4.14 (a). Very high cell viabilities upto high dose (400 µg/ml) mesoCaCO$_3$@CaFe$_2$O$_4$ was observed thus MTT assay on normal cells of mesoCaCO$_3$@CaFe$_2$O$_4$ NC confirmed it biocompatible nature. Anticancer activity of Dox loaded nanocarrier was also studied by MTT assay against cancer cell line. Cell inhibition of Hela cells incubated with free Dox, plain mesoCaCO$_3$@CaFe$_2$O$_4$ and mesoCaCO$_3$@CaFe$_2$O$_4$-Dox NC with different concentrations are shown in figure 4.4.14 (b). Cells were treated with 0.1, 1, 5, 10, 20 and 40µg/ml concentrion of free and loaded Dox. It was observed that blank nanocarrier does not showed much killing effect on Hela cells. Dox loaded nanocarrier, mesoCaCO$_3$@CaFe$_2$O$_4$ -Dox NC, has shown a promising killing effect on Hela cells like the free Dox. mesoCaCO$_3$@CaFe$_2$O$_4$-Dox NC has shown faster killing than free Dox upto 5µg/ml concentration. There after inhibition became slight slower than free Dox. The IC50 of free Dox and loaded Dox were found to be 10 and in between 10-20 µg/ml respectively. The maximum cell killing (at 40µg/ml) of free Dox and mesoCaCO$_3$@CaFe$_2$O$_4$-Dox NC were found to be ~66 and ~60 respectively. Even though the mesoCaCO$_3$@CaFe$_2$O$_4$-Dox NC has shown slightly lower cell inhibition than free Dox, but the free Dox molecules lacks in targeting ability which cause severe side effect on normal body parts. The slightly less toxicity of loaded Dox of mesoCaCO$_3$@CaFe$_2$O$_4$-Dox NC could be due to its slower release than diffusion of free Dox molecule. mesoCaCO$_3$@CaFe$_2$O$_4$-Dox NC advantages over free Dox such biocompatible to normal tissues, magnetic targeting ability, pH dependent site specific controlled release ability etc.

4.4.11 Conclusions

In this work, egg shell derived CaCO$_3$ based novel multifunctional magnetic mesoporous nanocarrier (mesoCaCO$_3$@CaFe$_2$O$_4$ NC) have been developed by green route using lemon juice and waste egg shell. CaFe$_2$O$_4$ NP was used as magnetic component and CTAB was used as soft template to generate pores. Prepared mesoCaCO$_3$@CaFe$_2$O$_4$ NC was characterized thoroughly for different physicochemical properties and plausible formation mechanism has been proposed. Particles size of CaFe$_2$O$_4$ NP and mesoCaCO$_3$@CaFe$_2$O$_4$ NC were found to be ~10 and ~150 nm, respectively. VSM analysis have revealed superparamagnetic natures of CaFe$_2$O$_4$ NP and mesoCaCO$_3$@CaFe$_2$O$_4$ NC. Anticancer drug loading and release study mesoCaCO$_3$@CaFe$_2$O$_4$ NC were conducted using Dox. A sustained

and pH dependent Dox release profile were obtained. Biocompatibility and cytotoxicity of meso$CaCO_3$@$CaFe_2O_4$ NC and meso$CaCO_3$@$CaFe_2O_4$-Dox NC were studied by MTT assays against RAW 264.7 cells and Hela cells. Obtained results suggested that prepared meso$CaCO_3$@$CaFe_2O_4$-Dox NC could have potential application in targeted drug delivery. The use of biocompatible and biodegradable meso$CaCO_3$@$CaFe_2O_4$ NC, prepared via a green route, in nanomedicine will be safe, inexpensive and environmental friendly.

4.4.12 References

[1] J. Kim, H.S. Kim, N. Lee, T. Kim, H. Kim, T. Yu, I.C. Song, W.K. Moon, T. Hyeon, Multifunctional Uniform Nanoparticles Composed of a Magnetite Nanocrystal Core and a Mesoporous Silica Shell for Magnetic Resonance and Fluorescence Imaging and for Drug Delivery, Angewandte Chemie 120(44) (2008) 8566-8569.
[2] J. Kim, J.E. Lee, J. Lee, J.H. Yu, B.C. Kim, K. An, Y. Hwang, C.-H. Shin, J.-G. Park, J. Kim, T. Hyeon, Magnetic Fluorescent Delivery Vehicle Using Uniform Mesoporous Silica Spheres Embedded with Monodisperse Magnetic and Semiconductor Nanocrystals, Journal of the American Chemical Society 128(3) (2006) 688-689.
[3] J.E. Lee, N. Lee, T. Kim, J. Kim, T. Hyeon, Multifunctional Mesoporous Silica Nanocomposite Nanoparticles for Theranostic Applications, Accounts of Chemical Research 44(10) (2011) 893-902.
[4] W.-H. Chen, G.-F. Luo, Q. Lei, F.-Y. Cao, J.-X. Fan, W.-X. Qiu, H.-Z. Jia, S. Hong, F. Fang, X. Zeng, R.-X. Zhuo, X.-Z. Zhang, Rational design of multifunctional magnetic mesoporous silica nanoparticle for tumor-targeted magnetic resonance imaging and precise therapy, Biomaterials 76(Supplement C) (2016) 87-101.
[5] Alvarez-Berr, #xed, M.P. os, N. Sosa-Cintron, M. Rodriguez-Lugo, R. Juneja, J.L. Vivero-Escoto, Hybrid Nanomaterials Based on Iron Oxide Nanoparticles and Mesoporous Silica Nanoparticles: Overcoming Challenges in Current Cancer Treatments, Journal of Chemistry 2016 (2016) 15.
[6] L. Khanna, N.K. Verma, PEG/CaFe2O4 nanocomposite: Structural, morphological, magnetic and thermal analyses, Physica B: Condensed Matter 427 (2013) 68-75.
[7] S. Sharma, A. Verma, B.V. Teja, G. Pandey, N. Mittapelly, R. Trivedi, P.R. Mishra, An insight into functionalized calcium based inorganic nanomaterials in biomedicine: Trends and transitions, Colloids and Surfaces B: Biointerfaces 133(Supplement C) (2015) 120-139.
[8] E.G.A. S. P. M. C. Souza, F. E. Morais1, E. V. Santos, M. L. Silva, C. A. Martinez-Huitle1, N. S. Fernandes, Determination of calcium in tablets containing calcium citrate using thermogravimetry (TG), Braz. J. Therm. Anal. 2(1) (2013) 17 - 22.
[9] K.M. Shigematsu Akinori, Toba Yasuhiro, Tomizawa Akira, Novel milk-derived magnesium/calcium materials and methods for producing the same, EP 1 008 303 A1, in: E.P. Office (Ed.) European Patent Office, 2000.
[10] H. Peng, K. Li, T. Wang, J. Wang, J. Wang, R. Zhu, D. Sun, S. Wang, Preparation of hierarchical mesoporous CaCO3 by a facile binary solvent approach as anticancer drug carrier for etoposide, Nanoscale Research Letters 8(1) (2013) 321.
[11] A. Samariya, S.N. Dolia, A.S. Prasad, P.K. Sharma, S.P. Pareek, M.S. Dhawan, S. Kumar, Size dependent structural and magnetic behaviour of CaFe2O4, Current Applied Physics 13(5) (2013) 830-835.
[12] M. Qasim, R.S. Braj, A.H. Naqvi, P. Paik, D. Das, Silver nanoparticles embedded mesoporous SiO 2 nanosphere: an effective anticandidal agent against Candida albicans 077, Nanotechnology 26(28) (2015) 285102.
[13] Y. Tian, J. Qi, W. Zhang, Q. Cai, X. Jiang, Facile, One-Pot Synthesis, and Antibacterial Activity of Mesoporous Silica Nanoparticles Decorated with Well-Dispersed Silver Nanoparticles, ACS Applied Materials & Interfaces 6(15) (2014) 12038-12045.
[14] H. Shi, L. Li, L. Zhang, T. Wang, C. Wang, D. Zhu, Z. Su, Designed preparation of polyacrylic acid/calcium carbonate nanoparticles with high doxorubicin payload for liver cancer chemotherapy, CrystEngComm 17(26) (2015) 4768-4773.
[15] J.M. Du, Z.M. Liu, Z.H. Li, B.X. Han, Y. Huang, J.L. Zhang, Synthesis of mesoporous SrCO3 spheres and hollow CaCO3 spheres in room-temperature ionic liquid, Micropor Mesopor Mat 83 (2005) 145-149.
[16] Y.W. Hou, A.G. Kong, X.H. Zhao, H.Y. Zhu, Y.K. Shan, Synthesis of high surface area mesoporous carbonates in novel ionic liquid, Mater Lett 63 (2009) 1061-1064.
[17] M. Qasim, K. Asghar, B.R. Singh, S. Prathapani, W. Khan, A.H. Naqvi, D. Das, Magnetically recyclable Ni0.5Zn0.5Fe2O4/Zn0.95Ni0.05O nano-photocatalyst: Structural, optical, magnetic and photocatalytic

properties, Spectrochimica Acta Part A: Molecular and Biomolecular Spectroscopy 137(Supplement C) (2015) 1348-1356.
[18] K. Asghar, M. Qasim, G. Dharmapuri, D. Das, Investigation on a smart nanocarrier with a mesoporous magnetic core and thermo-responsive shell for co-delivery of doxorubicin and curcumin: a new approach towards combination therapy of cancer, RSC Adv. 7(46) (2017) 28802-28818.
[19] L. Khanna, N.K. Verma, Size-dependent magnetic properties of calcium ferrite nanoparticles, Journal of Magnetism and Magnetic Materials 336 (2013) 1-7.
[20] M.J. Pirouz, M.H. Beyki, F. Shemirani, Anhydride functionalised calcium ferrite nanoparticles: A new selective magnetic material for enrichment of lead ions from water and food samples, Food Chemistry 170(Supplement C) (2015) 131-137.
[21] S. Li, Y. Ma, X. Yue, Z. Cao, Z. Dai, One-pot construction of doxorubicin conjugated magnetic silica nanoparticles, New Journal of Chemistry 33(12) (2009) 2414-2418.
[22] S. Kayal, R.V. Ramanujan, Doxorubicin loaded PVA coated iron oxide nanoparticles for targeted drug delivery, Materials Science and Engineering: C 30(3) (2010) 484-490.
[23] M. Qasim, K. Asghar, G. Dharmapuri, D. Das, Investigation of novel superparamagnetic Ni0.5Zn0.5Fe2O4@albumen nanoparticles for controlled delivery of anticancer drug, Nanotechnology 28(36) (2017) 365101.
[24] K.H. Min, H.S. Min, H.J. Lee, D.J. Park, J.Y. Yhee, K. Kim, I.C. Kwon, S.Y. Jeong, O.F. Silvestre, X. Chen, Y.-S. Hwang, E.-C. Kim, S.C. Lee, pH-Controlled Gas-Generating Mineralized Nanoparticles: A Theranostic Agent for Ultrasound Imaging and Therapy of Cancers, ACS Nano 9(1) (2015) 134-145.

Section 4.5: Synthesis and characterization of multifunctional NZF@mSiO$_2$ and NZF@mSiO$_2$-CuS-PEG

This section first describes the synthesis and characterization of $Ni_{0.5}Zn_{0.5}Fe_2O_4$@mesoporousSiO_2 (NZF@mSiO_2) NC followed by discussion on use of NZF@mSiO_2 NC for the development of NIR active multifunctional NZF@mSiO_2-CuS-PEG nanocomposites. After successful preparation and characterization of NZF@mSiO_2 NC, NZF@mSiO_2 was used to prepare a multifunctional NZF@mSiO_2-CuS-PEG.

4.5.1 Synthesis and characterization of NZF@mSiO$_2$ NC

The unique properties of being able to be guided by an external magnetic field make superparamagnetic MNP very useful core materials for nano-carrier design. For biomedical application such for drug delivery, the MNP needs to be stable in aqueous solutions, which can be achieved by the surface modification of MNP and thus by making core-shell nanoparticles. The coated shell material simultaneously provides several functions such as oxidation resistance of MNP core, prevention of agglomeration, provide biocompatibility, hydrophilicity, and functionality to hold drug molecules. Among the various type of shell materials, impervious silica layer is usually used to coat the magnetic core to achieve improved biocompatibility, stability and dispersibility. Mesoporous silica nanoparticles (MSNs) have been used as carriers for drug/gene/antimicrobial agents due to its biocompatibility, hydrophilicity, stability and drug loading ability (porosity) [1]. CTAB based templating technique has been generally used to synthesize MSNs with high surface areas, and tunable pore sizes. Pure MSN based nanocarriers (without any surface functionalization) lacks in tumor targeting ability which minimizes delivery of drug at tumor site. Magnetic targeting ability can be achieved in nanocarriers by incorporating MNP within MSN matrix. Magnetic tumor targeting is simple and inexpensive than antibody based targeting[2]. A primary aim of magnetic nanocarrier based drug delivery system is to develop a platform that effectively reduces systemic toxicity of drugs while retaining their pharmacological activity. Magnetic nanocarrier based drug delivery systems offer several advantages over the administration of molecular free drugs viz. specific targeting ability, enhanced permeability and retention (EPR),

controlled drug release, improved solubility and stability of drugs, low toxicity to normal cell, low clearance, long circulation time etc, which contribute to enhanced tumor cell death [2]. Soft magnetic Ni–Zn ferrites nanoparticles are one of the most versatile magnetic nanoparticles as they have high saturation magnetization, high Curie temperature, superparamagnetic nature, chemical stability, low coercivity and biodegradability. Recently, anticancer activity of Ni-Zn ferrite was conducted and it was reported that Ni–Zn ferrites nanoparticles have potential cytotoxicity against studied cancer cells- HT29, MCF-7, and HepG2 cells [3, 4].

In the present work, we have combined superparamagnetic $Ni_{0.5}Zn_{0.5}Fe_2O_4$ and MSN together in one entity to fabricate multifunctional nanocarrier for anticancer drug delivery application. In this study, $Ni_{0.5}Zn_{0.5}Fe_2O_4$@mesoporousSiO_2 (NZF@mSiO_2) core shell nanocarrier was synthesized by sol-gel method using pre-synthesized NZF NPs, TEOS (as a silica source) and CTAB (as sacrificial template) and characterized for different physicochemical properties. The structural and morphological properties were studied by X-ray powder diffraction (XRD), transmission electron microscope (TEM), and field emission scanning electron microscope (FESEM) techniques. XRD pattern and TEM micrographs confirm the coexistence of $Ni_{0.5}Zn_{0.5}Fe_2O_4$ and SiO_2 phases in the nanocomposites. Average crystallite size of $Ni_{0.5}Zn_{0.5}Fe_2O_4$ NPs was found to be around ~21 nm. Particles size of NZF@mSiO_2 measured by TEM and FESEM are found to be ~200-400 nm. High-resolution transmission electron microscopy (HRTEM) results confirm successful formation of NZF@mSiO_2 core shell nanocomposites having well symmetric structure and ellipsoidal shape. HRTEM analysis confirmed the presence of pores (5-10 nm) on the surface of SiO_2 nanosphere. Magnetic properties of NZF@mSiO_2 nanocarriers were studied by vibrating sample magnetometer (VSM) technique. NZF@mSiO_2 nanocarriers were found to be super-paramagnetic in nature with negligible coercivity and remanent magnetization. The M_s value for NZF@mSiO_2 were found to be 9.5 emu/gm respectively. These NZF@ mSiO_2 NPs could have potential applications in targeted drug delivery due to its magnetic tunability and biocompatibility.

4.5.1.1 Preparation and formation mechanism of NZF@mSiO_2 nanocarrier:

The twostep process was used in the preparation of NZF@mSiO_2 nanocarrier. First step involved the synthesis of superparamagnetic $Ni_{0.5}Zn_{0.5}Fe_2O_4$ nanoparticles. In the synthesis process, CTAB not only serves as the stabilizing surfactant for the dispersion of $Ni_{0.5}Zn_{0.5}Fe_2O_4$ nanoparticles in aqueous solvent but also as the template for the development of mesopores on

silica surface [5]. When $Ni_{0.5}Zn_{0.5}Fe_2O_4$ nanoparticlesand CTAB are mixed in water, CTAB aggregates to form soft assembly of micellar rod holding $Ni_{0.5}Zn_{0.5}Fe_2O_4$ nanoparticles due to hydrophobic interaction between the hydrophobic $Ni_{0.5}Zn_{0.5}Fe_2O_4$ nanoparticles and non-polar tails of CTAB. On TEOS addition to this solution hydrolysis and condensation of TEOS occurs and presence of these soft templates of CTAB containing $Ni_{0.5}Zn_{0.5}Fe_2O_4$ nanoparticles offers heterogeneous nucleation sites for silica deposition [2, 5]. Due to the continuous deposition of silica on CTAB soft template, a 3D meso-structure of silica network have been formed. CTAB can be removed by washing with suitable solvent (acidic ethanol solution, pH 1.4), or by calcinations above its decomposition temperature.

4.5.1.2 Structural analysis of NZF@mSiO₂ NC by XRD:

X-ray diffractometer has been used to study the phase and crystalline structure of prepared NZF@$mSiO_2$ nano-carrier. Fig. 4.5.1 (a) and (b) shows the powder XRD pattern of NZF@$mSiO_2$ nano-carrier and pure mesoporous silica ($mSiO_2$) nanoparticles respectively. A broad hump centred at ~ 22^o and few sharp characteristic diffraction peaks centred at 18, 30, 36, 37, 43, 53, 57, 63, and 74^o were observed in the XRD pattern of NZF@$mSiO_2$ nano-carrier. The broad hump ~22° confirmed the presence of amorphous silica in the nanocarrier [1]. All the sharp characteristic diffraction peaks can be attributed to the presence of cubic $Ni_{0.5}Zn_{0.5}Fe_2O_4$ NPs having (111), (220), (311), (222), (400), (422), (511), (440), and (533) reflection planes, respectively[6]. The observed sharp diffraction peaks in the XRD pattern of NZF@$mSiO_2$ nanocarrier matches well with the standard diffraction pattern of the spinel cubic crystal structure of $Ni_{0.5}Zn_{0.5}Fe_2O_4$ {JCPDS card No. 520278}. XRD pattern of pure mesoporous silica nanoparticles show presence of a broad hump at around 22^o without any other diffraction peaks. Presence of both broad and sharp diffraction peaks of silica and $Ni_{0.5}Zn_{0.5}Fe_2O_4$ nanoparticles respectively in XRD pattern of NZF@$mSiO_2$ nano-carrier confirm successful formation of nanocomposite nanocarrier and also confirm that the spinel cubic structure of $Ni_{0.5}Zn_{0.5}Fe_2O_4$ nano-crystals does not alter after coating with $mSiO_2$. The average crystallite size of $Ni_{0.5}Zn_{0.5}Fe_2O_4$ nanoparticles was estimated by Debye–Sherrer equation using most intense peak (311) and was found to be ~21 nm.

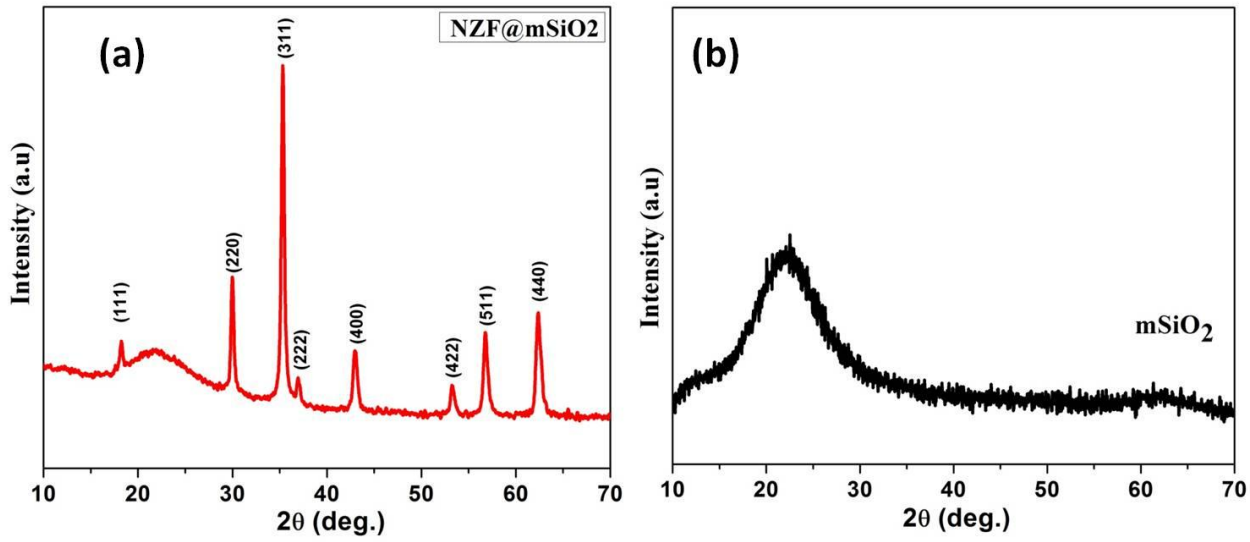

Figure 4.5.1. X-ray diffraction patterns of NZF@$mSiO_2$ nanocarrier (a) and pure mesoporous silica nanoparticles (b).

4.5.1.3 Morphological and structural analysis of NZF@$mSiO_2$ NC by TEM and FESEM:

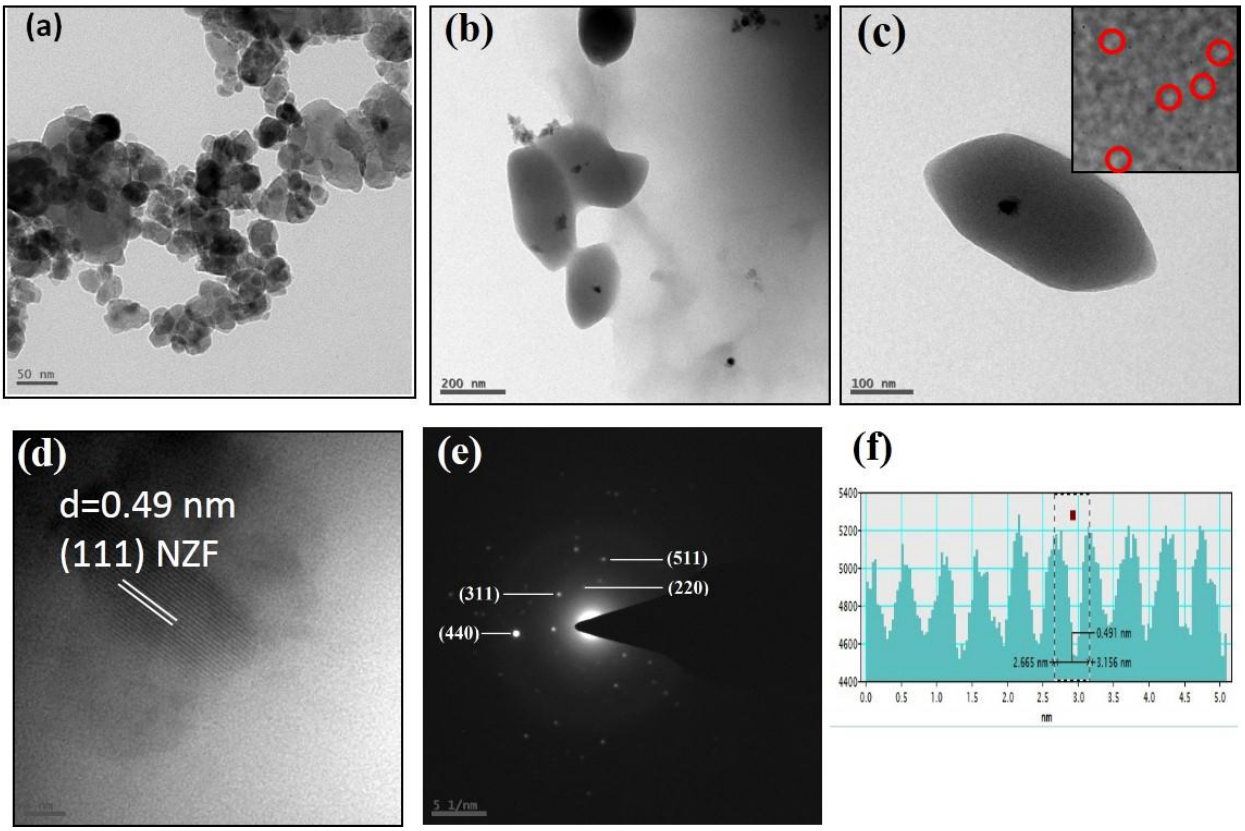

Figure 4.5.2. TEM micrographs of pure $Ni_{0.5}Zn_{0.5}Fe_2O_4$ NPs (a) and NZF@$mSiO_2$ nanocarrier (b-c). Inset of figure (c) show presence of pores (red circle). (d) HRTEM image of core part of nanocomposites that confirm presence of NZF with clear ordered atomic fringes. (e) indexed SAED pattern of NZF@mSiO2 nanoparticles. (f) is line profile through atomic fringes.

TEM and FESEM micrographs have been used to study the particle size and morphology of $Ni_{0.5}Zn_{0.5}Fe_2O_4$ NPs and NZF@$mSiO_2$ nano-carrier. Figure 4.5.2 (a) shows the TEM micrographs of $Ni_{0.5}Zn_{0.5}Fe_2O_4$ NPs. It was observed from TEM micrograph that synthesized $Ni_{0.5}Zn_{0.5}Fe_2O_4$ NPs were nearly spherical in shape. Particles size of $Ni_{0.5}Zn_{0.5}Fe_2O_4$ NPs was found to be ~20-25 nm. The estimated particles size value is matching well with the value calculated from XRD pattern, which suggests particle is made up of single crystal. Figure 4.5.2 (b) and 4.5.2 (c) show the TEM micrographs of NZF@$mSiO_2$ nanocarrier at different magnification. TEM analysis confirms the formation of mesoporous NZF@$mSiO_2$ nanocarrier with core shell type of nanocomposites. It can be observed from figure 4.5.2 (b) and 4.5.2 (c) that core shell nanocomposites are having well symmetric structure with ellipsoidal shape. Dark black $Ni_{0.5}Zn_{0.5}Fe_2O_4$ NPs of size 20-25 nm can be seen in the core of $mSiO_2$ nanocarrier. Due to the magnetic nature of $Ni_{0.5}Zn_{0.5}Fe_2O_4$, it absorbs more electron than mesoporous silica which make it darker in appearance than silica in the TEM micrograph of nanocarrier [6]. Mesoporous nature (less dense network) of silica nanoparticles also make it appear lighter (grey) in TEM micrograph. Dense silica nanoparticles of similar size are expected to appear relatively darker in TEM images due to high density. Inset of figure 4.5.2(c) clearly shows presence of pores (marked as red circle) of 5-10 nm in diameter on the silica surface. These mesopores are generated by decomposition of CTAB templates on calcinations at 500 ^{o} C.

HRTEM analysis also confirmed the formation of core shell nanocomposite, with a crystalline core of $Ni_{0.5}Zn_{0.5}Fe_2O_4$ nanoparticles coated with the amorphous silica shell as shown in figure 4.5.2 (d) Presence of very clear ordered lattice fringes of cubic $Ni_{0.5}Zn_{0.5}Fe_2O_4$ nanoparticles in the HRTEM image confirm presence of crystalline $Ni_{0.5}Zn_{0.5}Fe_2O_4$ nanoparticles in nanocarrier. The d spacing of plane is estimated by line profile (figure f) and found to be 0.49 nm which correspond to the (111) plane of $Ni_{0.5}Zn_{0.5}Fe_2O_4$ nanoparticles. Indexed SAED pattern of core shell nanocarrier further confirmed the presence of polycrystalline spinel cubic core in the nanocomposites (e). The diameter of mesopores depends on the diameter of formed sacrificial micellar rod due to hydrophobic interaction between nonpolar chains of CTAB molecules. Particles size of NZF@$mSiO_2$ core shell nano-carrier observed from TEM was found to be ~200-400 nm. Similar results were reported by J Kim et al. for iron oxide-mesoporous silica core shell nanocomposite [5].

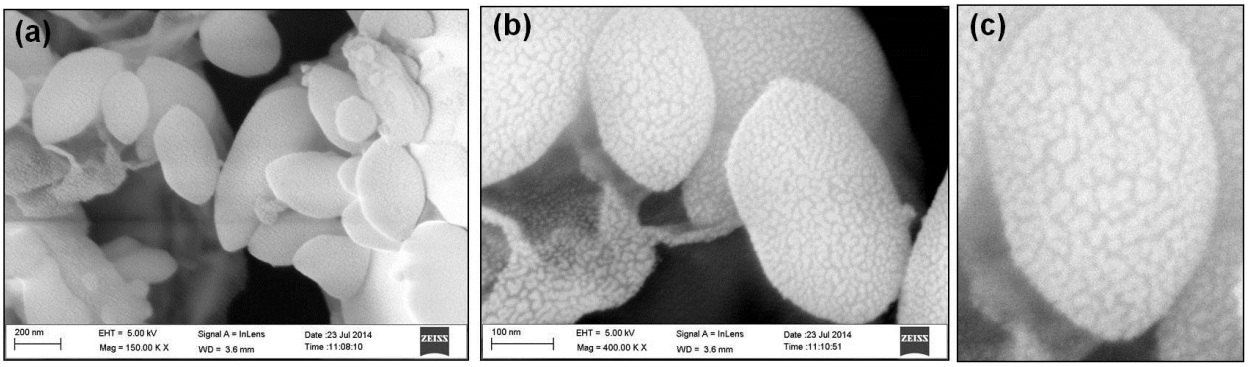

Figure 4.5.3. (a-c) FESEM micrographs of NZF@mSiO$_2$ nanocarriers. Enlarge image of single particle is shown in image (c).

Figure 4.5.3(a-c) shows the FESEM images of NZF@mSiO$_2$ nano-carrier It was observed that prepared nanocomposites particles are ellipsoidal in shape as observed under TEM. Enlarge images of single NZF@mSiO$_2$ nanocarrier is shown in figure 4.5.3(c). Particles size of NZF@mSiO$_2$ nano-carrier was found to ~ 200-400 nm. Appearance of rough surface of NZF@mSiO$_2$ nano-carrier in FESEM image suggests porous nature of mSiO$_2$. $Ni_{0.5}Zn_{0.5}Fe_2O_4$ NPs were not visible due to uniform coating of mSiO$_2$ on them. Obtained results are similar to the results obtained by TEM micrographs.

4.5.1.4 FTIR analysis of NZF@mSiO$_2$ NC:

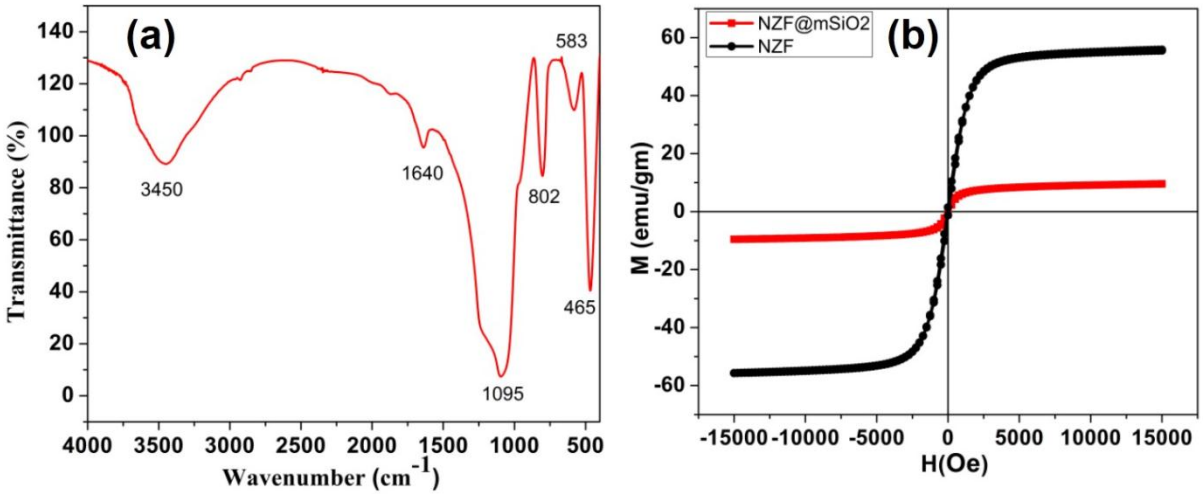

Figure 4.5.4. (a) FTIR spectra of NZF@mSiO$_2$ nanocarriers. (b)Room temperature magnetization-hysteresis (M-H) curve of NZF@mSiO$_2$ nanocarriers

Formation of NZF@mSiO$_2$ nano-carrier was also confirmed by FTIR analysis. Figure 4.5.4(a) shows FTIR spectra of NZF@mSiO$_2$ nano-carrier. Obtained spectra shows characteristic bands of silica and NZF NP confirming successful formation of NZF@mSiO$_2$

nano-carrier. The band at ~465, ~800 (Si-O-Si) and 1095 (Si-O-Si stretching) cm $^{-1}$ are characteristic bands of SiO_2. The bands at 583 can be attributed to the NZF NPs. The band at 1640 and 3450 can be assigned to the free H_2O and stretching of SiO-H present on the surface of silica.

4.5.1.5 Magnetic properties of NZF@mSiO$_2$ NC:

Magnetic property has been studied by VSM techniques and obtained room temperature M-H curve of $Ni_{0.5}Zn_{0.5}Fe_2O_4$ nanoparticles and NZF@mSiO$_2$ nano-carrier are shown in fig. 4.5.4(b). Both the samples were found to be superparamagnetic in nature with very low remanent magnetization and coercivity. The superparamagnetic behavior of NZF@mSiO$_2$ nano-carrier can be attributed to the smaller NZF NPs. Magnetic controllability of MNPs depends upon its saturation magnetization (M_s) value. The M_s values for NZF and NZF@ mSiO$_2$ were found to be 56 and 9.5 emu/gm respectively. Remanent magnetizations of NZF and NZF@mSiO$_2$ NPs are found to be 1.35 and 1.04 emu/gm respectively. The coercivity values are 36 and 79 Oe for NZF and NZF@mSiO$_2$ NPs, respectively. The slight increase in coercivity for the NZF@mSiO$_2$ NPs could be attributed to domain wall pining by the non-magnetic phase. Saturation magnetization (M_s) value of magnetic nanocomposites is proportionally dependent on magnetic content of the nanocomposite. In the present case low content of magnetic NZF NPs in the NZF@mSiO$_2$ nano-carrier is the reason for low M_s value of NZF@mSiO$_2$ nano-carrier. The M_s value of present system is sufficient for targeted drug delivery applications. This NZF@mSiO$_2$ nano-carrier could have potential to be used as biocompatible, inexpensive magnetic nano-carrier for anti-cancer targeted drug delivery.

4.5.2 Synthesis and characterization of NIR active multifunctional NZF@mSiO$_2$-CuS-PEG NC for 5Fluorouracil delivery and imaging

After successful preparation and characterization of NZF@mSiO$_2$ NC, NZF@mSiO$_2$ was used to prepare multifunctional NZF@mSiO$_2$-CuS-PEG for simultaneous multi-modal imaging and combined chemo- and photothermal therapies. Imaging and photo irradiation involving Near-infrared light (NIR, $\lambda = 700 \sim 1100$ nm) has attracted superior attention due to its deep penetration and minimal absorption in tissues. NPs which absorb light in NIR region are being investigated for photothermal based hyperthermia and imaging applications. The combination of photothermal therapy, hyperthermia chemotherapy could have better synergistic therapeutic effects than any of the single treatments alone [7]. Incorporating NIR active NPs in magnetic mesoporous silica (NZF@mSiO$_2$ NC) will provide a multifunctional

system which can simultaneously deliver multitask such as chemotherapy, imaging, phototherapy etc. CuS NPs have been reported as a new type of NIR based photothermal ablation agent for cancer treatment. The NIR absorption of CuS NP is based on the d-d transition of Cu^{2+} ions which is not affected by surrounding matrix unlike SPR based photothermal therapy using Au and Ag NPs, thus leading to higher photothermal ablation efficiency [8-11]. Low cost, d-d transition based NIR absorption ability, long term biocompatibility and a better tumor penetrating ability are advantages to the CuS NPs[12]. Higher NIR absorbance of CuS NP can enhance the efficiency to reduce the laser power for treatment. In this work, carboxylic functionalized CuS nanoparticles (which is known to absorb light in NIR region) were first prepared and then embedded on the surface of amine functionalized NZF@$mSiO_2$ followed by coating with PEG to obtain a multifunctional NZF@$mSiO_2$-CuS-PEG nanocarriers. Recently it has been reported the amine functionalization of silica enhanced loading capacity of 5Flu due to their similar hydrophilicity and opposite charges thus amine functionalized silica was used in this study [13]. The incorporated CuS NP can be used to generate thermal energy upon NIR laser irradiation, resulting ablation of cancerous cells. Anticancer drug 5 Fluorouracil (5Flu) was loaded in the NZF@$mSiO_2$-CuS-PEG nanocarriers to obtain a nanohybrid system as a therapeutic agent, which combine photothermal treatment with a controlled 5Flu release ability and also provide imaging ability. Prepared NZF@$mSiO_2$-CuS-PEG nanocarriers were characterized by XRD, TEM, FTIR UV-Vis-NIR, and VSM techniques. Embedding of CuS NPs on the surface of NZF@$mSiO_2$ NC was confirmed by XRD and TEM. Amine functional groups of mesoporous silica may help in loading of 5 Fluorouracil which is an anticancer drug. Loading of 5 Fluorouracil in the nanocarrier was confirmed by both FTIR and UV-Vis-NIR, spectroscopy techniques. MTT assay results show its suitability for drug deliver application. Presence of CuS on the NZF@$mSiO_2$-CuS-PEG make them suitable for imaging and chemo-photothermal therapy of cancer.

4.5.2.1 Formation of NZF@$mSiO_2$-CuS-PEG and NZF@$mSiO_2$-CuS-PEG-5Flu:

Schematic of NZF@$mSiO_2$-CuS-PEG NP formation from NZF@$mSiO_2$ is shown in figure 4.5.5. The NZF@$mSiO_2$ was first prepared by sol gel method as discussed above; then, the surface of silica was modified with amine group using APTES to get positive charged on the surface. The amine group were incorporated on the surface of mesoporous silica to facilitate excellent loading of negatively charged 5Flu as well as decoration of negatively charged CuS NP (due to presence of carboxyl group) [13]. After, surface modification of $mSiO_2$, negatively

charged CuS NPs were static adsorbed onto the surface of positively charged $mSiO_2$. The biocompatible PEG was further coated on the surface of NZF@$mSiO_2$-CuS NP to obtain NZF@$mSiO_2$-CuS-PEG NP. Sonication energy could have facilitated the coating of PEG on the surface of NZF@$mSiO_2$-CuS NP. Due to biocompatible and hydrophilic nature of PEG, surface coating of nanocarriers with PEG will enhance its biocompatibility, water dispersibility/stability, blood circulation time and the internalization efficiency.

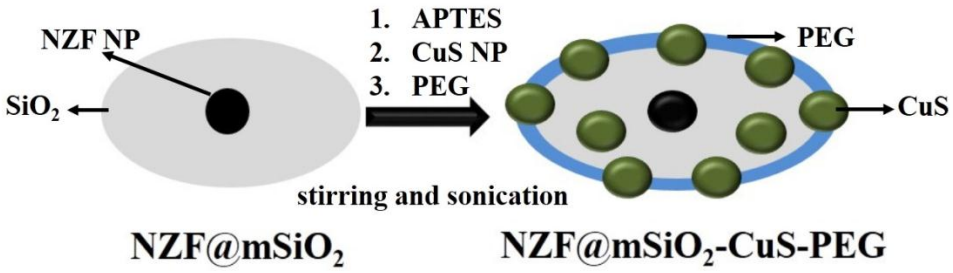

Figure 4.5.5. Schematic of NZF@$mSiO_2$-CuS-PEG NP formation from NZF@$mSiO_2$.

4.5.2.2 Structural characterizations of NZF@$mSiO_2$-CuS-PEG and NZF@$mSiO_2$-CuS-PEG-5Flu by XRD:

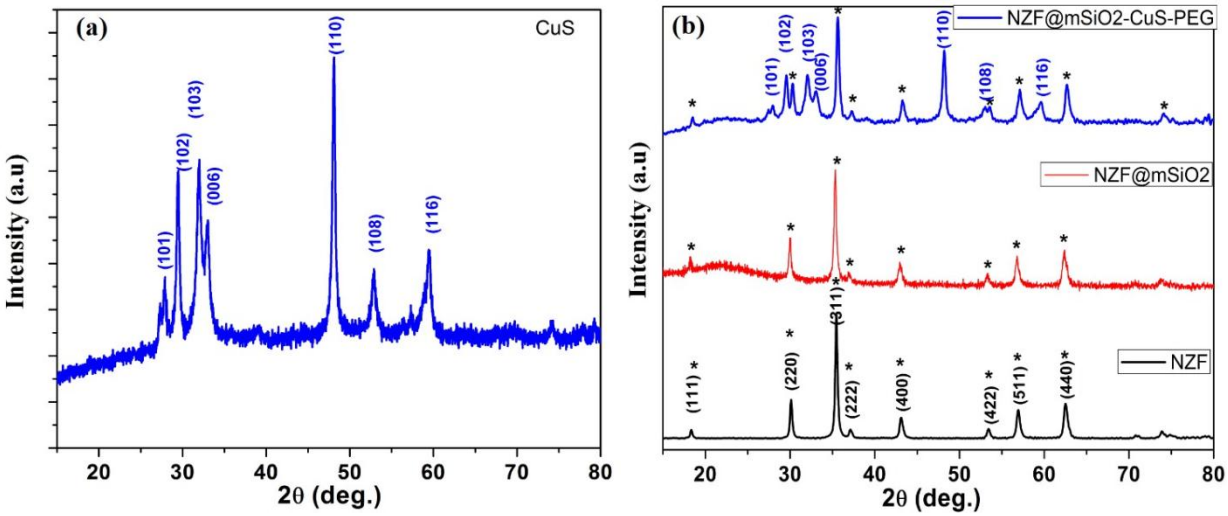

Figure 4.5.6. X-ray diffraction patterns of CuS NP (a). X-ray diffraction patterns of NZF NP, NZF@$mSiO_2$ and NZF@$mSiO_2$-CuS-PEG NC (b).

Crystalline structure and formation of prepared CuS NP and NZF@$mSiO_2$-CuS-PEG NC were studied using XRD analysis. Figure 4.5.6(a) shows XRD pattern of CuS NP which shows presence of characteristic peaks at 2Θ 27.9, 29.5, 32.0, 33.0, 48.1, 52.9, and 59.5. These peaks can have assigned to the (101), (102), (103), (006) (110), (108) and (116) planes of

hexagonal CuS NP respectively, confirming successful formation of CuS NP. The observed peaks match well with the standard data (PDF No 02-0820). Figure 4.5.6(b) shows X-ray diffraction patterns of NZF NP, NZF@$mSiO_2$ and NZF@$mSiO_2$-CuS-PEG NC. XRD pattern of NZF NP and NZF@$mSiO_2$ show sharp characteristic peaks of spinel cubic NZF NP. The peaks of NZF were assigned to the (111), (220), (311), (222), (400), (422), (511), (440), and (533) reflection planes. In case of NZF@$mSiO_2$ broad hump of amorphous mesoporous silica at 22^o was also observed. The reflection of plane of NZF NP were indexed in black color. These peaks of NZF were also marked with the star symbol (*) in all three XRD pattern. The peaks of CuS NP in XRD pattern of NZF@$mSiO_2$-CuS-PEG NC were indexed in blue color. Crystallite size of CuS NP and NZF was found to be ~21.7 and 21 nm. NZF@$mSiO_2$-CuS-PEG NC shows characteristic peaks of CuS and NZF NPs which confirm the formation of nanocomposite. Hump of silica at 22^o can also be observed. Thus, XRD analysis suggest successful formation of NZF@$mSiO_2$-CuS-PEG NC.

4.5.2.3 Morphological, structural and compositional analysis by TEM

Particles size and morphology of CuS NP and NZF@$mSiO_2$-CuS-PEG NC were studied by TEM. Figure 4.5.7 (a) shows TEM micrograph of CuS NP. Particles were found to be irregular in shape with size in range of 30-60 nm. Figure 4.5.7 (b-d) show TEM micrographs of NZF@$mSiO_2$-CuS-PEG NC at different magnification. Presence of smaller CuS NPs on bigger NZF@$mSiO_2$ can be seen clearly. Smaller CuS NPs on the surface of NZF@$mSiO_2$ are shown in images (c-d). HRTEM analysis of surface CuS NP were further carried out to confirm the formation of NZF@$mSiO_2$-CuS-PEG NC. HRTEM image of smaller surface CuS NP are shown in figure (e) which shows the presence of well-ordered atomic planes. The d spacing of these planes was estimated to be 0.31 nm which can be assigned to the (102) plane of hexagonal CuS. For better visualization and understanding IFFT analysis of the red marked area in (e) was carried out and is shown in (f). Further formation of NZF@$mSiO_2$-CuS-PEG NC was done by EDS analysis and obtained spectra is shown in (g). Presence of elemental peaks of Ni, Zn, Fe, Cu, S, O, and Si confirmed formation of NZF@$mSiO_2$-CuS-PEG NC. The CuS NP are hold on the surface of NZF@$mSiO_2$ through electrostatic attraction and the polymeric PEG could have also favored binding of CuS NP. Probably, due to very less amount of PEG and its thin coating, PEG was not distinctly visible as a separate layer in TEM micrograph. However, the existence of PEG on the surface of NZF@$mSiO_2$-CuS-PEG NC has been confirmed by FTIR analysis.

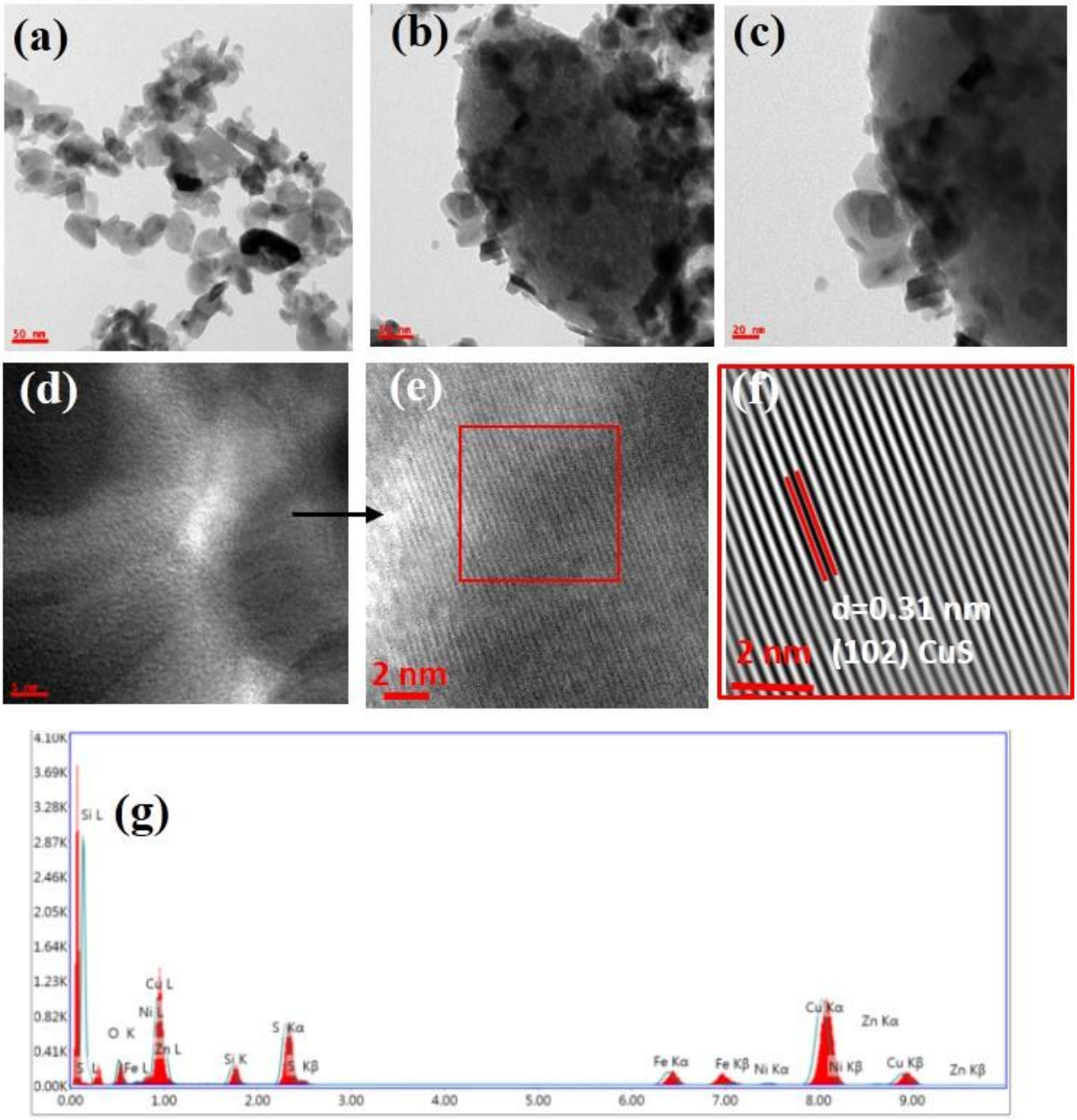

Figure 4.5.7. TEM micrographs of pure CuS (a) and NZF@mSiO$_2$-CuS-PEG NC (b-d). HRTEM image of indicated region of (d) is shown in (e). IFFT image of the red marked area in (e) is shown in (f). EDS spectra of NZF@mSiO$_2$-CuS-PEG NC is shown in (g).

4.5.2.4 Magnetic properties of NZF@mSiO$_2$-CuS-PEG NC

Magnetic properties of NZF@mSiO$_2$-CuS-PEG NC was studied by VSM analysis and obtained Room Temperature M-H curves is shown figure 4.5.8(a). NZF@mSiO$_2$-CuS-PEG NC was found to be superparamagnetic nature with the negligible coercivity and Mr values. Ms value of NZF@mSiO$_2$-CuS-PEG NC was found to be ~7 emu/g which is slightly less than

NZF@$mSiO_2$ due to presence of nonmagnetic CuS and PEG. The Mr and coercivity values of NZF@$mSiO_2$-CuS-PEG NC were found to be 0.58 and 62 Oe respectively. The Ms value of nanocarrier represent its magnetic targeting ability and it is proportionally dependent on the amount of magnetic component in the nanocarriers. In the present case, the obtained Ms values of the prepared NZF@$mSiO_2$-CuS-PEG NC is sufficient for drug delivery applications.

4.5.2.5 Functional groups and 5Flu loading study by FTIR

To further confirm the formation of NZF@$mSiO_2$-CuS-PEG and loading of 5Flu in NZF@$mSiO_2$-CuS-PEG, FTIR analysis of NZF@$mSiO_2$-CuS-PEG and NZF@$mSiO_2$-CuS-PEG-5Flu NC have been carried out and shown in figure 4.5.8(b). FTIR analysis of NZF@$mSiO_2$-CuS-PEG shows characteristic bands of all constituent species confirming successful formation of nanocomposites. The band at ~462, ~800 and 1092 cm^{-1} were assigned to the presence of SiO_2, and the bands at 415, and 556 are characteristic band of NZF NP which can be attributed to the octahedral and tetrahedral lattice vibrations [14] [6]. The bands at 586 cm-1 can be assigned to the Fe-O stretching vibration. The band at 1613 (symmetric stretching of C=O), 1106 (asymmetric stretching of C=O) and 615 cm-1 (vibration of Cu-S) can be assigned to the CuS NPs [15]. The bands at in between 1300-1500 cm-1 (one at 1350 cm-1 due to deformation vibration of PEG backbone) and two bands at 2850 and 2918 cm^{-1} in both the samples may have originated from PEG. The band at 2850 and 2918 cm^{-1} can be attributed to the aliphatic C-H of long alkyl chain methylene in PEG. FTIR spectra of 5Flu loaded. The band at 1550 cm^{-1} can be attributed to the vibration of N-H which suggest presence of amine group in sample. NZF@$mSiO_2$-CuS-PEG shows presence of all characteristic bands of NZF@$mSiO_2$-CuS-PEG in addition with few new characteristic bands of 5Flu which confirm loading of 5Flu in NZF@$mSiO_2$-CuS-PEG NC. The bands at 3264, 3069, 1650 and 1247 cm^{-1} in FTIR spectra of NZF@$mSiO_2$-CuS-PEG-5Flu NC were assigned to the presence of 5Flu [16] [17] [18]. The peak at 1650 cm^{-1} is attributed to the vibrations of C=O in 5-Flu. The peaks at 1650 cm−1 and 1247 cm−1 are prominent characteristic peaks of 5Flu [16]. The bands at 3264, 3069 cm^{-1} which have originated from aromatic C-H stretching vibration are assigned to 5Flu as in the NZF@$mSiO_2$-CuS-PEG-5Flu NC, 5Flu only has aromatic structure. The bands at 1247 cm^{-1} was assigned to the C-F stretching vibration of 5Flu[16].

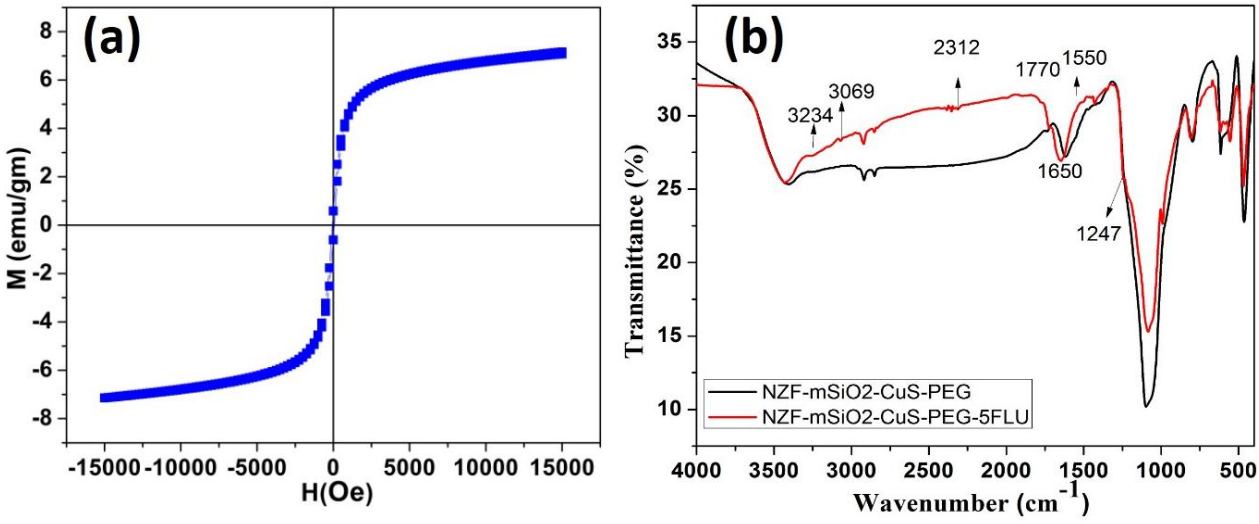

Figure 4.5.8. (a) Room temperature (M-H) curves of NZF@mSiO$_2$-CuS-PEG NC. (b) FTIR spectra of NZF@mSiO$_2$-CuS-PEG and NZF@mSiO$_2$-CuS-PEG-5Flu NC.

4.5.2.6 Thermal property (TGA analysis)

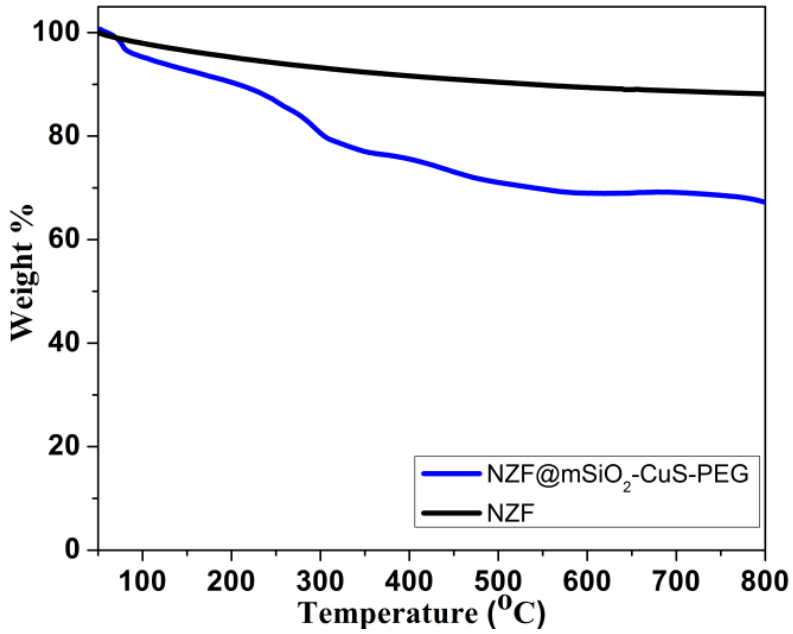

Figure 4.5.9. TGA curve of NZF NP and NZF@mSiO$_2$-CuS-PEG NC.

Thermal properties of nanocomposite and presence of PEG on the surface of mesoporous silica were analyzed by TGA analysis. Thermal degradation behavior of NZF NP and NZF@mSiO$_2$-CuS-PEG NC are shown in figure 4.5.9. Weight loss of ~3-7 % from both the sample below 150 ^{o}C can be attributed to the loss of physically adsorbed water molecules. In case of NZF NPs very minute total weight loss of ~12% was observed. NZF@mSiO$_2$-CuS-PEG NC has shown total weight loss of about ~32.5 %. The major weight was observed in between 150-550

^{o}C. The weight loss (23%) in between 150-550 ^{o}C may be attributed to the decomposition of CuS and PEG chains. After 550 ^{o}C there was very little (2.3%) till final temperature.

4.5.2.7 NIR absorption of NZF@mSiO$_2$-CuS-PEG-5Flu NC

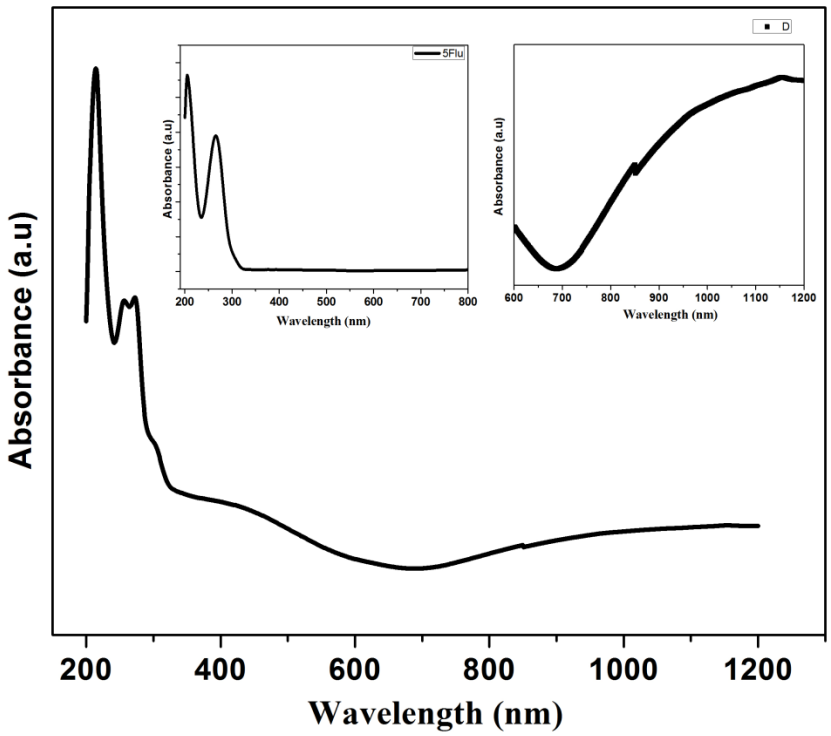

Figure 4.5.10. NIR-UV-Vis absorption spectra of NZF@mSiO$_2$-CuS-PEG-5Flu NC in wavelength range of 200-1200 nm. Enlarge absorption spectra of NZF@mSiO$_2$-CuS-PEG-5Flu NC in range of 600-1200 nm is shown in right side inset figure. UV-Vis absorption spectra of 5Flu drug is shown in left side inset figure.

Loading of 5Flu and presence of CuS NP in the NZF@mSiO$_2$-CuS-PEG NC were further supported by NIR-UV-Vis absorption study. Figure 4.5.10 shows NIR-UV-Vis absorption spectra of NZF@mSiO$_2$-CuS-PEG-5Flu NC in wavelength range of 200-1200 nm. A broad hump type of peak centering about 1100 nm can be assigned to the CuS NP which originated due to the d-d transitions of Cu^{+2} ions. The same absorption peak can clearly be observed in inset (right) graph of figure 4.5.10. In addition, two sharp absorption characteristic peaks of 5Flu below 300 nm (at 206 and 266 nm) wavelength can also be clearly seen which confirm presence of 5Flu in NZF@mSiO$_2$-CuS-PEG NC. For a reference, the UV-Vis absorption spectra of pure 5Flu have been inserted in the inset (left) graph of figure 9. The observed absorption band at 206 nm and 266 nm corresponds to the π–π* transition and n–π* transition of the 5Flu molecule, respectively [18].

4.5.2.8 5Flu loading and release study

Figure 4.5.11. shows UV-Vis absorption spectra of 5Flu before loading and 5Flu remained in supernatant, which was used to quantify the amount of 5Flu loading/release. The significant suppression of absorption intensity of supernatant indicates a good loading behavior of 5Flu. The LE and LC were found to be 79 and 21% respectively. For quantification of 5Flu throughout the experiment, standard calibration of 5Flu was plotted using absorbance of known concentration of 5Flu and shown in figure 4.5.12(a) ($y = 0.03457x + 0.01334$, $R^2 = 0.998$). This observation suggested the suitability of NZF@$mSiO_2$-CuS-PEG NC as drug for 5Flu drug in cancer treatment. The high loading capability of 5flu in the NZF@$mSiO_2$-CuS-PEG NC can be attributed to the similar hydrophilicity of drug and nanocarrier as well as their opposite charges which have enable high loading through electrostatic attraction and miscibility. To check suitability of NZF@$mSiO_2$-CuS-PEG-5Flu NC as drug efficient drug carrier, in vitro 5Flu release behavior was also studied and shown in figure 4.5.12(b). NZF@$mSiO_2$-CuS-PEG-5Flu NC has showed a fast drug release behavior than other prepared nanocarrier. The release rate depends on many factors such as types of interaction between drug and carriers, pore size, solubility of drug in release media, pH and temperature of media etc. A rapid drug release was observed in first 12 hours where ~56% of loaded 5Flu has been release, thereafter release rate become relatively slow and only ~13 % loaded 5Flu released in between 12 to 80 hours. After 80 hours of incubation total 5Flu release was observed to be ~69 %. The sustained release rate could be due the presence of PEG on the surface of NZF@$mSiO_2$-CuS-PEG-5Flu NC.

4.5.2.9 Biocompatibility test

For biomedical application nanocarrier must be biocompatible in nature, thus the biocompatibility of blank NZF@$mSiO_2$-CuS-PEG NC have been against normal RAW 264.7 cells. Figure 4.5.13 shows the cell viability of normal RAW 264.7 cells dosed with different concentration of NZF@$mSiO_2$-CuS-PEG NC. NZF@$mSiO_2$-CuS-PEG NC was found to be biocompatible in nature as it has not shown much killing even at high dose (400 µg/ml). No killing was observed till 100 µg/ml dose of NZF@$mSiO_2$-CuS-PEG NC. 80% cell viability was observed at maximum dose of 400 µg/ml. Thus, the prepared nanocarrier are biocompatible and have very potentials to be used as drug carrier for cancer treatment.

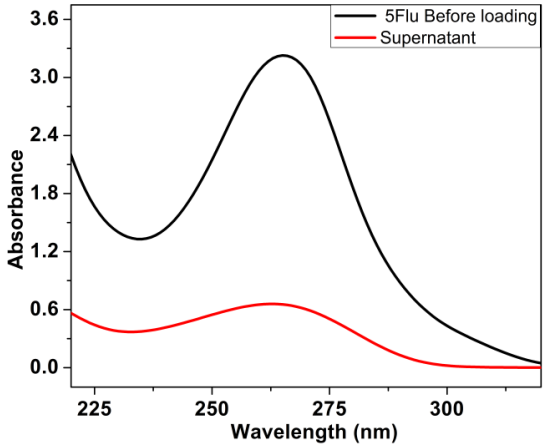

Figure 4.5.11. UV-Vis absorption spectra of 5Flu before loading and 5Flu remained in supernatant.

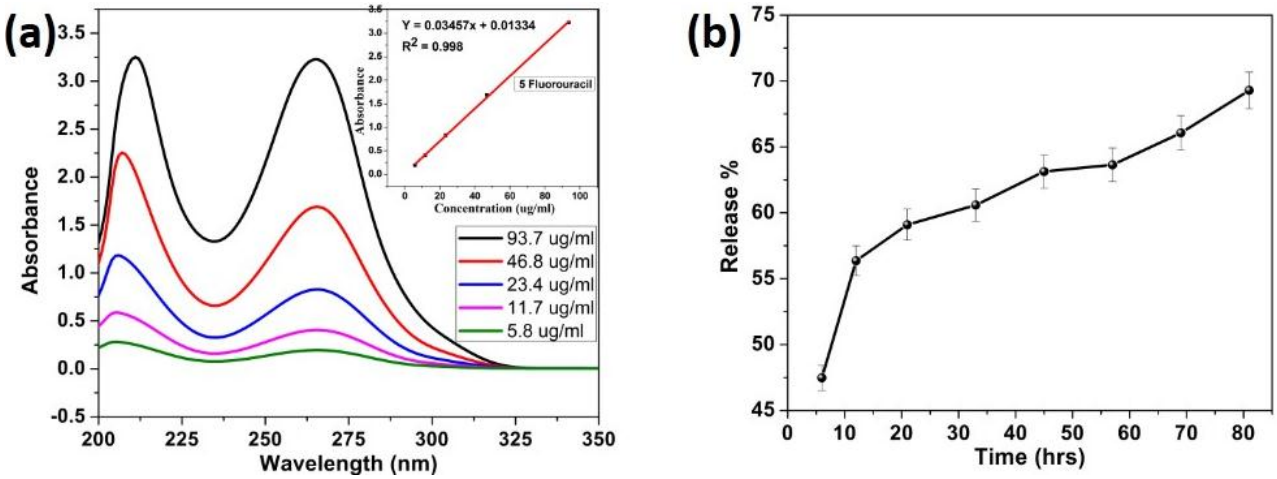

Figure 4.5.12 (a) UV-vis absorption spectra of different known concentration 5Flu with corresponding standard calibration. (b) 5Flu released profile from NZF@mSiO$_2$-CuS-PEG-5Flu NC.

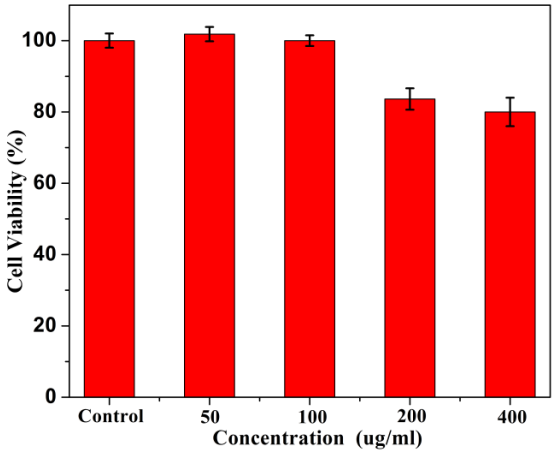

Figure 4.5.13. Cell viability of normal cells (RAW 264.7 cells) treated with different concentration of NZF@mSiO$_2$-CuS-PEG NC.

4.5.3 Conclusions

First $Ni_{0.5}Zn_{0.5}Fe_2O_4$@mesoporousSiO_2 (NZF@mSiO_2) core shell nanocarrier was successfully synthesized by sol-gel method and characterized for its structural, morphological and magnetic properties. Then, NZF@mSiO_2 was used to prepare multifunctional NZF@mSiO_2-CuS-PEG NC for simultaneous multi-modal imaging and combined chemo- and photothermal therapies. Particles size of NZF@mSiO_2 measured by TEM and FESEM are found to be ~200-400 nm. Morphology of the particles is found to be ellipsoidal in shape. NZF@mSiO_2 nanocarriers were found to be super-paramagnetic in nature with negligible coercivity and remanent magnetization. The M_s values for NZF and NZF@ mSiO_2 were found to be 56 and 9.5 emu/gm respectively. Embedding of CuS NPs on the surface of NZF@mSiO_2 NC was confirmed by XRD and TEM analysis. Loading and release behavior of NZF@mSiO_2-CuS-PEG NC using anticancer drug 5 Fluorouracil have studied. The LE and LC were found to be 79 and 21% respectively. MTT assay results show biocompatible nature of nanocarriers thus its suitability for drug deliver application. Due to biocompatible, porous, superparamagnetic and hydrophilic nature, NZF@mSiO_2-CuS-PEG-5Flu NC nanocarriers are very suitable for targeted drug delivery applications.

4.5.4 References

[1] M. Qasim, R.S. Braj, A.H. Naqvi, P. Paik, D. Das, Silver nanoparticles embedded mesoporous SiO 2 nanosphere: an effective anticandidal agent against Candida albicans 077, Nanotechnology 26(28) (2015) 285102.
[2] Y. Tian, X. Jiang, X. Chen, Z. Shao, W. Yang, Doxorubicin-loaded magnetic silk fibroin nanoparticles for targeted therapy of multidrug-resistant cancer, Advanced materials 26(43) (2014) 7393-8.
[3] M.S. Al-Qubaisi, A. Rasedee, M.H. Flaifel, S.H. Ahmad, S. Hussein-Al-Ali, M.Z. Hussein, E.E. Eid, Z. Zainal, M. Saeed, M. Ilowefah, S. Fakurazi, N. Mohd Isa, M.E. El Zowalaty, Cytotoxicity of nickel zinc ferrite nanoparticles on cancer cells of epithelial origin, International journal of nanomedicine 8 (2013) 2497-508.
[4] M.S. Al-Qubaisi, A. Rasedee, M.H. Flaifel, S.H. Ahmad, S. Hussein-Al-Ali, M.Z. Hussein, Z. Zainal, F.H. Alhassan, Y.H. Taufiq-Yap, E.E. Eid, I.A. Arbab, B.A. Al-Asbahi, T.J. Webster, M.E. El Zowalaty, Induction of apoptosis in cancer cells by NiZn ferrite nanoparticles through mitochondrial cytochrome C release, International journal of nanomedicine 8 (2013) 4115-29.
[5] J. Kim, J.E. Lee, J. Lee, J.H. Yu, B.C. Kim, K. An, Y. Hwang, C.-H. Shin, J.-G. Park, J. Kim, T. Hyeon, Magnetic Fluorescent Delivery Vehicle Using Uniform Mesoporous Silica Spheres Embedded with Monodisperse Magnetic and Semiconductor Nanocrystals, Journal of the American Chemical Society 128(3) (2006) 688-689.
[6] M. Qasim, K. Asghar, B.R. Singh, S. Prathapani, W. Khan, A.H. Naqvi, D. Das, Magnetically recyclable Ni0.5Zn0.5Fe2O4/Zn0.95Ni0.05O nano-photocatalyst: Structural, optical, magnetic and photocatalytic properties, Spectrochimica Acta Part A: Molecular and Biomolecular Spectroscopy 137(Supplement C) (2015) 1348-1356.
[7] G. Song, Q. Wang, Y. Wang, G. Lv, C. Li, R. Zou, Z. Chen, Z. Qin, K. Huo, R. Hu, J. Hu, A Low-Toxic Multifunctional Nanoplatform Based on Cu9S5@mSiO2 Core-Shell Nanocomposites: Combining Photothermal- and Chemotherapies with Infrared Thermal Imaging for Cancer Treatment, Advanced Functional Materials 23(35) (2013) 4281-4292.
[8] G. Yang, R. Lv, F. He, F. Qu, S. Gai, S. Du, Z. Wei, P. Yang, A core/shell/satellite anticancer platform for 808 NIR light-driven multimodal imaging and combined chemo-/photothermal therapy, Nanoscale 7(32) (2015) 13747-13758.

[9] L. Guo, I. Panderi, D.D. Yan, K. Szulak, Y. Li, Y.-T. Chen, H. Ma, D.B. Niesen, N. Seeram, A. Ahmed, B. Yan, D. Pantazatos, W. Lu, A Comparative Study of Hollow Copper Sulfide Nanoparticles and Hollow Gold Nanospheres on Degradability and Toxicity, ACS Nano 7(10) (2013) 8780-8793.
[10] Z. Zha, S. Wang, S. Zhang, E. Qu, H. Ke, J. Wang, Z. Dai, Targeted delivery of CuS nanoparticles through ultrasound image-guided microbubble destruction for efficient photothermal therapy, Nanoscale 5(8) (2013) 3216-3219.
[11] Y. Li, W. Lu, Q. Huang, C. Li, W. Chen, Copper sulfide nanoparticles for photothermal ablation of tumor cells, Nanomedicine 5(8) (2010) 1161-1171.
[12] W. Lingjie, W. Ming, Z. Yongyi, Z. Da, Z. Aixian, L. Xiaolong, L. Jingfeng, Multifunctional PEG modified DOX loaded mesoporous silica nanoparticle@CuS nanohybrids as photo-thermal agent and thermal-triggered drug release vehicle for hepatocellular carcinoma treatment, Nanotechnology 26(2) (2015) 025102.
[13] X. She, L. Chen, C. Li, C. He, L. He, L. Kong, Functionalization of Hollow Mesoporous Silica Nanoparticles for Improved 5-FU Loading, Journal of Nanomaterials 2015 (2015) 9.
[14] M. Jang, J.K. Park, E.W. Shin, Lanthanum functionalized highly ordered mesoporous media: implications of arsenate removal, Microporous and Mesoporous Materials 75(1) (2004) 159-168.
[15] M. Saranya, C. Santhosh, R. Ramachandran, P. Kollu, P. Saravanan, M. Vinoba, S.K. Jeong, A.N. Grace, Hydrothermal growth of CuS nanostructures and its photocatalytic properties, Powder Technology 252(Supplement C) (2014) 25-32.
[16] O.Ş. Merve Olukman, Ebru Kondolot Solak, Release of Anticancer Drug 5-Fluorouracil from Different Ionically Crosslinked Alginate Beads Journal of Biomaterials and Nanobiotechnology, 2012, 3, 3 (2012) 469-479
[17] B. Banerji, S.K. Pramanik, S. Mandal, N.C. Maiti, K. Chaudhuri, Synthesis, characterization and cytotoxicity study of magnetic (Fe3O4) nanoparticles and their drug conjugate, RSC Advances 2(6) (2012) 2493-2497.
[18] C. Chen, L.K. Yee, H. Gong, Y. Zhang, R. Xu, A facile synthesis of strong near infrared fluorescent layered double hydroxide nanovehicles with an anticancer drug for tumor optical imaging and therapy, Nanoscale 5(10) (2013) 4314-4320.

Section 4.6: Multifunctional NZF/$Zn_{0.95}Ni_{0.05}O$ and NZF/$Zn_{0.95}Ni_{0.05}O$-$mSiO_2$ nanocomposites

Heterostructure nanoparticles comprising of magnetic cores and luminescent shells are getting increasing attention in biomedical applications such as magnetic separation, smart nanocarrier based targeted drug delivery and detection of cancer cells, bacteria and viruses [1]. In this section, first, synthesis and characterization of a novel magnetically controllable NZF/$Zn_{0.95}Ni_{0.05}O$ (NZF@Zn), core shell NC will be discussed. After successful preparation and characterization of magneto-optical NZF@Zn NC, it was used to prepared multifunctional NZF@Zn-$mSiO_2$ nano-system. Second part of this section discusses about synthesis and characterization of NZF@Zn-$mSiO_2$ nano-system and its use for the delivery of anticancer drug (curcumin). The ultimate aim was to get multifunctional magnetic nanoparticles and to add drug reservoir to the synthesized NZF@Zn NC. Thus, the prepared single NZF@Zn-$mSiO_2$ and NZF@Zn-$mSiO_2$-Cur nano-system has magnetic, and optical properties along with drug loading ability, which could be used for multimodal imaging and drug delivery applications.

4.6.1 Development, properties and application of magneto-optical NZF@Zn nanocomposites:

Nanocomposites based nano-system having magnetic as well as optical properties are increasingly being studied and developed due to their potential use in biomedical applications including imaging, drug delivery etc. In fact, this type of novel bifunctional nanocomposite which exhibit magnetic-optical properties are excellent agent for imaging (confocal and MRI) and targetable nanocarrier through harnessing of their optical and magnetic properties respectively [1]. The combination of ZnO which is having good optical properties with magnetic NZF NP provide an excellent magneto-optical nanocomposite (NZF@Zn NC) which may find several biomedical applications ranging from multimodal imaging to drug delivery [2]. Further, these type of heterostructures have been proven to have a superior photocatalytic activity. A nanophotocatalist fasten the degradation/conversion of toxic and complex waste compound into the simple non-toxic species using light. The increasing extent of waste water generation from hospitals/textile/laboratory is posing a serious threat to environmental remediation [3]. Constant disposal of noxious organic pollutants lead to unrealizable side effects, since the mineralization efficiency of these pollutants by conventional mineralization methods is inadequate[4]. The use of nanoparticles as catalysts in organic transformations has

attracted considerable interest in recent years, because of their larger surface area-to-volume ratio [5]. Thus, development of nanophotocatalyts with high degradation efficiency will be very useful for degradation biomedical waste such as disposal from hospitals. The commonly used non-magnetic semiconductor photocatalyst possess three main limitations and those are less visible light activity, poor recovery, and fast recombination of the generated electron-hole pairs. Incorporation of ferrite in ZnO helps in improving the quantum yield of ZnO by slowing down the recombination of photogenerated electrons and holes. Since pure ZnO is not suitable for absorption and utilization of visible region of the solar spectrum, in this study Ni doped ZnO ($Zn_{0.95}Ni_{0.05}O$) with a band gap of ~2.95 eV and $Ni_{0.5}Zn_{0.5}Fe_2O_4$ (band gap ~2.2eV) have been chosen to prepare NZF@Zn NC nanophotocatalysts for visible light active, magnetically separable, and recyclable photocatalytic activity. Visible light absorption ability of $Zn_{0.95}Ni_{0.05}O$ could also provide optical imaging ability in NZF@Zn NC using light source of visible region. It is worthy to mention here that exposure to light source of UV region is harmful to body. In this work, NZF@Zn NC with varying amount of NZF (15%NZF@Zn, 40%NZF@Zn and 60%NZF@Zn), have been prepared by sol gel technique using egg albumen to combine the interesting properties of both ferrite and ZnO. The structural, morphological, optical, magnetic, and photocatalytic properties of the synthesized NZF@Zn NC were studied by XRD, HRTEM, FESEM, PL, UV-Vis spectroscopy, and VSM techniques. Powder XRD, TEM, FTIR and energy dispersive spectroscopic (EDS) analyses confirm coexistence of $Ni_{0.5}Zn_{0.5}Fe_2O_4$ and $Zn_{0.95}Ni_{0.05}O$ phases in the catalyst. VSM show all samples to be super-paramagnetic in nature and M_s decrease with decreasing ferrite content in the NC. These NZF@Zn NCs show excellent photocatalytic activities on Rhodamin dye. In the present investigation, $Ni_{0.5}Zn_{0.5}Fe_2O_4/Zn_{0.95}Ni_{0.05}O$ nanocomposites have been prepared, for the first time, using egg albumen as biotemplate, which is environment friendly and cost effective.

4.6.1.1 Structural analysis by XRD

Figure 4.6.1(a) shows the Powder XRD patterns of NZF, 15%NZF@Zn, 40%NZF@Zn, 60%NZF@Zn, and $Zn_{0.95}Ni_{0.05}O$ recorded in the 2Θ range of 20^o - 80^o. The XRD patterns of $Ni_{0.5}Zn_{0.5}Fe_2O_4$ nanoparticles demonstration the sharp diffraction peaks (marked with *) of (220), (311), (222), (400), (422), (511) (440) and (533) planes at 2 Θ 30°, 35°, 43°, 53°, 57°, 62° and 74^o. These observed characteristic peaks confirmed the spinel cubic structure of the crystalline $Ni_{0.5}Zn_{0.5}Fe_2O_4$ (JCPDS card No. 520278). XRD pattern of $Zn_{0.95}Ni_{0.05}O$ nanoparticles show the diffraction peaks (marked with #) of (100), (002), (101), (102), (110), (103), (200), (112), (201), (004) and (202) planes at $2\theta = 31.1^o$, 33.7^o, 35.5^o, 46.8^o,

55.9°, 62.2°, 65.7°, 67.3°, 68.4°,72°, and 76.3° which, confirmed its hexagonal wurtzite structure (JCPDS card No. 790207). XRD patterns of nanocomposites, 15%NZF@Zn, 40%NZF@Zn and 60%NZF@Zn show characteristic peaks of both $Ni_{0.5}Zn_{0.5}Fe_2O_4$ and $Zn_{0.95}Ni_{0.05}O$ materials, which confirmed the formation of polycrystalline nanocomposites. The peak intensity of the ferrite's peaks increases with increasing weight fraction of $Ni_{0.5}Zn_{0.5}Fe_2O_4$ nanoparticle in the composites and similar results have been reported by Roychowdhury et al. [6]. In XRD patterns of these nanocomposites, no extra peaks of impurity have been noticed. The average crystallite sizes of $Ni_{0.5}Zn_{0.5}Fe_2O_4$ and $Zn_{0.95}Ni_{0.05}O$ were calculated from the broadening of the corresponding most intense diffraction peaks, ((311) for NZF and (101) for $Zn_{0.95}Ni_{0.05}O$) using the Debye–Scherrer equation and found to be ~16-25 nm and ~ 22-27 nm respectively. Digital image of all powdered samples ($Ni_{0.5}Zn_{0.5}Fe_2O_4$, 15%NZF@Zn, 40%NZF@Zn and 60%NZF@Zn and $Zn_{0.95}Ni_{0.05}O$) are also shown with respective pattern. NZF and ZnO sample are deep brown and white respectively. The nanocomposites exhibit intermediate colour of both native component that also suggest formation nanocomposites. The colour of nanocomposite becoming dark brown from light brown with increase in the NZF content.

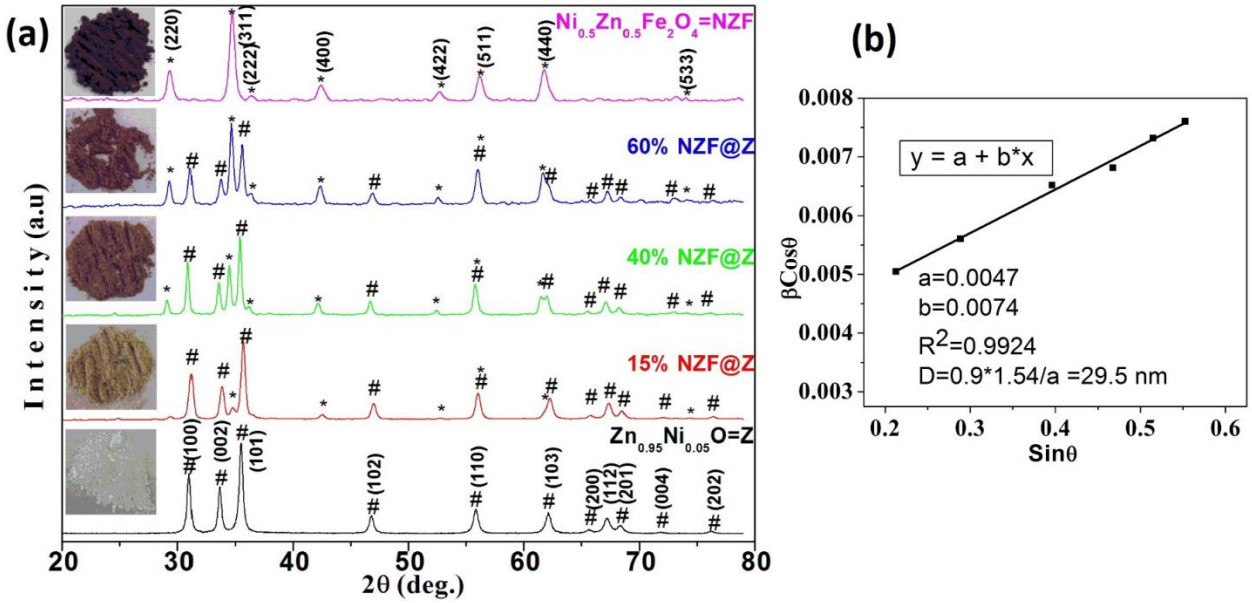

Figure. 4.6.1 (a) XRD pattern of $Ni_{0.5}Zn_{0.5}Fe_2O_4$, 15%NZF@Zn, 40%NZF@Zn and 60%NZF@Zn and $Zn_{0.95}Ni_{0.05}O$ $Ni_{0.5}Zn_{0.5}Fe_2O_4$ (Marked with *), $Zn_{0.95}Ni_{0.05}O$ (marked with #)}. Digital image of all powdered samples are also shown with respective pattern. (b) Williamson-Hall plot of 40%NZF@Zn nanocomposite.

Lattice strain in the samples could be another reason for the broadening of XRD peak. The contributions of lattice strain & crystallite size to broadening of diffraction peaks have been

separated out using Williamson-Hall equation, $\beta\cos\theta = 0.9\lambda/D + 4\varepsilon\sin\theta$, [7] where D is effective crystallite size and ε is effective strain. Figure 4.6.1(b) shows the Williamson-Hall plot (βcosθ vs Sinθ) for a representative sample, 40%NZF@Zn. From the linear fit to the experimental data, the crystalline size was estimated from the y-intercept and the strain ε from the slope of the fitted line. Lattice strains, ε, in $Zn_{0.95}Ni_{0.05}O$ and $Ni_{0.5}Zn_{0.5}Fe_2O_4$ phases were found to be~ -0.006-0.004, both in pristine phases and nanocomposites. Similar strain values have been reported earlier for Fe_3O_4/ZnO nanocomposite & ZnO nanoparticle[6, 7]. A shift in (101) peak position in the diffraction pattern of $Zn_{0.95}Ni_{0.05}O$ can be attributed to the presence of strain in the crystal lattice. The effective crystallite sizes, estimated by Williamson-Hall method, were found to be 17-27 nm and 20-30 nm for $Ni_{0.5}Zn_{0.5}Fe_2O_4$ and $Zn_{0.95}Ni_{0.05}O$ respectively. The values of estimated crystallite sizes showed good agreement between both the method (Debye–Scherrer's &Williamson-Hall). The obtained lattice parameters, estimated by Powder X-ray software, are a = b = 3.27 A^o, c = 5.24 A^o for $Zn_{0.95}Ni_{0.05}O$ and a = b = c = 3.387 A^o for $Ni_{0.5}Zn_{0.5}Fe_2O_4$.

4.6.1.2 FESEM and TEM Analysis:

The FESEM micrographs of NZF NP (a) & 40%NZF@Zn (b) with corresponding EDS spectra (c & d) and TEM images of NZF NP(a) & 40%NZF@Zn (b) with corresponding diffraction patterns are shown in fig. 4.6.2 & 4.6.3 respectively. It has been noticed from FESEM and TEM micrographs that particle sizes in NZF are more uniform than those in 40%NZF@Zn NC. NZF NPs are nearly spherical with particle sizes ~ 22± 6 nm measured both by FESEM and TEM, as shown in fig. 4.6.2(a) and 4.6.3(a) respectively. The particles size distribution graph has been shown in the insets of the respective figures (4.6.2a & 4.6.3a). The distribution is broader in pure NZF than that in 40%NZF@Zn. The bigger particle sizes of 40%NZF@Zn NC than pure NZF NP is due to the coating of $Zn_{0.95}Ni_{0.05}O$ around the surface of NZF NP. The average particle sizes for 40%NZF@Zn was ~70±17 nm, estimated by FESEM & TEM. Fig. 4.6.2(b) shows the formation of agglomerates of 40%NZF@Zn nanoparticles but the distribution of particle sizes is narrower (as shown in inset of fig. 4.6.2(b)) than that in pure NZF, as shown in inset of fig. 4.6.2 (a). The smaller particle sizes (~ 22 nm) of 40%NZF@Zn in figure 4.6.2 (b) could be due to uncoating of $Ni_{0.5}Zn_{0.5}Fe_2O_4$ nanoparticles as also noticed by another researcher[8]. In TEM image of 40%NZF@Zn the NZF particles (appear dark) are seen to be surrounded by $Zn_{0.95}Ni_{0.05}O$ particles (appear grey) confirming the coating of the former by the later. Since ferrite is magnetic in nature it absorbs more electron than $Zn_{0.95}Ni_{0.05}O$ and hence appear darker than ZnO in the TEM image (fig. 4.6.4b) [9]. The

EDS spectra (fig. 4.6.2(c,d)) of $Ni_{0.5}Zn_{0.5}Fe_2O_4$ and 40%NZF@Zn samples show only the presence of Fe, Ni, Zn, and O in stoichiometric ratio, without any impurity peak, confirming the purity of the phases. In 40%NZF@Zn the mass ratio of Fe to Zn is ~0.37, which is close to the expected value 0.365. In 40%NZF@Zn the weight% of O, Fe, Ni, and Zn are found to ~33.05, 16.65, 5.14, and 45.15 respectively.

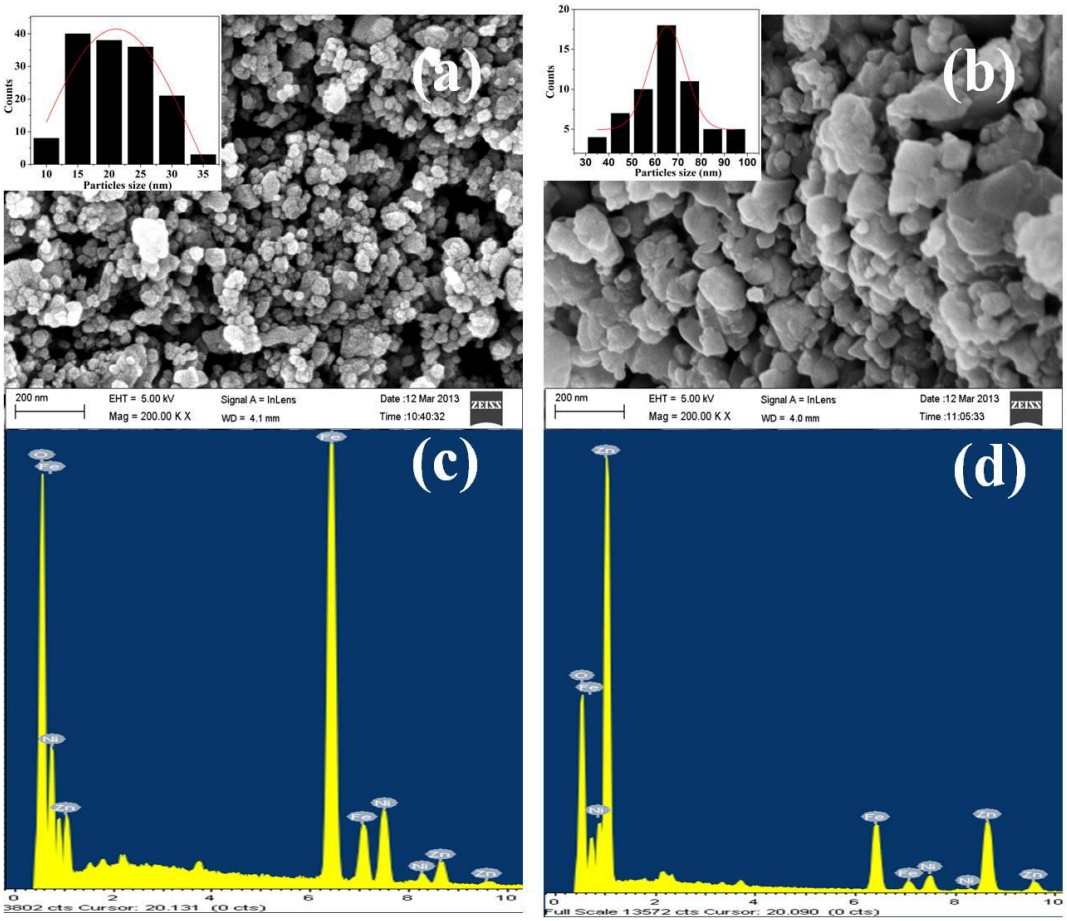

Figure. 4.6.2 FESEM micrographs with particles size distribution histogram of NZF (a), 40%NZF@Zn NC (b) and corresponding EDS spectra (c, d).

Figures 4.6.3 (c,d) show the selected area electron diffraction (SAED) patterns of NZF NP and 40%NZF@Zn NC. The SAED pattern of $Ni_{0.5}Zn_{0.5}Fe_2O_4$ shows distinct dotted ring pattern, which confirms the polycrystalline nature of the cubic spinel $Ni_{0.5}Zn_{0.5}Fe_2O_4$ nanoparticles. The SAED pattern was indexed for cubic structure by estimating the d-spacing from the ring pattern and comparing with the JCPDS card No. 520278 for NZF. 40%NZF@Zn sample was also observed to be polycrystalline in nature. The SAED pattern of 40%NZF@Zn shows a complex and mixed dotted ring pattern, which is due to the presence of both the phases,

cubic $Ni_{0.5}Zn_{0.5}Fe_2O_4$ and hexagonal $Zn_{0.95}Ni_{0.05}O$ [6]. Presence of both phases have also been confirmed by indexing the SAED patterns of other nanocomposites investigated in this study.

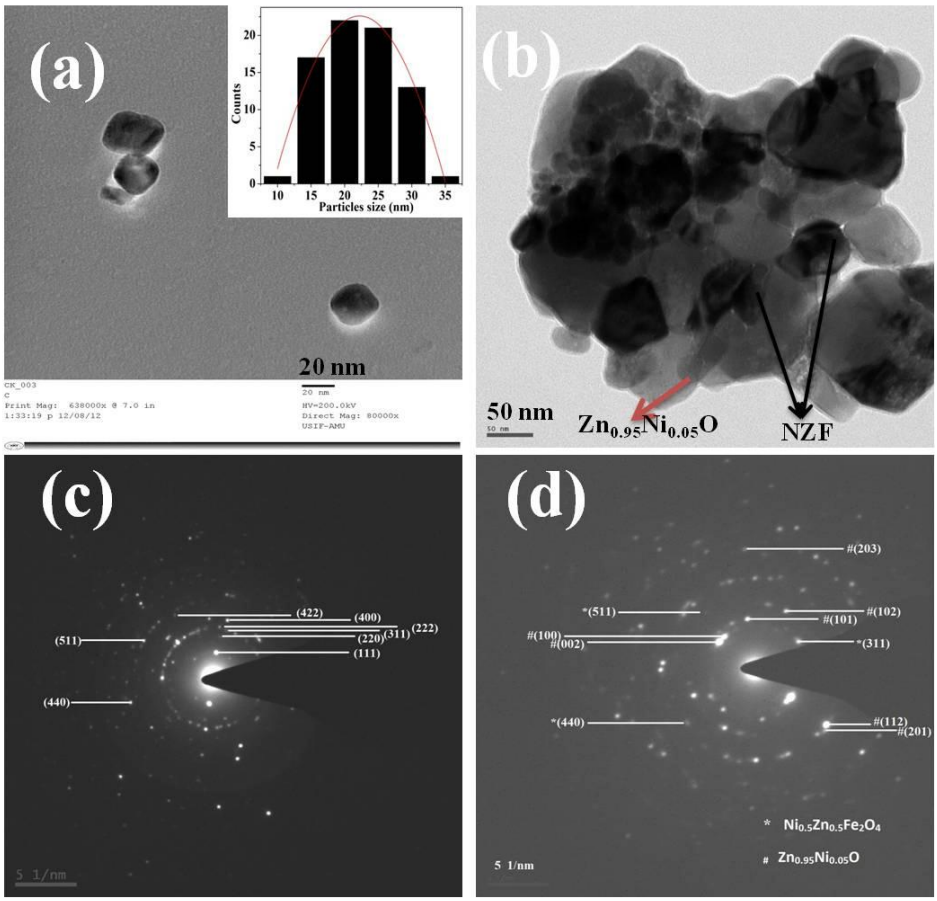

Figure. 4.6.3 (a) TEM micrographs of NZF NP with inset shows the particles size distribution, (b) TEM image of 40%NZF@Zn nanocomposite. (c)Indexed SAED pattern of spinel cubic $Ni_{0.5}Zn_{0.5}Fe_2O_4$ (JCPDS card No. 520278) (d) Indexed SAED pattern of 40%NZF@Zn nanocomposite which shows both spinel cubic $Ni_{0.5}Zn_{0.5}Fe_2O_4$ and hexagonal $Zn_{0.95}Ni_{0.05}O$ present in the sample (JCPDS card No. 790207).

4.6.1.3 Role of egg Albumen:

The mechanism involved in the synthesis of NZF@Zn NC using egg albumen could be explained as follows. Egg albumen or egg white contains different types of proteins such as, ~60% ovalbumin, ~12% Ovotransferrin, ~11% Ovomucoid etc. These proteins have polar-COOH (hydrophilic) and nonpolar-alkyl (hydrophobic) groups. It is very difficult to obtain stable dispersion of bare ferrite NPs due to its hydrophobic nature. When ferrite NPs are sonicated along with albumen these polymeric proteins wrap the surface of NPs and the hydrophilic parts of the protein interact with water giving rise to stability of the suspension. Ovotransferrin is well known for its iron binding property. Ovotransferrin folds into two globular lobes, each containing an iron binding site located within the interdomain cleft of each

lobe[10]. These iron binding sites may also provide affinity toward iron of ferrites and help in decoration of ovotransferrin on ferrite nanoparticles leading to improved stability of the resultant suspension. NZF NPs dispersed in water with egg albumen (water:albumen ratio ~2:3 and ferrite concentration ~10mg/ml) shows improved stability than only in water, as shown in digital photograph in fig. 4.6.4(a). NZF NPs in water are seen to settle within 12 minutes of dispersion, whereas with egg albumen it is stable upto 3 hours. To find out the role of albumen in the synthesis process TEM analysis of albumen treated NZF NPs was carried out after repeated washing with water. Formation of 5-6 nm thick amorphous layer of albumen around the crystalline NZF NPs has been confirmed by HRTEM analysis as shown in figures 4.6.4(b-d). $Ni_{0.5}Zn_{0.5}Fe_2O_4$ nanoparticles decorated with albumen on its surface provide nucleation sites for $Zn_{0.95}Ni_{0.05}O$ deposition [11]. Metal binding tendency of albumen may attract zinc precursor to selectively nucleate on it [12]. $Zn(OH)_2$ is form when zinc nitrate reacts with H_2O. Functional group of egg protein chelate with Zn atom and form protein-$Zn(OH)_2$ complex that further convert to hyderozincite intermediate. On calcination at ~500 ^oC the hyderozincite intermediate decompose to give ZnO [13]. The detailed mechanistic aspect of synthesis of pure ZnO nanoparticles using egg albumin as biotemplate has been discussed in previous report [13].

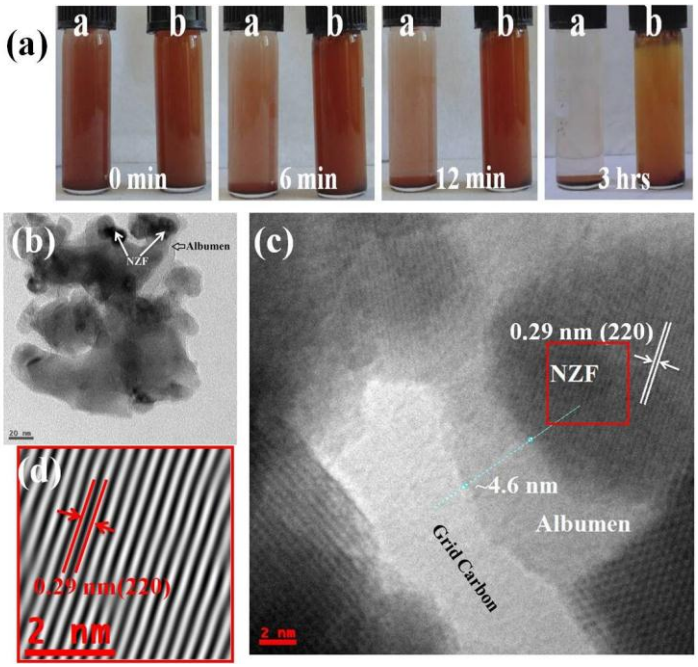

Figure. 4.6.4 (a) The digital photograph shows the stability of dispersed NZF NP in water without-a and with egg albumen-b with respect to time. (b) TEM image of egg albumen coated NZF NPs. (c, d) HRTEM image of crystalline NZF nanoparticle, covered with ~5 nm thick amorphous albumen layer. Inverse Fast Fourier transform from the framed part in (c) is shown in the (d).

4.6.1.4 Optical properties:

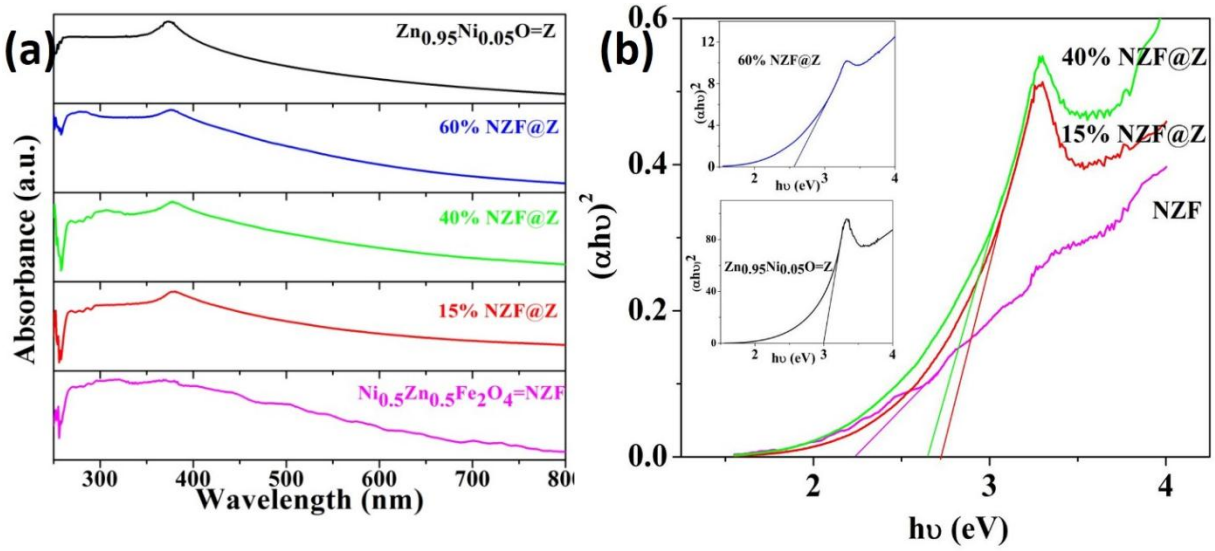

Figure. 4.6.5 (a) UV-Vis absorption spectra of all the samples, ($Ni_{0.5}Zn_{0.5}Fe_2O_4$, 15%NZF@Zn, 40%NZF@Zn, 60%NZF@Zn, and $Zn_{0.95}Ni_{0.05}O$). **(b)** Tauc plot depicting energy band gap of $Ni_{0.5}Zn_{0.5}Fe_2O_4$, 15%NZF@Zn, 40%NZF@Zn in the main panel & 60%NZF@Zn and $Zn_{0.95}Ni_{0.05}O$ in the inset.

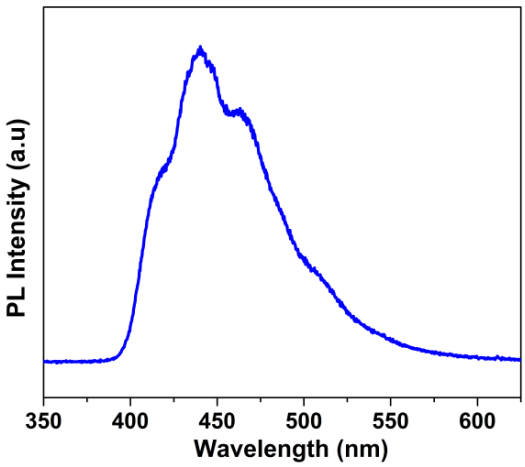

Figure. 4.6.6. Room Temperature PL spectra of 60%NZF@Zn NC.

UV–Visible absorption spectroscopy is a powerful method to discover the optical properties of semiconducting nanoparticles. The absorbance of a material depends on several factors such as band gap, oxygen deficiency, surface roughness and impurity centers. Fig. 4.6.5 (a) shows UV–visible absorption spectra of NZF, 15%NZF@Zn, 40%NZF@Zn, 60%NZF@Zn and $Zn_{0.95}Ni_{0.05}O$. A sharp absorption peak at ~373-380 nm has been observed for $Zn_{0.95}Ni_{0.05}O$ and all nanocomposites. This characteristic absorption peak can be allocated to the intrinsic band-gap absorption of $Zn_{0.95}Ni_{0.05}O$ nanoparticles due to the electron

transitions from valence band to the conduction band (O_{2p}-Zn_{3d}) [13, 14]. Presence of absorbance peak corresponding to $Zn_{0.95}Ni_{0.05}O$ in all samples confirms the formation of nanocomposites. No sharp absorption peak corresponding to $Ni_{0.5}Zn_{0.5}Fe_2O_4$ was observed in the wavelength range studied in this investigation.

Optical band gaps of $Zn_{0.95}Ni_{0.05}O$, 15%NZF@Zn, 40%NZF@Zn, 60%NZF@Zn, and NZF were estimated using the Tauc relationship, $\alpha h\nu = A(h\nu - Eg)^n$, where α is the absorption coefficient, A is a constant, h is the Planck's constant, ν is the photon frequency, and E_g is the optical band gap. The value of n depends on the electronic transition types such as n= ½ is for direct allowed transition and n = 2 for indirect allowed transition. An extrapolation of the linear region of plot $(\alpha h\nu)^2$ vs hν gives the value of the optical band gap, E_g, as shown in fig. 4.6.5(b). Energy band gaps of $Zn_{0.95}Ni_{0.05}O$, 15%NZF@Zn, 40%NZF@Zn, 60%NZF@Zn, and $Ni_{0.5}Zn_{0.5}Fe_2O_4$ were 2.98, 2.72, 2.64, 2.54, and 2.24 eV respectively. The observed energy band gap of $Zn_{0.95}Ni_{0.05}O$ nanoparticles is much lower than that reported for pure ZnO nanoparticles (3.5 eV for ZnO with 16 nm crystallite size) [15]. Energy band gaps of the nanocomposites are found to decrease with increasing NZF content in the nanocomposites. This is due to the reduced band gap energy of $Zn_{0.95}Ni_{0.05}O$ in the nanocomposites in presence of NZF. This reduction in band gap energy has been explained in the literature in terms of mixing of the 4s orbital of Fe and Zn and formation of the conduction band of $Zn_{0.95}Ni_{0.05}O$ at lower energy [6, 16]. It may also be due to the formation of sub band/s within the band gap of $Zn_{0.95}Ni_{0.05}O$ due to doping of metal ions from NZF resulting in lowering of band gap energy. Optical properties of prepared NZF@Zn NC also have been studied by photo-luminescent spectro-photometer. Room temperature PL spectrum of 60%NZF@Zn NC obtained at excitation wavelength of 355 nm is shown in figure 4.6.6. The PL spectra shows, broad visible emission bands ranging from 400 to 550 nm which can related to band edges, surface and defect emissions. The emission peak at 415 nm originated from band edges emission of $Zn_{0.95}Ni_{0.05}O$ NP. The band at 440 and 462 nm which are also in the same visible region can be assigned to the different intermediate band and defects level in 60%NZF@Zn NC nanostructures. A low intense green emission at 510 nm could be attributed to the intrinsic defects such as oxygen vacancies or zinc interstitials. Imaging using light of wavelengths above 400 nm are biomedically relevant because of their applicability in fluorescence assays using a flow cytometer or confocal microscope[1]. Similar, observation for similar kind of system such as Fe_3O_4-ZnO and $CoFe_2O_4$-ZnO nanocomposites were made by other researcher [17, 18].Thus,

photoluminescence spectra confirmed that prepared NZF@Zn NC is photo-luminescent in nature and can be used for biomedical applications.

4.6.1.5 Chemical boding analysis

Available functional group on nanoparticles and formation of nanocomposites were examined by FTIR analysis. FT-IR spectra of 15%NZF@Zn, 40%NZF@Zn, 60%NZF@Zn, and NZF are shown in fig. 4.6.7. The IR spectra of NZF NP shows two principle absorption bands in the wavelength range 400-600 cm^{-1}, the first band is around 422 cm^{-1} and the second around 577 cm^{-1}. These two vibration bands can be attributed to the intrinsic lattice vibrations of octahedral and tetrahedral coordination complexes in the spinel structure, respectively [19]. The broad absorption band ~400-600 cm^{-1} in all samples could arise from the simultaneous presence and overlapping of Zn-O vibration mode at 453 cm^{-1} in ZnO and two above mentioned absorption bands i.e. at 577 cm^{-1} and 422 cm^{-1} in ferrite [6]. In IR spectra of 15%NZF@Zn, 40%NZF@Zn and 60%NZF@Zn nanocomposites, presence of Fe-O vibration mode at 577 cm^{-1} as shoulder has been observed, which increases with increase in ferrite content in these samples. Therefore, IR results also confirm successful formation of nanocomposites. In addition to these absorption peaks, the absorption band centered at ~1121cm^{-1} may be attributed to the vibration mode of C-O, which could indicate the presence of decomposition products of albumen as impurities in the samples [20]. The absorption band at ~2364 cm^{-1} can be assigned to trace of adsorbed or atmospheric CO_2 [21].

4.6.1.6 Magnetic properties:

The room temperature magnetization behavior (M-H curve) of NZF, 60%NZF@Zn, 40%NZF@Zn, & 15%NZF@Zn are shown in fig. 4.6.8. Many magnetic parameters such as, saturation magnetization (M_s), remanent magnetization (M_R) and coercivity (H_c) have been noted from the magnetization curves. Magnetic controllability of magnetic nanocarriers depends upon its Ms value. The M_s values for NZF, 60%NZF@Zn, 40%NZF@Zn, & 15%NZF@Zn were found to be 56, 33, 23, and 8 emu/gm respectively. The Ms values of all the system are much sufficient for magnetically targeted drug delivery applications. It is found that M_s decreases linearly with decrease in ferrite content in these composite samples (fig. 4.6.8 inset). The decreasing M_s value is consistent with the increasing non-magnetic content in these samples [6]. Magnetization behavior at lower field shows all the samples to be super-paramagnetic in nature with very low remanent magnetization and coercivity. M_R of all the samples are found to be ~ 0.4-1.4 emu/gm. The coercivities are 37, 44, 48 and 54 Oe for NZF, 60%NZF@Zn, 40%NZF@Zn and 15%NZF@Zn respectively. The increasing coercivity of the

samples with increasing $Zn_{0.95}Ni_{0.05}O$ content could be attributed to increasing domain wall pining by the non-magnetic $Zn_{0.95}Ni_{0.05}O$ phase in these composites.

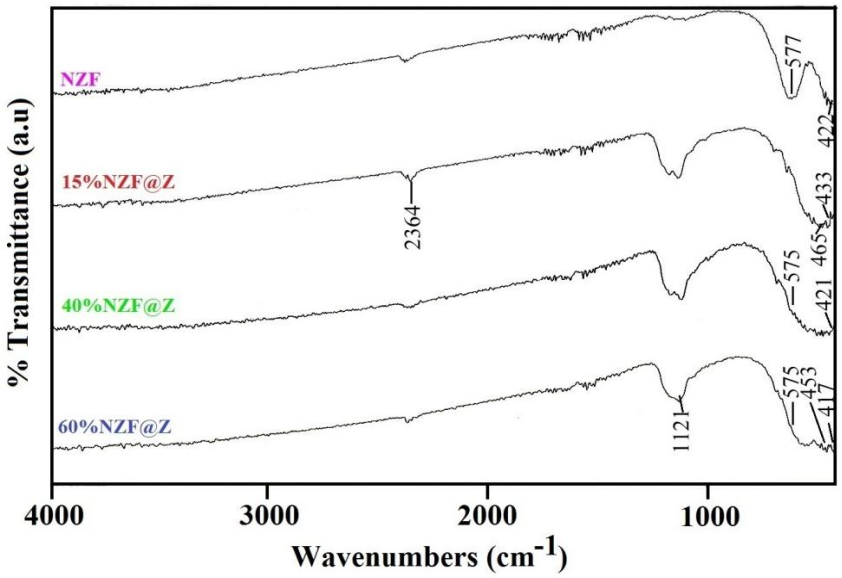

Figure. 4.6.7 FTIR spectra of NZF NP, 15%NZF@Zn, 40%NZF@Zn and 60%NZF@Zn nanocomposites.

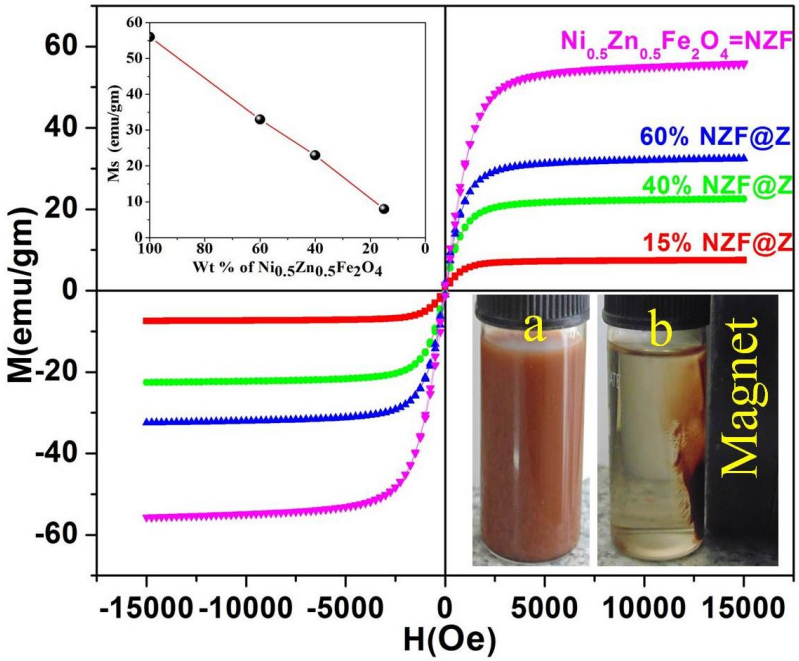

Figure. 4.6.8 Room temperature magnetization behavior (M-H) of all the samples in an applied field upto15000 Oe. The inset at the top shows linear variation of Ms as a function of varying weight percent (wt%) of NZF NP in the nanocomposites. Digital image, in the other inset shows dispersed NZF@Zn nanocomposite in water (10 mg/ml), a) Without magnet, b) near the magnet.

The superparamagnetic behavior of NZF NP could be attributed to very small particle sizes (~22 nm) of this sample. The smaller size particles may be equivalent to single domain (magnetic) particles, where thermal vibration surpass the energy barrier for its spin reversal leading to superparamagnetic behavior. Magnetic controllability or separation ability of the dispersed NZF@Zn nanocomposites in water has also been demonstrated & shown as a digital image in the other inset of fig. 4.6.8, a) without magnet, and b) near the magnet. It is observed that prepared nanocomposite has good dispersibility in water and can be easily controlled (or separated out from the solution) by applying an external magnetic field. Thus, the magnetic photocatalysts could be used repeatedly and opens up a possibility of recyclability. In addition, such magnetically targetable nanocomposites could be easily targeted to specific location of body by applying external magnetic field.

4.6.1.7 Photocatalytic activity and analysis:

Photocatalytic activity measurement:

The photocatalytic activities of the samples were estimated using Rhodamine B (RhB) dye under solar light irradiation. All photocatalytic experiments were carried out under similar conditions on sunny days between 11 am and 3 pm. In the photocatalytic experiment, 50 µg/mL of $Zn_{0.95}Ni_{0.05}O$, 15%NZF@Z, 40%NZF@Z, 60%NZF@Z, and $Ni_{0.5}Zn_{0.5}Fe_2O_4$ catalysts were added to 50 mL dye solution (of concentration 20 µg/mL). Before irradiation the suspensions containing RhB dye and $Zn_{0.95}Ni_{0.05}O$, 15%NZF@Z, 40%NZF@Z, 60%NZF@Z, and $Ni_{0.5}Zn_{0.5}Fe_2O_4$ were stirred in dark for 60 minutes to ensure the establishment of an adsorption/desorption equilibrium. 5 mL aliquots were magnetically filtrated at a fixed time interval (60 minutes) and was analyzed for the variation in maximum absorption band using a UV-vis spectrophotometer. The photo-decoloration of the RhB dye via the photocatalytic activities of $Zn_{0.95}Ni_{0.05}O$, 15%NZF@Z, 40%NZF@Z, 60%NZF@Z, and $Ni_{0.5}Zn_{0.5}Fe_2O_4$ was calculated following the formula:

$$\text{Photo-decoloration efficiency (\%)} = \frac{Co - C}{Co} X100$$

where Co is the RhB dye initial concentration before photo-decoloration and C is the absorbance after different time intervals.

Analysis of Photocatalytic activity:

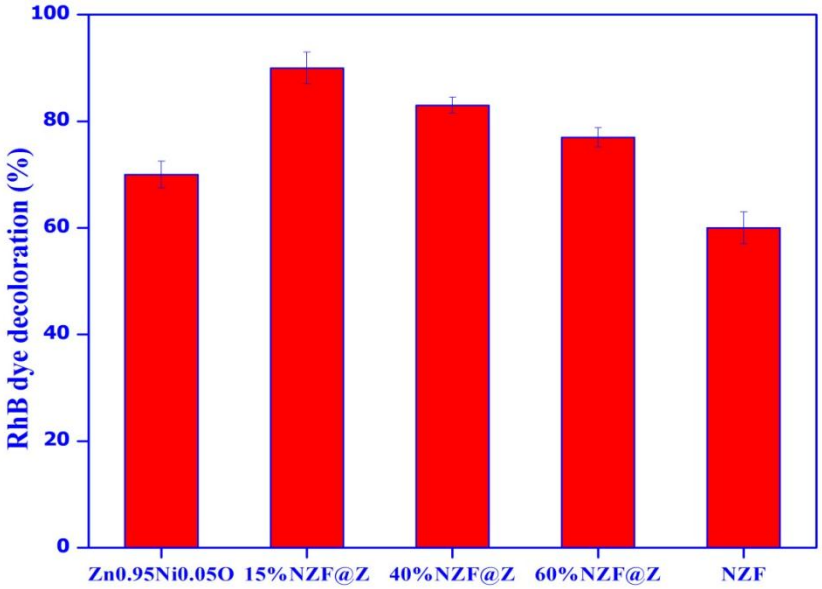

Figure. 4.6.9 (A) RhB dye photo-decolouration efficiency of $Zn_{0.95}Ni_{0.05}O$, 15%NZF@Zn, 40%NZF@Zn, 60%NZF@Zn and NZF photocatalysts under solar light irradiation.

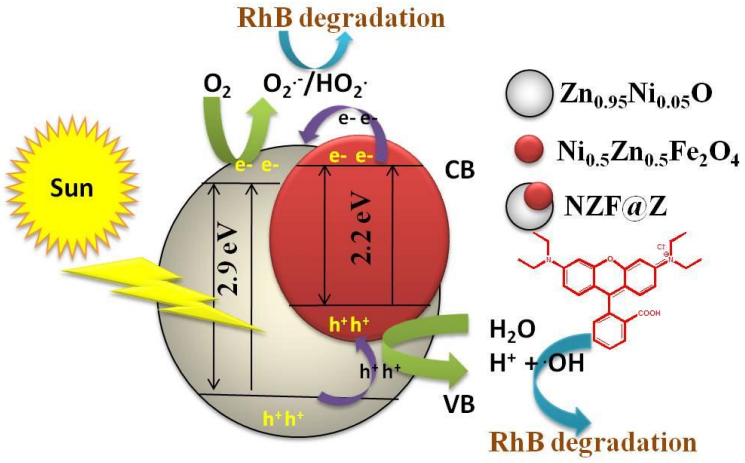

Figure. 4.6.9(B) Schematic diagram illustrating the mechanism of photo-decoloration of RhB dye on $Ni_{0.5}Zn_{0.5}Fe_2O_4/Zn_{0.95}Ni_{0.05}O$ surface under exposure to solar light.

Enhanced visible-light driven photo-activity has been observed for some heterostructure semiconductor nanocomposites previously [3, 21], which motivated us to study the photocatalytic activity of NZF@Zn NC. The high photocatalytic activity of metal oxide nanocomposites was attributed to the enhanced separation efficiency of photoinduced carriers (electrons and holes) through electronic interaction. Thus, photo-discoloration study of RhB dye using $Zn_{0.95}Ni_{0.05}O$, 15%NZF@Zn, 40%NZF@Zn, 60%NZF@Zn, and NZF as photocatalysts was performed under solar light irradiation. The extent of photo-decolouration

of RhB dye by $Zn_{0.95}Ni_{0.05}O$, 15%NZF@Z, 40%NZF@Z, 60%NZF@Z, and NZF under solar light irradiation, at 25°C, is shown in fig. 4.6.9(A). The obtained photo-decolouration data, under solar light irradiation, shows the promise of photocatalytic activity of $Zn_{0.95}Ni_{0.05}O$, 15%NZF@Z, 40%NZF@Z, 60%NZF@Z, and NZF. All the nanocomposites have shown better photocatalytic activity than pure $Zn_{0.95}Ni_{0.05}O$ or $Ni_{0.5}Zn_{0.5}Fe_2O_4$. The enhanced photo-decoloration rates of RhB dye, observed in this study, may be attributed to the reduced carriers (photo-induced) recombination through electronic interaction in these nanocomposites[22]. The reduced carrier recombination can be understood more clearly as bellow. When light is absorbed by a pure semiconductor particle, an electron is excited from VB to CB and an e−/h+ pair is formed. The generated e− and h+ may travel to the surface of particle and react with adsorbed species resulting in the desired process (degradation of dye), or they may recombine i.e. undesired process. The holes react with surface hydroxyl groups (OH−) and H_2O, to form highly reactive •OH radicals (reactive oxygen species) which degrade organic dye molecule. The undesired high e− and h+ recombination slows down the photocatalysis process especially in case of pure semiconductor photocatalysts. To enhance the efficiency, the e−/h+ recombination has to be minimized. A scheme to reduce the recombination of e− and h+ is to prepare heterostructure/nanocomposite with hetrojunction [23]. The band potentials of the component material in the nanocomposite form a heterojunction with a straddling gap, which may facilitate the transfer of charge carriers and retard the electron hole recombination, resulting in improved photocatalytic performance [21]. In other word, combining two photocatalysts with different band gap positions effectively causes a greater separation of e-/h+ pairs, allowing more of the species to be available for reactions to degrade organic species [24] [25].

In the present case, the chemical interactions between the photocatalysts ($Zn_{0.95}Ni_{0.05}O$, 15%NZF@Z, 40%NZF@Z, 60%NZF@Z, and $Ni_{0.5}Zn_{0.5}Fe_2O_4$) and the charged groups of RhB molecules lead to significant adsorption followed by high photo-decoloration. The absorption of photons with sufficient energy (~2.98, 2.72, 2.64, 2.54, and 2.24 eV of $Zn_{0.95}Ni_{0.05}O$, 15%NZF@Zn, 40%NZF@Zn, 60%NZF@Zn, and NZF, respectively) is the necessary condition for photochemical reactions to proceed on the photocatalyst surface. The band edges position (VB and CB) of the AB_2O_4 type ferrite ($ZnFe_2O_4$/$NiFe_2O_4$) lies above the corresponding band edges positions of ZnO respectively [3] [24] [28]. Reported CB and VB potential of $ZnFe_2O_4$ is nearly at -1.54 eV (vs NHE) and +0.38 eV (vs NHE) respectively[26, 27]. The CB and VB potential of ZnO is nearly at -0.76 eV (vs NHE) and ~ +2.7 eV (vs NHE)

respectively[28, 29]. Fig. 4.6.9(B) shows the schematic of the possible mechanism in this photocatalysis process. Under solar light irradiation, the electrons (e^-) from the filled valence bands (VB) of $Ni_{0.5}Zn_{0.5}Fe_2O_4$ and $Zn_{0.95}Ni_{0.05}O$ will be excited to the respective empty conduction bands (CB), separately giving an equal number of holes (h^+) in the corresponding VBs. The presence of $Ni_{0.5}Zn_{0.5}Fe_2O_4$ nanoparticles will favour the utilization of visible region of the spectrum due to its narrow band gap (2.2 eV) thereby enhancing the photocatalytic activity under visible light irradiation [24] [21].Moreover, the difference in band structures of $Ni_{0.5}Zn_{0.5}Fe_2O_4$ and $Zn_{0.95}Ni_{0.05}O$ will facilitate photoinduced electrons transfer from the CB of $Ni_{0.5}Zn_{0.5}Fe_2O_4$ to that of $Zn_{0.95}Ni_{0.05}O$ and holes transfer from the VB of $Zn_{0.95}Ni_{0.05}O$ to that of $Ni_{0.5}Zn_{0.5}Fe_2O_4$, respectively[3]. These processes will efficiently hinder the recombination of photogenerated electron–hole pairs and considerably enhance the photocatalytic activity under solar light irradiation. The resulted electron-hole pairs recombine or migrated to the surface of the particles and retort either with H_2O or OH^- to form $OH^{\bullet}$, which have strong oxidation ability and can destroy the dye molecules completely. The electrons will also react with adsorbed molecular oxygen to form superoxide radical anion, $O_2^{-\bullet}$ ions, which will further react with water to give $OH^{\bullet}$ [3]. Thus, as a magnetic semiconductor material, NZF might not only add recyclability and visible light activity to the catalyst nanoparticles, but also offer some synergetic enhancement of the catalytic activity by forming the hybrid structure [26].

Prepared visible light active and magnetically controllable NZF@Zn NC could find potential application in biomedical field such as targeted drug delivery, photocatalysis based degradation of biomedical waste, optical imaging etc. due to its magneto-optical properties.

4.6.2 Synthesis and characterization of multifunctional NZF@Zn-mSiO_2 nanocomposite:

Nanocomposites based nano-system having magnetic as well as optical properties are increasingly being studied and developed due to their potential use in biomedical applications including imaging, drug delivery etc [1]. In the above part, NZF and ZnO based nanocomposites (NZF@Zn) were prepared by sol gel technique using egg albumen to combine interesting properties of both ferrite and ZnO. After successful preparation and characterization of magneto- optical NZF@Zn NC, it was used to prepared multifunctional NZF@Zn-mSiO_2 nano-system. In other words, To, get multifunctional magnetic nanoparticles and to add drug

reservoir to the synthesized nanocomposites, we have prepared NZS@Zn-mSiO_2 nanocomposites. Thus, the prepared single NZF@Zn-mSiO_2 nano-system has magnetic, and optical properties along with drug loading ability, which could be used for multimodal imaging and drug delivery applications.

4.6.2.1 Formulation of multifunctional NZF@Zn-mSiO_2 nanocomposite

The prepared NZF@Zn NC was incorporated in mesoporous silica nanosphere using a simple method to obtained hydrophilic, biocompatible, multifunctional NZF@Zn-mSiO_2 nanocarrier. The preparation method of NZF@Zn-mSiO_2 nanocarrier, first, involved hydrolysis and condensation of TEOS in the presence of aligned CTAB based template and NZF@Zn NC in alkaline medium. Then the obtained product containing CTAB template were calcined to remove burn out unwanted CTAB. The removal of template has generated mesoporous structure in the SiO_2 nanosphere of the size of their micellar diameter. The prepared NZF@Zn-mSiO_2 nanocarrier was characterized for its structural, morphological, magnetic and drug loading/release properties using different techniques. Biocompatibility of the NZF@Zn-mSiO_2 nanocarrier was studied using MTT assay. Curcumin(Cur), which is well known for its anticancer and antimicrobial activity was used to study the loading and release behavior of NZF@Zn-mSiO_2 nanocarrier. It is worthy to mention here that even though the Cur is having very good anticancer activity against variety of cancer cells, but its less water solubility hinders its efficacy thus reduces practical applications. Loading and parceling of Cur through a hydrophilic nanocarriers such mSiO_2 could minimize such issues and improve therapeutic efficacy of Cur.

4.6.2.2 HRTEM and SAED analysis of multifunctional **60%NZF@Zn NC**

Figure 4.6.10 (a) shows TEM image of 60%NZF@Zn NC at low (a) and high (b) magnifications. It was observed that NZF NPs (dark black) are surround by ZnO (grey) layer around it. The size of NZF@Zn NC was found to vary from 30-100 nm. A very clear grey color layer of ZnO on the darker NZF NP can be seen in the figure (b). To confirm that the core region is made up of NZF and the shell is made up of ZnO, HRTEM analysis of both the region have been carried out. Atomic planes in the HRTEM of core region shows the d spacing of 0.29 nm which is matching well with the (220) plane of spinel cubic NZF NPs (shown in (c)). HRTEM image of marked core region (red box in (b)) of particle is shown in figure (c). IFFT analysis clearly shows presence of well-ordered atomic planes of NZF NP. Line profile through

atomic planes showing d spacing is shown in right side inset of figure (c). IFFT processed image of HRTEM micrograph of another core region of different NZF@Zn NC particle, which is shown in (d) also suggest core to be NZF as its d spacing (0.47 nm) is matching with d spacing of (111) plane of NZF NP. HRTEM image of shell region (marked as green box in (b)) is shown in image (e) the d spacing of the observed planes in the coating region was found to be 0.28 nm and can be attributed to the (100) plane of ZnO. Inset image of (e) shows IFFT image of region indicated by arrow. Further confirmation of presence of both the phases NZF and ZnO in the nanocomposite was done through the SAED analysis of NZF@Zn NC. (f) Indexed SAED diffraction pattern of 60%NZF@Zn NC which has shown a complex dotted ring pattern having diffraction spot from both the NZF and ZnO phases. The pattern arises from NZF were indexed in red color and marked with (*) symbol. Whereas the reflections arisen from ZnO were indexed in white and marked with (#) symbol. Thus, HRTEM and SAED analysis confirm the formation of NZF@Zn NC.

4.6.2.3 Structural analysis of NZF@Zn-mSiO$_2$ NC (XRD)

Figure 4.6.11 shows XRD patterns of NZF@Zn, NZF@Zn-mSiO$_2$, and mSiO2. XRD pattern of NZF@Zn NC shows characteristic diffraction peaks of both ZnO marked with # symbol) and NZF (marked with * symbol) that confirm its successful formation. XRD result of NZF@Zn has already been discussed above. XRD pattern of NZF@Zn-mSiO$_2$ NC shows presence of sharp diffraction peaks of NZF-ZnO and broad hump of mesoporous silica [30] [31]. The diffraction peaks corresponding to the NZF and ZnO in the XRD pattern of ZF@Zn-mSiO$_2$ NC have been marked with * and # symbol respectively. The XRD pattern of pure mesoporous silica does not shows any sharp diffraction peaks due to its amorphous nature. A broad hump at ~22^o which is the characteristic of amorphous nature was observed. No other peaks of impurity phase were observed in any diffraction pattern. The simultaneous presence of a hump of mesoporous silica and peaks of NZF@Zn in XRD pattern of NZF@Zn-mSiO$_2$ NC confirm the formation of nanocomposite.

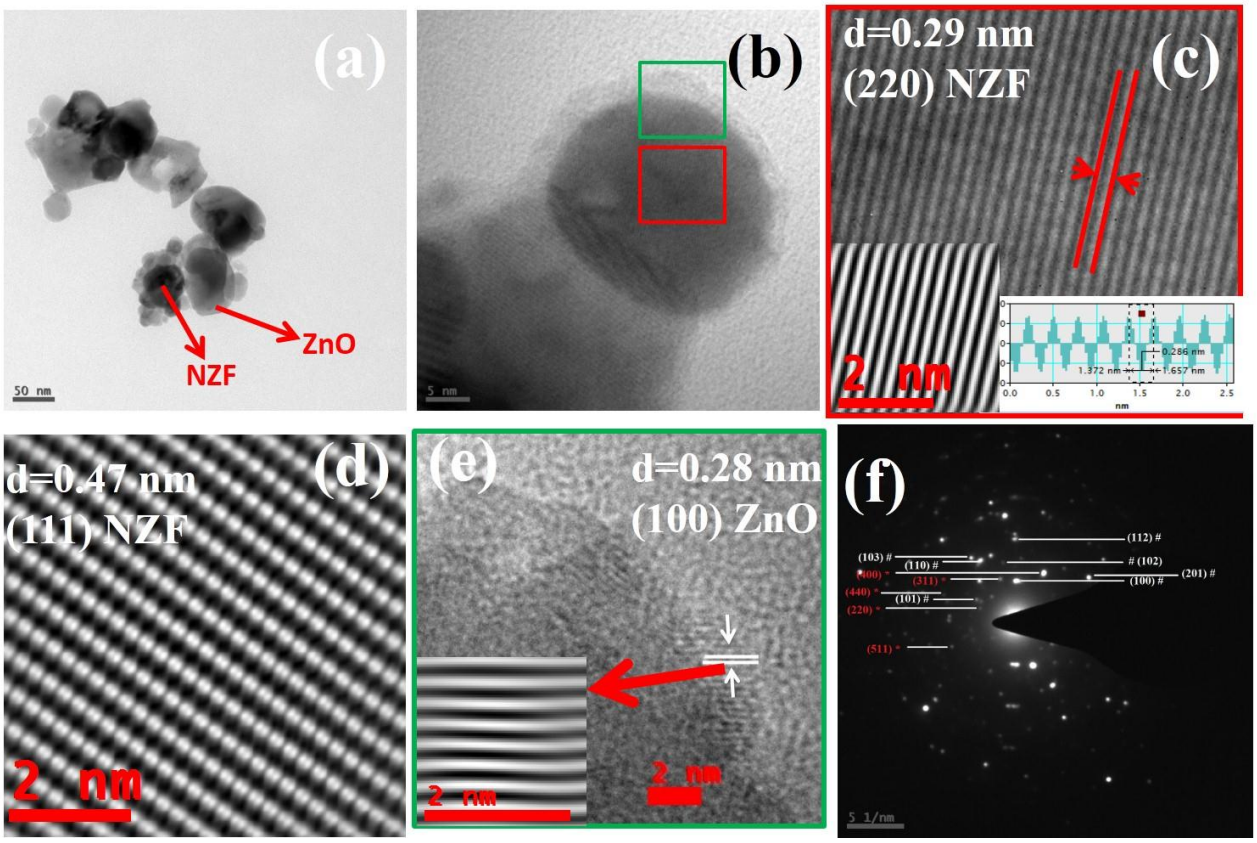

Figure 4.6.10.TEM image of 60%NZF@Zn NC at low (a) and high (b) magnifications. (c) HRTEM image of marked core region (red box in (b)) of particle. Left side inset image of (c) shows IFFT image of the same region where it is placed. Right side inset of (c) shows line profile through the atomic plane in IFFT image. IFFT processed image of HRTEM micrograph of core region of another different NZF@Zn NC particle. HRTEM image of shell region (marked as green box in (b)). Inset image of (e) shows IFFT image of region indicated by arrow. (f) Indexed SAED diffraction pattern of 60%NZF@Zn NC.

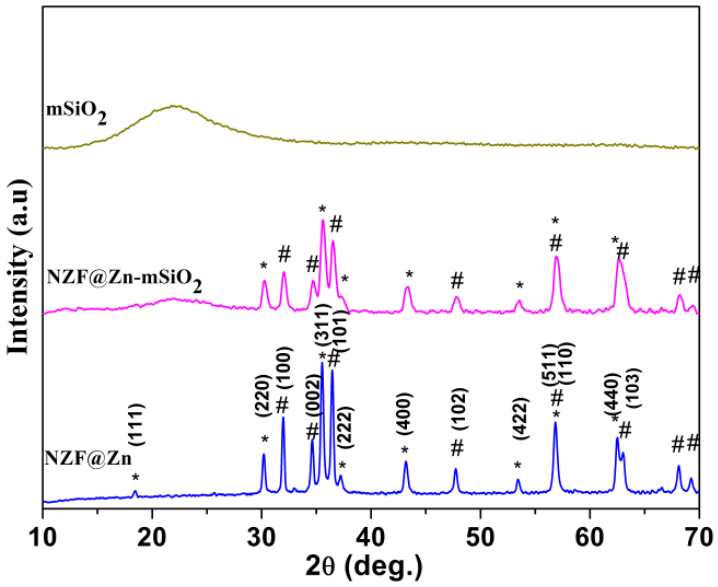

Figure 4.6.11. XRD patterns of NZF@Zn NC, NZF@Zn-mSiO$_2$ NC, and mSiO$_2$ NP.

4.6.2.4 Morphological analysis of NZF@Zn-mSiO$_2$ NC

Morphology and particles size of NZF@Zn-mSiO$_2$ NC were studied suing FESEM and TEM techniques. Figure 4.6.12 (a-b) shows FESEM micrographs of NZF@Zn-mSiO$_2$ NC. Formation of spherical shape NZF@Zn-mSiO$_2$ NC was observed. The particle was found to vary between 150-300 nm. Due to smaller size and being impregnated within mSiO$_2$ nanosphere, the NZF@Zn nanoparticles were not clearly observed in FESEM micrograph. Figure 4.6.13(a) shows the TEM image of pure mesoporous silica nanoparticle (mSiO$_2$ NP) prepared in the same way but without using NZF@Zn NC. Particles were found to be spherical to egg shape in morphology. The size of the mSiO$_2$ NP was found to be in between 160-180 nm. Mesoporous structure of mSiO$_2$ NP can be observed clearly. The presence of white spots on the particles and very light fluffy appearance of particles suggested mesoporous nature of prepared mSiO$_2$ NP. It is worthy to mention that solid silica nanoparticles of such size will appear very dark in TEM image. The white spots on the particles are pores generated by removal of CTAB template. Figure 4.6.13 (b-d) TEM micrographs of NZF@Zn-mSiO$_2$ NC at low and magnifications. It was observed that NZF@Zn-mSiO$_2$ NC particles are spherical in shape and has size in the range of 150-300 nm. It was observed that smaller NZF@Zn are well incorporated within the mesoporous silica matrix of size 150-300 nm. The darker appearance in the core region of NZF@Zn-mSiO$_2$ NC is due to the presence of more amount of NZF@Zn NP in center of silica particle. Presence of smaller NZF@Zn NP (dark black particles) in bigger mSiO$_2$ NP (grey) can clearly be seen in figure 4.6.13 (c &d). It can be observed that NZF@Zn particles are embedded in the in bigger mSiO$_2$ nanosphere. It was notice that the presence of NZF@Zn particles is more in the core region than outer surface region.

Figure 4.6.13 (e) shows HRTEM image of NZF@Zn-mSiO$_2$ NC. Presence of pore of diameter 5-7 nm (red circle) and crystalline NZF@Zn particles were observed. HRTEM analysis of the darker particles present within the silica matric was carried and it was found that atomic d spacing of darker particles is matching with that of NZF@Zn particles. Figure 4.6.13 (f) shows enlarge images of the marked region of (e) to show the presence of atomic planes on the darker particles. Presence of well-ordered atomic plane on the darker particles confirmed presence of crystalline NZF@Zn particles in the NZF@Zn-mSiO$_2$ nanocomposite as its d spacing (d ~0.25 nm) is matching with the (311) plane of NZF NP. It is need, to mention here that the matrix silica is amorphous in nature and does not shows any ordered atomic planes.

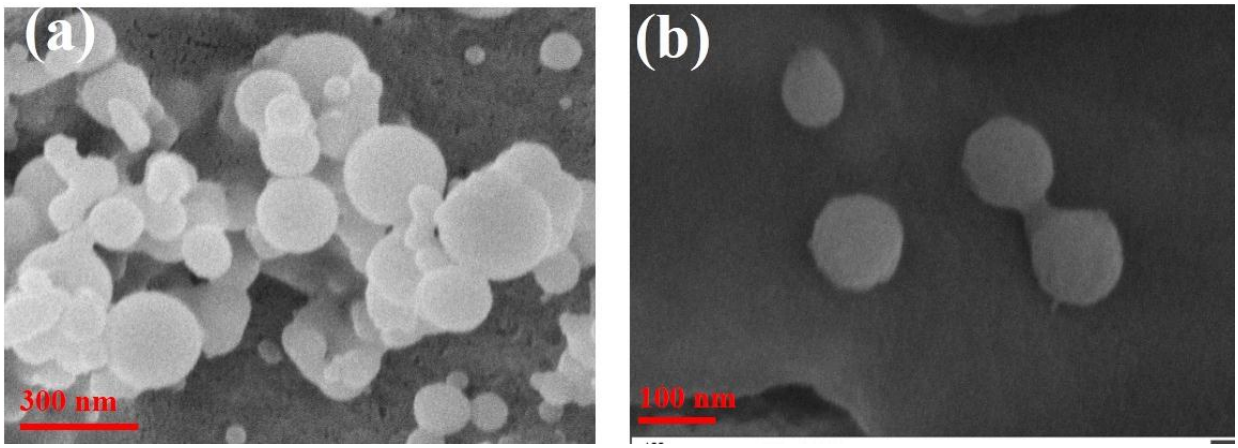

Figure 4.6.12. FESEM micrographs of NZF@Zn-mSiO$_2$ NC at low and high magnifications.

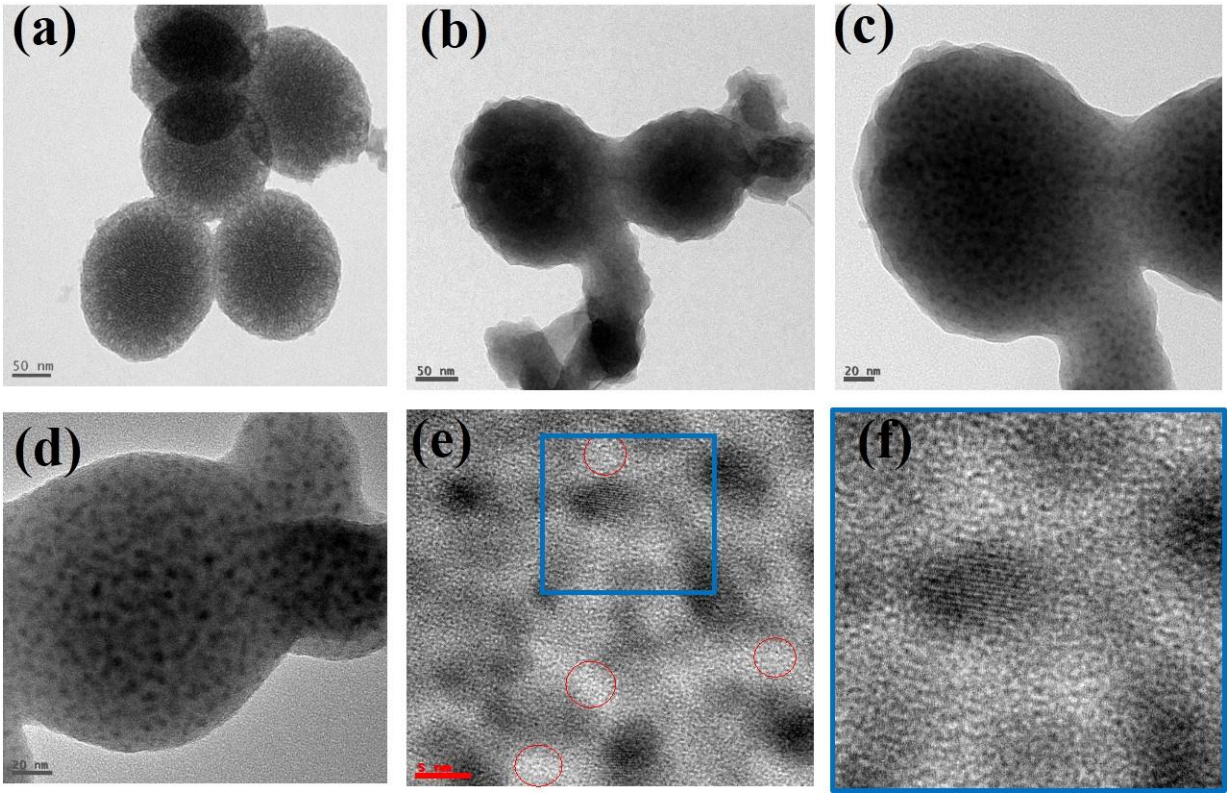

Figure 4.6.13. (a) TEM micrograph of mSiO$_2$ NP. (b-d) TEM micrographs of NZF@Zn-mSiO$_2$ NC at low and magnifications. (e) HRTEM image of NZF@Zn-mSiO$_2$ NC. (f) Enlarge images of the marked region of (e) to show the presence of atomic planes on the darker nanoparticles.

4.6.2.5 N_2 adsorption-desorption analysis

Further, presence of mesoporous on the NZF@Zn-mSiO$_2$ NC has also been suggested by the N_2 adsorption-desorption isotherms of NZF@Zn-mSiO$_2$ NC (Fig. 4.6.14). The result displays presence of clear hysteresis loop which is characteristic of the mesoporous structure.

The sharp increases in the adsorption amount, in the pressure range 0.7< P/Po <0.9, is due to the capillary condensation of N_2 gas in mesopores. These observations confirmed formation of mesoporous NZF@Zn-mSiO_2 NC. BET, Single point and Langmuir surface area of NZF@Zn-mSiO_2 NC were found to be in between ~ 12-19 m^2/g. The pore size and distribution were also calculated from the desorption branch of the isotherm using the Barrett–Joyner–Halenda (BJH) method. The pore size distribution (inset of Fig. 4.6.14) reveals presence of different sized pores. The average pore size was found to be ~11.7 nm. Two major peaks in the pore size distribution plots were observed at ~4 and 8.4 nm. Single point adsorption total pore volume was estimated at P/Po = 0.98 is found to be 0.04 cm^3/g.

4.6.2.6 Magnetic properties

M-H curve of NZF@Zn-mSiO_2 and NZF@Zn NC are shown in the figure 4.6.15. From this M-H plot different magnetic parameter for NZF@Zn-mSiO_2 and NZF@Zn NC have been extracted. The sample have shown superparamagnetic behavior. The detailed magnetic properties of NZF@Zn NC have been discussed above. The superparamagnetic behavior of these samples was attributed to the presence of very small size NZF NPs (equal to single domain). The magnetic controllability and targetability of a magnetic nanocarrier is govern by its Ms values. The Ms values of NZF@Zn and NZF@Zn-mSiO_2 NC were found to be 32 and 4.2 emu/gm respectively. The sudden reduction in the Ms value of NZF@Zn-mSiO_2 NC than NZF@Zn is due to the presence of more amount of nonmagnetic phase (silica). The Ms value of a magnetic nanocarrier can be increase or decrease by changing amount of magnetic phase in the magnetic nanocarrier. The Mr value of NZF@Zn and NZF@Zn-mSiO_2 NC were found to be 1.44 and 0.21 emu/gm respectively. The coercivity value of NZF@Zn and NZF@Zn-mSiO_2 NC were found to be 44 and 39 Os respectively. The decrease in the Mr and coercivity of NZF@Zn-mSiO_2 NC than NZF@Zn may be attributed to the fine dispersion and less agglomeration of NZF@Zn in nonmagnetic silica matrix. The nonmagnetic boundaries of around magnetic phase could have facilitated easy randomization of magnetic domains. NZF@Zn-mSiO_2 NC could find potential in magnetically controlled drug delivery applications. Soft magnetic and superparamagnetic nature and porous structure of NZF@Zn-mSiO_2 NC make it very useful candidate for biomedical application.

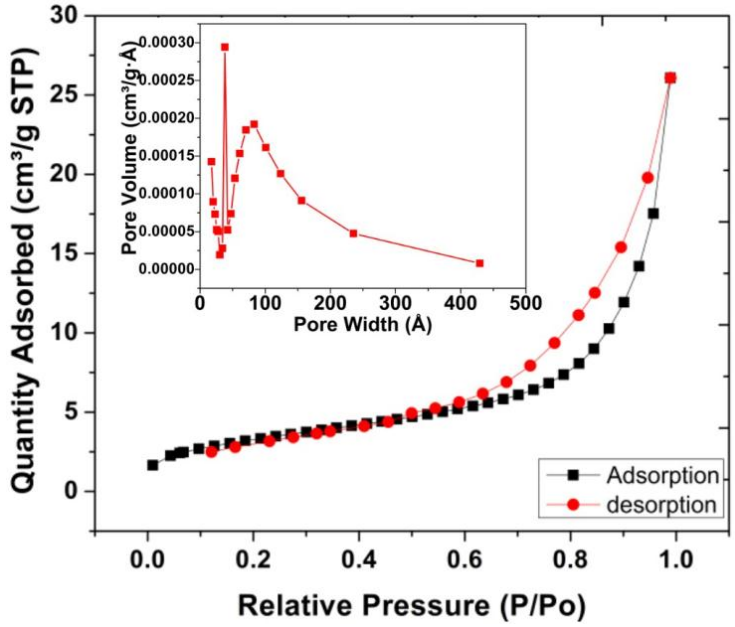

Figure 4.6.14. BET N_2-adsorption (black) and -desorption (red) isotherms of NZF@Zn-mSiO_2 NC. Inset figure shows the BJH pore size distribution plotted using the desorption isotherm.

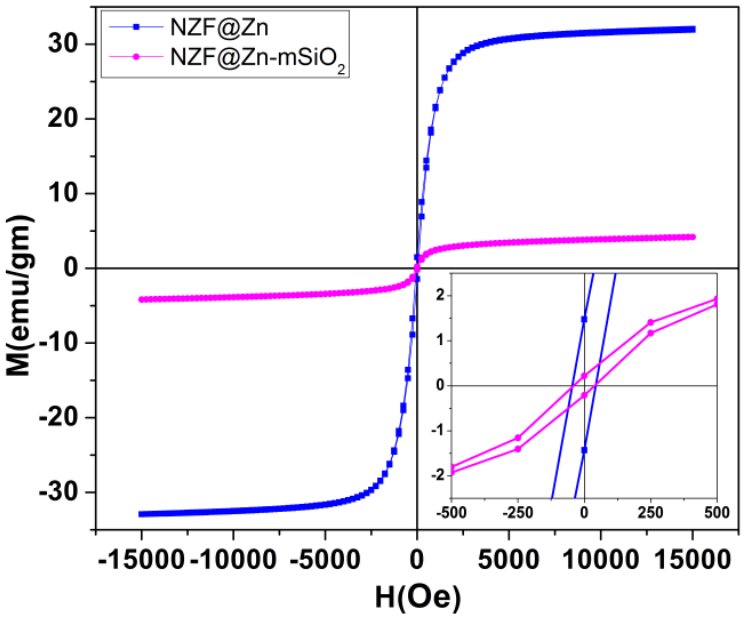

Figure 4.6.15. M-H curve of NZF@Zn-mSiO_2 and NZF@Zn NC. Inset figure shows enlarge M-H curve to show Mr and coercivity values.

4.6.2.7 Analysis of functional groups and loading of Cur into NZF@Zn-mSiO₂ by FTIR

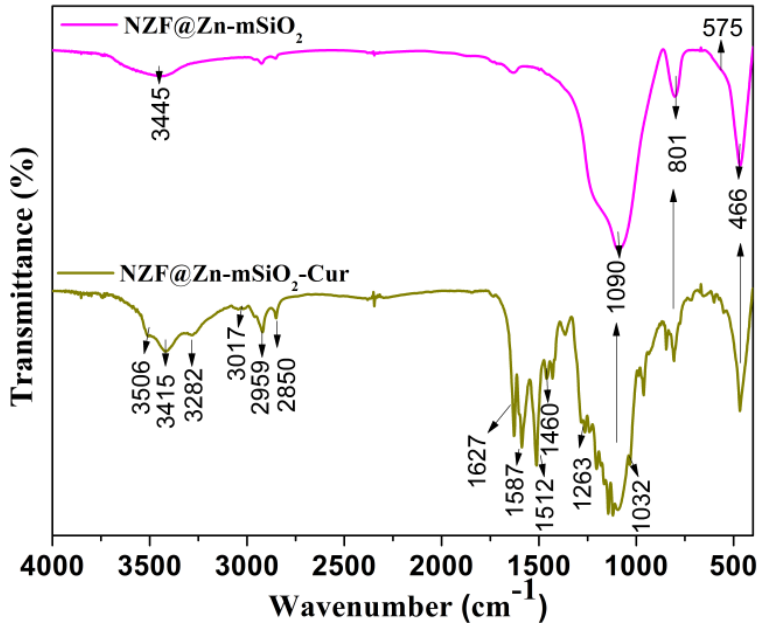

Figure 4.6.16. FTIR spectra of NZF@Zn-mSiO₂ and NZF@Zn-mSiO₂-Cur NC.

Functional properties and formation of NZF@Zn-mSiO₂ NC as well as loading of hydrophobic Cur in NZF@Zn-mSiO₂ NC were examined by FTIR analysis. Figure 4.6.16 shows FTIR spectra of NZF@Zn-mSiO₂ and NZF@Zn-mSiO₂-Cur NC. FTIR spectra of NZF@Zn-mSiO₂ NC shows characteristic peaks of silica (1090, 801, and 466 cm^{-1} due to Si-O-Si) and NZF@Zn (400-600 cm^{-1}) which confirm its formation. The characteristic bands NZF, ZnO SiO_2 present in range of 400-600 cm^{-1} have coupled together resulting a major band at 466 cm^{-1} with a shoulder at ~575 cm^{-1} which can be assigned to NZF NP. The peak at 3445 cm^{-1} can be assigned to the OH group present the surface of silica. FTIR spectra of NZF@Zn-mSiO₂-Cur NC shows presence of all the characteristic band of NZF@Zn-mSiO₂ NC with few additional characteristic band of loaded Cur which confirm its successful loading in nanocarrier. The band arises from loaded Cur were observed at 3506 cm^{-1} (free –OH group vibration), 3282 cm^{-1} (-OH stretching), 3017 cm^{-1} (C-H stretching of aromatic ring), 2956 (C-H asymmetric stretching of CH_3), 2850 cm^{-1} (C-H stretching of CH_3), 1627 cm^{-1} (stretching vibration of C=O, C=C), 1587 cm^{-1} (C=C aromatic),1512 cm^{-1} (C=O stretching), 1460 cm^{-1} (CH_2 bending), 1263 cm^{-1} (stretching of enol C-O) and 1032 (stretching of C-O-C) [32] [33]. After Cur loading the band at 3445 cm^{-1}(OH group of silica) of NZF@Zn-mSiO₂ NC had shifted to 3415 cm^{-1} and it could be due to interaction between the OH group of silica and curcumin. Thus, presence of characteristic bands of Cur in the FTIR spectra of NZF@Zn-

$mSiO_2$-Cur NC confirmed its loading and also suggested its compatibility with NZF@Zn-$mSiO_2$ NC as no alteration in the chemical structure of Cur was observed.

4.6.2.8 Cur loading and release study

Figure 4.6.17 (a-f) show results related to loading and release of Cur for NZF@Zn-$mSiO_2$ NC. Due to good anticancer activity and no systemic toxicity of Cur, it was chosen to load into NZF@Zn-$mSiO_2$ NC. Commonly, drugs are loaded into nanocarriers by via weak noncovalent interactions, such as, physical adsorption or entrapment, electrostatic interaction and π−π stacking etc. Metal ion−ligand interactions i.e (interaction between Cur with divalent metal ions) based loading of Cur on ZnO NP has been reported recently. In this study, Cur loading in mesoporous silica based nanocarrier via ZnO nanoparticles (Zn^{2+}-Cur) has been demonstrated[34]. Presence of ZnO in the NZF@Zn-$mSiO_2$ NC also make Cur a suitable and compatible drug for NZF@Zn-$mSiO_2$ NC. Further, Cur of Cur in mesoporous silica based nanocarrier will improve its solubility in biological medium. Figure 4.6.17 (a) shows UV-Vis absorption spectra of Cur loaded NZF@Zn-$mSiO_2$ NC (NZF@Zn-$mSiO_2$-Cur NC) which shows presence of characteristic absorption peak of Cur at ~420 nm wavelength. Appearance of characteristic absorption peak of Cur in the UV-Vis absorption spectra of NZF@Zn-$mSiO_2$-Cur NC confirm presence or loading of Cur in the nanocarrier. It also suggests that chemical structure of Cur has not changed after loading into NZF@Zn-$mSiO_2$ NC which shows its compatibility with NZF@Zn-$mSiO_2$ NC. Figure 4.6.17 (b) shows UV-Vis absorption spectra of Cur before loading and Cur in supernatant which was used estimate amount of Cur loaded in NZF@Zn-$mSiO_2$ NC as well as left in supernatant. The drastic decrease in the absorption intensity of Cur in supernatant than of before loading shows excellent loading ability of Cur in NZF@Zn-$mSiO_2$ NC. The different physicochemical interactions between Cur molecules and NZF@Zn-$mSiO_2$ NC could be responsible the excellent loading of Cur in NZF@Zn-$mSiO_2$ NC. Electrostatic interactions between Cur and functional groups of silica as well as electrostatic interaction between Cur and ZnO could have played a major role. The Cur loading efficiency and loading capacity of NZF@Zn-$mSiO_2$ NC were found to be 84 % and 17% respectively. The observed loading efficiency and loading capacity of NZF@Zn-$mSiO_2$ NC are very high which shows that NZF@Zn-$mSiO_2$ NC has good potential as a nanocarrier for Cur delivery. For the quantification of Cur during its loading and release study, a standard calibration curve of Cur was plotted using absorption intensity of different known concentration of Cur. UV-Vis absorption spectra of different known concentration of Cur and

corresponding calibration curve are shown in figure 4.6.17 (c) and (d) respectively. In vitro Cur release behavior from NZF@Zn-mSiO$_2$-Cur NC was studied using UV-Vis spectroscopy. Figure 4.6.17 (e) shows UV-Vis absorption spectra of Cur released from NZF@Zn-mSiO$_2$-Cur NC at different time in PBS. Increase in the absorption intensity with time can be seen in this figure. Figure 4.6.17 (f) shows Cur release profile in PBS medium with different time. It was observed that till 10 hours the Cur release was ~7% and it became ~ 12 % up to 24 hours. Till final incubation time of 48 hours only ~19 % Cur release was observed. The overall Cur release behavior was found to be sustained in nature. Sustained and slow release of anticancer drug is desirable for a long-term effect of drug as well as to reduce systemic toxicity.

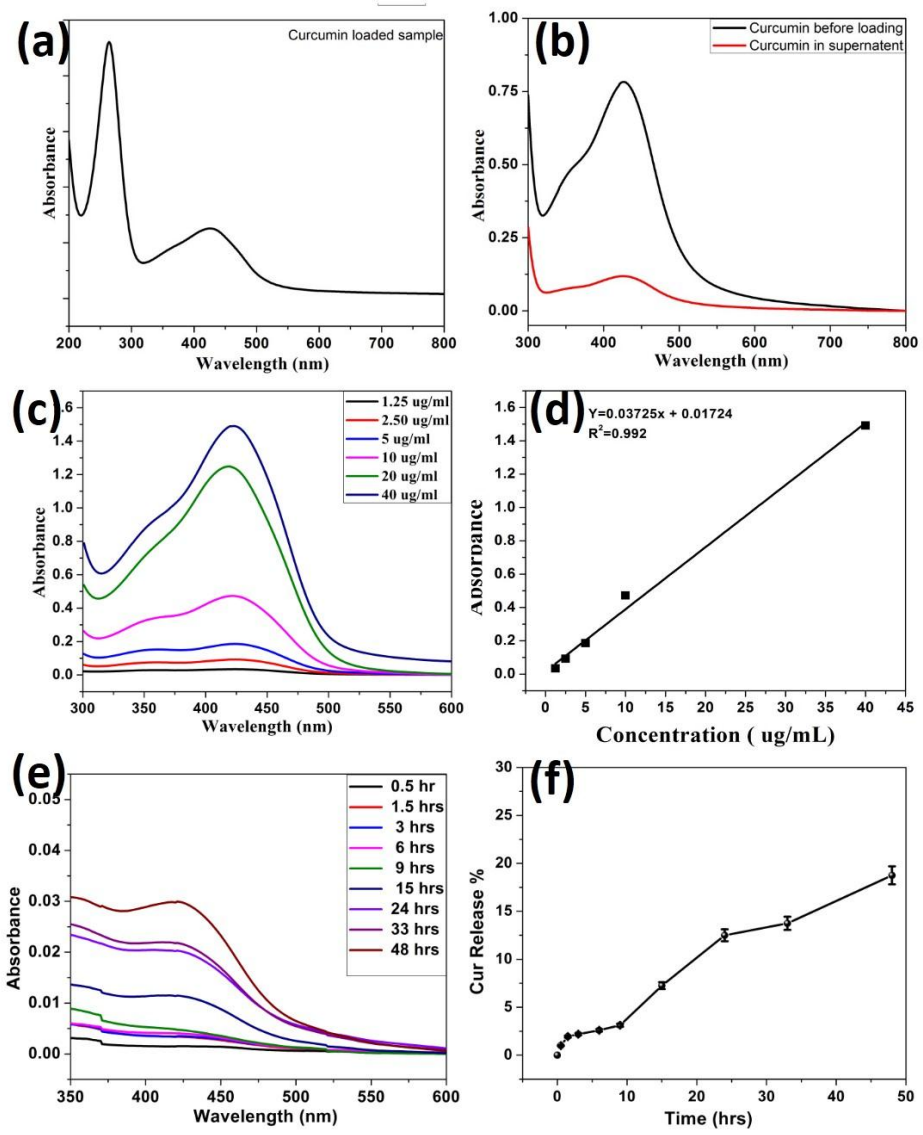

Figure 4.6.17. (a) UV-Vis absorption spectra of Cur loaded NZF@Zn-mSiO$_2$ NC (NZF@Zn-mSiO$_2$-Cur NC. (b) UV-Vis absorption spectra of Cur before loading and Cur in supernatant. UV-Vis absorption spectra of different known concentration of Cur and corresponding

calibration curve are shown in figure (c) and (d) respectively. (e) UV-Vis absorption spectra of Cur released from NZF@Zn-mSiO$_2$-Cur NC at different time in PBS. (f) Time dependent Cur release profile in PBS medium.

4.6.2.9 Biocompatibility study

For biomedical application nanocarrier must be biocompatible in nature. The in vitro biocompatibility of NZF@Zn-mSiO$_2$ NC was checked against normal RAW264.7 macrophages cells. Dose dependent cell viability of RAW264.7 cells are shown in figure 4.6.18. The cells were treated with 50, 100, 200, 400, and 800 µg/ml of NZF@Zn-mSiO$_2$ NC. No killing was observed till 200 µg/ml dose of NZF@Zn-mSiO$_2$ NC. About 79% cells viability was observed at highest dose of 800 µg/ml. Thus, prepare NZF@Zn-mSiO$_2$ NC dosed not shows toxic effect on the normal cells and is suitable for nanocarrier based drug delivery application. A very high biocompatibility of NZF@Zn-mSiO$_2$ NC can be attributed to the biocompatible coating of mesoporous silica.

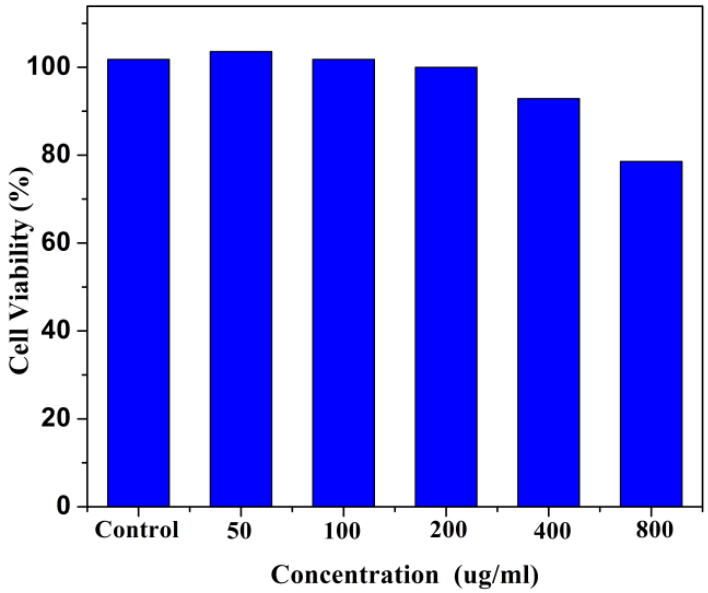

Figure 4.6.18. Dose dependent cell viability of RAW264.7 cells treated with NZF@Zn-mSiO$_2$ NC.

4.6.3. Conclusions

A novel, visible light active and magnetically guidable $Ni_{0.5}Zn_{0.5}Fe_2O_4/Zn_{0.95}Ni_{0.05}O$ nanocomposites that combine the magnetic and optical properties have been synthesized successfully by a simple and cost-effective sol gel technique using egg albumen as biotemplate. Various characterization techniques have been used to characterize their structural, optical, and magnetic properties. Enhanced photo-decoloration of the Rhodamine B dye molecules by

NZF@Z photocatalysts, compare to that by pure $Ni_{0.5}Zn_{0.5}Fe_2O_4$ or $Zn_{0.95}Ni_{0.05}O$, have been observed under solar light irradiation. Narrow band gap of $Ni_{0.5}Zn_{0.5}Fe_2O_4$ (2.2 eV), relatively low band gap of $Zn_{0.95}Ni_{0.05}O$ (2.95 eV), and reduced electrons-holes recombination through electronic interactions have contributed significantly to this visible light active photocatalysis process. This novel visible light active & magnetically separable photocatalyst may immensely contribute to environmental remediation. After successful preparation and characterization of magneto- optical NZF@Zn NC, it was used to prepared multifunctional NZF@Zn-mSiO_2 nano-system which combine superparamagnetic magnetic, and optical properties along with drug loading properties. The prepared NZF@Zn-mSiO_2 nanocarrier was characterized for its structural, morphological, magnetic properties using different techniques. Curcumin has been loaded in the NZF@Zn-mSiO_2 nanocomposite and a sustained release behavior was observed. A high LE (84%) and LC (21%) were observed. MTT assay results suggested that nanoparticles are biocompatible in nature. The prepared NZF@Zn-mSiO_2 NC could find potential application in targeted drug delivery and also suitable modal imaging due to the presence of magneto-optical NZF@ZnO in mesoporous silica.

4.6.4 References

[1] N.-H. Cho, T.-C. Cheong, J.H. Min, J.H. Wu, S.J. Lee, D. Kim, J.-S. Yang, S. Kim, Y.K. Kim, S.-Y. Seong, A multifunctional core–shell nanoparticle for dendritic cell-based cancer immunotherapy, NATURE NANOTECHNOLOGY 6 (2011) 675.
[2] Z.-Y. Zhang, H.-M. Xiong, Photoluminescent ZnO Nanoparticles and Their Biological Applications, Materials 8(6) (2015) 3101–3127.
[3] L. Sun, R. Shao, L. Tang, Z. Chen, Synthesis of ZnFe2O4/ZnO nanocomposites immobilized on graphene with enhanced photocatalytic activity under solar light irradiation, Journal of Alloys and Compounds 564(Supplement C) (2013) 55-62.
[4] P. Sathishkumar, N. Pugazhenthiran, R.V. Mangalaraja, A.M. Asiri, S. Anandan, ZnO supported CoFe2O4 nanophotocatalysts for the mineralization of Direct Blue 71 in aqueous environments, Journal of hazardous materials 252-253(Supplement C) (2013) 171-179.
[5] K.K. Senapati, C. Borgohain, P. Phukan, Synthesis of highly stable CoFe2O4 nanoparticles and their use as magnetically separable catalyst for Knoevenagel reaction in aqueous medium, Journal of Molecular Catalysis A: Chemical 339(1) (2011) 24-31.
[6] A. Roychowdhury, S.P. Pati, A.K. Mishra, S. Kumar, D. Das, Magnetically addressable fluorescent Fe3O4/ZnO nanocomposites: Structural, optical and magnetization studies, Journal of Physics and Chemistry of Solids 74(6) (2013) 811-818.
[7] Y.P. V.D. Mote, B.N. Dole, , Williamson–Hall analysis in estimation of lattice strain in nanometer-sized ZnO particles, , J. Theor. Appl. Phys. 6 (2012) 6.
[8] N. Guskos, S. Glenis, G. Zolnierkiewicz, J. Typek, P. Berczynski, A. Guskos, D. Sibera, U. Narkiewicz, Magnetic properties of ZnFe2O4 ferrite nanoparticles embedded in ZnO matrix, Applied Physics Letters 100(12) (2012) 122403.
[9] X. Tang, K.-a. Hu, Preparation and electromagnetic wave absorption properties of Fe-doped zinc oxide coated barium ferrite composites, Materials Science and Engineering: B 139(2) (2007) 119-123.
[10] J. Wu, A. Acero-Lopez, Ovotransferrin: Structure, bioactivities, and preparation, Food Research International 46(2) (2012) 480-487.
[11] C. Borgohain, K.K. Senapati, K.C. Sarma, P. Phukan, A facile synthesis of nanocrystalline CoFe2O4 embedded one-dimensional ZnO hetero-structure and its use in photocatalysis, Journal of Molecular Catalysis A: Chemical 363-364(Supplement C) (2012) 495-500.
[12] Z. Durmus, A. Baykal, H. Kavas, M. Direkçi, M.S. Toprak, Ovalbumin mediated synthesis of Mn3O4, Polyhedron 28(11) (2009) 2119-2122.

[13] M. Shoeb, R.S. Braj, A.K. Javed, K. Wasi, N.S. Brahma, B.S. Harikesh, H.N. Alim, ROS-dependent anticandidal activity of zinc oxide nanoparticles synthesized by using egg albumen as a biotemplate, Advances in Natural Sciences: Nanoscience and Nanotechnology 4(3) (2013) 035015.
[14] F. Nouroozi, F. Farzaneh, Synthesis and characterization of brush-like ZnO nanorods using albumen as biotemplate, Journal of the Brazilian Chemical Society 22 (2011) 484-488.
[15] S.A. Ansari, A. Nisar, B. Fatma, W. Khan, A.H. Naqvi, Investigation on structural, optical and dielectric properties of Co doped ZnO nanoparticles synthesized by gel-combustion route, Materials Science and Engineering: B 177(5) (2012) 428-435.
[16] R. Abdullah Mirzaie, F. Kamrani, A. Anaraki Firooz, A.A. Khodadadi, Effect of α-Fe2O3 addition on the morphological, optical and decolorization properties of ZnO nanostructures, Materials Chemistry and Physics 133(1) (2012) 311-316.
[17] A. Roychowdhury, A.K. Mishra, S.P. Pati, D. Das, Synthesis and characterization of multifunctional Fe3O4-ZnO nanocomposite, AIP Conference Proceedings 1447(1) (2012) 283-284.
[18] G. Zhang, W. Xu, Z. Li, W. Hu, Y. Wang, Preparation and characterization of multi-functional CoFe2O4–ZnO nanocomposites, Journal of Magnetism and Magnetic Materials 321(10) (2009) 1424-1427.
[19] S. Singhal, S. Jauhar, J. Singh, K. Chandra, S. Bansal, Investigation of structural, magnetic, electrical and optical properties of chromium substituted cobalt ferrites ($CoCrxFe2-xO4$, $0\leqslant x\leqslant 1$) synthesized using sol gel auto combustion method, Journal of Molecular Structure 1012(Supplement C) (2012) 182-188.
[20] T. Prakash, R. Jayaprakash, D. Sathya Raj, S. Kumar, N. Donato, D. Spadaro, G. Neri, Sensing properties of ZnO nanoparticles synthesized by using albumen as a biotemplate for acetic acid monitoring in aqueous mixture, Sensors and Actuators B: Chemical 176(Supplement C) (2013) 560-568.
[21] L. Kong, Z. Jiang, T. Xiao, L. Lu, M.O. Jones, P.P. Edwards, Exceptional visible-light-driven photocatalytic activity over BiOBr-ZnFe2O4 heterojunctions, Chemical communications 47(19) (2011) 5512-5514.
[22] J.A. Khan, M. Qasim, B.R. Singh, S. Singh, M. Shoeb, W. Khan, D. Das, A.H. Naqvi, Synthesis and characterization of structural, optical, thermal and dielectric properties of polyaniline/CoFe2O4 nanocomposites with special reference to photocatalytic activity, Spectrochimica Acta Part A: Molecular and Biomolecular Spectroscopy 109(Supplement C) (2013) 313-321.
[23] R. Sahoo, A. Roy, C. Ray, C. Mondal, Y. Negishi, S.M. Yusuf, A. Pal, T. Pal, Decoration of Fe3O4 Base Material with Pd Loaded CdS Nanoparticle for Superior Photocatalytic Efficiency, The Journal of Physical Chemistry C 118(21) (2014) 11485-11494.
[24] E. Casbeer, V.K. Sharma, X.-Z. Li, Synthesis and photocatalytic activity of ferrites under visible light: A review, Separation and Purification Technology 87(Supplement C) (2012) 1-14.
[25] S. Rana, R.S. Srivastava, M.M. Sorensson, R.D.K. Misra, Synthesis and characterization of nanoparticles with magnetic core and photocatalytic shell: Anatase TiO2–NiFe2O4 system, Materials Science and Engineering: B 119(2) (2005) 144-151.
[26] S. Zhang, J. Li, M. Zeng, G. Zhao, J. Xu, W. Hu, X. Wang, In Situ Synthesis of Water-Soluble Magnetic Graphitic Carbon Nitride Photocatalyst and Its Synergistic Catalytic Performance, ACS Applied Materials & Interfaces 5(23) (2013) 12735-12743.
[27] S. Boumaza, A. Boudjemaa, A. Bouguelia, R. Bouarab, M. Trari, Visible light induced hydrogen evolution on new hetero-system ZnFe2O4/SrTiO3, Applied Energy 87(7) (2010) 2230-2236.
[28] A. Belhadi, S. Boumaza, M. Trari, Photoassisted hydrogen production under visible light over NiO/ZnO hetero-system, Applied Energy 88(12) (2011) 4490-4495.
[29] T.J. Jacobsson, T. Edvinsson, Photoelectrochemical Determination of the Absolute Band Edge Positions as a Function of Particle Size for ZnO Quantum Dots, The Journal of Physical Chemistry C 116(29) (2012) 15692-15701.
[30] M. Qasim, K. Asghar, B.R. Singh, S. Prathapani, W. Khan, A.H. Naqvi, D. Das, Magnetically recyclable Ni0.5Zn0.5Fe2O4/Zn0.95Ni0.05O nano-photocatalyst: Structural, optical, magnetic and photocatalytic properties, Spectrochimica Acta Part A: Molecular and Biomolecular Spectroscopy 137(Supplement C) (2015) 1348-1356.
[31] M. Qasim, J. Ananthaiah, S. Dhara, P. Paik, D. Das, Synthesis and Characterization of Ultra-Fine Colloidal Silica Nanoparticles, Advanced Science, Engineering and Medicine 6(9) (2014) 965-973.
[32] S. Jambhrunkar, S. Karmakar, A. Popat, M. Yu, C. Yu, Mesoporous silica nanoparticles enhance the cytotoxicity of curcumin, RSC Advances 4(2) (2014) 709-712.
[33] P.R.K. Mohan, G. Sreelakshmi, C.V. Muraleedharan, R. Joseph, Water soluble complexes of curcumin with cyclodextrins: Characterization by FT-Raman spectroscopy, Vibrational Spectroscopy 62(Supplement C) (2012) 77-84.
[34] F. Muhammad, A. Wang, M. Guo, J. Zhao, W. Qi, G. Yingjie, J. Gu, G. Zhu, pH Dictates the Release of Hydrophobic Drug Cocktail from Mesoporous Nanoarchitecture, ACS Applied Materials & Interfaces 5(22) (2013) 11828-11835.

Section 4.7: Multifunctional $mSiO_2$@AgNPs and $mSiO_2$@Ag-Fe_3O_4@P(Nipam) NC for antimicrobial and drug delivery application

In the first part of this section, synthesis, characterization and antifungal activity of Ag embedded mesoporous silica nanoparticles ($mSiO_2$@AgNPs) have been discussed. Second part of this section discuss about development of magnetically controllable/separable and thermoresponsive $mSiO_2$@Ag-Fe_3O_4@P(Nipam) NC and characterization using various techniques.

4.7.1 Silver nanoparticles embedded mesoporous SiO_2 nanosphere: an effective anticandidal agent against Candida albicans 077

The outbursts of contagious diseases caused by different pathogenic microbes and the development of antibiotic resistance against conventional pharmaceutical antibiotics have encouraged pharmaceutical companies and researchers to search for new antimicrobial agents[1-4]. Candida albicans is a diploid fungus that causes common infections such as, denture stomatitis, thrush, urinary tract-infections, etc. Immunocompromised patients get severely infected by this fungus. Development of an effective anticandidal agent against this pathogenic fungus, therefore, will be very useful for practical application. In this work, Ag embedded mesoporous silica nanoparticles ($mSiO_2$@AgNPs) have successfully been synthesized and their anticandidal activities against C. albicans have been studied[5]. $mSiO_2$@AgNPs nanoparticles (d~400nm) were designed using pre-synthesized Ag nanoparticles and TEOS as precursor for SiO_2 in presence of CTAB as easily removable soft template. A simple, cost-effective, and environmentally friendly approach has been adopted to synthesize silver (Ag) nanoparticles using silver nitrate and leaf extract of *Azadirachta indica*. The mesoporous silica not only helps the silver nanocrystals to disperse in aqueous solution by protecting the active material from aggregation, but also provides a good stability, long term antimicrobial activity and good binding to microbial cells. The mesopores, with size equivalent diameter of the micellies (d = 4-6 nm), were generated on the SiO_2 surface by calcination after removal of the CTAB template. The morphology and surface structure of $mSiO_2$@AgNPs were characterized through XRD, FTIR, PSA, PL, UV-Vis spectroscopy, AFM, FESEM, BET, and HRTEM. The HRTEM micrograph reveals the well ordered mesoporous structure of the SiO_2 sphere. The antifungal activities of $mSiO_2$@AgNPs on *C. albicans cell* have been studied

through microscopy and are seen to increase with increasing dose of $mSiO_2$@AgNPs, suggesting $mSiO_2$@AgNPs to be a potential antifungal agent for C. albicans 077.

4.7.1.1 Preparation of $mSiO_2$@AgNPs

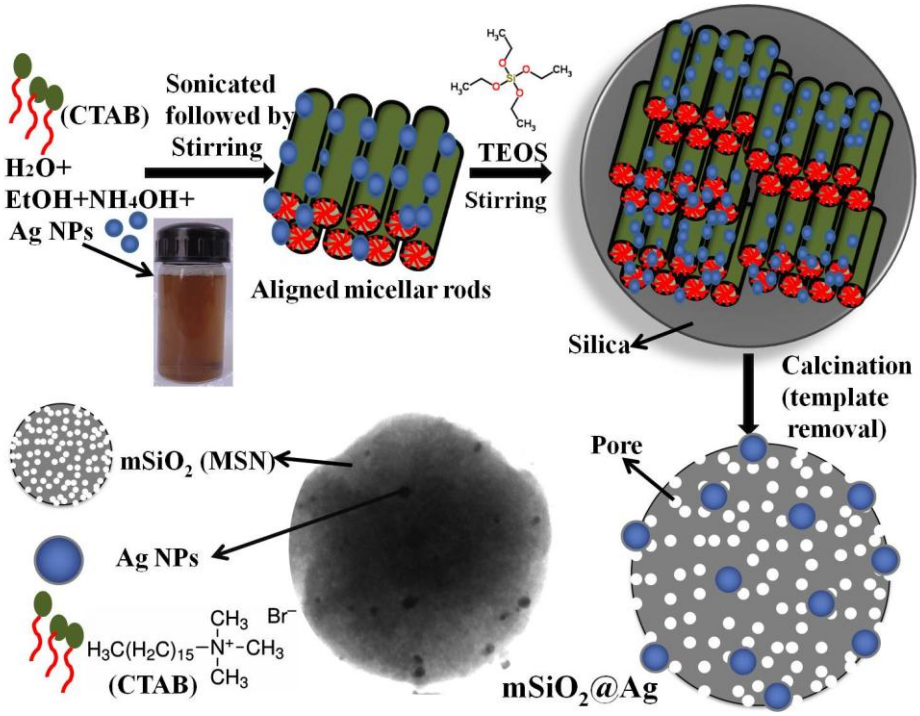

Schematic 4.7.1. Formation schematic of $mSiO_2$@Ag by the condensation of TEOS in presence of Ag NPs and CTAB.

Schematic 4.7.1 shows the formation schematic of $mSiO_2$@Ag by the condensation of TEOS in presence of Ag NPs and CTAB. For the synthesis of $mSiO_2$@Ag, first colloidal Ag nanoparticles with aligned micellar rods were obtained by dispersing Ag NPs with CTAB in alkaline mixture of water and alcohol. Ag embedded mesoporous silica nanosphere was prepared by hydrolysis and condensation of TEOS on aligned micellar rod of CTAB and Ag NPs and its subsequent calcination for the removal of CTAB.

4.7.1.2 Structural characterizations of $mSiO_2$@AgNPs

The phase and structure of $mSiO_2$@AgNPs was evaluated by powder X-ray diffraction (XRD) using CuKα radiation (CuKα= 1.540598 A^o) at room temperature. Figure 4.7.1 shows the X-ray diffraction pattern of $mSiO_2$@AgNPs and pure $mSiO_2$. XRD patterns confirm the presence of metallic Ag NPs within $mSiO_2$ network as well as the overall formation of crystalline $mSiO_2$@Ag nanocomposite. A broad diffraction peak around 23^O and sharp diffraction peaks at about 37.4^O, 43.6^O, 64.0^O, 76.8^O were appeared in the XRD pattern of

$mSiO_2$@AgNPs. The XRD pattern of pure $mSiO_2$ shows only one broad diffraction peak around 23^O and no other sharp peak has been observed. The broad peak around 23^O in both XRD pattern can be attributed to amorphous nature of silica. All these sharp diffraction peaks can be attributed to the presence of FCC polycrystalline Ag NPs with (111), (200), (220), and (311) reflection planes, respectively (space group: Fm-3m (no. 225), JCPDS File No. 65-8428).The mean crystallite size of Ag NPs was estimated by Debye Sherrer formula and found to be ~27 nm. Lattice constant of Ag NPs, estimated from the Powder X software, was found to be 4.07 Å , which is in agreement with previous report[6]. The lattice constant of Ag NPs is slightly lower than that of bulk Ag and it is due to the nano-sizing effect. Presence of both broad and sharp characteristic diffraction peaks of silica and Ag in the XRD pattern of $mSiO_2$@Ag nanocomposites confirm the formation of $mSiO_2$@Ag nanocomposites. Similar XRD pattern for silica-Ag system has been reported earlier[7].

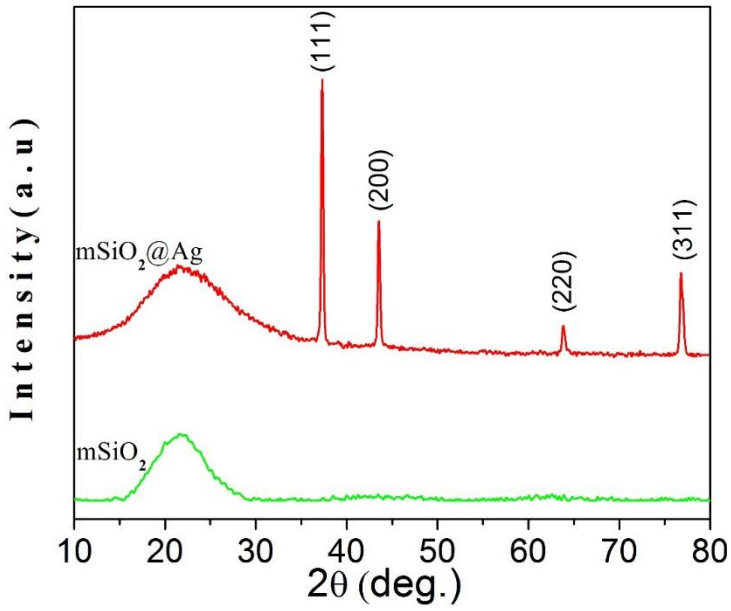

Figure 4.7.1: XRD Pattern of $mSiO_2$@Ag nanocomposite and $mSiO_2$.

4.7.1.3 Analysis of Structure, size and morphology by FESEM, TEM and AFM

Morphology and surface property of $mSiO_2$@AgNPs have been studied by using FESEM, TEM and AFM techniques. Figure 4.7.2 (a-b) shows the FESEM micrographs of $mSiO_2$@AgNPs. It is observed from the micrograph (Figure 2a) that $mSiO_2$ nanospheres are spherical in shape with ~400 nm diameter. Smaller size NPs of diameter around ~15-50 nm can also be seen on the surfaces of $mSiO_2$ nanospheres. These are the AgNPs that are embedded on the surfaces of $mSiO_2$ nanospheres.

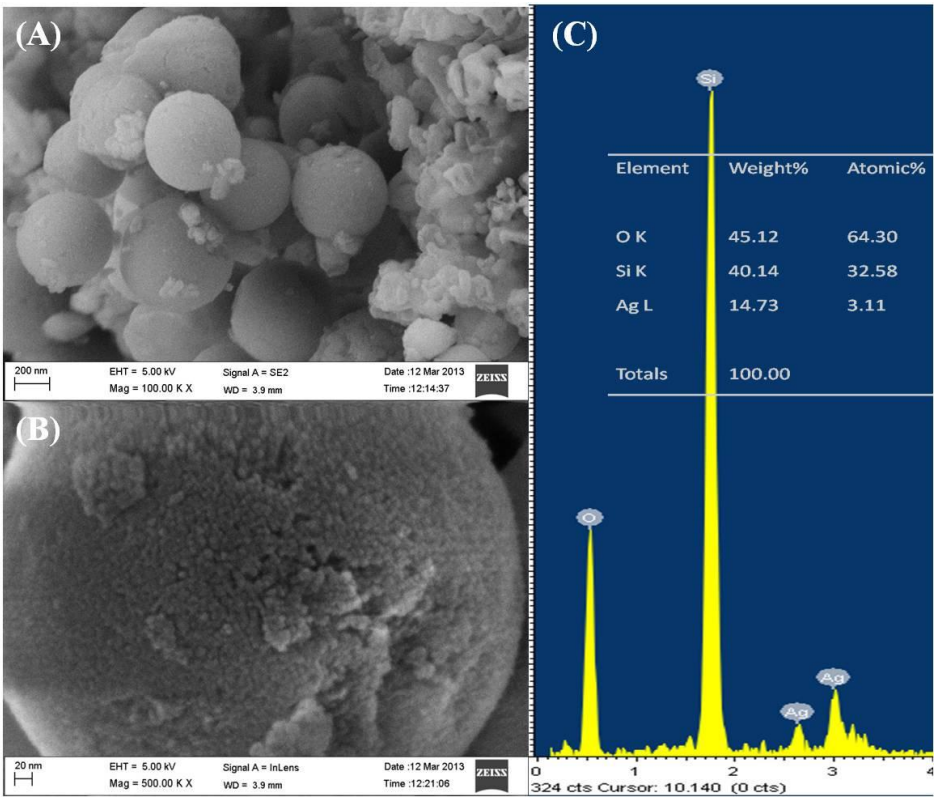

Figure 4.7.2. FESEM micrographs of (a) $mSiO_2$@AgNPs at low magnification (b) at high magnification, respectively, (c) Compositional analysis by energy dispersive spectroscopy (EDS).

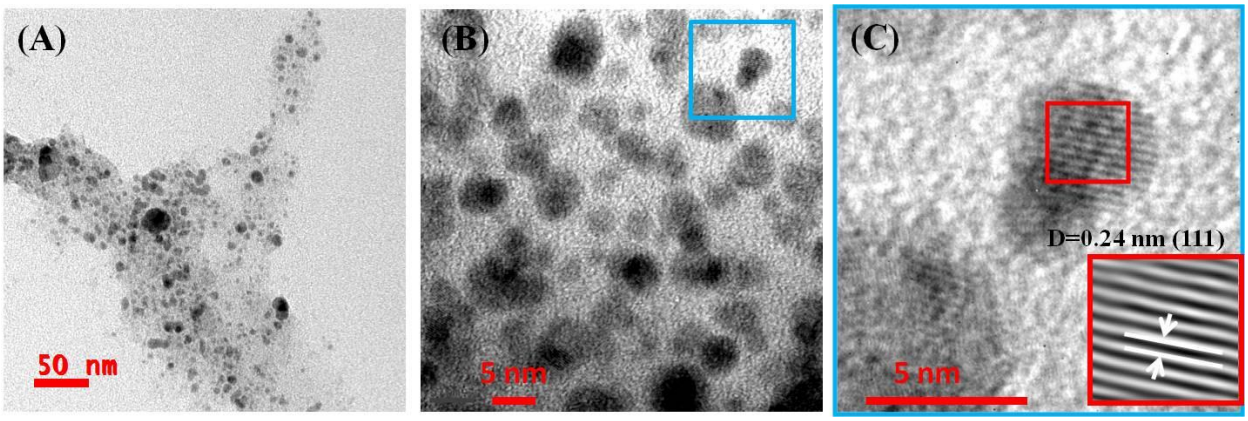

Figure 4.7.3. (A) TEM images of as prepared Ag NPs are shown in figure A (low) and B (high magnification), respectively. Figure C is enlarged portion of Blue framed Square in figure B to show lattice fringes of crystalline Ag NPs. Inverse Fast Fourier transform (IFFT) from the red framed part in (C) is shown in the inset of figure C.

From the high magnification (at 500 KX) FESEM image of $mSiO_2$@AgNPs nanospheres, at fig. 4.7.2(b), it is observed that the surface of the sphere is not smooth and it is very rough. The surface roughness may arise due to the presence of pores on the surface of $mSiO_2$ nanospheres or due to the presence of embedded Ag NPs on the surface. Indeed, the

smaller size Ag NPs are clearly seen on the surface of $mSiO_2$ nanospheres in high magnification image (fig. 4.7.2b). Elemental composition of the $mSiO_2$@Ag nanocomposite was analyzed by EDS and the results are shown in Figure (4.7.2c). EDS spectrum was recorded from the region with densely populated $mSiO_2$@Ag nanocomposite particles. EDS spectrum shows the presence of Si, Oxygen and Ag atoms in the composite sample. The appearance of Ag peak in the spectrum confirms the presence of Ag in the $mSiO_2$@Ag nanocomposite. No extra peak from impurities was observed.

Figure 4.7.3 (A-C) shows the TEM micrographs of Ag NPs. It is observed from the micrograph (Figure 4.7.3A & 4.7.4B) that Ag NPs are spherical in shape with ~5-30 nm diameters. HRTEM image confirms crystalline nature of Ag NPs and is shown in fig. 4.7.3C. d-spacing of Ag NPs is estimated to be 0.24 nm and it corresponds to the (111) plane of cubic Ag (fig. 4.7.3c). Thus, HRTEM result confirms successful formation of Ag NPs. Figure 4(A&B) shows TEM images of pure $mSiO_2$ without Ag NPs. From the TEM micrograph, the average size of $mSiO_2$ nanospheres was found to be about 400 nm and the shape of the nanosphere was observed to be spherical (fig. 4.7.4 A). The mesopore's channels with size equivalent diameter to the micellar rod (d ~4 nm) were observed on the $mSiO_2$ and are shown in fig. 4.7.4B. These imprinted channels are formed due to removal of CTAB template during calcination. Figures 4.7.4(C to F) show TEM images of $mSiO_2$@AgNPs. The spherical Ag NPs of diameter 10-50 nm can be easily seen on the $mSiO_2$ nanospheres. Figures 4.7.4(C&D) show light and dark field TEM images respectively of $mSiO_2$@AgNPs of the same region. In the light field image (fig. 4.7.4C) AgNPs on the surface of $mSiO_2$ nanospheres are seen as dark black dots and silica is appears grey in colour. In the dark field image (fig. 4.7.4D) Ag NPs are seen as white shining particles. This contrast is due to the crystalline nature of Ag NPs against the amorphous $mSiO_2$ nanospheres. High magnification images of $mSiO_2$@AgNPs (figures. 4.7.4E&F) show the embedded Ag NPs in the $mSiO_2$ nanospheres, and the presence of mesopore's channels in the $mSiO_2$ matrix (fig. 4.7.4E). It is also found that Ag NPs are uniformly distributed throughout the silica matrix. Some of the Ag NPs are seen to be embedded on the surface of silica nanosphere and covered with a thin layer of silica giving rise to better binding with the $mSiO_2$ nanospheres. Inset of figure 4.7.4F clearly shows the presence of mesopores (marked with red circles) of diameter about 4-6 nm on the silica nanosphere.

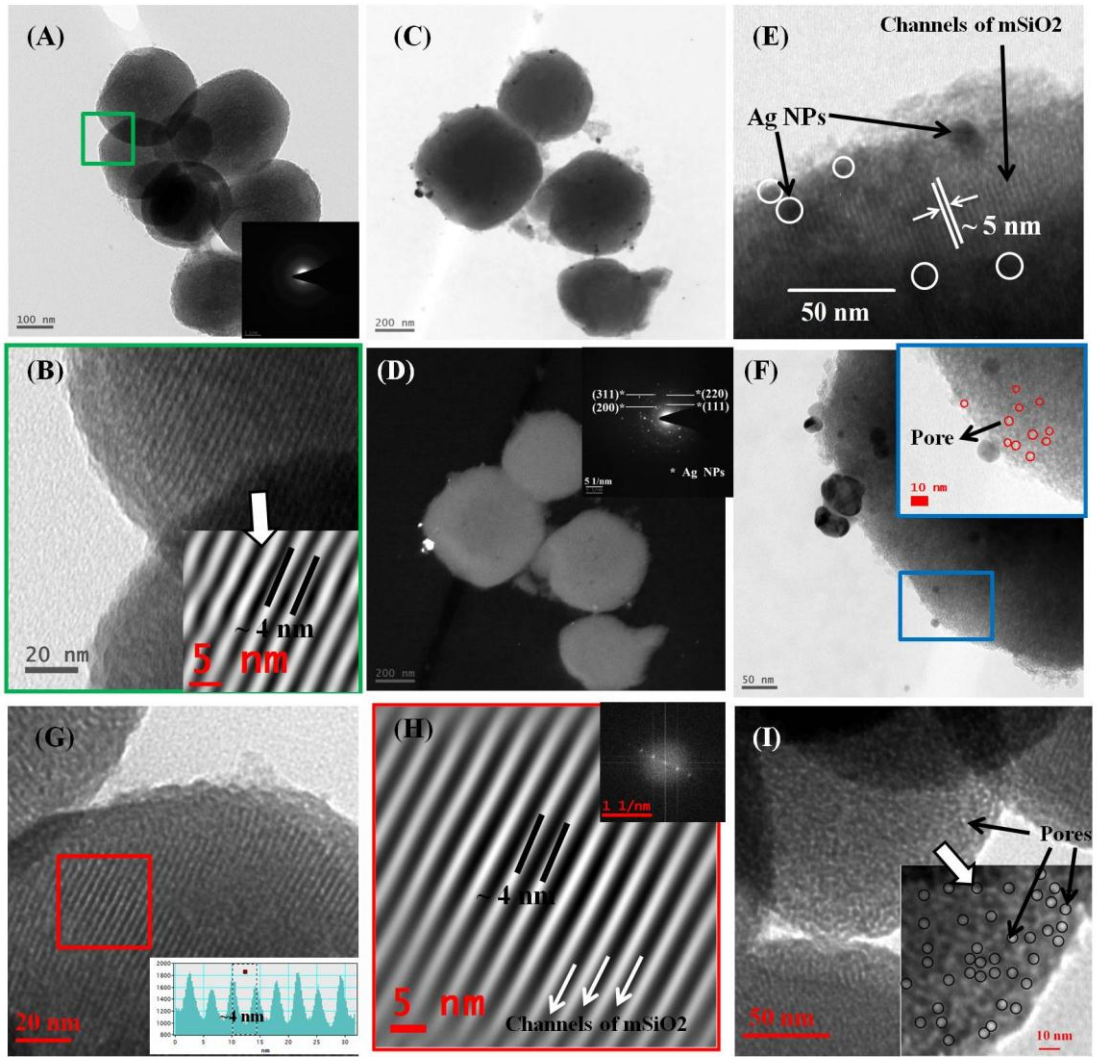

Figure 4.7.4. HRTEM micrographs of pure $mSiO_2$ nanoparticles are shown in fig. A (relatively low magnification) and B (high magnification), respectively. The Inset of figure (B) shows the IFFT image of the region indicated by arrow. Bright field (C) and dark field (D) micrographs of $mSiO_2$@AgNPs. The presence of Ag NPs and pore channels of $mSiO_2$ (inset of fig. F) of $mSiO_2$@AgNPs are shown in HRTEM images (E &F). The Inset of the figure (D) shows the indexed SAED pattern of $mSiO_2$@AgNPs, indicating Ag NPs to be embedded in $mSiO_2$ matrix. HRTEM micrograph, with incident electron beam perpendicular to channels of $mSiO_2$, is shown in fig. G. The Inset of figure (G) shows the line profile graph through the channels. IFFT image and corresponding FFT pattern from the red framed part in (G) are shown in figure H. HRTEM micrograph, with incident electron beam parallel to pores channels of $mSiO_2$, is shown in fig. I. Inset of Fig. I is enlarged portion of region indicated by arrow to show open pores (black circle) on $mSiO_2$.

The indexed SAED pattern of $mSiO_2$@AgNPs (inset of fig. 4.7.4D) shows dotted ring pattern, which is the signature of polycrystalline AgNPs in the $mSiO_2$ nanospheres. The SAED pattern was indexed for cubic structure by estimating the d-spacing from the ring pattern and comparing with the JCPDS card No. 65-8428 for Ag. SAED pattern of pure $mSiO_2$ does not

show any specific ring pattern as shown in the inset of fig. 4.7.4A. Absence of any diffraction pattern and cloudy nature of SAED pattern is due to the amorphous nature of $mSiO_2$ particle. Figures (G) and (I) show HRTEM micrographs taken with incident beam perpendicular and parallel to channels of $mSiO_2$, respectively, which clearly reveals the presence of ordered pore channels on SiO_2 nanosphere surface. The d spacing of channels obtained from line profile is found to be ~4 nm, which could be assigned to the (100) reflection of highly ordered 2D hexagonal symmetry[8, 9].

From figure (I) the pore sizes (black circle) are estimated to be ~4-6 nm. For clear visualization and better understanding of pore channels of $mSiO_2$ at higher magnification Fast Fourier Transformation (FFT) and Inverse Fast Fourier Transformation (IFFT) of a selected region of HRTEM image have been carried out and is shown in figure (H). IFFT image clearly shows the presence of array of ordered channels with spacing of ~4 nm that is assigned to (100) plane of 2D hexagonal symmetry[9]. Array of channels is a characteristic of the mesostructured of the SiO_2 [10]. First diffraction spot from the center of the FFT diffraction pattern corresponding to ~4 nm periodicity could be assigned to the (100) plane [8, 9]. Its higher order reflection (200) is also visible in the FFT diffraction pattern. A unit cell parameter (a_o) of ~4.6 nm has been estimated considering d_{100} = 4 nm. Obtained information is in good agreement with those reported in the literature [8-10]. Thus, IFFT image and corresponding FFT pattern also confirmed the ordered meso-structure of the SiO_2 matrix.

Particles size, shape and surface topography of $mSiO_2$@AgNPs were analyzed by atomic force microscopy (AFM). Figure 4.7.5 shows the AFM images of $mSiO_2$@AgNPs. The $mSiO_2$@Ag nanoparticles were found to be spherical in shape and hence the AFM data correlates well with the FESEM and TEM results. The size of the particles was estimated to be in between 250-400 nm. Surface of the $mSiO_2$@Ag nanosphere was observed to be quite rough with irregular morphology. Smaller Ag NPs nanoparticles (indicated by arrow in fig. 4.7.5A) of size 30-50 nm can be seen on the surface of bigger mesoporous silica nanosphere.

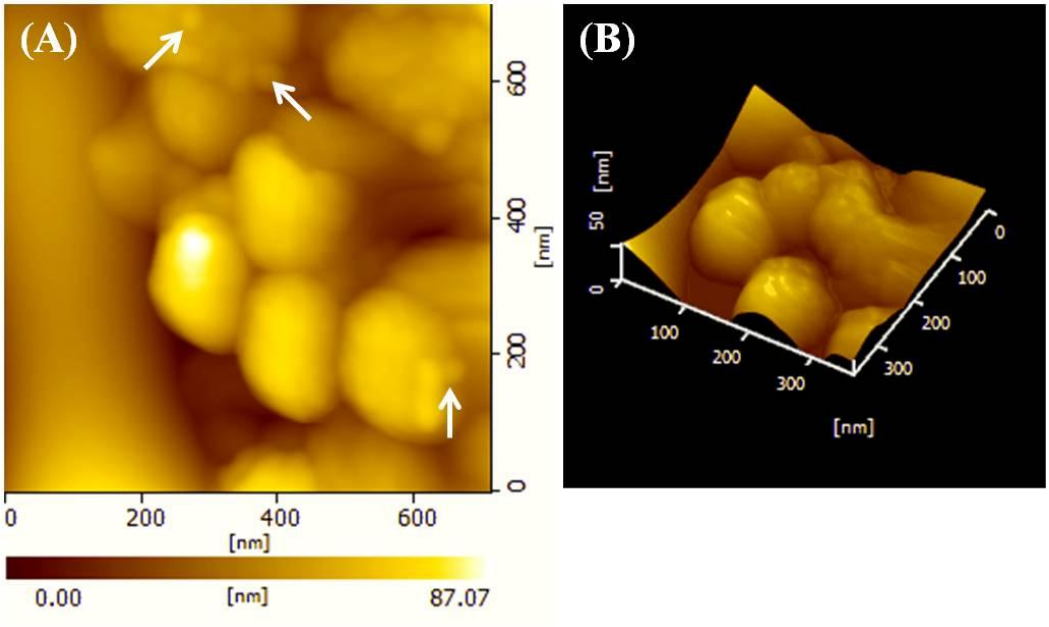

Figure 4.7.5. 2D (A) and 3D (B) Atomic Force Microscope (AFM) images of $mSiO_2$@AgNPs. Arrow marks indicate the presence of Ag NPs on $mSiO_2$.

4.7.1.4 Dynamic light scattering (DLS) analysis

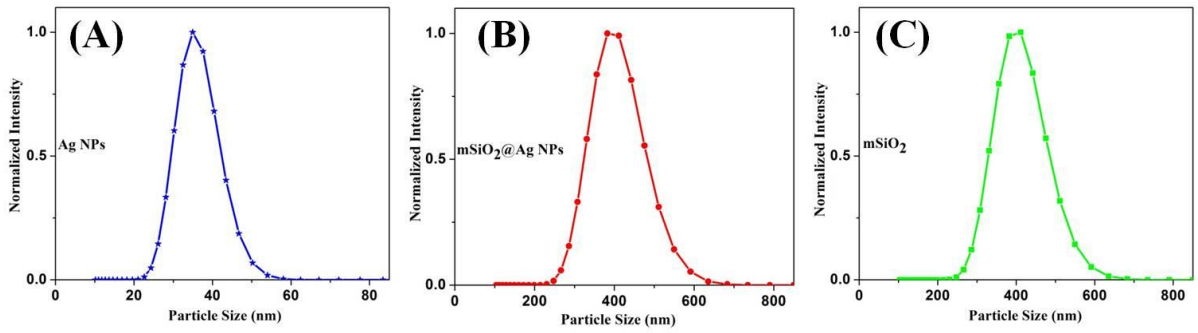

Figure 4.7.6. Hydrodynamic particle size distribution of Ag NPs (A), $mSiO_2$@AgNPs (B) and $mSiO_2$ (C) measured by Particles Size Analyzer (PSA) in liquid media.

Particles sizes were also estimated in liquid suspension, by a Particle Size Analyzer (PSA) using dynamic light scattering (DLS) technique. Hydrodynamic diameters of the as prepared Ag NPs, $mSiO_2$@AgNPs and $mSiO_2$, obtained by PSA, are shown in Figure 4.7.6(A-C). Mean hydrodynamic particle sizes were found to be ~35 nm, ~401 nm and ~405 nm for the Ag NPs, $mSiO_2$@AgNPs and $mSiO_2$ respectively. The particle sizes of $mSiO_2$@AgNPs and $mSiO_2$ obtained by TEM, FESEM and PSA data are in agreement. The particle size of Ag NPs

obtained by PSA is slightly more than the size obtained by TEM and it may be due to presence of biomolecules on surface of Ag NPs or agglomeration of smaller Ag NPs.

4.7.1.5 Optical characterization of $mSiO_2$@AgNPs

UV-Vis absorption spectra of $mSiO_2$@AgNPs and $mSiO_2$ nanospheres are shown in figure 4.7.7(a). The spectra of $mSiO_2$@AgNPs shows characteristic surface plasmon resonance (SPR) absorption peak centered at 400 nm. This is due to the SPR of Ag NPs, which is attributed to the coupling between the oscillation of the electron cloud on the surface of the Ag NPs and the incident electromagnetic wave in the quasi-static regimen [11]. It is also observed that the spectra of $mSiO_2$ nanospheres do not show any characteristic SPR absorption peak. Presence of SPR peak from Ag NPs in the spectrum confirms the presence of Ag NPs on $mSiO_2$ nanospheres, as has been observed in earlier studies[12]. UV-Vis absorption spectra of $mSiO_2$ show maximum absorption (λ_{max}) at ~250 nm wavelength. The optical phenomena in silica nanoparticles, is related to the presence of different defects such as oxygen and silicon vacancies associated with incomplete formation of Si-O-Si tetrahedral network at the silica surface. The above absorption range (~250 nm) may be attributed to the presence of surface paramagnetic E′centers, such as paramagnetic positively charged oxygen vacancies (≡Si•Si≡), or neutral dangling Si bonds (≡Si•)[13]. The synthesized $mSiO_2$@AgNPs is found to be photoluminescent, as shown in figure 4.7.7(b). The spectrum was obtained at 355 nm excitation wavelength. The PL spectrum is centered at 475 nm with two other emission peaks at 510 nm and 665 nm. These peaks can be attributed to the presence of Ag NPs in the $mSiO_2$@AgNPs, which are photoluminescent in nature. Presence of three emission peaks in PL spectrum could be due to different sizes of Ag NPs in the $mSiO_2$@AgNPs samples. Nanosize metal particles, such as Au and Ag, are known to exhibit novel size-dependent optical properties. The photoluminescence property of Ag NPs is dependent on the size of the Ag nanoparticles, and the spectra shift to higher energies with decreasing particle sizes [14]. The three visible PL peaks observed in the current study could be assigned to radiative recombination of the Fermi level electrons and sp- or d-band holes[14, 15]. The photoluminescence process in Ag NPs involves first excitation of electrons from occupied d bands to states above the Fermi level. Electron–phonon and hole–phonon scattering processes, then lead to an energy loss in the form of radiative recombination of an electron from an occupied sp band with the hole [15].

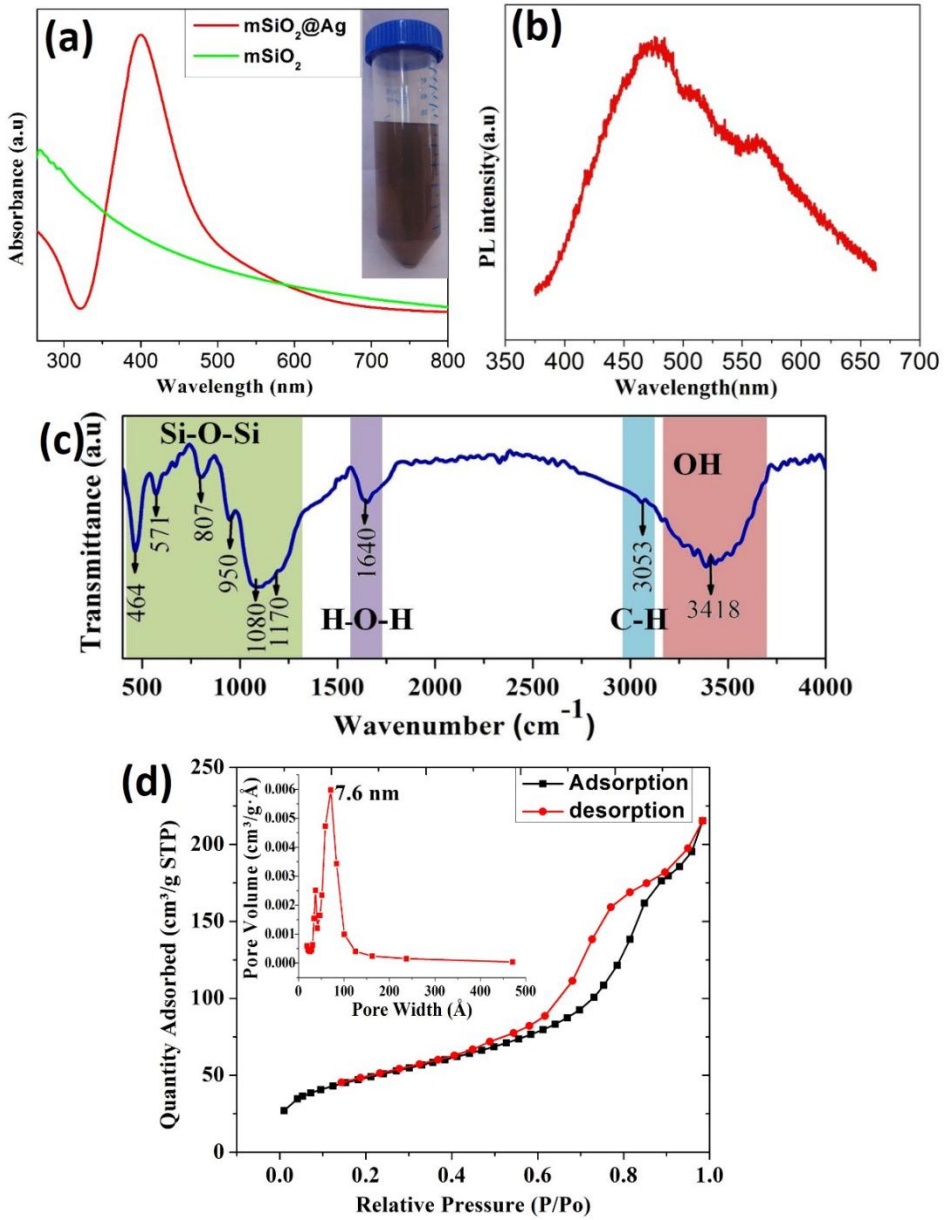

Figure 4.7.7: (a) UV-Vis absorption spectra of $mSiO_2$ and $mSiO_2$@Ag nanocomposite. Inset figure shows photograph of $mSiO_2$@AgNPs dispersed in water. (b) PL spectra of $mSiO_2$@Ag nanocomposite at 355 nm excitation wavelength. (c) FTIR spectra of $mSiO_2$@AgNPs. The different absorption region has been marked in different colors. (d) BET N_2-adsorption (black) and -desorption (red) isotherms of $mSiO_2$@AgNPs. Inset of figure (d) shows the corresponding pore size distribution calculated from desorption isotherm.

4.7.1.6 Characterization of chemical structure of $mSiO_2$@AgNPs

Functional groups and types of chemical bonds present in $mSiO_2$@AgNPs were investigated by FTIR technique. FTIR analysis of $mSiO_2$@AgNPs was conducted in KBr pellets. Figure 4.7.7(c) shows the FTIR spectrum of $mSiO_2$@AgNPs. The FTIR spectrum shows absorption bands arising from asymmetric vibration of Si–O (1080 cm^{-1}), Si–OH (950

cm^{-1}), and symmetric vibration of Si–O (807 cm^{-1}). These bands are indicative of dense silica network in the $mSiO_2$@AgNPs structure. The intense and broad band appearing at 1080–1170 cm^{-1} could be assigned to asymmetric stretching vibrations of Si–O–Si. The band at ~ 464 cm^{-1} corresponds to bending mode of Si–O–Si· The broad band around 3418 cm^{-1} can be attributed to surface silanols and adsorbed water molecules, whose deformational vibrations cause the absorption band near 1640 cm^{-1} [7]. The 1640 cm^{-1} band is due to scissor bending vibration of molecular water. The small band at 2900-3053 cm^{-1} can be assigned to the stretching mode of C-H bond and it may be due to the minute residual organic species in the pore of $mSiO_2$ nanosphere.

4.7.1.7 N_2 physisorption study

The N_2 adsorption-desorption study of $mSiO_2$@AgNPs has been conducted to evaluate the surface area and structural properties (Fig. 4.7.7(d)). The result exhibits characteristics of a type-IV isotherm with H_1 hysteresis loop and is indicative of the mesoporous structure of $mSiO_2$@AgNPs[16]. The stepwise increase in the adsorption, in the pressure range 0.5< P/Po <0.9, is due to the capillary condensation of N_2 gas in the mesopores. The BET surface area is also calculated using adsorption data, in the low-pressure range (0.05< P/Po<0.27), and found to be 172.3 m^2/g. Single point surface area (at P/Po = 0.27) and Langmuir surface area are found to be 167.7 and 258.9 m^2/g, respectively. The pore size and distribution were also calculated from the desorption branch of the isotherm using the Barrett–Joyner–Halenda (BJH) method. The pore size distribution (inset of Fig. 4.7.7(d)) data reveals the average diameter of the pores ~7.6 nm, which is uniform and correlates well with the HRTEM results. Single point adsorption total pore volume was estimated to be 0.33 cm^3/g at P/Po = 0.98.

4.7.1.8 Anticandidal activity of $mSiO_2$@AgNPs

It has already been reported in the literature that nanocomposites having silver nanocrystals have high antimicrobial activities against bacteria, virus, and fungi [3]. Fast global increase in the extent of resistant clinical isolates of *Candida albicans*, has attracted the research community attention to develop new anticandidal agents. Emergence of resistance in microbes to newly developed antimicrobial agents suggests that even new families of antimicrobial agents will have a short life assurance. Presently, the scientific community is focused more to nanoparticles, looking for new leads to introduce better nano-antimicrobial

drugs against MDR *Candida albicans* strains[17]. Silver nanoparticles are excellent antimicrobial agents, because of their larger antimicrobial contact area with the microbes. Therefore, in the current study the anticandidal activity of $mSiO_2$@AgNPs has been investigated against MDR *Candida. albicans* 077. In vitro killing assay and SEM observation of *Candida albicans* 077 culture treated with different concentrations of $mSiO_2$@AgNPs, are shown in Fig. 4.7.8A and Fig. 4.7.8B, respectively. Zone of inhibition around $mSiO_2$@AgNPs for *Candida albicans* 077 culture treated with different concentrations (0, 2 and 8 µg/mL) of antifungal agent is shown in Fig. 4.7.8C. The disc diffusion, in vitro killing assay and SEM observation reveal that the $mSiO_2$@AgNPs efficiently inhibits the growth of *Candida albicans* 077 depending on its dose. Increasing concentration of $mSiO_2$@AgNPs decreases the growth of *Candida albicans* 077. As expected, no zone of inhibition was observed in control culture. Zone of inhibition was found to increase with increase in dose of $mSiO_2$@AgNPs. The growth inhibition results, based on the growth curve analysis of *Candida albicans* 077 treated with different amount (0, 2 and 8 µg/mL) of $mSiO_2$@AgNPs, are shown in figure 4.7.9. The control sample of *Candida albicans* 077 cells showed a normal growth pattern with active exponential phase till ~22 h before attaining nearly stationary phase. The antifungal activity of $mSiO_2$@AgNPs against *Candida albicans* 077 leads to significant concentration-dependent suppression of growth and reduced exponential phases of *Candida albicans* 077. The results obtained from anticandidal tests show that the tested human pathogenic and MDR *Candida albicans* 077 fungus were sensitive to $mSiO_2$@AgNPs even at lower dose of 2 to 8 µg/mL.

From the obtained results and existing literatures the mechanism of anticandidal activity of $mSiO_2$@AgNPs as shown in schematic 4.7.2 could be attributed to the combination of more than one phenomenon such as, 1) release of silver ions (Ag^+) from the pores of $mSiO_2$@AgNPs and its subsequent uptake by the fungal cells followed by disruption of ATP production and DNA replication, 2) generation of reactive oxygen species (ROS) by Ag NPs and Ag^+, and 3) direct damage and distortion of cell membrane by $mSiO_2$@Ag nanoparticles followed by disruption and leakage of cellular contents[18]. All of the above phenomena either directly or indirectly lead to the significant inhibition of fungal cell growth. Release of silver ion (Ag^+) from the encapsulated Ag NPs through the pores of mesoporous silicate material have previously been reported and it was stated that well dispersed distribution of Ag NPs makes Ag ions release steadily from mesoporous materials over a long period leading to a long-term antibacterial effect[16]. Since Ag ions are known to have antimicrobial properties, it is expected that release of silver ions from $mSiO_2$@AgNPs is responsible for, or at least a part

of, their anticandidal activity. Due to high affinity for thiol group, Ag^{+} ions can interact with thiol groups present in the cysteine residues vital proteins, which will result in inactivation of enzyme proteins and disruption of respiration from ATP synthesis [19]. Higher concentration of Ag+ ions has been shown to interact with cytoplasmic components and nucleic acids[20]. The release Ag ions from $mSiO_2$@AgNPs move inside the cell producing reactive oxygen species (ROS) through redox reaction with oxygen. This process induces oxidative stress in the cells, resulting in inhibition of cell growth, and eventually cell death. The excess generation of ROS can attack membrane lipids leading to the breakdown of the cell membrane (leakage of cellular content) and mitochondrial function or cause DNA damage or disruption of its replication[21, 22]. Keuk Jun Kim et al have studied the ability of nano-Ag particles to affect the integrity of the plasma membrane of fungal cells and reported that AgNPs perturb the membrane lipid bilayers, causing the leakage of ions and other materials, forming pores, and dissipating the electrical potential of the membrane [22]. All of the above mentioned phenomena (leakage of cellular content, DNA damage, stopped ATP synthesis etc.) lead to cell death. Damage or disruption of C. albicans cells by $mSiO_2$@AgNPs have been supported by SEM micrographs of $mSiO_2$@AgNPs treated C. albicans cell culture (figure 8B). It may be reasonable to presume that such nanostructured $mSiO_2$@AgNPs, having well distributed Ag NPs, will benefit, preventing corrosion & agglomeration, and prolonging the release time of Ag ions from AgNPs embedded in mesoporous matrix leading to enhanced and long-term antibacterial effects. We anticipate that the antibacterial efficiency of $mSiO_2$@AgNPs can be further improved by increasing the loading content of AgNPs in $mSiO_2$ matrix. Both Guangxin Gu et al.m [23] and J. X. Wang et al. [24], in separate works, reported that the antibacterial property of Ag-SiO_2 system strongly depends on the loading of AgNPs in SiO_2 matrix and the antibacterial activity increases with increasing loading of the AgNPs.

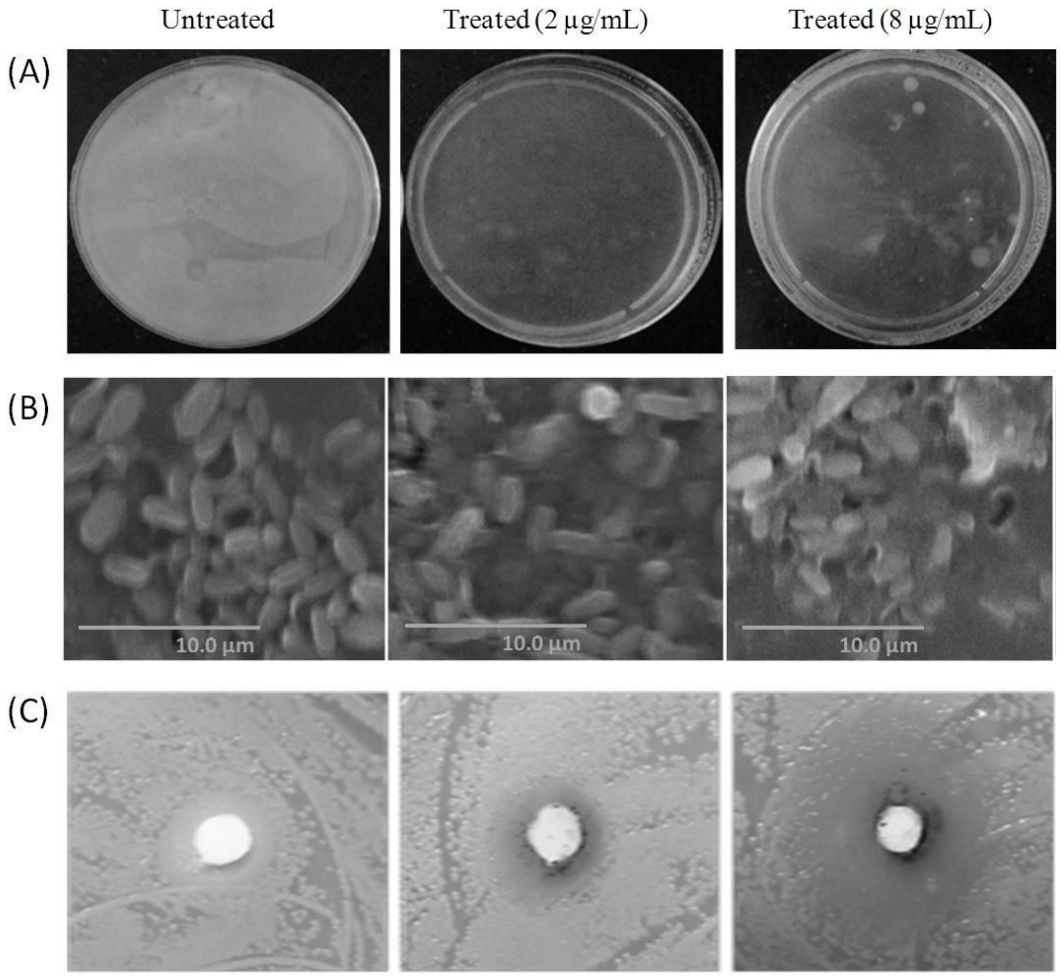

Figure 4.7.8. Anticandidal activity of $mSiO_2$@AgNPs. (A) In-vitro killing assay. (B) SEM based observation of change in cell morphology of Candida albicans 077, when treated. (C) Zone inhibition assay.

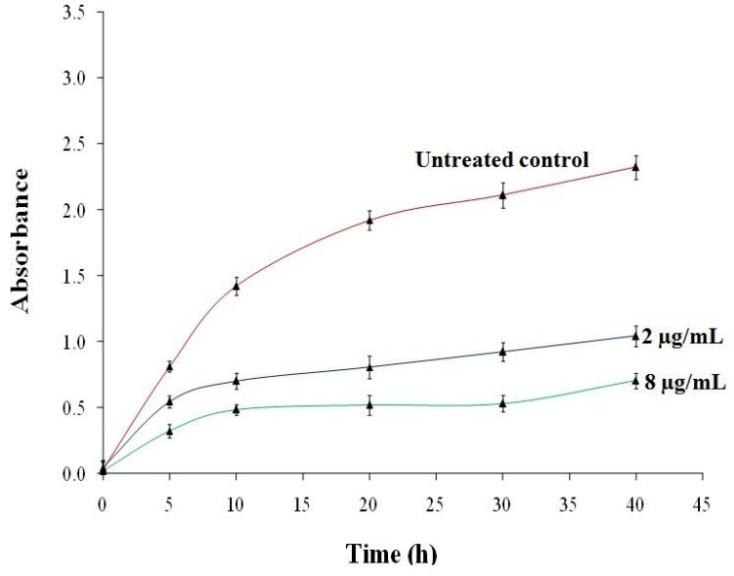

Figure 4.7.9. Growth curve analysis depicting the growth inhibition of Candida albicans 077 in the presence of different concentrations of $mSiO_2$@AgNPs.

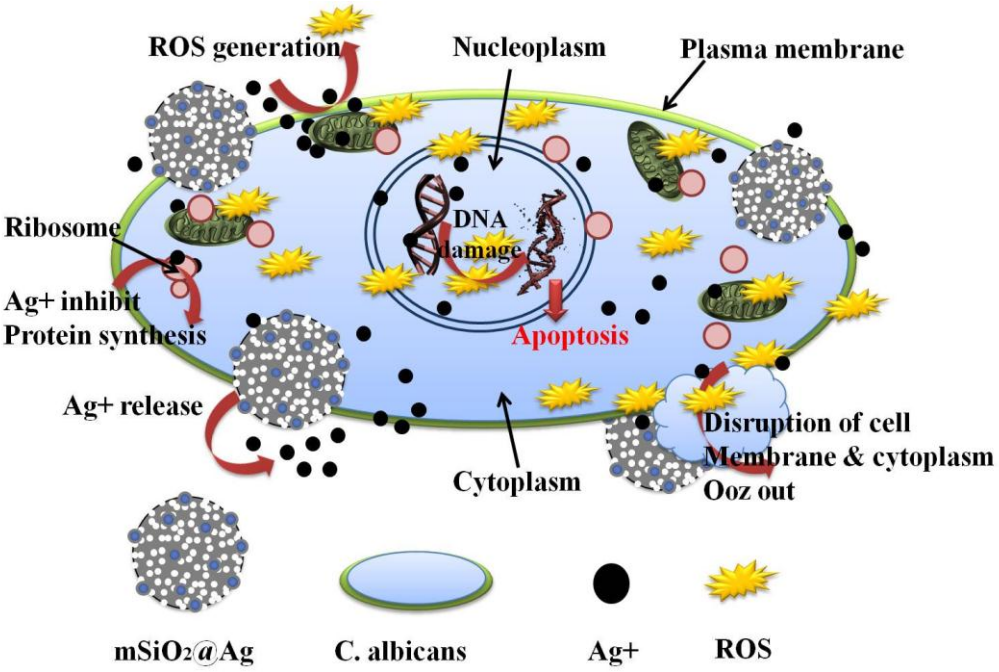

Schematic 4.7.2. Schematic of the antifungal action mechanism of $mSiO_2$@AgNPs on Candida Albicans 077. Few important phenomena such as the release of Ag ions, generation of ROS, DNA damage and disruption of cell membrane etc. have been represented in the schematic

4.7.2 Synthesis and characterization of magnetically controllable and thermoresponsive multifunctional $mSiO_2$@Ag-Fe_3O_4@P(Nipam) NC:

Incorporation of Ag NPs and MNP in the $mSiO_2$ nanocarriers give it multifunctional properties which enabled us to use it for imaging, tracking and chemo-photothermal therapy applications. Mesoporous silica NPs provide good stability and dispersibility to the antibacterial Ag NPs and presence of MNP can provide magnetic separability and controllability [25-27]. Combining only MNPs with MSN even though can provide magnetic targeting but lacks in tracking and imaging ability. Incorporation of imaging agent such as Ag to such magnetic mesoporous nano-system will result formation of multimodal multifunctional nanocarriers. Surface coating with thermos-responsive PNIPAM, facilitates nanocarrier with a temperature dependent release of payloads. In order to expand the multifunctionality of $mSiO_2$-AgNPs based hybrid composites or to add magnetic controllability and thermoresponsive-ness to it, incorporation Fe_3O_4 NPs and coating P(Nipam) have been done to get $mSiO_2$@Ag-Fe_3O_4 and $mSiO_2$@Ag-Fe_3O_4@P(Nipam) respectively. $mSiO_2$-Ag-Fe_3O_4 was prepared by simple sol gel process using AgNPs, Fe_3O_4 NPs, TEOS, and CTAB (as a template).

$mSiO_2$@Ag-Fe_3O_4@P(Nipam) NC was prepared by in situ coating of P(Nipam) on the surface of $mSiO_2$@Ag-Fe_3O_4 in the presence of oxidizer and crosslinker. Prepared smart nanocomposites have been characterized by XRD, SEM, EDS, TEM, FTIR, and VSM technique. Presence of characteristic diffraction peak of both Fe_3O_4 NPs and Ag NPs in the XRD pattern of $mSiO_2$@Ag-Fe_3O_4 confirm the successful formation of nanocomposite. TEM and HRTEM image confirm presence of AgNPs and Fe_3O_4 NPs in silica nanosphere and show coating of P(Nipam) polymer of 10 nm thickness. Magnetically controllable and thermoresponsive $mSiO_2$@Ag-Fe_3O_4@P(Nipam) NC could be very useful as intelligent antimicrobial agent which can kill microbes through release of Ag at physiological temperature when encounter with cells but does not release payloads at room temperature. $mSiO_2$@Ag-Fe_3O_4@P(Nipam) NC could also find application as nanocarrier in targeted chemo-photothermal therapy of cancer and targeted magnetic delivery of Ag NPs in medicinal and disinfection applications and its subsequent removal my magnetic field. Such system could find potential application in many biomedical fields including magnetic disinfectant with enhanced stability and antimicrobial activity, and recyclable surface-enhanced Raman scattering (SERS) material.

4.7.2.1 Structural characterizations

Formation and crystalline nature of $mSiO_2$@Ag-Fe_3O_4 were studied by XRD analysis. Figure 4.7.10 shows the XRD pattern of $mSiO_2$@Ag-Fe_3O_4 NC. In XRD pattern, characteristic peaks of Fe_3O_4 and Ag along with a hump of amorphous silica were observed. The peaks indexed in black colour with (220), (311), (400), (422), (511) and (440) plane are characterstic reflections of spinel cubic Fe_3O_4. The peaks indexed in blue colour with (111), (200), (220), and (311) plane are characterstic reflections of Ag NP. A hump at 22^o can be assigned to the presence amorphous silica. Presence of characteristic diffraction peak of both Fe_3O_4 NPs and Ag NPs along with a hump of amorphous silica in the XRD pattern of $mSiO_2$@Ag-Fe_3O_4 confirm the successful formation of nanocomposite. The crystallite size of incorporated Fe_3O_4 NPs was found (using 311peak) be ~10 nm. No other peaks of impurity have been observed in XRD pattern

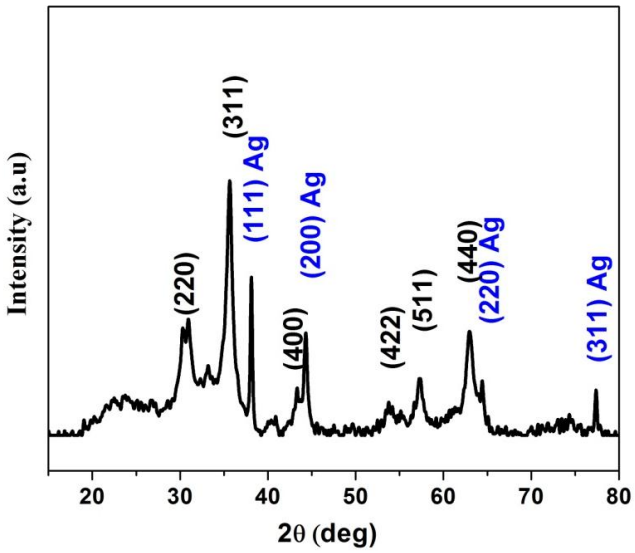

Figure 4.7.10. XRD pattern of $mSiO_2$@Ag-Fe_3O_4 NC.

4.7.2.2 Particles size, structure and morphology

a) SEM, TEM and EDS analysis of $mSiO_2$@Ag-Fe_3O_4 NC:

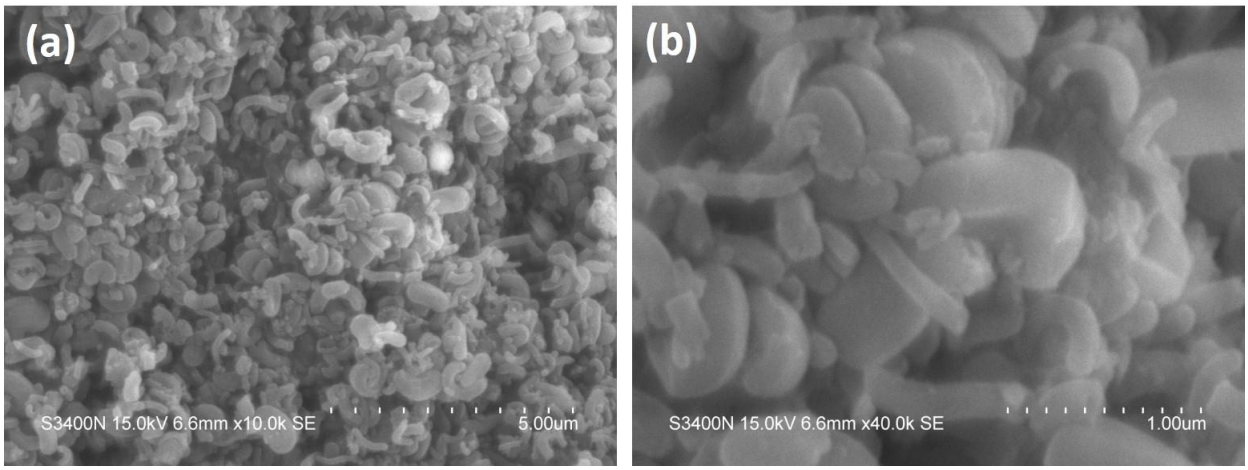

Figure 4.7.11. SEM micrographs of $mSiO_2$@Ag-Fe_3O_4 NC at low and high magnifications.

SEM and TEM were used to study the particles size and morphology of $mSiO_2$@Ag-Fe_3O_4 NC. Figure 4.7. 11(a-b) shows SEM micrographs of $mSiO_2$@Ag-Fe_3O_4 NC which showed the formation of elongated particles with bent and worm like morphology of $mSiO_2$@Ag-Fe_3O_4 NC. The width and length of particles varies from ~150-300 nm and ~500-750 nm respectively. Due to very small size of Ag NPs, they were not visible in these SEM image at magnification.

Figure 4.7.12(a-c) shows TEM micrographs of $mSiO_2$@Ag-Fe_3O_4 NC at low to high magnifications which also showed the formation of elongated particles with bent and worm

like morphology. TEM also showed similar particles size as from SEM. It can be seen in the TEM images that bigger $mSiO_2$ (grey appearance) is embedded with smaller size Ag NPs (black dot appearance) and Fe_3O_4 NP (black particle) (figure 4.7.12(c-d)). Relatively bigger embedded particles could be Fe_3O_4 NP whereas smaller particles may Ag NP. TEM micrographs of $mSiO_2$@Ag-Fe_3O_4 NC showing presence of ordered pore channels (indicated by arrows which are parallel to channels) on mesoporous silica is shown in figure 4.7.12 (d). These channels are generated by removal of CTAB and are characteristic feature of $mSiO_2$. EDS spectra of $mSiO_2$@Ag-Fe_3O_4 NC is shown in figure 4.7.12 (e). Appearance of peaks of Ag, Fe, Si, and O elements in EDS spectra $mSiO_2$@Ag-Fe_3O_4 NC suggested the presence of $mSiO_2$, Ag and Fe_3O_4 in $mSiO_2$@Ag-Fe_3O_4 NC.

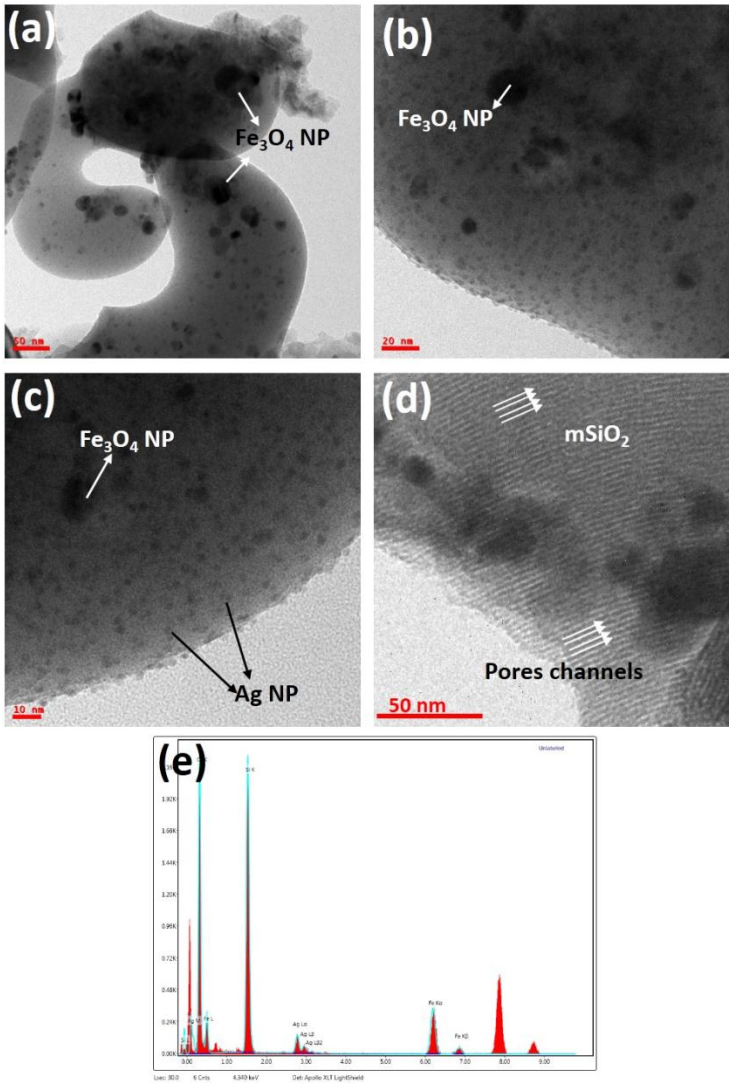

Figure 4.7.12. (a-c) TEM micrographs of $mSiO_2$@Ag-Fe_3O_4 NC at low and high magnifications. (d) TEM micrographs of $mSiO_2$@Ag-Fe_3O_4 NC showing presence of ordered pore channels in mesoporous silica. (e) EDS spectra of $mSiO_2$@Ag-Fe_3O_4 NC.

Further, confirmation of presence of Ag and Fe_3O_4 in $mSiO_2$@Ag-Fe_3O_4 NC were made by HRTEM analysis. Figure 4.7.12 (f) shows the HRTEM micrographs of $mSiO_2$@Ag-Fe_3O_4 NC which showed presence of atomic fringes of Ag and Fe_3O_4 NP. HRTEM of two different embedded particles showed d spacing values 0.48 and 0.31 nm which were assigned to the (111) and (220) plane of Fe_3O_4 NP. Another particle showed d spacing 0.24 nm which was assigned to the (111) plane of Ag NP.

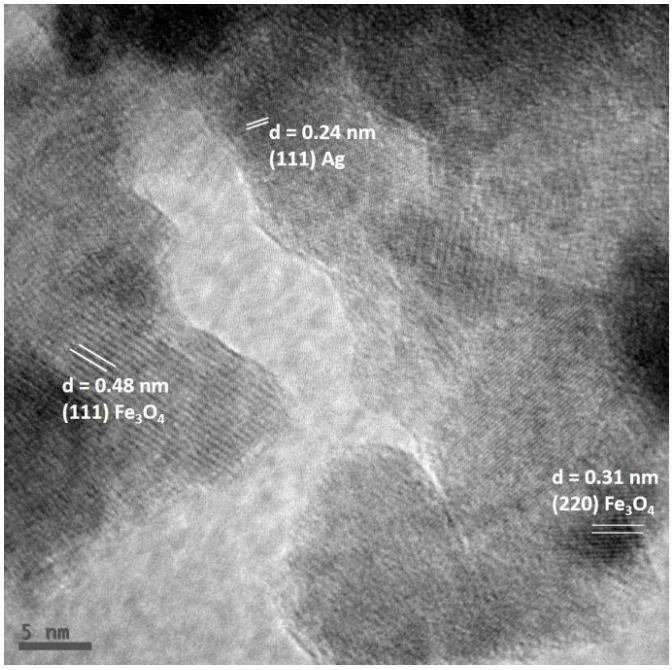

Figure 4.7.12. (f) HRTEM micrographs of $mSiO_2$@Ag-Fe_3O_4 NC.

b) TEM analysis of $mSiO_2$@Ag-Fe_3O_4@P(Nipam) NC:

Figure 4.7.13(a-d) shows TEM micrographs of $mSiO_2$@Ag-Fe_3O_4@P(Nipam) NC at low to high magnifications which clearly showed the coating of P(Nipam) polymer on $mSiO_2$@Ag-Fe_3O_4 NC particles. Particles were found to be elongated in shape. Presence of smaller darker nanoparticles on bigger $mSiO_2$ particles can be seen which suggested that coating process of polymer does not affected them. A light grey layer of P(Nipam) polymer over the surface of $mSiO_2$@Ag-Fe_3O_4 NC particles can clearly be seen in figure 4.7.13 (c-d). The thickness of coating layer of found to varies from 5-10 nm. A good binding between polymer layer and $mSiO_2$@Ag-Fe_3O_4 NC surface has been observed and coating is intact in nature.

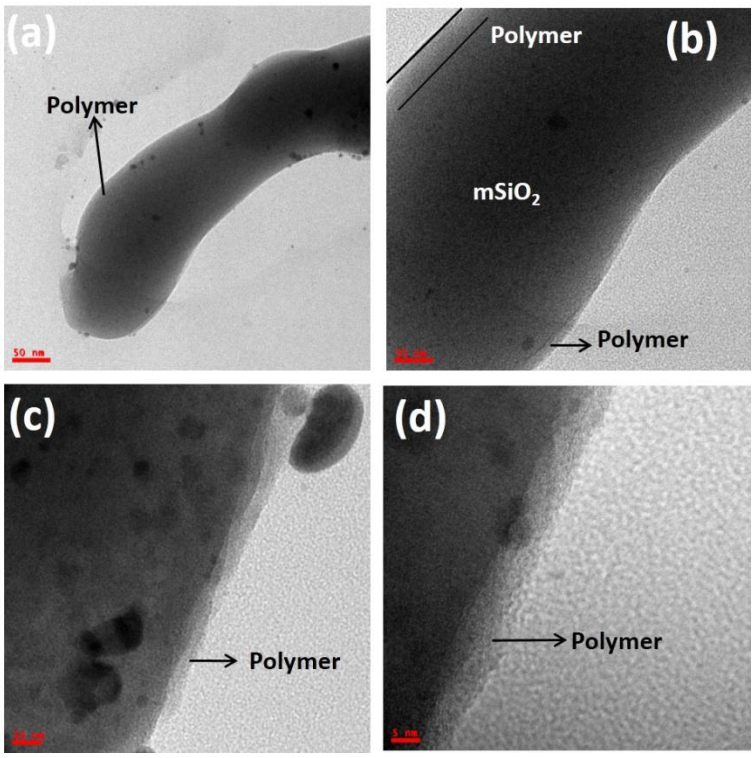

Figure 4.7.13 (a-d) TEM micrographs of $mSiO_2$@Ag-Fe_3O_4@P(Nipam) NC at low to high magnifications.

4.7.2.3 Characterization of chemical structure

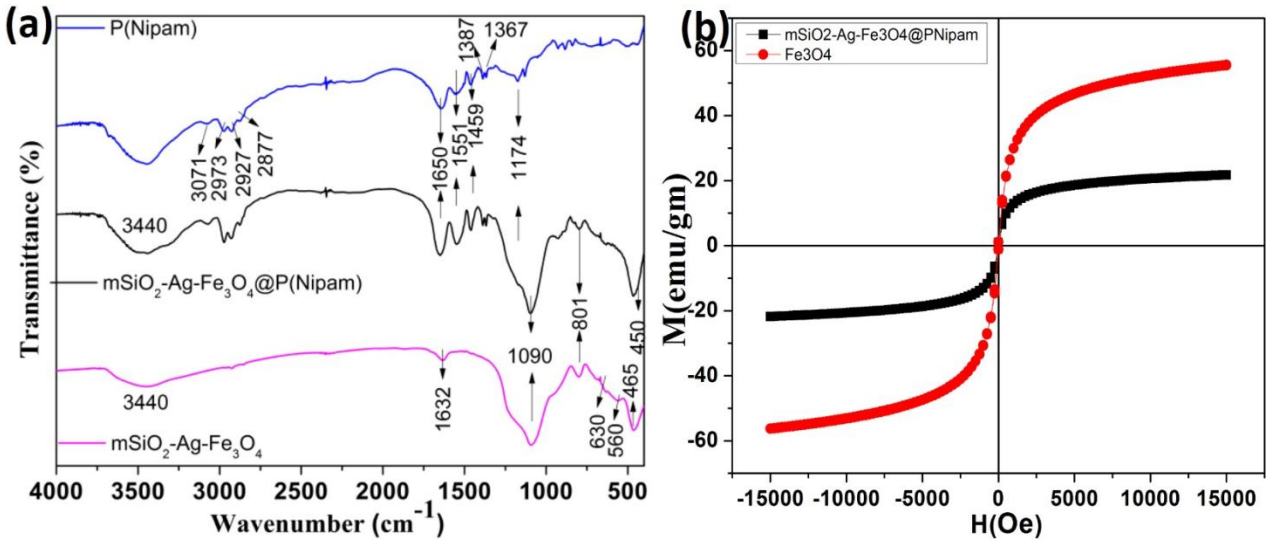

Figure 4.7.14. (a) FTIR spectra of $mSiO_2$@Ag-Fe_3O_4 NC, $mSiO_2$@Ag-Fe_3O_4@P(Nipam) NC and pure P(Nipam). (b) Room temperature M-H curve of Fe_3O_4 NP and $mSiO_2$@Ag-Fe_3O_4@P(Nipam) NC.

Further confirmation about the formation of $mSiO_2$@Ag-Fe_3O_4 NC and coating of P(Nipam) on $mSiO_2$@Ag-Fe_3O_4 NC were made by FTIR analysis. FTIR spectra of $mSiO_2$@Ag-Fe_3O_4 NC, $mSiO_2$@Ag-Fe_3O_4@P(Nipam) NC and pure P(Nipam) are shown in figure 4.7.14(a). FTIR spectra of $mSiO_2$@Ag-Fe_3O_4 NC shows the characteristic band of Fe_3O_4 NP and SiO_2 which suggest successful formation of $mSiO_2$@Ag-Fe_3O_4 NC. Bands at 400-650 cm^{-1} such as 450, 560 and 630 cm^{-1} in FTIR spectra of $mSiO_2$@Ag-Fe_3O_4 NC can be assigned to the Fe_3O_4 NP [28]. They have arisen from the stretching of octahedral and tetrahedral coordination complexes. The bands at 465, 801, and 1090 cm^{-1} can be attributed to the silica matrix [29]. The bands at 1632 and 3440 cm^{-1} in IR spectra of $mSiO_2$@Ag-Fe_3O_4 NC can be assigned to free H_2O and OH. FTIR spectra of $mSiO_2$@Ag-Fe_3O_4@P(Nipam) NC shows all the characteristic band of $mSiO_2$@Ag-Fe_3O_4 NC along with additional characteristic bands of coated P(Nipam) which confirm successful formation of $mSiO_2$@Ag-Fe_3O_4@P(Nipam) NC. FTIR spectra of pure P(Nipam) also has been done to show the characteristic band positions of P(Nipam). In FTIR spectra of $mSiO_2$@Ag-Fe_3O_4@P(Nipam) NC and P(Nipam), the bands at ~ 1367, 1387, 1459, 1551 and 1650 cm^{-1} are characteristic bands of P(Nipam) [28]. The IR spectra at 1650 cm^{-1} is due to the stretching vibration of C=O from amide I. The band at 1551 and 1459 cm^{-1} can be attributed to secondary amide N-H. The doublet absorption bands at 1387 and 1367 cm^{-1} can be assigned to the –CH vibration modes of isopropyl group of NIPAM (deformation of methyl group $(CH_3)_2$) [30]. In addition, smaller bands in IR spectra of $mSiO_2$@Ag-Fe_3O_4@P(Nipam) NC and P(Nipam) at ~ 2973, 2927 and 2877 cm^{-1} are due to symmetric and asymmetric stretching of CH, CH_2 and CH_3, respectively. A broad absorption peak at 3440 cm^{-1} was assigned to stretching vibration of –NH in NIPAM and OH in silica. Thus, simultaneous presence of characteristic band of P(Nipam), SiO_2 and Fe_3O_4 confirmed the formation of $mSiO_2$@Ag-Fe_3O_4@P(Nipam) NC.

4.7.2.4 Magnetic properties

Room temperature M-H curve of Fe_3O_4 NP and $mSiO_2$@Ag-Fe_3O_4@P(Nipam) NC are shown in figure 4.7.14 (b). Many magnetic parameters have been derived from the magnetization curve. Fe_3O_4 NP and $mSiO_2$@Ag-Fe_3O_4@P(Nipam) NC were found to superparamagnetic in nature, thus they have showed negligible remanat magnetization (M_R) and coercivity values. The superparamagnetic behavior of Fe_3O_4 NP and $mSiO_2$@Ag-Fe_3O_4@P(Nipam) NC were resultant of very small size of Fe_3O_4 NPs. The M_S values of Fe_3O_4 NP and $mSiO_2$@Ag-Fe_3O_4@P(Nipam) NC were observed to be 55.5 and 21.7 emu/gm

respectively. Ms value of 21.7 emu/gm is very high and good for nanocarrier based biomedical application and this type of magnetic nanocarrier can easy be controlled/targeted/separated using magnetic source. The M_R values of Fe_3O_4 NP and $mSiO_2$@Ag-Fe_3O_4@P(Nipam) NC were measured to be in between ~1 to 1.16 emu/gm. The coercivity values were found to be in between 20-35 Os for both the samples.

4.7.2.5 Biocompatibility study

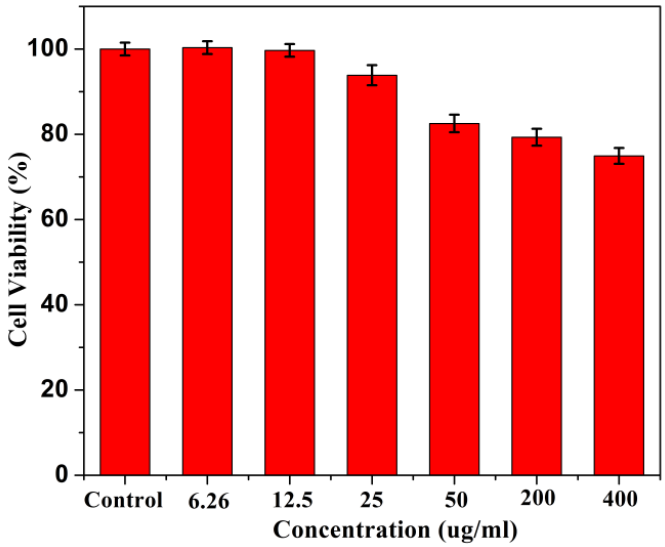

Figure 4.7.15. shows the cell viabilities of RAW 264.7 cells treated with different dose of $mSiO_2$@Ag-Fe_3O_4@P(Nipam) NC.

For biomedical application nanocarrier must be biocompatible in nature. Thus, biocompatibility of prepared $mSiO_2$@Ag-Fe_3O_4@P(Nipam) NC was studied by MTT assay against normal RAW 264.7 cells. Figure 4.7.15 shows the cell viabilities of RAW 264.7 cells treated with different dose of $mSiO_2$@Ag-Fe_3O_4@P(Nipam) NC. Prepared $mSiO_2$@Ag-Fe_3O_4@P(Nipam) NC was found to be biocompatible against the tested normal cells as no significant cell inhibition was observed up to high dose of 400 µg/ml. It was observed that at starting dose up to 12.5 µg/ml no cell inhibition was observed thereafter dose dependent cell viabilities were seen. A good cell viability of ~ 80% at high dose of 200 µg/ml of $mSiO_2$@Ag-Fe_3O_4@P(Nipam) NC was observed. At highest given dose (400 µg/ml) of $mSiO_2$@Ag-Fe_3O_4@P(Nipam) NC, the only 25% cell inhibition was observed. Thus, MTT assay result indicate the biocompatible nature of $mSiO_2$@Ag-Fe_3O_4@P(Nipam) NC.

4.7.3 Conclusion

In first part of this section, $mSiO_2$@Ag nanoparticles have successfully been prepared and their anticandidal activities against MDR *Candida. albicans 007* have been studied. A simple, cost-effective, and environmental friendly approach has been followed to synthesize Ag NPs using silver using nitrate and leaf extract of *Azadirachta indica*. Hydrolysis and condensation of TEOS in the presence of CTAB and Ag NPs have been carried out for synthesis of $mSiO_2$@AgNPs. Structural, morphological and physiochemical properties of $mSiO_2$@AgNPs have been studied using XRD, FTIR, FESEM, EDS, HRTEM, PL and UV-Vis spectrophotometer. A possible mechanism is suggested for the anticandidal activity of SiO_2@AgNPs against *C. albicans* 077. These $mSiO_2$@Ag nanoparticles may be used as a promising alternative to the current technologies involving the use of silver nanoparticles and silver-doped materials as antimicrobial coatings and colloidal suspensions. In addition, magnetically controllable and thermoresponsive $mSiO_2$@Ag-Fe_3O_4@P(Nipam) NC has also been successfully prepared by in situ coating of P(Nipam) on the surface of $mSiO_2$@Ag-Fe_3O_4 in the presence of oxidizer and crosslinker. Prepared smart nanocomposites have been characterized by structural, morphological and magnetic properties. Multifunctional $mSiO_2$@Ag-Fe_3O_4@P(Nipam) NC could be very useful as intelligent antimicrobial agent which can kill microbes through release of Ag when encounter with them. $mSiO_2$@Ag-Fe_3O_4@P(Nipam) NC could also find application as nanocarrier in chemo-photothermal therapy of cancer.

4.7.4 References

[1] J.D.D. Pitout, The latest threat in the war on antimicrobial resistance, The Lancet Infectious Diseases 10(9) (2010) 578-579.
[2] P.-R. Hsueh, New Delhi Metallo-β-lactamase-1 (NDM-1): An Emerging Threat Among Enterobacteriaceae, Journal of the Formosan Medical Association 109(10) (2010) 685-687.
[3] D.V. Quang, P.B. Sarawade, A. Hilonga, J.-K. Kim, Y.G. Chai, S.H. Kim, J.-Y. Ryu, H.T. Kim, Preparation of silver nanoparticle containing silica micro beads and investigation of their antibacterial activity, Applied Surface Science 257(15) (2011) 6963-6970.
[4] J.A. Khan, M. Qasim, B.R. Singh, W. Khan, D. Das, A.H. Naqvi, Polyaniline/CoFe2O4 nanocomposite inhibits the growth of Candida albicans 077 by ROS production, Comptes Rendus Chimie 17(2) (2014) 91-102.
[5] M. Qasim, R.S. Braj, A.H. Naqvi, P. Paik, D. Das, Silver nanoparticles embedded mesoporous SiO 2 nanosphere: an effective anticandidal agent against Candida albicans 077, Nanotechnology 26(28) (2015) 285102.
[6] M.A. Majeed Khan, S. Kumar, M. Ahamed, S.A. Alrokayan, M.S. AlSalhi, Structural and thermal studies of silver nanoparticles and electrical transport study of their thin films, Nanoscale Research Letters 6(1) (2011) 434.
[7] J. Han, P. Fang, W. Jiang, L. Li, R. Guo, Ag-Nanoparticle-Loaded Mesoporous Silica: Spontaneous Formation of Ag Nanoparticles and Mesoporous Silica SBA-15 by a One-Pot Strategy and Their Catalytic Applications, Langmuir 28(10) (2012) 4768-4775.
[8] S. Inagaki, S. Guan, T. Ohsuna, O. Terasaki, An ordered mesoporous organosilica hybrid material with a crystal-like wall structure, Nature 416 (2002) 304.

[9] M.-S.A. Meléndez-Ortiz H I, García-Cerda L A, Castruita G and Perera-Mercado Y A, Hydrothermal synthesis of mesoporous silica MCM-41 using commercial sodium silicate J. Mex. Chem. Soc. 57(73-79) (2013).
[10] J. Agundez, I. Diaz, C. Marquez-Alvarez, J. Perez-Pariente, E. Sastre, High acid catalytic activity of aluminosilicate molecular sieves with MCM-41 structure synthesized from precursors of colloidal faujasite, Chemical communications (1) (2003) 150-151.
[11] Y.-S.I. Ojeda-Martínez M L, Zamudio-Ojeda A, Gálvez-Gastelum F J, Machuca-Gonzalez R and Velásquez Ordone C, SiO2-Ag generation by sol-gel
technique for antibacterial use D8 Digest J. Nanomater. Biostruct. 8 (2013) 409–414.
[12] X. Ye, Y. Zhou, J. Chen, Y. Sun, Deposition of silver nanoparticles on silica spheres via ultrasound irradiation, Applied Surface Science 253(14) (2007) 6264-6267.
[13] I.A. Rahman, P. Vejayakumaran, C.S. Sipaut, J. Ismail, C.K. Chee, Size-dependent physicochemical and optical properties of silica nanoparticles, Materials Chemistry and Physics 114(1) (2009) 328-332.
[14] Y. Zhao, Y. Jiang, Y. Fang, Spectroscopy property of Ag nanoparticles, Spectrochimica Acta Part A: Molecular and Biomolecular Spectroscopy 65(5) (2006) 1003-1006.
[15] M. A, Photoluminescence of metals, Phys. Rev.Lett. 22 (1969) 185.
[16] Y. Tian, J. Qi, W. Zhang, Q. Cai, X. Jiang, Facile, One-Pot Synthesis, and Antibacterial Activity of Mesoporous Silica Nanoparticles Decorated with Well-Dispersed Silver Nanoparticles, ACS Applied Materials & Interfaces 6(15) (2014) 12038-12045.
[17] A.F. Wady, A.L. Machado, V. Zucolotto, C.A. Zamperini, E. Berni, C.E. Vergani, Evaluation of Candida albicans adhesion and biofilm formation on a denture base acrylic resin containing silver nanoparticles, Journal of Applied Microbiology 112(6) (2012) 1163-1172.
[18] C. Marambio-Jones, E.M.V. Hoek, A review of the antibacterial effects of silver nanomaterials and potential implications for human health and the environment, Journal of Nanoparticle Research 12(5) (2010) 1531-1551.
[19] K.B. Holt, A.J. Bard, Interaction of Silver(I) Ions with the Respiratory Chain of Escherichia coli: An Electrochemical and Scanning Electrochemical Microscopy Study of the Antimicrobial Mechanism of Micromolar Ag+, Biochemistry 44(39) (2005) 13214-13223.
[20] W.J. Feng Q L, Chen G Q, Cui F Z, Kim T N and Kim J O, A mechanistic study of the antibacterial effect of silver ions on on E. coli and S. aureus J. Biomed. Mater. Res. 52 (2000) 662–668.
[21] J.S. Kim, E. Kuk, K.N. Yu, J.-H. Kim, S.J. Park, H.J. Lee, S.H. Kim, Y.K. Park, Y.H. Park, C.-Y. Hwang, Y.-K. Kim, Y.-S. Lee, D.H. Jeong, M.-H. Cho, Antimicrobial effects of silver nanoparticles, Nanomedicine: Nanotechnology, Biology and Medicine 3(1) (2007) 95-101.
[22] K.-J. Kim, W.S. Sung, B.K. Suh, S.-K. Moon, J.-S. Choi, J.G. Kim, D.G. Lee, Antifungal activity and mode of action of silver nano-particles on Candida albicans, BioMetals 22(2) (2009) 235-242.
[23] G. Gu, J. Xu, Y. Wu, M. Chen, L. Wu, Synthesis and antibacterial property of hollow SiO2/Ag nanocomposite spheres, Journal of Colloid and Interface Science 359(2) (2011) 327-333.
[24] J.-X. Wang, L.-X. Wen, Z.-H. Wang, J.-F. Chen, Immobilization of silver on hollow silica nanospheres and nanotubes and their antibacterial effects, Materials Chemistry and Physics 96(1) (2006) 90-97.
[25] X. Zhang, H. Niu, J. Yan, Y. Cai, Immobilizing silver nanoparticles onto the surface of magnetic silica composite to prepare magnetic disinfectant with enhanced stability and antibacterial activity, Colloids and Surfaces A: Physicochemical and Engineering Aspects 375(1) (2011) 186-192.
[26] H.H. Park, S. Park, G. Ko, K. Woo, Magnetic hybrid colloids decorated with Ag nanoparticles bite away bacteria and chemisorb viruses, Journal of Materials Chemistry B 1(21) (2013) 2701-2709.
[27] S.-S. Chen, H. Xu, H.-J. Xu, G.-J. Yu, X.-L. Gong, Q.-L. Fang, K.C.-F. Leung, S.-H. Xuan, Q.-R. Xiong, A facile ultrasonication assisted method for Fe3O4@SiO2-Ag nanospheres with excellent antibacterial activity, Dalton Transactions 44(19) (2015) 9140-9148.
[28] K. Asghar, M. Qasim, G. Dharmapuri, D. Das, Investigation on a smart nanocarrier with a mesoporous magnetic core and thermo-responsive shell for co-delivery of doxorubicin and curcumin: a new approach towards combination therapy of cancer, RSC Adv. 7(46) (2017) 28802-28818.
[29] M. Jang, J.K. Park, E.W. Shin, Lanthanum functionalized highly ordered mesoporous media: implications of arsenate removal, Microporous and Mesoporous Materials 75(1) (2004) 159-168.
[30] X. Hu, X. Hao, Y. Wu, J. Zhang, X. Zhang, P.C. Wang, G. Zou, X.-J. Liang, Multifunctional hybrid silica nanoparticles for controlled doxorubicin loading and release with thermal and pH dually response, Journal of materials chemistry. B, Materials for biology and medicine 1(8) (2013) 1109-1118.

Section 4.8: Mesoporous $CaFe_2O_4$ NPs ($mesoCaFe_2O_4$ NPs)

In this section synthesis and characterization of mesoporous $CaFe_2O_4$ nanoparticles ($mesoCaFe_2O_4$ NPs) by different methods have been discussed.

Due to excellent loading capacity, mesoporous magnetic nanoparticles are widely studied for their biomedical applications such as in magnetically controlled delivery of anti-cancer drugs. Creation of mesoporous within magnetic nanoparticle itself will not only simplify the hectic synthesis process (required for heterostructure based mesoporous magnetic nanoparticles) but also provide good magnetic properties [1]. In addition, the ferrites of Ni, Mn, Co, Zn although possess good magnetic properties, their inherent toxicity after certain amount reduces their reliability. This, raises worries on their biocompatibility and their effectiveness for biomedical applications. Ferrites of calcium are expected to be more biocompatible since calcium is inherently non-toxic [2]. In this work, $mesoCaFe_2O_4$ NPs were prepared by simple coprecipitation route followed by calcination. Calcination has resulted in the generation of mesopores via the removal of template as well as formation of $mesoCaFe_2O_4$ NPs. XRD, HRTEM, BET analysis confirmed successful formation of $mesoCaFe_2O_4$ NPs. VSM results have suggested superparamagnetic nature of $mesoCaFe_2O_4$ NPs. MTT assays results of $mesoCaFe_2O_4$ NPs against normal cells suggested its biocompatibility. Prepared $mesoCaFe_2O_4$ NPs was loaded with Dox and its release study was performed. $mesoCaFe_2O_4$ NPs based drug nanocarrier could find potential application in magnetic drug delivery application because of biocompatibility and high loading ability. Two different, $mesoCaFe_2O_4$-1 and $mesoCaFe_2O_4$-2 NPs were prepared using oleic acid and CTAB respectively.

4.8.1 Characterizations of $mesoCaFe_2O_4$-1 nanocluster prepared using oleic acid

4.8.1.1 Structural properties

Phase formation and crystalline nature of $mesoCaFe_2O_4$ NPs were studied by powdered XRD analysis. Figure 4.8.1 shows XRD pattern of $mesoCaFe_2O_4$-1 NPs calcined at 400 and 600 ^oC. Both the samples show presence of all the characteristic peaks belonging to Fe_3O_4 type spinel cubic structure confirming that the sample is single phase and crystallizes in cubic spinel structure (PDF Number: 88-315). Absence of impurity peaks in the diffraction patterns suggested its high purity. Thus, the sharp diffraction peaks of (220), (311), (400), (422), (511)

and (440) planes at 2Θ 30°, 36°, 43°, 53°, 57°, and 63° respectively can be assigned to the Fe_3O_4 type spinel cubic $CaFe_2O_4$ NPs. In case of 600 °C, slightly increase in the peaks intensity was observed which could be due to increase in the crystallinity of the sample. Crystallite sizes calculated using Debye sherrer formula of meso$CaFe_2O_4$-1 NPs calcined at 400 and 600 °C were found to be 13 and 14 nm respectively. The lattice constant of meso$CaFe_2O_4$-1 NPs calcined at 400 and 600 °C were found to be 8.37 and 8.34 Å. Similar XRD pattern and observation for nanocrystalline $CaFe_2O_4$ has been reported earlier [3].

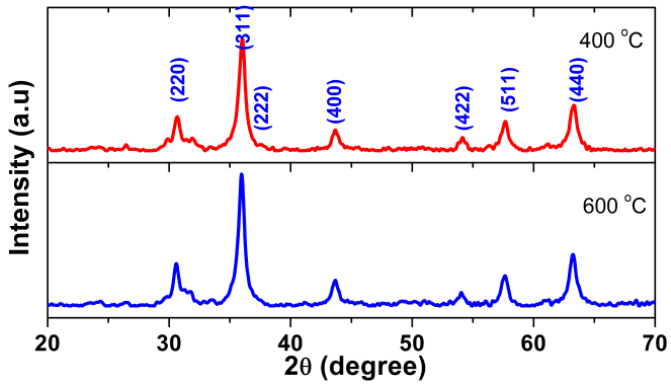

Figure 4.8.1. XRD pattern of meso$CaFe_2O_4$-1 NPs calcined at 400 and 600 °C.

4.8.1.2 Particles size and morphology

Particles size and morphology of meso$CaFe_2O_4$ NPs were studied by TEM analysis. Figure 4.8.2 (a-c) shows TEM micrographs of meso$CaFe_2O_4$-1 NPs calcined at 400 °C at different magnifications. Particles were found to be irregular in shape ranging from spherical to elongated particles. The average particles size was found to be ~30 nm. The particles size distribution of meso$CaFe_2O_4$-1 NPs calcined at 400 °C is shown in figure 4.8.2(d) which shows particles size ranges in between 20-60 nm. It was observed that bigger mesoporous nanoparticles are formed by many smaller particles or crystallite. From the TEM it was observed that particles are mesoporous in nature and mesopores present (white spot on the particles) on meso$CaFe_2O_4$-1 NPs can be seen in the TEM images. Mesoporous present on the particles have been marked with red circles in figure 4.8.2(c). Two sizes of pores were observed on the particles first in range of ~2-7 nm and second in the range of ~10-25 nm. These pores could have generated due to the removal of oleic acid and aggregation of primary particles with interparticle cavities. Presence of white dots of diameter on particles confirms the presence of pores. Figure 4.8.2 (e) and (f) shows FESEM micrograph of meso$CaFe_2O_4$-1 NPs calcined at 400 °C corresponding particles size distribution respectively. Here also particles were found to

be of different morphologies ranging irregular to spherical. The number of spherical particles were more and can been seen clearly in FESEM image. The mean particles size was found to ~37 nm.

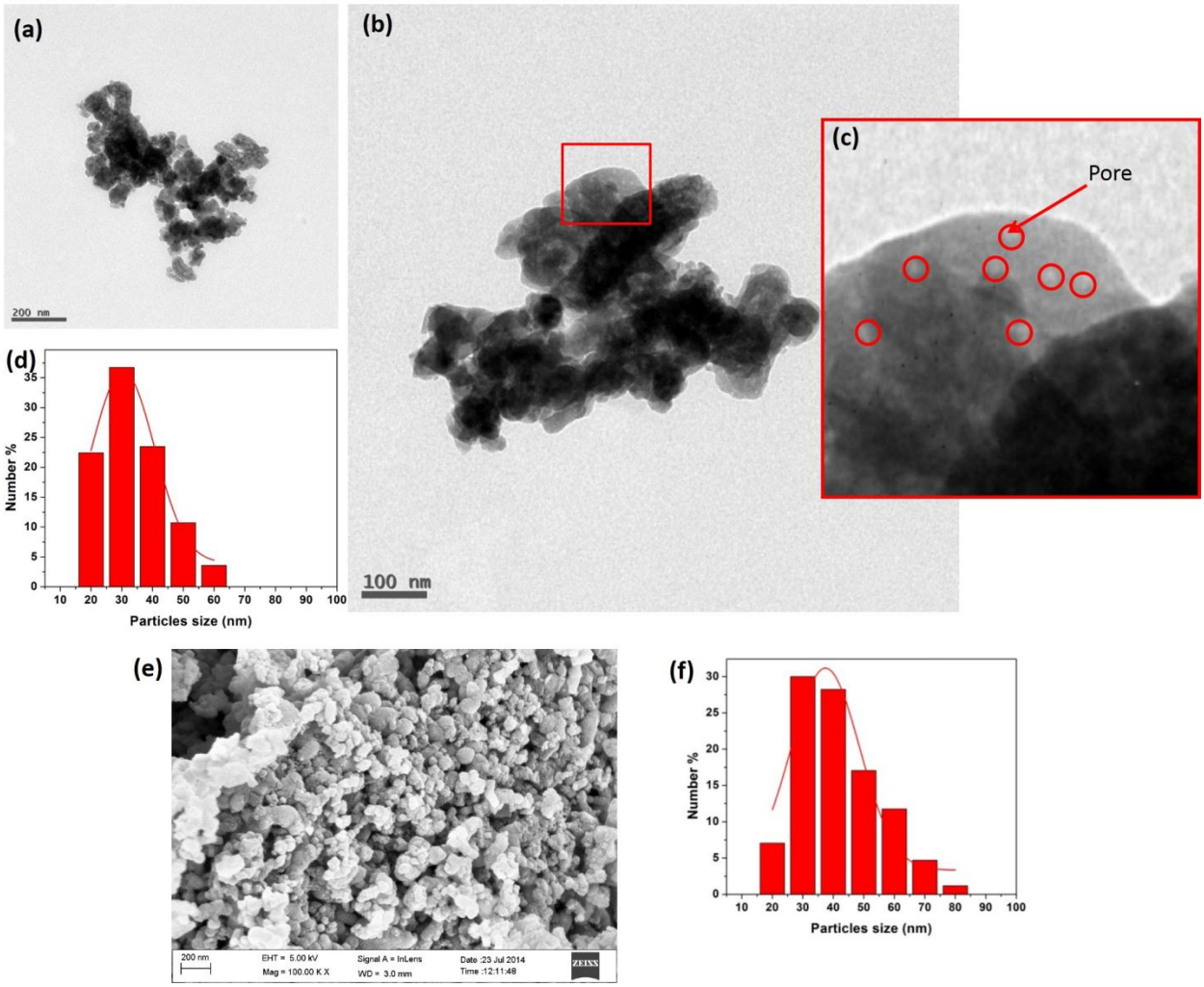

Figure 4.8.2. (a-b) TEM micrographs of meso$CaFe_2O_4$-1 NPs calcined at 400 ^oC. (c) Enlarge image of red framed region in (b). (d) Particles size distribution of meso$CaFe_2O_4$-1 NPs calcined at 400 ^oC. FESEM micrograph (e) of meso$CaFe_2O_4$-1 NPs calcined at 400 ^oC with corresponding particles size distribution (f).

Figure 4.8.3 (a-d) shows low and high magnification TEM micrographs of meso$CaFe_2O_4$-1 NPs calcined at 600 ^oC. Formation of mesoporous and hollow meso$CaFe_2O_4$-1 nanosphere was observed. It was observed from figure 4.8.3 (a & b) that mesoporous particles are spherical in shape and the particle size was found to be in between 50-90 nm. It was observed that bigger meso$CaFe_2O_4$ nanoclusters or nanosphere of size 50-100 nm are formed by fused or interconnected aggregation of many smaller $CaFe_2O_4$ crystallite of size 7-15 nm. Presence of white spot on these mesoporous meso$CaFe_2O_4$ nanoclusters suggested presence of

mesopores. It can be seen that mesoporosity is mainly due to the interparticle cavity in 3D agglomerate. TEM micrograph of single meso$CaFe_2O_4$ NPs nanoclusters is shown in figure 4.8.3(b) which shows hollow nature of these mesoporous nanocluster. It was observed that wall of the hollow nanocluster is composed of large number of very small crystallite. Presence of pores on the particles can also be seen in high magnification images figure (b-c). HRTEM analysis of these nanocluster confirm the presence of large number of well crystalline $CaFe_2O_4$ nanocrystal in wall region and also shows presence of pores. HRTEM micrograph showing half of single meso$CaFe_2O_4$-1 NPs nanosphere is shown in figure 4.8.3(c). Presence of well-ordered atomic plane with d spacing of 0.31 nm ((220) plane) in enlarge HRTEM image (figure 4.8.3d) confirmed the formation of nanocluster by many well crystalline $CaFe_2O_4$ nanocrystal. The pores size on the surface of nanocluster was found to be in between 2-7 nm. The size of central hollow space was found to be 10-30 nm.

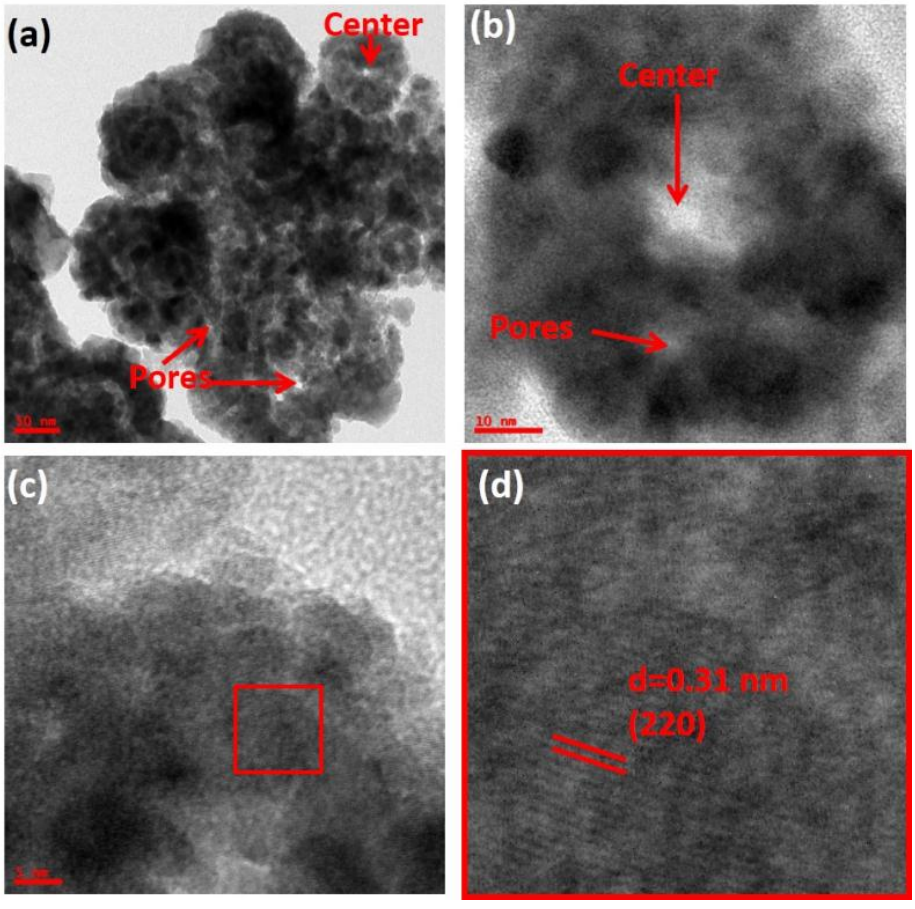

Figure 4.8.3. (a) TEM micrograph of meso$CaFe_2O_4$-1 NPs calcined at 600 ^oC. (b) TEM micrograph of single meso$CaFe_2O_4$-1 NPs. (c) HRTEM micrograph showing half of single meso$CaFe_2O_4$-1 NPs. (d) Enlarge HRTEM image of red framed region in (c).

4.8.1.3 Formation mechanism of nanoclustered mesostructure

Formation of these nanocluster can be explained as follow. Addition of oleic acid in the pre-generated nuclei or primary particles resulted formation of oleic acid coated $CaFe_2O_4$ nanocrystals. Due to high surface energy, these smaller oleic acid coated $CaFe_2O_4$ primary particles could have aggregated around free excess oleic acid via hydrophobic interaction to formed bigger nanocluster of size 50-100 nm that is mesostructured-oleic acid complex [4]. Further removal of organic oleic acid from these nanocluster (mesostructured-oleic acid complex) on calcination has resulted in the formation of mesoporous hollow nanocluster [4]. Previous literature and TEM observations suggest that crystalline nanocrystals in these mesoporous nanosphere are hold together by an amorphous matrix [5] [6]. Detailed discussion about the formation mechanism of these kind of nanoclustered mesostructured are discussed in previous literatures [4] [7].

4.8.1.4 N2 adsorption-desorption study

Further, presence of mesoporous on the meso$CaFe_2O_4$-1 NPs calcined at 400 and 600 ^oC. have also been suggested by the N_2 adsorption-desorption isotherms of meso$CaFe_2O_4$-1 NPs calcined at 400 and 600 ^oC (Fig. 4.8.4a-b). Both the isotherm display presence of clear hysteresis loop which is characteristic of the mesoporous structure. The sharp increases in the adsorption amount, in the pressure range $0.8< P/Po <0.9$, is due to the capillary condensation of N_2 gas in mesopores. These observations confirmed formation of mesopores in meso$CaFe_2O_4$-1 NPs. All three, BET, single point and Langmuir surface area of meso$CaFe_2O_4$-1 NPs (400 ^oC) were found to be in between ~ 16-25 m^2/g. BET, single point and Langmuir surface area of meso$CaFe_2O_4$-1 NPs (600 ^oC) were found to be in between ~ 14-22 m^2/g. Single point adsorption total pore volume of meso$CaFe_2O_4$-1 NPs calcined at 400 and 600 ^oC were estimated at P/Po = 0.98 are found to be ~0.07 and ~0.05 cm^3/g respectively. It was notice that in both the case the surface area and pore volume are less which is probably due to the presence of less number of pores. In the present case mesoporous nature was obtained mainly through interparticle spacing than intra-particles which could be reason for less surface area and pore volume. In addition, porosity further can be increased by choosing suitable surfactant which serve as templet and generate a good volume of porosity within the particles.

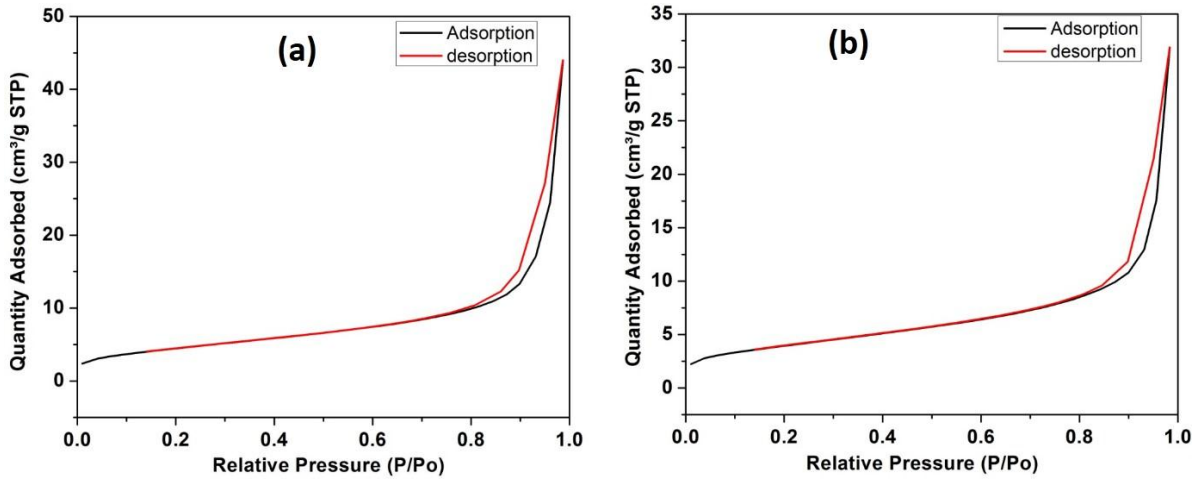

Figure 4.8.4. N_2 adsorption desorption isotherm of meso$CaFe_2O_4$-1 NPs calcined at 400 (a) and 600 ^oC (b).

4.8.1.5) Magnetic properties

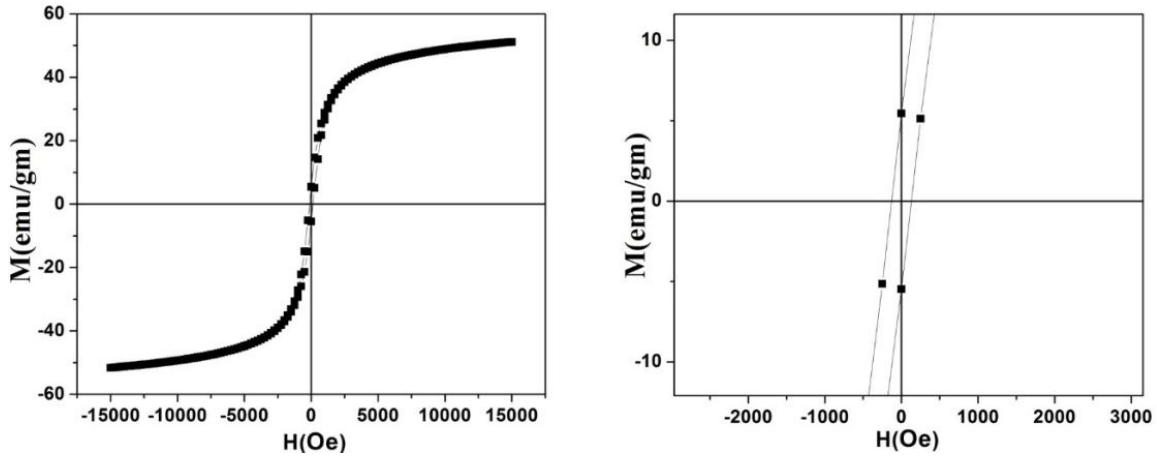

Figure 4.8.5. M-H curve of meso$CaFe_2O_4$-1 NPs (400 ^oC) (left). Right sided figure shows enlarge M-H curve to show M_R and coercivity values.

M-H curve of meso$CaFe_2O_4$-1 NPs (400 ^oC) is shown in the figure 4.8.5. From this M-H plot different magnetic parameter have been extracted. No much coercivity and remanat magnetization were observed thus the meso$CaFe_2O_4$-1 NPs have shown superparamagnetic behavior. The superparamagnetic behavior of these meso$CaFe_2O_4$-1 NPs was attributed to the very small size $CaFe_2O_4$ (equal to single domain). The magnetic controllability and targetability of a magnetic nanocarrier is govern by its Ms values. The Ms values of meso$CaFe_2O_4$-1 NPs was found to be 51 emu/gm respectively. M_R and coercivity of values were found to be 5.46 and 128 Os respectively. Due to its very high Ms value (than heterostructure based mesoporous magnetic nanocarriers) and superparamagnetic nature

mesoCaFe$_2$O$_4$-1 NPs could find potential application in magnetically controlled drug delivery applications.

4.8.2 Characterizations of mesoCaFe$_2$O$_4$-2 NP prepared using CTAB template

4.8.2.1 Structural properties

Aiming to increase the porosity of the mesoporous CaFe$_2$O$_4$ NPs, namely, mesoCaFe$_2$O$_4$-2 NP has been prepared using CTAB as sacrificial template via coprecipitation route. Crystalline nature of mesoCaFe$_2$O$_4$-2 NP was studied by powdered XRD. Figure 6 shows XRD pattern of powdered mesoCaFe$_2$O$_4$-2 NP. Appearance of weak intense and broad characteristic peaks of Fe$_3$O$_4$ type spinel cubic system suggest formation of nanocrystalline spinel cubic CaFe$_2$O$_4$ NPs. It was observed from the XRD pattern that the crystallite size of mesoCaFe$_2$O$_4$-2 NP is very small.

4.8.2.2 Particles size, structure and morphology by TEM

Figure 4.8.7 (a-c) show TEM micrographs at low and high magnification of mesoCaFe$_2$O$_4$-2 NPs. From the TEM micrographs of mesoCaFe$_2$O$_4$-2 NPs, formation of random shaped 3D mesoporous aggregates (100-200 nm) consisting of smaller CaFe$_2$O$_4$ nanoparticle (size 10-15 nm) have been observed. These mesoporous particles (mesoCaFe$_2$O$_4$-2 NP) of size 100-200 nm are high porous in nature. The presence of white spots on the mesoCaFe$_2$O$_4$-2 NPs confirmed its porous nature. Further confirmation of presence of pores were made by high magnification TEM analysis. In the high magnification TEM image (figure 4.8.7c), it was observed that smaller CaFe$_2$O$_4$ nanoparticles have pores of average size ~ 5-6 nm within its center. One single smaller CaFe$_2$O$_4$ nanoparticle of size 12 nm and having pore of size 5.5 nm in the center has been marked in figure 4.8.7(c). Each pore was found to be surround by a wall of thickness ~3-5 nm. Thus, the crystallite size of CaFe$_2$O$_4$ is very small (~ 3-5 nm). These pores of sizes equivalent with the diameter of micelle size of CTAB have been generated via by CTAB. The typical size of a micelle is ~ 5 nm [8]. The arrangements of pores were found to be disordered in nature. Intraparticle pores were found in every smaller CaFe$_2$O$_4$ nanoparticle and interconnected 3D network of these smaller porous nanoparticle have resulted in the formation of bigger mesoporous nano-system. Formation mechanism of CTAB assisted synthesis mesoCaFe$_2$O$_4$-2 NPs could be explained as below. CTAB micellar rods formed in alkaline aqueous medium were used as soft template. Coprecipitation of Fe and Ca precursor on these templates have resulted in the formation of intermediate CaFe$_2$O$_4$-CTAB complex.

Further calcination of intermediate $CaFe_2O_4$-CTAB complex have resulted in the formation of meso$CaFe_2O_4$-2 NPs. Pores size and its distribution as well as TEM observation suggest generation of pores via CTAB.

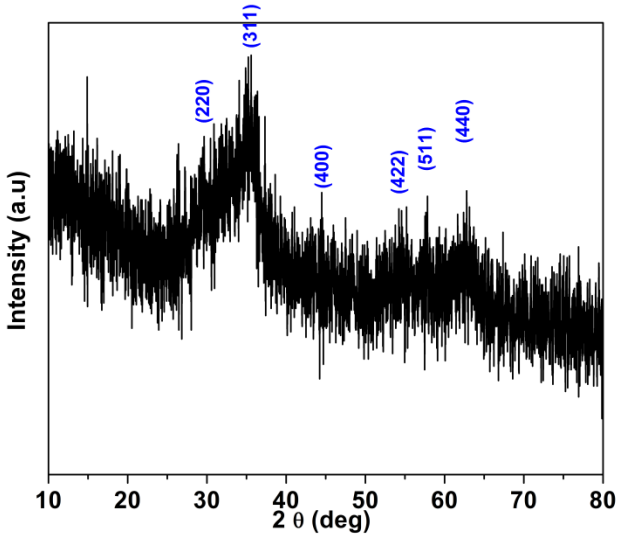

Figure 4.8.6. XRD pattern of meso$CaFe_2O_4$-2 NP.

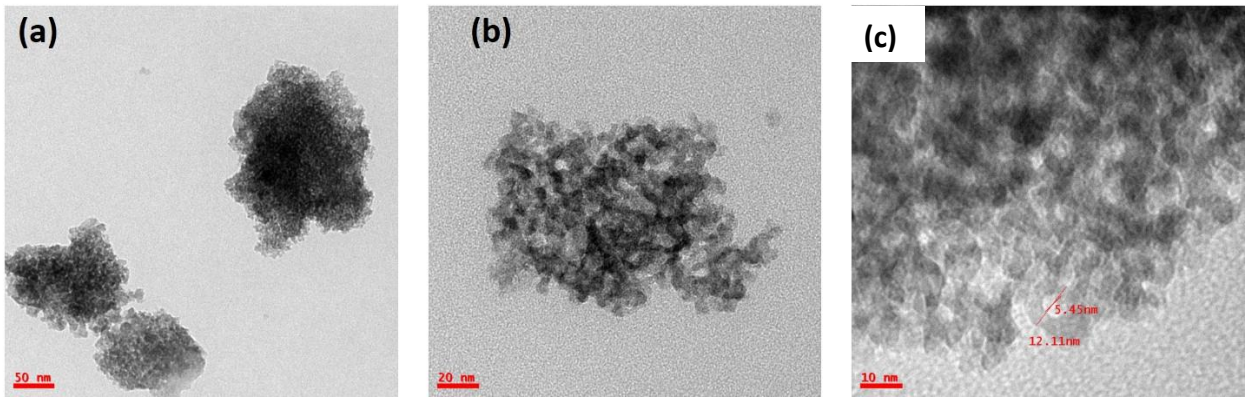

Figure 4.8.7. (a-c) TEM micrographs of mesoporous $CaFe_2O_4$ NPs prepared using CTAB as sacrificial template (meso$CaFe_2O_4$-2 NP).

4.8.2.3 N_2 adsorption desorption isotherm

Further confirmation of presence porosity and mesoporous structure of meso$CaFe_2O_4$-2 NP was studied by BET analysis. The N_2 adsorption desorption isotherm of meso$CaFe_2O_4$-2 NP is shown in figure 4.8.8(a). It was observed from the isotherm that sample is highly mesoporous in nature as it has shown presence of well-defined hysteresis in N_2 adsorption-desorption isotherm. It is worthy to mention that hysteresis in N_2 adsorption-desorption isotherm is characteristic indication of mesoporous structure. Observed isotherm and hysteresis could be

put into standard Type IV isotherm and H1 hysteresis categories of IUPAC which are symbolic of mesoporous structure meso$CaFe_2O_4$-2 NP. Capillary condensation of N_2 gas in the mesopores has resulted the rapid increase in adsorption isotherm in between 0.4 to 0.9 P/Po. Single point surface area (at P/Po = 0.27) was found to be 93 m_2/g. The BET and Langmuir specific surface area of meso$CaFe_2O_4$-2 NP were found to be 95.5 and 143.3 m^2/g respectively. Figure 4.8.8(b) shows pore size distribution graph of meso$CaFe_2O_4$-2 NP which was obtained from desorption isotherm using BJH method. The pore size distribution was found to be narrow and with uniform monodispersed pores. Presence of single peak indicate monodispersed nature of pores. The pore diameter was found to be 5.2 nm which is in well agreement with the pore size obtained from TEM micrographs. These pores of size nearly equal to micelle size of CTAB are generated via CTAB removal [1] [8]. Uniformity of pore size and absence of any other peak in pore size distribution suggested generation of pore only through the CTAB. The pore volume of meso$CaFe_2O_4$-2 NP was found to be 0.142 cm^3/g. Comparable range of porosity were recently reported for the mesoporous Fe_3O_4 NPs [1]. Recently Jian-Liang Cao et al has reported surface area of 94 m^2/g for mesoporous $CoFe_2O_4$ prepared via CTAB assisted method [9]. For CTAB assisted mesoporous $ZnFe_2O_4$ NP also similar ranges of porosity has been reported [10]. The obtained surface area and pore volume of meso$CaFe_2O_4$-2 NP is many fold higher than those of meso$CaFe_2O_4$-1 NP. Higher porosity of a nanocarrier is desired for drug delivery application which provide high drug loading capacity. Therefore, for further studies such Dox loading/release experiments and biocompatibility test MTT assay, meso$CaFe_2O_4$-2 NP were used.

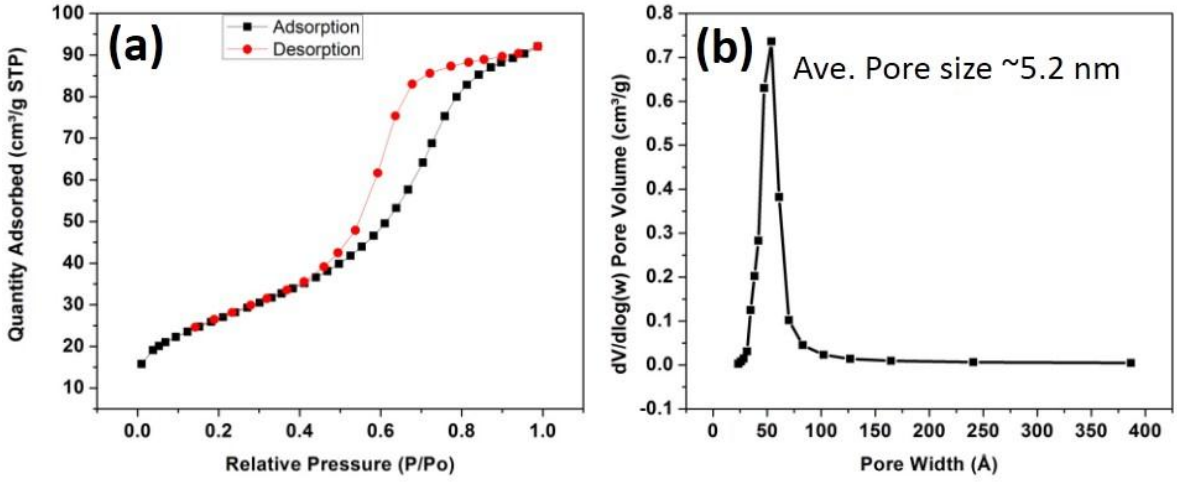

Figure 4.8.8. (a) N_2 adsorption and desorption isotherm of the meso$CaFe_2O_4$-2 NP. (b) pore size distribution of meso$CaFe_2O_4$-2 NP obtained from desorption isotherm.

4.8.2.4 Dox loading and release study

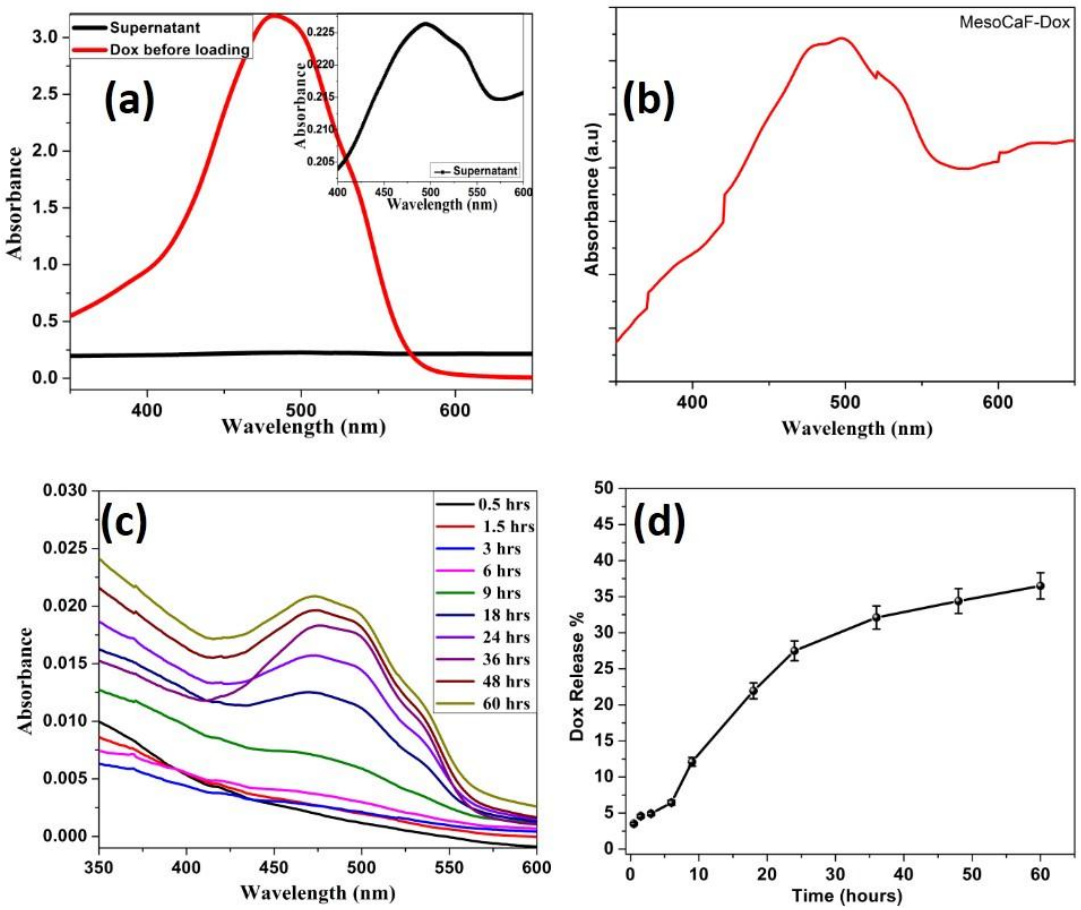

Figure 4.8.9. (a) Combined UV-Vis absorption spectra of Dox before loading and remained Dox in supernatant. Inset figure of (a) shows only UV-Vis absorption spectra of Dox remained in supernatant. (b) (UV-Vis absorption spectra of Dox loaded meso$CaFe_2O_4$ NP (meso$CaFe_2O_4$-Dox NP). (c) UV-Vis absorption spectra of Dox released from meso$CaFe_2O_4$-Dox NP at different time in PBS. (d) Time dependent Dox release profile in PBS of meso$CaFe_2O_4$-Dox NP.

Figure 4.8.9(a) shows UV-Vis absorption spectra of Dox before loading and Dox in supernatant which were used calculate the amount of Dox loaded in meso$CaFe_2O_4$-2 NP as well as left in supernatant. The complete suppression of absorption intensity of Dox in supernatant than of before loading shows excellent loading ability of Dox in meso$CaFe_2O_4$-2 NP. The Dox loading efficiency and loading capacity of meso$CaFe_2O_4$-2 NP were found to be 93 % and 4.6 % respectively. The obtained loading efficiency and loading capacity of meso$CaFe_2O_4$-2 NP are very high which shows that meso$CaFe_2O_4$-2 NP has good potential as a nanocarrier for targeted Dox delivery.

Loading of Dox in meso$CaFe_2O_4$-2 NP was confirmed by UV-Vis absorption spectra of Dox loaded meso$CaFe_2O_4$-2 NP (meso$CaFe_2O_4$-Dox NP). Figure 4.8.9(b) shows UV-Vis

absorption spectra of meso$CaFe_2O_4$-Dox NP. Appearance of characteristic absorption peak of Dox at ~500 nm wavelength in the UV-Vis absorption spectra of meso$CaFe_2O_4$-Dox NP also confirmed loading of Dox in meso$CaFe_2O_4$-Dox NP. After successful loading of Dox in meso$CaFe_2O_4$-2 NP and its confirmation, in vitro release study Dox from meso$CaFe_2O_4$-Dox NP were carried out in PBS. In vitro Dox release behavior from meso$CaFe_2O_4$-Dox NP were studied using UV-Vis spectroscopy. Figure (c) shows UV-Vis absorption spectra of Dox released from meso$CaFe_2O_4$-Dox NP at different time in PBS medium. Increase in the absorption intensity with time can be seen in the figure which is due to the increase in accumulative amount of Dox in releasing medium with time. Figure (d) shows Dox release profile in PBS medium with different time. It was observed that up to 24 hours the Dox release was ~27% and which reached to ~ 36 % up to final 60 hours. In the starting hours (up to 24 hours) the release rate was faster and there after it became very slow. The overall Dox release behavior was found to be sustained in nature. Sustained and slow release of anticancer drug is desirable for a long-term effect as well as to reduce systemic toxicity of anticancer drug.

4.8.2.5 Biocompatibility study

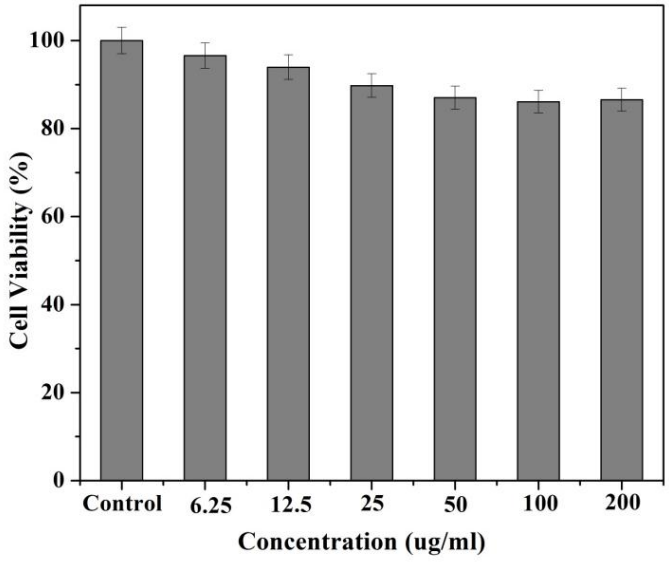

Figure 4.8.10. (a) Cell viabilities obtained by MTT assay of RAW 264.7 cells incubated with different amount of meso$CaFe_2O_4$-2 NP.

For drug delivery application nanocarrier must be biocompatible. The in vitro biocompatibility of meso$CaFe_2O_4$-2 NP was studied against normal RAW264.7 macrophages cells. Dose dependent cell viability of RAW264.7 cells are shown in figure 4.8.10. The cells were treated with 6.25, 12.5, 25, 50, 100, and 200 µg/ml of meso$CaFe_2O_4$-2 NP. A dose dependent very

minute killing of cells was observed. About 87% cells viability was observed at highest dose of 200 µg/ml. Thus, prepared meso$CaFe_2O_4$-2 NP dosed not shows toxic effect on the normal cells and is suitable for nanocarrier based drug delivery application. The good biocompatibility of meso$CaFe_2O_4$-2 NP can be attributed to the inherent biocompatible nature of constituent elements of meso$CaFe_2O_4$-2 NP such Calcium and Iron.

4.8.3 Conclusions

meso$CaFe_2O_4$ NPs have been synthesized by two different method. Obtained meso$CaFe_2O_4$ NPs were characterized for their structural, morphological and magnetic properties. meso$CaFe_2O_4$-2 NP prepared using CTAB assisted method showed more porosity than oleic acid based meso$CaFe_2O_4$-1 NP. XRD, HRTEM, BET analysis confirmed successful formation of meso$CaFe_2O_4$ NPs. VSM results have suggested superparamagnetic nature of meso$CaFe_2O_4$ NPs. MTT assays results of meso$CaFe_2O_4$ NPs against normal cells suggested its biocompatibility. Prepared meso$CaFe_2O_4$ NPs showed a good Dox loading ability with sustained Dox release behavior. A high LE (93%) and LC (4.6 %) were observed. meso$CaFe_2O_4$ NPs based drug nanocarrier could find potential application in targeted drug delivery application because of biocompatibility, magnetic nature and high loading ability.

4.8.4 References

[1] K. Asghar, M. Qasim, G. Dharmapuri, D. Das, Investigation on a smart nanocarrier with a mesoporous magnetic core and thermo-responsive shell for co-delivery of doxorubicin and curcumin: a new approach towards combination therapy of cancer, RSC Adv. 7(46) (2017) 28802-28818.
[2] L. Khanna, N.K. Verma, PEG/CaFe2O4 nanocomposite: Structural, morphological, magnetic and thermal analyses, Physica B: Condensed Matter 427 (2013) 68-75.
[3] A. Samariya, S.N. Dolia, A.S. Prasad, P.K. Sharma, S.P. Pareek, M.S. Dhawan, S. Kumar, Size dependent structural and magnetic behaviour of CaFe2O4, Current Applied Physics 13(5) (2013) 830-835.
[4] B.Y. Yu, S.-Y. Kwak, Assembly of magnetite nanocrystals into spherical mesoporous aggregates with a 3-D wormhole-like pore structure, Journal of materials chemistry 20(38) (2010) 8320.
[5] W. Zhang, X. Zheng, S. Shen, X. Wang, Doxorubicin-loaded magnetic nanoparticle clusters for chemo-photothermal treatment of the prostate cancer cell line PC3, Biochemical and Biophysical Research Communications 466(2) (2015) 278-282.
[6] J. Liu, Z. Sun, Y. Deng, Y. Zou, C. Li, X. Guo, L. Xiong, Y. Gao, F. Li, D. Zhao, Highly water-dispersible biocompatible magnetite particles with low cytotoxicity stabilized by citrate groups, Angewandte Chemie 48(32) (2009) 5875-9.
[7] C. Cheng, Y. Wen, X. Xu, H. Gu, Tunable synthesis of carboxyl-functionalized magnetite nanocrystal clusters with uniform size, Journal of materials chemistry 19(46) (2009) 8782.
[8] P.S.G.a.V.K. Aswal, Micellar structure and inter-micelle interactions in micellar solutions: Results of small angle neutron scattering studies, CURRENT SCIENCE 80(8) (2001) 972-979.
[9] J.-L. Cao, Z.-L. Yan, Y. Wang, G. Sun, X.-D. Wang, H. Bala, Z.-Y. Zhang, CTAB-assisted synthesis of mesoporous CoFe2O4 with high carbon monoxide oxidation activity, Materials Letters 106 (2013) 322-325.
[10] M. Su, C. He, V.K. Sharma, M. Abou Asi, D. Xia, X.Z. Li, H. Deng, Y. Xiong, Mesoporous zinc ferrite: synthesis, characterization, and photocatalytic activity with H2O2/visible light, Journal of hazardous materials 211-212 (2012) 95-103.

CHAPTER 5: SUMMARY AND CONCLUSIONS

Chapter 5

Summary and conclusions

In this thesis, preparation, characterization and biomedical applications of different advanced multifunctional magnetic nanoparticles have been discussed. This chapter gives summary and conclusions of the results of the present work and the scopes for future research in this area.

Chapter 1 described a general introduction about the area and multifactional magnetic nanoparticles (MFMNPs) for biomedical applications. A thorough critical review on the preparation of MNPs, various MFMNPs and their associated problems and objectives of the present research have been discussed have been discussed in *chapter 2*. *Chapter 3* described the details of synthesis processes. First, different types of MNPs have been synthesized and characterized. Then, different multifunctional nanocomposites nanoparticles such as NZF@Alb, Fe_3O_4@Alb, CF@Alb, $mSiO_2$-$CaFe_2O_4$@P(Nipam-Aa), meso$CaCO_3$@$CaFe_2O_4$, NZF@$mSiO_2$, NZF@$mSiO_2$-CuS-PEG, NZF/$Zn_{0.95}Ni_{0.05}O$, NZF/$Zn_{0.95}Ni_{0.05}O$-$mSiO_2$, $mSiO_2$@AgNPs, $mSiO_2$@Ag-Fe_3O_4@P(Nipam) and meso$CaFe_2O_4$ NPs have been prepared. Obtained results on above mentioned samples have been discussed in different sections of the *chapter 4*.

5.1 Synthesis and characterization of different magnetic nanoparticles (MNPs):

Different MNPs (such as Fe_3O_4 NPs, $CoFe_2O_4$ NPs, $Ni_{0.5}Zn_{0.5}Fe_2O_4$, and $CaFe_2O_4$ NPs) having size ~10-30 nm, with monodispersed, well crystalline, superparamagnetic in nature have successfully been synthesized by simple methods and characterized.

5.2 Albumen based magnetic nanoparticles (NZF@Alb & NZF@Alb-Dox NPs and Fe_3O_4@Alb & CF@Alb NPs):

Inexpensive, biocompatible and highly functional egg albumen has been demonstrated as a versatile coating material for MNPs. Novel, multifunctional, pH responsive, magnetically guidable, water dispersible, biocompatible and superparamagnetic NZF@Alb, NZF@Alb-Dox NPs, Fe_3O_4@Alb NP, Fe_3O_4@Alb-Dox NP, and CF@Ab NP have been successfully prepared by simple and eco-friendly method using egg albumen and characterized by various techniques. Average particles size of NZF@Alb, Fe_3O_4@Alb NP and CF@Alb were found to be in between 100-120 nm. Dox LE and LC of NZF@Alb were found ~90% and ~5% respectively. A sustained and pH dependent Dox release profile was observed. In vitro anticancer activity of

NZF@Alb-Dox (IC_{50} value ~20µg/ml) and Fe_3O_4@Alb-Dox NPs (IC_{50} value in between 20-40 µg/ml) against HeLa cells were also carried out by MTT assay and both have shown a promising anticancer activity. A large Ms values (NZF@Alb NPs-36 emu/gm, Fe_3O_4@Alb-25.7 emu/gm, CF@Alb- ~64 emu/gm) for nanocarrier has been observed. It is suggested that this scalable and pH responsive albumen based magnetic nanoformulation would have potential application in targeted and controlled delivery of anticancer drugs, hyperthermia and MRI for cancer treatment.

5.3 Thermoresponsive multifuntional $mSiO_2$-$CaFe_2O_4$@P(Nipam-Aa) nanocomposites: Biocompatible, magnetic, multifunctional, thermoresponsive, and novel $mSiO_2$-$CaFe_2O_4$@P(Nipam-Aa) nanocomposite (size ~330 nm) have successfully been synthesized and characterized. It was also observed that MPS modification on $mSiO_2$ surface, improve the coating of P(Nipam-Aa) polymer on surface of $mSiO_2$. The superparamagnetic $mSiO_2$-$CaFe_2O_4$@P(Nipam-Aa) NC (Ms value ~7-10 emu/g) has showed very good Dox loading efficiency (~98%) and loading capacity (~6%), which are highest among the studied systems. A sustained and temperature dependent Dox release behavior was obtained. An enhanced anticancer activity than free Dox against Hela cells was observed with the IC_{50} value in between ~5 ug/ml. The present nanoformulation could get application in targeted and controlled drug delivery and chemo-hyperthermia therapy.

5.4 Multifunctional mesoCaCO₃@CaFe₂O₄ NC prepared by green route:

In this work, egg shell derived $CaCO_3$ based novel, pH responsive, magnetically guidable, biocompatible and superparamagnetic multifunctional mesoporous nanocarrier (mesoCaCO₃@CaFe₂O₄ NC) (of size ~150 nm) have been developed for the first time by green route using lemon juice and waste egg shell. mesoCaCO₃@CaFe₂O₄ NC showed a good M_s values of 20 emu/g. Apart from a good Dox loading ability (LE ~95% and LC~4%) a sustained and pH dependent Dox release profile were obtained which is required for drug delivery. IC_{50} value of mesoCaCO₃@CaFe₂O₄-Dox NC against Hela cells were found to be in between 10-20 µg/ml. Prepared mesoCaCO₃@CaFe₂O₄-Dox NC are suitable for application in pH triggered targeted drug delivery. The use of biocompatible and biodegradable mesoCaCO₃@CaFe₂O₄ NC, prepared via a green route, in nanomedicine will be safe, inexpensive and environmental friendly.

5.5 Multifunctional NZF@mSiO$_2$ and NZF@mSiO$_2$-CuS-PEG:

First, biocompatible and superparamagnetic NZF@mSiO$_2$ core shell nanocarrier of size ~200-400 nm was successfully synthesized and then it was used to prepare novel NIR active multifunctional NZF@mSiO$_2$-CuS-PEG NC for simultaneous multi-modal imaging and combined chemo- and photothermal therapies. The M_s values for superparamagnetic NZF, NZF@mSiO$_2$ and NZF@mSiO$_2$-CuS-PEG NC were found to be 56, 9.5 and 7 emu/gm respectively. The very high 5 Fluorouracil loading ability of NZF@mSiO$_2$-CuS-PEG NC (LE 79% and LC 21%) was attributed to the amine functionalization of mesoporous silica. NZF@mSiO$_2$-CuS-PEG-5Flu NC has showed a relatively fast drug release (56% in 12hrs and 13 % in between12-80 hrs) behavior than other prepared nanocarrier. MTT assay against normal RAW 264.7 cells showed biocompatible nature of nanocarriers.

5.6 Multifunctional NZF/Zn$_{0.95}$Ni$_{0.05}$O (NZF@Zn) and NZF/Zn-mSiO$_2$ nanocomposites:

Magneto-optical NZF@Zn NCs (size ~70 nm) have been synthesized successfully by a simple and cost-effective sol gel technique using egg albumen and characterized for their structural, optical, and magnetic properties. Magnetically separable and visible light active NZF@Zn NC showed enhanced photo-decoloration of the RhB dye, compare to that by pure NZF or Zn$_{0.95}$Ni$_{0.05}$O, under solar light irradiation. NZF@Zn NC may be very useful for the photodegradation of toxic biomedical waste. In second part of this work, multifunctional NZF@Zn-mSiO$_2$ nano-system (size ~150-300 nm) which combine superparamagnetic and optical properties along with drug loading ability, have been prepared and characterized using different techniques. The Ms values of superparamagnetic NZF@Zn-mSiO$_2$ NC was found to be 4.2 emu/gm. A high Curcumin loading (LE 84% and LC 21%) and sustained Cur release (~19 % release upto 48 hrs) behavior were observed. Prepared NZF@Zn-mSiO$_2$ NC dose not shows toxic effect on the normal cells may be due to the coating of biocompatible silica. The NZF@Zn-mSiO$_2$-Cur NC is suitable candidate for simultaneous multimodal imaging and chemotherapy for cancer treatment.

5.7 Multifunctional mSiO$_2$@AgNPs and mSiO$_2$@Ag-Fe$_3$O$_4$@P(Nipam) NC:

In first part of this work, mSiO$_2$@Ag NPs (size ~400nm) have successfully been prepared, characterized and their anticandidal activities against *Candida. albicans 007* have been studied. These mSiO$_2$@Ag NPs have shown excellent anticandidal activities and could be a promising alternative to the conventional Ag based antimicrobial agents. Mesopores (~4-6 nm) were generated by removal of CTAB template. A possible mechanism is suggested for the

anticandidal activity of SiO_2@AgNPs against *C. albicans* 077. In addition, magnetically controllable, biocompatible, and thermoresponsive multifuntional $mSiO_2$@Ag-Fe_3O_4@P(Nipam) NC has also been successfully prepared by in situ coating of P(Nipam) on the surface of magneto-optical $mSiO_2$@Ag-Fe_3O_4 in the presence of oxidizer and crosslinker. Prepared smart nanocomposites have been characterized by structural, morphological and magnetic properties. Ms value of $mSiO_2$@Ag-Fe_3O_4@P(Nipam) NC was found to be 21.7 emu/gm which is very high and good enough to be controlled/targeted/separated using external magnetic source. Prepared $mSiO_2$@Ag-Fe_3O_4@P(Nipam) NC was found to be biocompatible against normal cells. Multifunctional $mSiO_2$@Ag-Fe_3O_4@P(Nipam) NC could act as intelligent antimicrobial agent, multi modal imaging agent and could also find application in chemo-photothermal therapy cancer treatment.

5.8 Mesoporous $CaFe_2O_4$ NPs (meso$CaFe_2O_4$ NPs):

In this work, different meso$CaFe_2O_4$ NPs have been synthesized by coprecipitation route followed by calcination. Obtained meso$CaFe_2O_4$ NPs were characterized for their structural, morphological and magnetic properties. meso$CaFe_2O_4$-2 NP prepared using CTAB as template showed more porosity than oleic acid based meso$CaFe_2O_4$-1 NP. meso$CaFe_2O_4$ NP was found biocompatible in nature. meso$CaFe_2O_4$ NPs has good Dox loading ability (LE 93% and LC 4.6 %) with sustained Dox release behavior were observed. meso$CaFe_2O_4$ NPs based drug nanocarrier could find potential application in targeted drug delivery.

Nanocarrier containing $CaFe_2O_4$ or Fe_3O_4 NPs as magnetic unit and mesoSiO_2 or $CaCO_3$ or albumen as drug reservoir could find potential application in drug delivery because of it biocompatibility and good drug loading ability. All the results presented in this thesis are significant contributions to the design and development of advanced MFMNPs for biomedical applications and may open enormous opportunities for the simultaneous or combined therapeutic and diagnostic applications.

5.9 Future scope of the work:

The presented work may be taken forward in many aspects as follows. Biocompatibility, control release ability and specific targeting ability of these nanocarrier may further be enhanced by functionalization with suitable biodegradable polymers and biomolecules such as, PLGA, lipids, PEG, antibodies and ligands etc. Extensive biological evaluations and long term biological effect (both *in vitro* and *in vivo*) of these prepared MFMNPs are needed, particularly if these nanosystems are to be translated into clinic. Degradation study (of both core MNPs and

carrier materials), long term stability of prepared multifunctional nanosystems should be studied in physiological conditions. Magnetic hyperthermia triggered drug release from the thermoresposive magnetic nanoparticles and heating ability of prepared MFMNPs should be evaluated in the presence of alternative magnetic field. Multimodal or MRI based imaging ability of these MFMNPs may be evaluated and further different imaging agent such as fluorescent quantum dot, radio nuclei, dye molecules may incorporated to enhanced multifunctionality of the prepared systems.